Thermal analysis of the Wire and Arc Additive Manufacturing process using the F.E. method

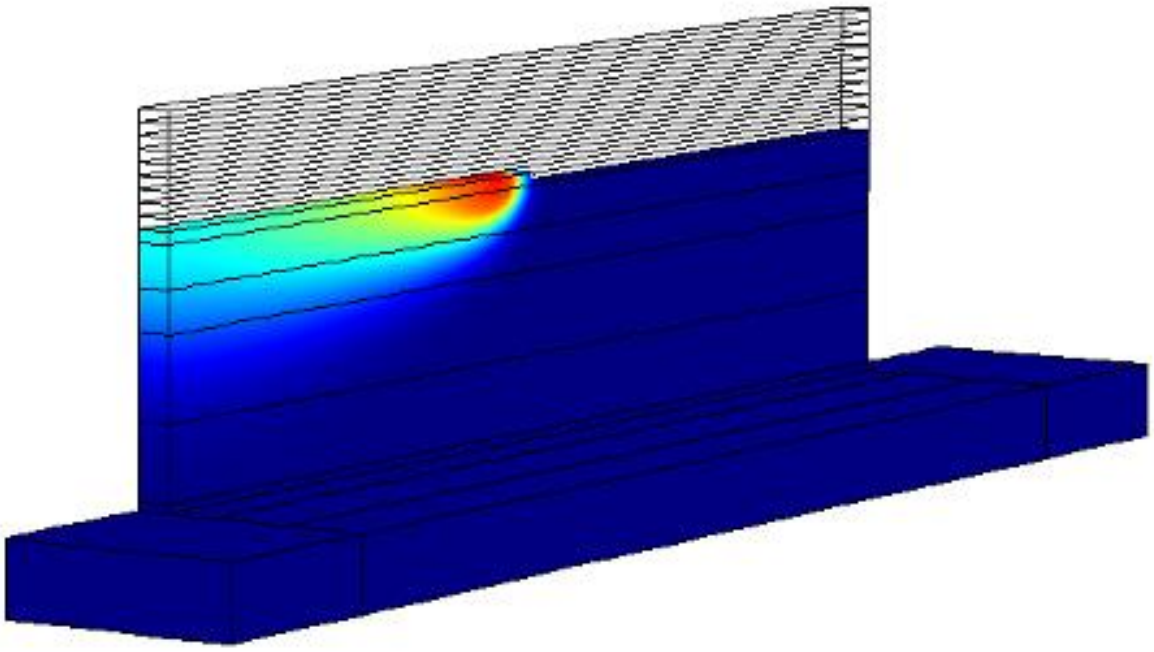

TU Delft

Author: R.N. Veenstra

Thermal analysis of the Wire and Arc Additive Manufacturing process using the F.E. method

By

R.N. Veenstra

in partial fulfilment of the requirements for the degree of

Master of Science
in Mechanical Engineering
Materials Engineering & Applications

at the Delft University of Technology,
to be defended publicly on Friday August 25, 2023, at 2:00 PM.

Student number:	1368109	
Supervisor:	Dr.ir. M.J.M. Hermans,	TU Delft
Thesis committee:	Dr. V. Popovich,	TU Delft
	Dr.ir. C. Goulas,	University of Twente

TU Delft

Acknowledgements

With this master thesis I conclude my study Mechanical Engineering at the University of Technology in Delft. Throughout my studies I have become interested in welding technology, as it combines the technical fields of mechanical engineering and materials science.

The completion of this thesis was at times challenging, I would therefore like to thank the people that supported me during this period.

First of all, I want to express my gratitude to Dr.ir. Marcel Hermans for your support during this research project and a previous project on the topic of welding parameter optimization to Improve the productivity and prevent welding defects in the transition to welding of thick-walled structures. In this regard, I also want to acknowledge Prof.Dr. Ian Richardson. It gave me the opportunity to do research in a topic in which I am very interested. I have always appreciated the discussions as they provided useful insights and guidance, and motivated me to become more experienced in the subject of computational mechanics and materials science.

In addition, I want to thank Dr.ir. Constantinos Goulas for your encouragement during this research project and your support to implement the cooling method in an experimental setup and develop a method to study the effect of the cooling methods on the microstructure of the deposited material in the wire and arc additive manufacturing process. Hereby, I also want to acknowledge the people of the MSE department, in particular the lab technicians Jurriaan van Slingerland and Remko Seijffers. Further, I appreciated the meetings with Vamsi Paruchuri to explore the most suitable techniques to describe the temperature field that is experienced in the wire and arc additive manufacturing process using the F.E. method.

In conclusion, I want to emphasize that the past period has been very valuable to me. I look forward to sharing my experiences and taking on new challenges.

Delft, University of Technology R.N. Veenstra
August 2023

Table of Contents

Abstract

In this research, a thermal analysis of the wire and arc additive manufacturing process is presented based on the F.E. method. The F.E. model that is presented in this research allows to describe the temperature field that is experienced by both the component and the deposited material in the wire and arc additive manufacturing process.

In the wire and arc additive manufacturing process a component is produced by the subsequent addition of layers of metal using a moving welding heat source. An important aspect of the wire and arc additive manufacturing process is the temperature field that is experienced by the component, characterized by the periodic thermal cycling of the temperature values. The locally varying temperature field affect the microstructural transformations and the microstructural morphology of the deposited material that constitutes the component. In this regard, the temperature field has a significant effect on the stress distribution, microstructure and the mechanical properties of the component. Without the control of the temperature field that results from the the wire and arc additive manufacturing process, the stress induced deformations result in a poor dimensional accuracy, a poor surface finish and the loss of the structural integrity. Further, the formation of undesired microstructural characteristics is promoted without the adequate temperature control causing the deterioration of the mechanical properties.

Two cooling methods are proposed to control the heat dissipation from the component to the environment based on the application of an interlayer waiting time and immersing the component into a cooling medium. The effect of the cooling methods is studied by reviewing variations of the cooling methods using five test cases, considering variations of the cooling methods defined as natural cooling, active substrate cooling and active component cooling. The wire and arc additive manufacturing process is implemented in an experimental setup and the F.E. model, whereby a multilayer weld deposit is deposited on top of a stationary component base wall. The effectiveness of the cooling methods is evaluated in terms of the temperature field that is experienced by the material constituting both the component and the multilayer weld deposit. While the microstructure that results from the application of the cooling methods is evaluated regarding the deposited material constituting the multilayer weld deposit.

An important quality of the F.E. model that is presented in this research is to describe the temperature field that is experienced by the deposited material in the wire and arc additive manufacturing process. In contrast to the traditional method of monitoring the substrate temperature, the F.E. model allows to describe the temperature field that is experienced by the deposited material that constitutes both the multilayer weld deposit and the component. Accordingly, the F.E. model is capable to describe the effect of the locally attained temperature field on the microstructure of the deposited material constituting the multilayer weld deposit in terms of the thermal characteristics including the temperature distribution, the locally attained temperature values, the cooling rates and the temperature gradients throughout the component.

The results show a significant effect of the cooling methods on the temperature field that is experienced by the material constituting both the multilayer weld deposit and the component. Indicating that the cooling methods that are proposed in this research are effective to control the microstructure and the temperature field that is experienced by the component in the wire and arc additive manufacturing process. The resulting microstructure is characterized in terms of the microstructural morphology and the microstructural constituents, using optical microscopy based on the average grain size and the distribution of alloying elements throughout the material constituting the multilayer weld deposit. In addition, the average grain size and the distribution of the alloying elements throughout the material are evaluated in terms of the hardness values.

1 Introduction

1.1 Background

In this research, a thermal analysis of the wire and arc additive manufacturing process is presented based on the F.E. method. The F.E. model that is presented in this research allows to describe the temperature field that is experienced by both the component and the deposited material in the wire and arc additive manufacturing process.

1.1.1 Wire and arc additive manufacturing process

This research focuses on the wire and arc additive manufacturing process whereby an arc welding heat source is used for the production of components by the subsequent addition of layers of material, as illustrated in Figure 1.

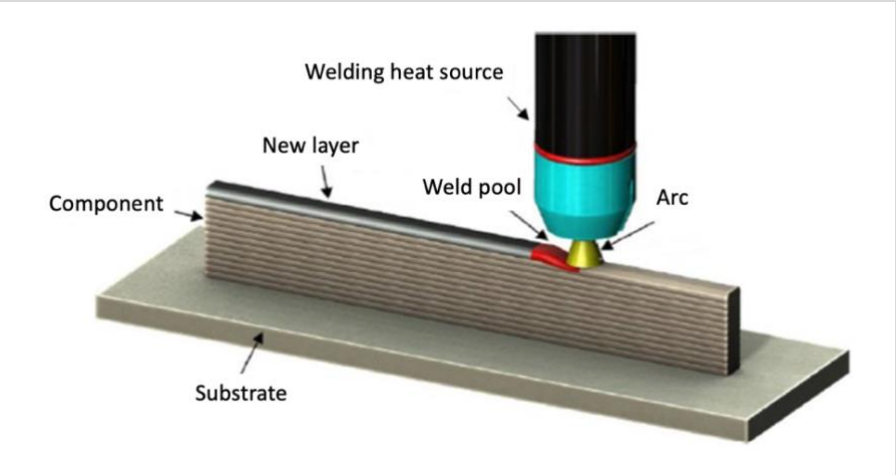

Figure 1: Schematic representation of the wire and arc additive manufacturing process [1].

The wire and arc additive manufacturing process is a promising technique to manufacture medium to large-scale metal components that are expensive to manufacture with conventional production methods (e.g., milling, casting) [2], [3]. Therefore, the wire and arc additive manufacturing technology has a great potential to produce complex near-net-shape metal components on-demand. In addition to the increased production efficiency and cost-effectiveness, the wire and arc additive manufacturing technology enables to improve and optimize the design of metal components that cannot be achieved with conventional production processes [4], [5]. As an example, three components that are produced by the wire and arc additive manufacturing process using computer aided design, are shown in Figure 2.

Figure 2: Components that are produced by the wire and arc additive manufacturing process. [a] Hollow propeller blade, NiBrAl; [b] Robot arm with optimized topology, stainless steel 316L; [c] Rocket Thruster with added functionalities, stainless steel 308L [6].

1.1.1.1 Metal additive manufacturing processes

The metal additive manufacturing processes using the direct energy deposition method are categorized based on the energy source and the material that is used for the material deposistion, as shown in Figure 3.

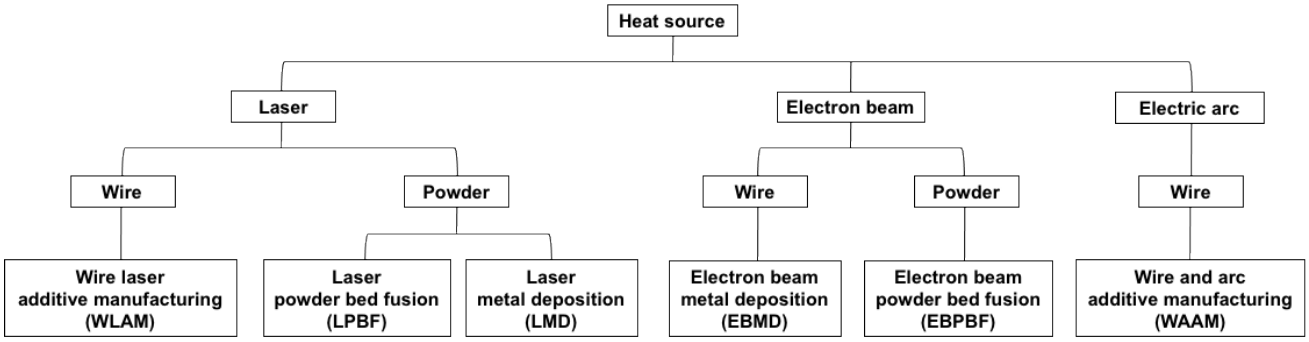

Figure 3: Classification of the metal additive manufacturing processes based on the energy source and the material deposistion [7].

In the laser-based and electron beam-based additive manufacturing processes, the material is either supplied in the form of a metal powder or a metal wire. The laser-based and electron beam-based processes are superior in terms of a dimensional accuracy. However, the application of these techniques is restricted due to the high costs and the low process efficiency [2], [4]. Accordingly, these techniques are suitable for the production of small complex shaped components with a high geometrical complexity [3].

In the wire and arc additive manufacturing (WAAM) process, an electric arc welding process is used for the material deposition. Accordingly, both the heat input and the material deposition are governed by the arc welding heat source [1]. The high deposition rate and the high process efficiency of the arc welding heat source allows to produce components with a low to medium geometrical complexity [4]. In this manner, the wire and arc additve manufacturing process allows to produce complex near-net-shape components with a good surface finish and good material properties [2], [5]. Another important aspect of the wire and arc additive manufacturing process is the broad range of materials that is available for the arc welding process including aluminium, steel, bronze, and copper-based alloys [3], [4]. A comparison of various metal additive manufacturing processes, is shown in Figure 4 and Table 1.

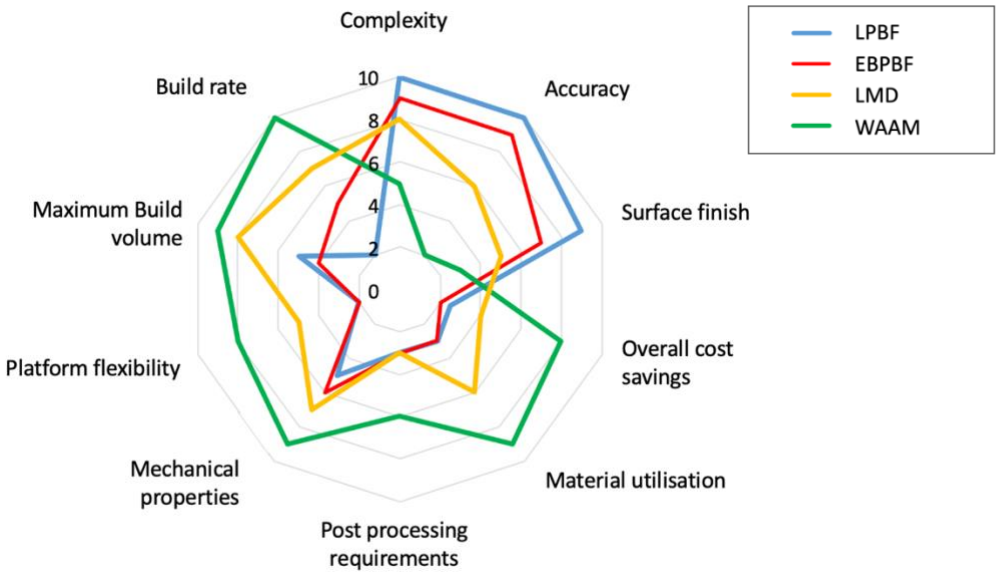

Figure 4: Comparison of a selection of metal additive manufacturing processes [8].

Table 1: Technical characteristics of various metal additive manufacturing processes [8].

	LPBF	EBPBF	LMD	WAAM
Energy [W]	$100 - 1000$	~ 3500	$\sim 500 - 3000$	$2000 - 3000$
Process efficiency [−]	$2\ \% - 5\ \%$	$15\ \% - 20\ \%$	$2\ \% - 5\ \%$	$70\ \%$
Dimensional accuracy [mm]	± 0.04	± 0.05	± 0.13	± 0.2
Build rate [kg/h]	$0.1 - 0.18$	$0.26 - 0.36$	$0.1 - 0.141$	$0.5 - 0.4$
Maximum Build volume [mm^3]	$500 \times 350 \times 300$	$200 \times 200 \times 180$	$900 \times 1500 \times 900$	Unlimited
Layer Thickness [µm]	$20 - 100$	~ 100	$500 - 1000$	$1000 - 2000$
Surface Roughness [µm]	$4 - 11$	$25 - 35$	$20 - 50$	500
Minimum Build size [µm]	$40 - 200$	100	$150 - 200$	2000

As shown in Figure 4, the wire and arc additive manufacturing process is superior compared to the laser-based and electron beam-based processes among other aspects in terms of process efficiency, deposition rate, process flexibility, material utilisation, mechanical properties and the maximum component size [8].

1.1.1.2 Challenges

An important aspect of the wire and arc additive manufacturing process is the temperature field that is experienced by the deposited material that forms the component. In the wire and arc additive manufacturing process, both the heat input and the material deposition are governed by the arc welding heat source [1]. Accordingly, the component is subjected to a non-linear temperature field that is characterized by the periodic thermal cycling of the temperature values [9]. The locally varying temperature field affects the resulting microstructure of the material constituting the component. In this regard, the temperature field has a significant effect on the stress distribution, microstructure, and the mechanical properties of the component [5], [3].

Without the control of the temperature field that results from the wire and arc additive manufacturing process, the stress induced deformations result in a poor dimensional accuracy, a poor surface finish and the loss of the structural integrity of the component [10], [11]. Further, the formation of undesired microstructural characteristics is promoted without the adequate temperature control causing the deterioration of the mechanical properties [5], [2]. Although the components that are produced by the wire and arc additive manufacturing process possess high density and excellent strength properties, the components are prone to high residual stresses and distortions due to the high heat input and the high deposition rates that are associated with the arc welding heat source [12]. As an illustration, the loss of the structural integrity that can occur as a result of poor temperature control in the wire and arc additive manufacturing process, is shown in Figure 5.

Figure 5: Thin wall twist bottle produced by the wire and arc additive manufacturing process. [a] Natural cooling; [b] Active substrate cooling [13].

In previous studies different methods are proposed to control the temperature field in the wire and arc additive manufacturing process. The most common approach is through the application of an interlayer waiting time, defined by either a fixed idle time or a fixed interlayer temperature [14], [15]. Another method is the application of a cooling medium to increase the heat dissipation from the component to the environment. The cooling medium can either be applied in the form of a cooling gas that is aimed at the deposited material or by immersing the component into a cooling medium .

The use of a cooling medium to increase the heat dissipation from the component to the environment allows to control the temperature field that is experienced during the deposition process of the wire and arc additive manufacturing process. Hence, the resulting microstructure and the mechanical properties of the deposited material that forms the component can be controlled, and the thermal induced residual stresses and distortions can be mitigated [16]. Further, the productivity of the wire and arc additive manufacturing process can be improved by reducing the interlayer waiting time while maintaining a high deposition rate [2].

This research aims to provide a better insight in the locally attained temperature field and the effect on the resulting microstructure of the deposited material in the wire and arc additive manufacturing process. Although various studies are available on the numerical simulation of the thermal analysis of the laser-based and electron beam-based additive manufacturing processes. The thermal analysis of the wire and arc additive manufacturing process is currently still developing as a research topic [2], [11]. In this research, two cooling methods are proposed to control the heat dissipation from the component to the environment based on the application of an interlayer waiting time and immersing the component into a cooling medium. A schematic representation of the heat input and the heat dissipation in the wire and arc additive manufacturing process considering both natural cooling and the application of a cooling medium, is shown in Figure 6.

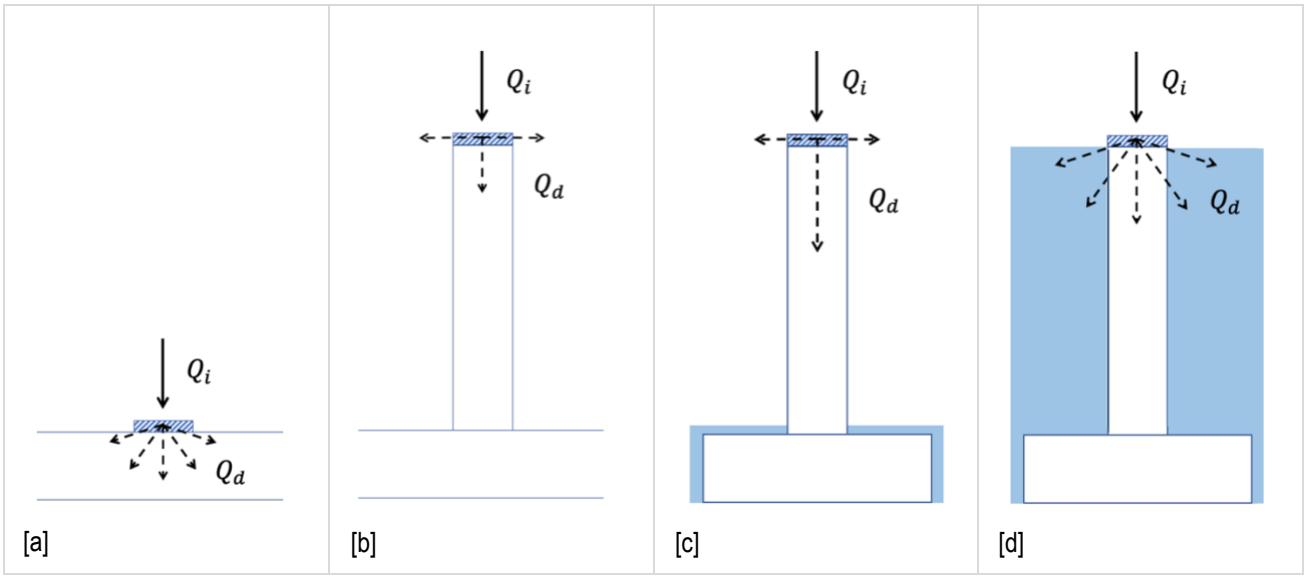

Figure 6: Schematic representation of the heat input (Q_i) and the heat dissipation (Q_d) in the wire and arc additive manufacturing process, based on [17]. [a] Natural cooling: substrate; [b] Natural cooling: component; [c] Active substrate cooling; [c] Active component cooling.

1.2 Research objective

The main objective of this research is to provide a thermal analysis of the wire and arc additive manufacturing process using the F.E. method. Two cooling methods are proposed to control the heat dissipation from the component to the environment based on the application of an interlayer waiting time and immersing the component into a cooling medium. The effect of the cooling methods on the temperature field and the resulting microstructure is evaluated by reviewing variations of the cooling methods considering five test cases.

1.2.1 Research method

In this research, two cooling methods are proposed to control the heat dissipation from the component to the environment:

1. Increased interlayer wating time
2. Application of a cooling medium

The cooling methods are evaluated using the followiing test cases:

i. Natural cooling

Test case 1: Natural cooling; interlayer waiting time of 40s.
Test case 2: Natural cooling; interlayer waiting time of 80s.

ii. Active substrate cooling

Test case 3: Active substrate cooling; interlayer waiting time of 20s.
Test case 4: Active substrate cooling; interlayer waiting time of 40s.

iii. Active component cooling

Test case 5: Active component cooling; interlayer waiting time of 40s.

In the case of natural cooling, the heat dissipation from the component to the environment is accommodated by free convection to air. While in the case of both active substrate cooling and active component cooling, a cooling medium is used to increase the heat dissipation from the component to the environment. With regard to active substrate cooling, the substrate is immersed into the cooling medium. While in the case of active component cooling, both the substrate and the component base wall are immersed into the cooling medium.

The cooling methods are evaluated by implementing the wire and arc additive manufacturing process in an experimental setup and the F.E. model. In this research, a multilayer weld deposit is deposited on top of a component base wall by the subsequent addition of layers of material. The layers of material are added in the form of single-pass weld layers by the deposition of a metal wire under the influence of a moving welding heat source.

The effectiveness of the cooling methods is described in terms of the temperature field that is experienced by the deposited material constituting the multilayer weld deposit and the component using the F.E. method. Accordingly, the F.E. model that is presented in this research is used to describe the resulting microstructure of the deposited material considering the locally attained chemical composition and the temperature field that result from the application of the cooling methods as defined in the test cases 1 to 5.

1.3 Research outline

The F.E. model that is presented in this research allows to describe the thermal analysis of the wire and arc additive manufacturing process, as shown in Figure 7.

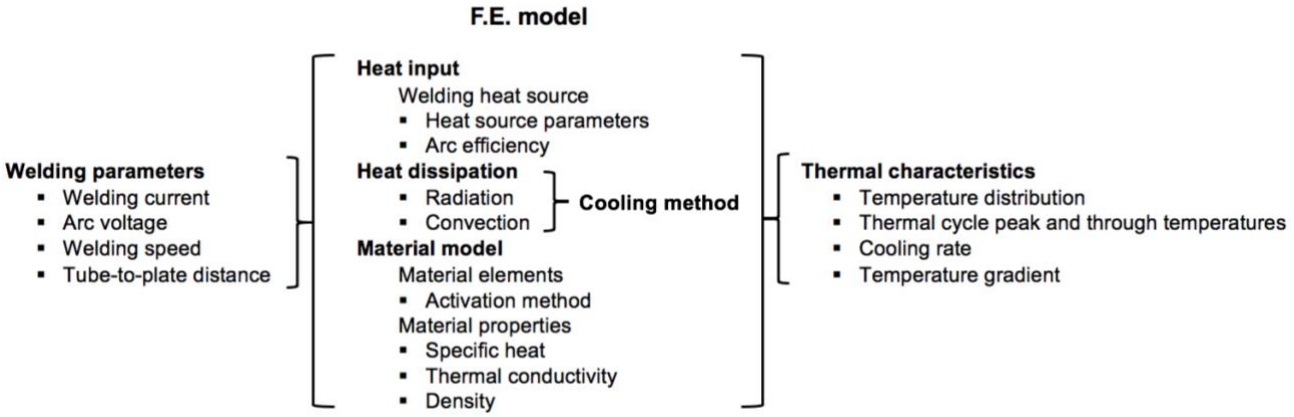

Figure 7: Thermal analysis of the wire and arc additive manufacturing process using the F.E. method, based on [18].

In the F.E. model, the temperature field that is experienced by both the deposited material and the component is described by the three-dimensional heat conduction equation. The heat input that is transferred to both the deposited material and the component by the moving welding heat source is modelled by the Goldak double-ellipsoid heat source model. The heat dissipation from the component to the environment is described by both convection and radiation from the outside surface areas of the component. Accordingly, the cooling methods as defined in the test cases 1 to 5 are described in the F.E. model in terms of the interlayer waiting time and the appropriate thermal boundary conditions at the outside surface areas of the component.

An essential aspect of the wire and arc additive manufacturing process is the modelling of the material addition during the deposition process. In the F.E. model, the material deposition in the wire and arc additive manufacturing process is modelled using an activation method. In this research, the material deposition is modelled by the sequential activation of the successive material elements using the quiet element method. Further, the temperature dependent material properties are included in the three-dimensional heat conduction equation.

1.3.1 Thermal analysis

The F.E. model is implemented in COMSOL Multiphysics version 5.3, the results are processed with MATLAB.

The characteristic temperature field that is experienced by the component in the wire and arc additive manufacturing process, is shown in Figure 8.a. Representing the temperature values that are recorded by the physically attached thermocouples in the experiments and calculated at the temperature measurement points in the F.E. model.

An important quality of the F.E. model that is presented in this research is to describe the effect of locally attained temperature field on the microstructure of the deposited material constituting the multilayer weld deposit. In contrast to the traditional method of monitoring the substrate temperature, the F.E. model allows to describe the temperature field that is experienced by the deposited material constituting both the multilayer weld deposit and the component. As shown in Figure 8.b, the temperature values that are calculated in the F.E. model can be related to the microstructural transformation temperatures to define the resulting microstructure of the deposited material in the wire and arc additive manufacturing process considering a simulated multilayer weld deposit.

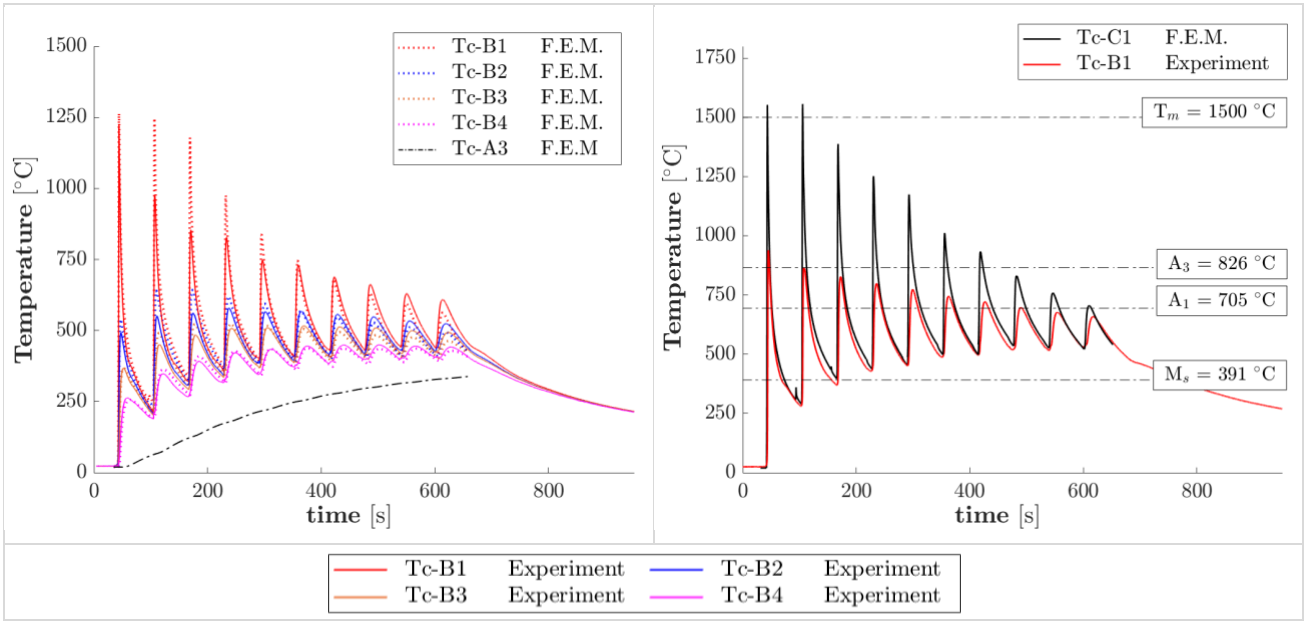

Figure 8: Characteristic temperature field of the wire and arc additive manufacturing process. [a] Substrate and component base wall; [b] Deposited material: multilayer weld deposit.

The F.E. method that is presented in this research allows to describe the effect of locally attained the temperature field on the microstructure of the deposited material constituting the multilayer weld deposit. Accordingly, the F.E. model is used to describe the effect of the cooling methods on the microstructure of the deposited material in terms of the thermal characteristics including the temperature distribution, the locally attained temperature values, the cooling rates and the temperature gradients throughout the component.

The microstructure that results from the application of the cooling methods is described in terms of the microstructural morphology and the microstructural constituents regarding the material constituting the multilayer weld deposit. The microstructural constituents and the microstructural morphology are identified using optical microscopy based on the average grain size and the distribution of alloying elements throughout the material. In addition, the average grain size and the distribution of the alloying elements throughout the material are evaluated in terms of the hardness values.

1.3.2 Research tasks

This research is summarized in the following research tasks:

I. Formulate a F.E. model.
   - Study the ability of the F.E. model to describe the temperature field that is experienced in the wire and arc additive manufacturing process.

II. Implement an experimental setup.
   - Study the effectiveness of the cooling methods to control the temperature field that is experienced in the wire and arc additive manufacturing process.

III. Microstructural analysis.
   - Study the effect of the cooling methods on the microstructure the deposited material in the wire and arc additive manufacturing process.
   - Study the capability of the F.E. model to describe the effect of the cooling methods on the microstructure of the deposited material in the wire and arc additive manufacturing process.

2 Experimental setup

2.1 Process parameters

In this research, the gas metal arc welding (GMAW) process is used as the heat source in the wire and arc additive manufacturing process. The GMAW process is operated in the pulsed transfer mode to reduce the heat input of the welding process and control the process stability in terms of both the weld fusion and the weld bead shape during the deposition process. The process parameters that are used in the experiments during the deposition of the single-pass weld layers, are shown in Table 2.

Table 2: Process parameters of the wire and arc additive manufacturing process in the experimental setup.

Process parameter	Property	
Base material	S355	
Wire material	X90; 1.2 mm; solid wire	
Welding method	GMAW; pulsed transfer mode	
Welding speed	6.5	mm/s
Wire feed speed	4	m/min
Welding current	115	A
Arc voltage	21.2	V
Contact tube-to-work distance	15	mm
Shielding gas	15	l/min; Ar + 18% CO_2
Cooling medium	Water	

The welding heat source is mounted on a 3-axis CNC machine, controlling the position of the welding heat source. The control script of the linear actuators controlling the movement of the welding heat source relative to the component, is provided in Appendix A.1. With regard to both active substrate cooling and active component cooling, a cooling tank is applied to contain the cooling medium. The experimental setup including the welding equipment that is used in the experiments is shown in Figure 9.

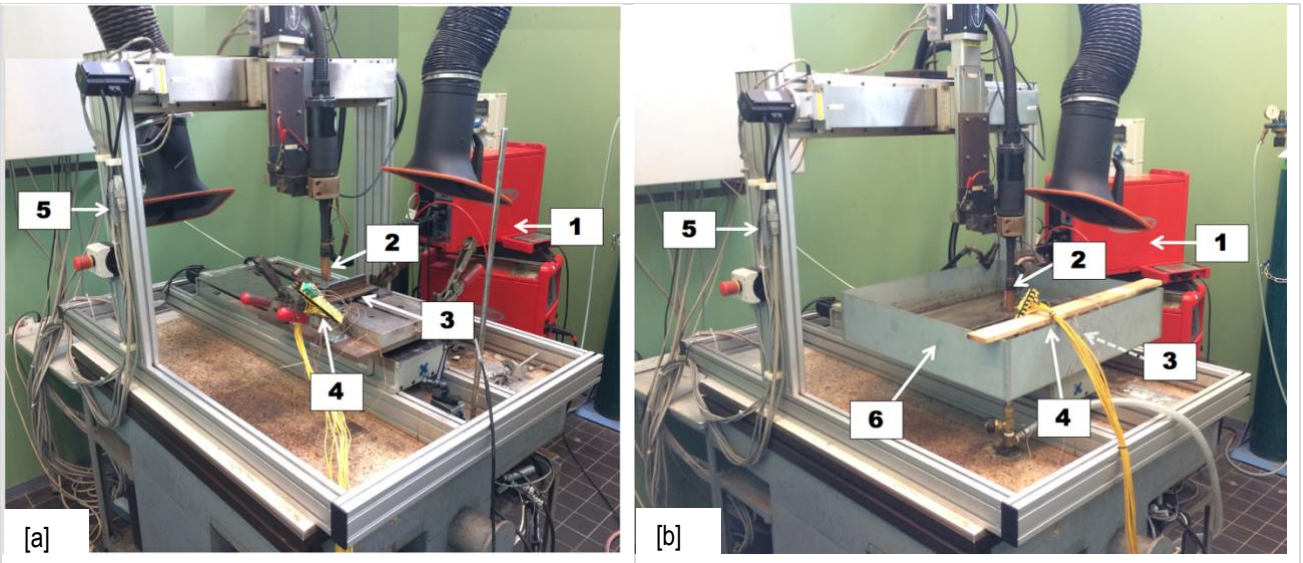

1	Welding power source; TransPulse Synergic 5000
2	Welding heat source
3	WAAM component
4	Thermocouples
5	3-axis CNC machine
6	Cooling tank

Figure 9: The experimental setup including the welding equipment and cooling method. [a] Natural cooling; [b] Active substrate cooling and active component cooling.

2.1.1 Material deposition

In the wire and arc additive manufacturing process, the component is produced by the subsequent addition of layers of material. The layers of material are added in the form of single-pass weld layers by the deposition of a metal wire under the influence of a moving welding heat source. By the subsequent deposition of the single-pass weld layers, a multilayer weld deposit is formed. The multilayer weld deposit is deposited on top of a component base wall, as shown in Figure 10.

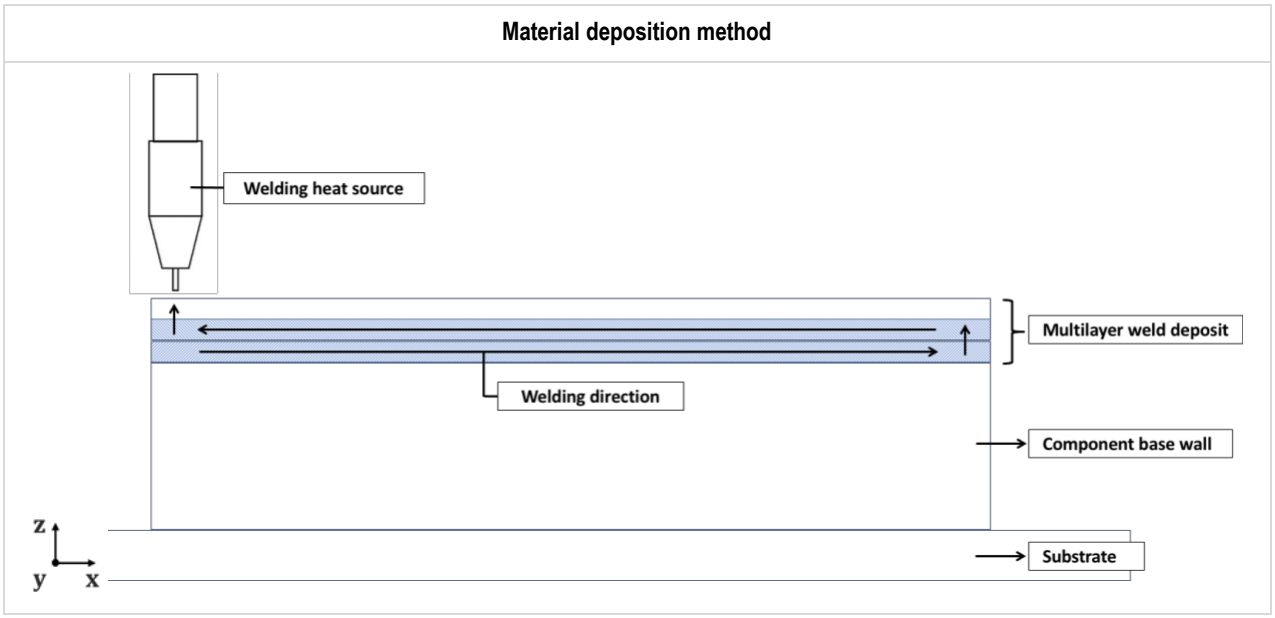

Figure 10: Material deposition of the wire and arc additive manufacturing process in the experimental setup.

As shown in Figure 10, the single-pass weld layers are deposited by the movement of the welding heat source following the reverse deposition method. According to the coordinate system, the x-direction is defined as the welding direction, the y-direction is the through-thickness direction and the z-direction is the building direction.

The movement of the welding heat source is relative to the stationary component. The position of the welding heat source along the welding direction during the deposition process is prescribed by the welding speed of the welding heat source. The position of the welding heat source with respect to the through-thickness direction is kept constant. The movement of the welding heat source in the building direction is imposed between the depostion of the single-pass weld layers, to preserve a constant contact tube to work distance. Further, a fixed interlayer wating time is prescribed following the deposition of the individual single-pass weld layers, as defined for the five test cases.

The material constituting both the component base wall and the single-pass weld layers of the multilayer weld deposit are deposited by the GMAW process, using the wire material X90. The component base wall is positioned on a substrate of the material S355. The dimensions of the substrate, the component base wall and the single-pass weld layers of the multilayer weld deposit, are shown in Table 3.

Table 3: The dimensions of the component and the single-pass weld layers of the multilayer weld deposit.

	Width [mm]	Height [mm]	Length [mm]
Substrate	60	9	200
Component base wall	8	30	150
Single-pass weld layer	8	1.5	150

2.1.2 Temperature measurement

The temperature field that is experienced by the component is represented by the temperature values that are calculated at the temperature measurement points in the F.E. model and recorded by the physically attached thermocouples in the experiments.

With regard to the substrate and the component base wall, the temperature field is described by both the temperature values that are recorded by the physically attached thermocouples in the experiments and calculated at the temperature measurement points in the F.E. model. While the temperature field that is experienced by the simulated multilayer weld deposit is described by the temperature values that are calculated at the temperature measurement points that are uniquely defined in the F.E. model.

As shown in Figure 11, the temperature measurement points that are positioned at the outside surface areas of the substrate and the component base are wall are indicated by Tc-A and Tc-B respectively. The temperature measurement points Tc-C and Tc-D refer to the temperature measurement points that are uniquely defined in the F.E. model regarding the simulated multilayer weld deposit.

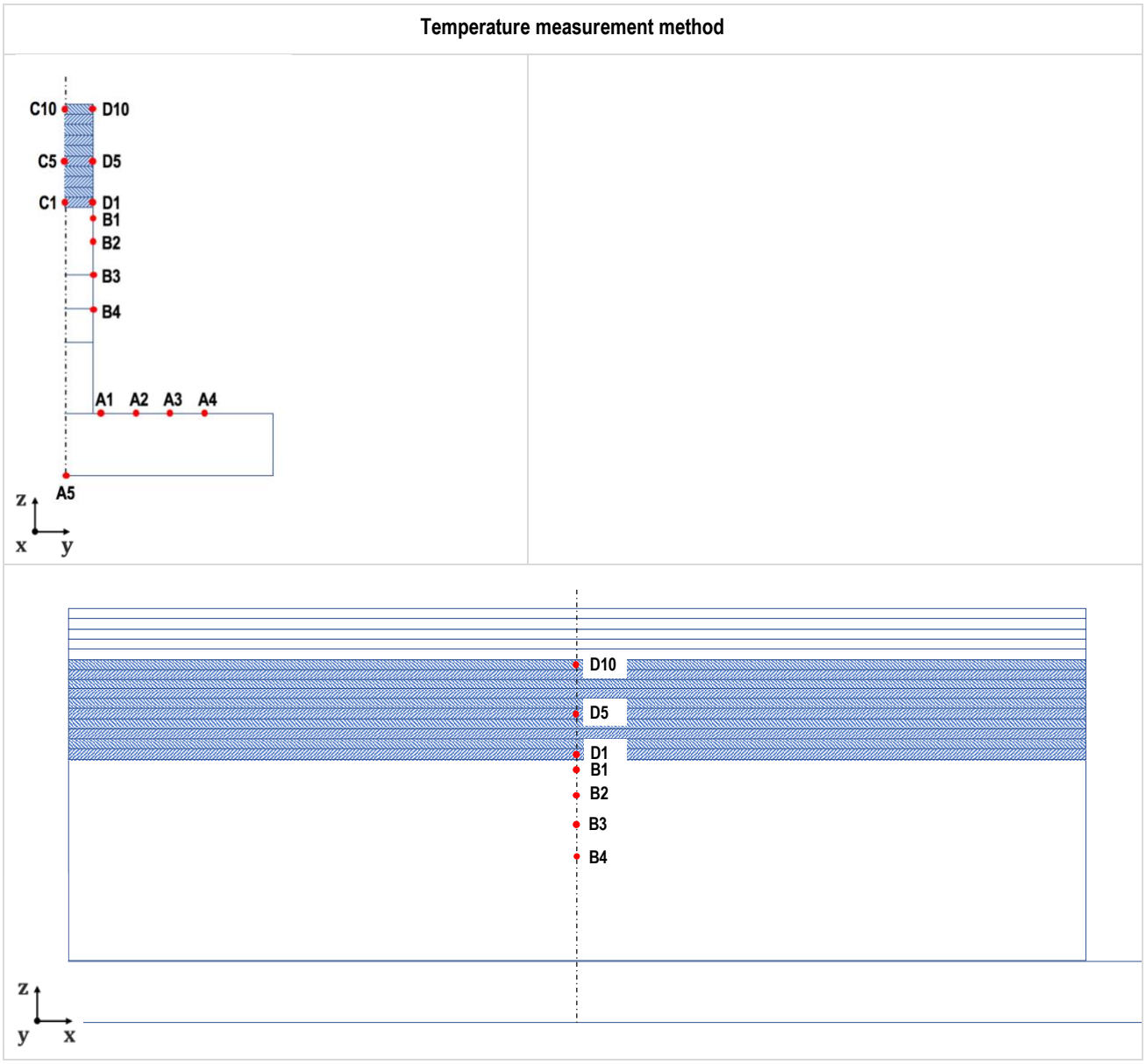

Figure 11: Temperature measurement of the wire and arc additive manufacturing process in the experimental setup.

2.2 Experimental measurement

The experimental measurement values refer to both the voltage and current values, and the temperature values that are recorded in the experiments. The experimental current and arc voltage values define the total arc power that is delivered by the welding heat source to the component. The experimental temperature values are used to calibrate the F.E. model by fitting the temperature values that are calculated at the temperature measurement points the F.E. model and the corresponding temperature values that are measured the physically attached thermocouples in the experiments.

2.2.1 Current and voltage measurement

The experimental voltage values are measured between the contact tube and the worktable, as shown in Figure 12.a. The current measurement values are recorded using a current clamp that is attached at the return lead of the electrical circuit, as shown in Figure 12.b.

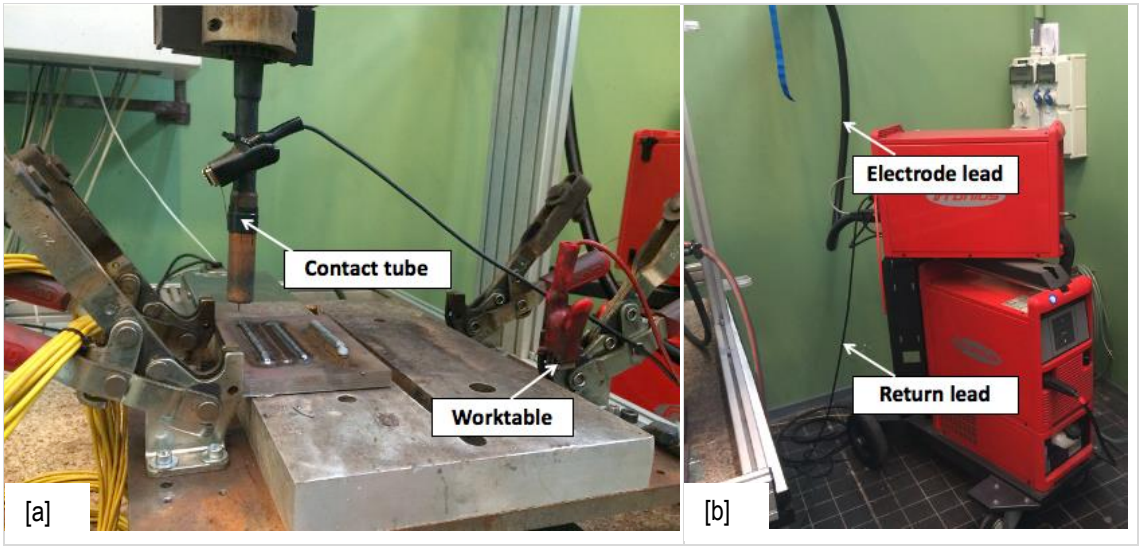

Figure 12: Current and voltage measurement of the wire and arc additive manufacturing process. [a] Voltage measurement; [b] Current measurement.

In this research, the GMAW process is operated in the pulsed transfer mode by setting the wire feed speed. The effect of the wire feed speed on the waveform characteristics and the heat input is described considering the wire feed speeds of $3, 4$ and $5\ m/min$.

2.2.1.1 Current and voltage waveform characteristics

In this research, the Fronius TransPulse Synergic 5000 power source is operated in the pulsed transfer mode by setting the wire feed speed after preselecting the wire material, the wire diameter and the shieling gas type, referred to as one-knob control [19]. The current waveform characteristics corresponding to the wire feed speeds of $3, 4$ and 5 m/min, are shown in Table 4.

Table 4: Current waveform characteristics corresponding to the wire feed speeds of $3, 4$ and $5\ m/min$.

	I_p [A]	t_p [ms]	I_d [A]	t_d [ms]	I_b [A]	t_b [ms]	f [Hz]
3 [m/min]	505.8	1.37	104.9	2.03	21.7	11.1	69.0
4 [m/min]	515.2	1.36	132.6	2.33	26.7	7.5	89.8
5 [m/min]	524.2	1.45	131.6	2.14	26.1	6.7	106.7

The process stability including the deposition rate and the weld quality are controlled by the current waveform characteristics of the pulsed GMAW process. To achieve a constant metal transfer, the wire feed speed must be balanced by the burn-off rate of the consumable electrode wire material [20]. Therefore, a constant metal transfer is maintained by the adjustment of the current waveform characteristics or the corresponding wire feed speed [21]. According to Table 4, it is found that for the Fronius TransPulse Synergic 5000 welding power source that is operated in the pulsed transfer mode using one-knob control, the deposition rate is increased by adjusting the pulse frequency.

2.2.1.2 Heat input

The arc power that is delivered by the welding heat source is defined by the product of the arc voltage and the welding current. Hence, the arc power that is delivered by the welding heat source is determined based on the welding current and arc voltage measurement values.

The values of the average current and the average voltage are defined by the average values of the instantaneous current measurement values and the instantaneous voltage measurement values, as defined in Equation 1 and Equation 2 respectively.

$$I_{AV} = \frac{1}{n} \sum_{i=1}^{n} I_i \quad [1]$$

$$U_{AV} = \frac{1}{n} \sum_{i=1}^{n} U_i \quad [2]$$

I_{AV} Average current value $[A]$

U_{AV} Average voltage value $[V]$

n Number of measurement values

I_i Instantaneous current measurement value $[A]$

U_i Instantaneous voltage measurement value $[V]$

The current and voltage values corresponding to the wire feed speeds of $3, 4$ and $5\ m/min$, are shown in Table 5.

Table 5: Average current and voltage values corresponding to the wire feed speeds of 3, 4 and 5 m/min.

	I_{AV} [A]	U_{AV} [V]	I_{EXP} [A]	U_{EXP} [V]	$\frac{I_{AV} - I_{EXP}}{I_{EXP}}$ [%]	$\frac{U_{AV} - U_{EXP}}{U_{EXP}}$ [%]
3 [m/min]	83.2	20.8	75	20.7	10.1	0.5
4 [m/min]	115.0	21.2	101	20.8	13.8	1.7
5 [m/min]	132.6	22.2	119	21.9	11.4	1.4

According to Table 5, it is observed that for the considered wire feed speeds, the average current values that are calculated based on the instantaneous current measurement values are on average $11.8\ \%$ higher compared to the experimental current values that are recorded by the power supply. While, the calculated average voltage values based on the instantaneous current measurement values and the experimental average voltage values are of the same order.

In literature, different methods are proposed for calculating the arc power based on the current and voltage measurement values [22], [23]. The average arc power is defined as the product of the average current and the

average voltage measurement values, as defined in Equation 3. While, the average instantaneous arc power is calculated based on the instantaneous voltage and current measurement values, as defined in Equation 4.

$$P_{AV} = I_{AV} \cdot U_{AV} \quad [3]$$

$$P_{INST} = \frac{1}{n} \sum_{i=1}^{n} I_i \, U_i \quad [4]$$

P_{AV} Average arc power $[W]$

P_{INST} Average instantaneous arc power $[W]$

n Number of measurement values

The values of the average arc power corresponding to the wire feed speeds of 3, 4 and 5 $\mathrm{m/min}$, are shown in Table 6.

Table 6: Average arc power values corresponding to the wire feed speeds of 3, 4 and 5 m/min.

	P_{INST} [W]	P_{AV} [W]	P_{EXP} [W]	$\frac{P_{AV} - P_{EXP}}{P_{EXP}}$ [%]	$\frac{P_{INST} - P_{EXP}}{P_{EXP}}$ [%]
3 [m/min]	2352.3	1730.6	1552.5	11.5	51.5
4 [m/min]	3288.1	2438.0	2100.8	16.1	56.5
5 [m/min]	3928.6	2943.7	2606.1	13.0	50.7

The experimental average arc power is defined by the product of the average value of the current and voltage that are recorded by the power supply. It is observed that for the considered wire feed speeds, the calculated average arc power based on the average voltage and current measurement values is on average 13.5 % higher compared to the experimental average arc power. While, the average instantaneous arc power that is calculated based on the instantaneous voltage and current measurement values is on average 52.9 % higher compared to the experimental average arc power.

The experimental current and voltage values corresponding to the wire feed speeds 3, 4 and 5 $\mathrm{m/min}$, are provided in Appendix A.4. The recorded current and voltage values for the wire feed speed of 4 $\mathrm{m/min}$, is shown in Figure 13.

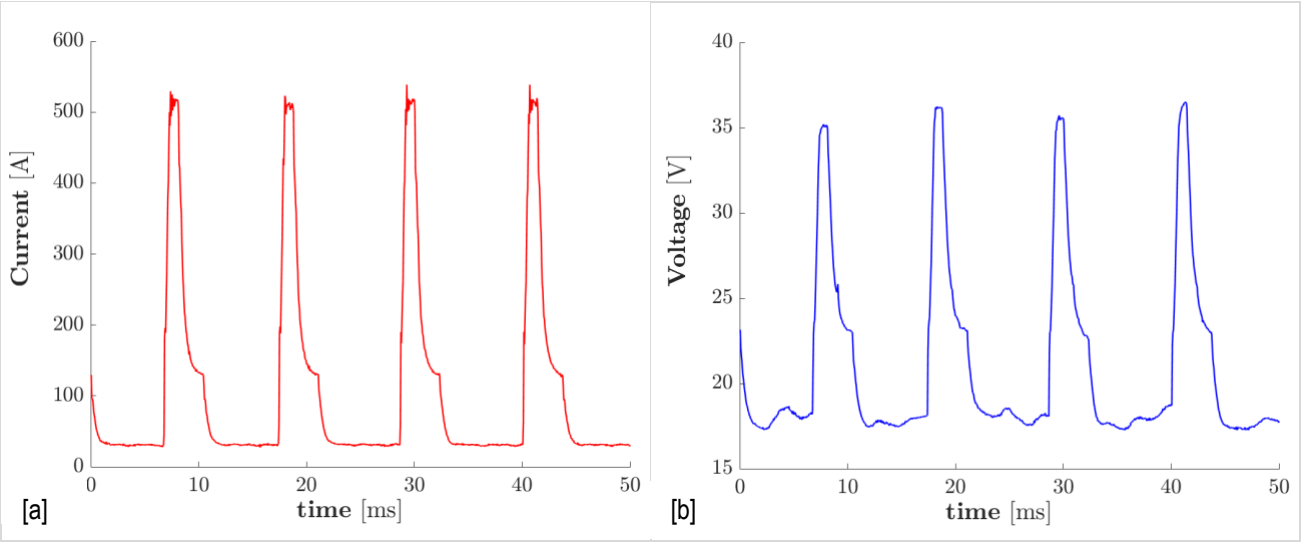

Figure 13: Experimental current and voltage values, recorded at a sampling rate 20 kHz and bandwidth 50 kHz. [a] Current measurement values 4 m/min; [b] Voltage measurement values 4 m/min.

2.2.2 Temperature measurement

The experimental temperature values are recorded by the physically attached K-type thermocouples. The thermocouples are attached by means of spot welding at the outside surface areas of the component at the mid-length position of the component base wall to exclude the start and end-effects, as shown in Figure 14.

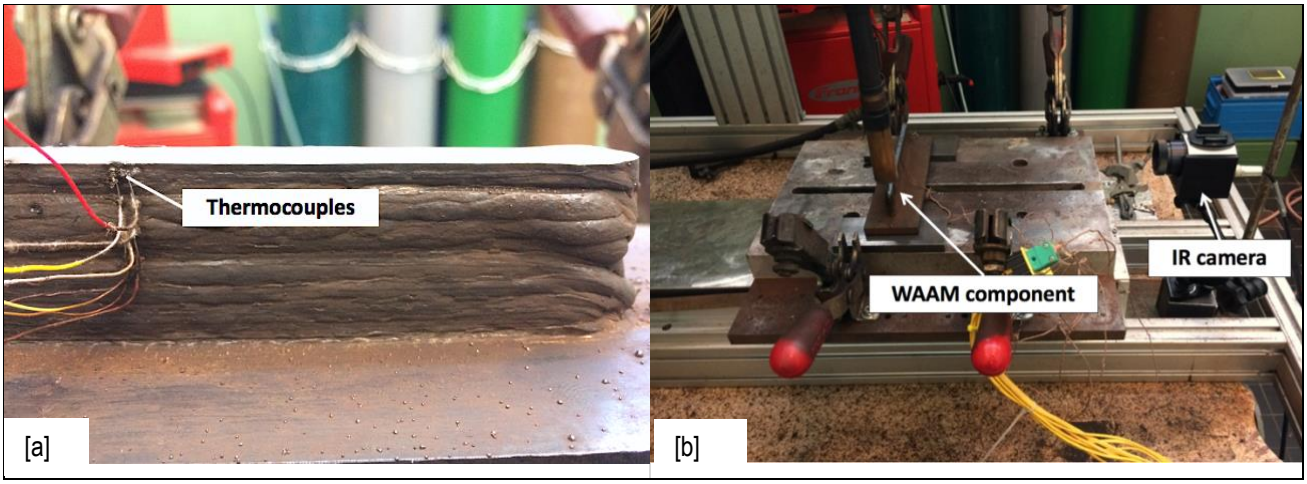

Figure 14: Temperature measurement of the wire and arc additive manufacturing process. [a] Physically attached K-type thermocouples; [b] IR camera.

The electrical circuit of a K-type thermocouple is shown in Figure 15. The electrical circuit of the K-type thermocouple consists of two dissimilar metal wires that are attached at the metallic surface of the component, indicated by the measuring point. The wires are connected to two copper wires in the connector, indicated by the reference point. In the case of the K-type thermocouple, the two dissimilar metal wires consist of the nickel alloys Chromel and Alumel [24].

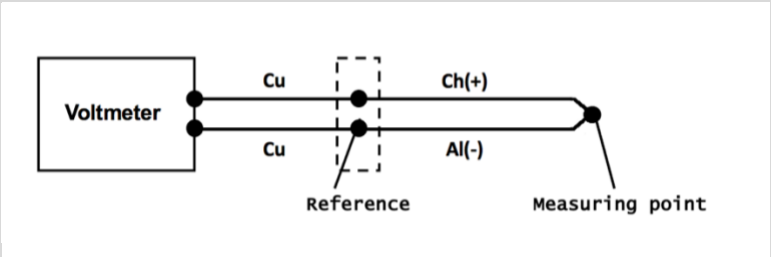

Figure 15: Electrical circuit of the K-type thermocouple [24].

The temperature measurement by a thermocouple is based on the thermoelectric effect. During the temperature measurement, the measuring point and the reference point experience a different temperature value. Since the two wires are of a different composition, a small direct current is established that can be detected by an output voltage. The output voltage is related to the temperature of the component [25], defined in Equation 5.

$$U \sim T_{obj} - T_{ref} \quad [5]$$

T_{obj} Temperature of the object $[K]$

T_{ref} Temperature of the reference $[K]$

According to Equation 5, the output voltage is proportional to the temperature difference between the measuring point and the reference .

2.2.2.1 Measurement accuracy

The K-type thermocouple possesses a high accuracy and stability over a wide temperature range, defined by a linear voltage characteristic in the temperature range between -200 °C and 1250 °C. In this temperature range, the accuracy is equal to +/- 2.2 °C [25].

The measurement accuracy of the K-type thermocouples is validated by the calibration of the temperature values that are recorded by the physically attached K-type thermocouples and the IR camera at the outside surface areas of the component indicated Area 1 and Area 2, as shown in Figure 16.

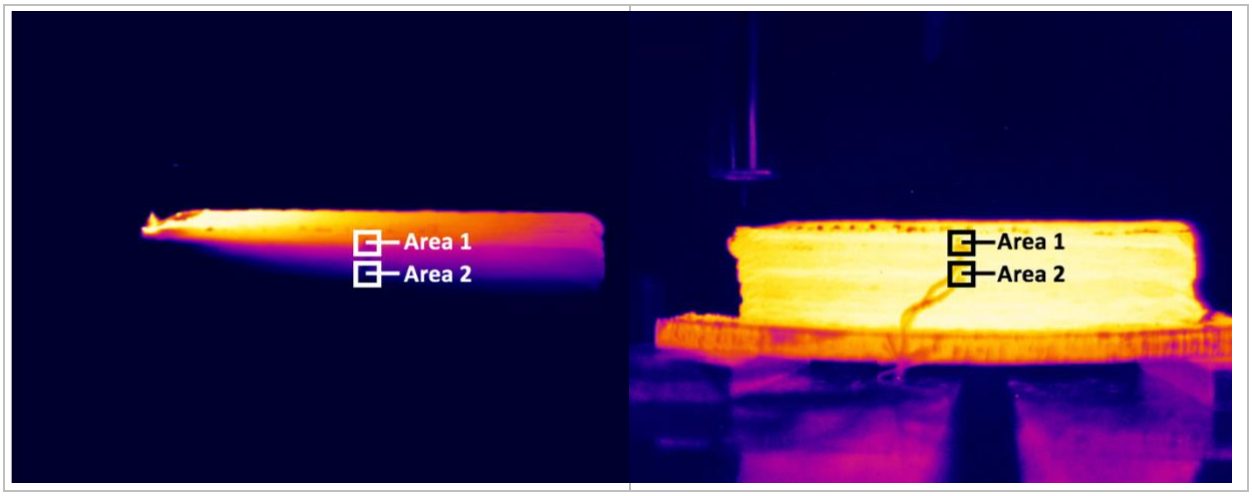

Figure 16: Calibration of the physically attached K-type thermocouples and the IR camera at the outside surface areas of the component indicated Area 1 and Area 2, considering an emissivity equal to 0.95.

The temperature measurement by IR imaging is based on the measurement of the energy that is emitted from the object surface. The IR camera provides stable results in the temperature range between -20 °C and 900 °C, with an accuracy of +/- 2 °C [26].

The energy that is emitted from the object surface is radiated in the form of electromagnetic radiation. According to Planck's law, the electromagnetic radiation depends on the temperature and is a function of the wavelength, defined by the spectral radiation. For higher temperatures, the maximum of the spectral radiation shifts toward shorter wavelengths. During the temperature measurement, the infrared radiation is focussed onto the detector in the IR camera. The temperature dependence of the electrical resistance of the sensitive elements of the detector in the IR camera results in an output signal. The energy that is emitted from the object surface is in accordance with the radiative heat flux. Accordingly, the output signal of the IR camera is related to the temperature of the component [26], as defined in Equation 6.

$$U \sim \varepsilon \left(T_{obj}^4 - T_{amb}^4\right) \qquad [6]$$

$$U = C \left(\varepsilon T_{obj}^n + (1-\varepsilon) T_{amb}^n - T_{FPA}^n\right)$$

U Output voltage $[V]$

C Device constant $\left[\frac{V}{K^n}\right]$

ε Emissivity $[-]$

T_{obj} Temperature of the object $[K]$

T_{amb} Temperature of background radiation $[K]$

T_{FPA} Temperature of the device $[K]$

In Equation 6, the background radiation is accounted for by the reflected radiation from the environment, and the radiation from the device. Further, since the infrared radiation only covers a part of the electromagnetic spectrum, the exponent n depends on the wavelength [26]. The device constant includes the Stefan-Boltzmann constant, as defined in Equation 14. Accordingly, the object temperature using IR imaging is defined in Equation 7.

$$T_{obj} = \sqrt[n]{\frac{U - C(1-\varepsilon)T_{amb}^{n} + CT_{pyr}^{n}}{C\varepsilon}} \quad [7]$$

For metals, the emissivity is strongly dependent on the surface conditions of the metallic surface. According to literature, for polished metallic surfaces, the emissivity is in the range of 0.2 - 0.4. While, for oxidized metallic surfaces the emissivity is in the range of 0.6 - 0.9, and for surface temperatures near the melting temperature the emissivity is in the range of 0.9 - 0.95 [26]. The temperature values that are recorded by the physically attached K-type thermocouples and the IR camera considering an emissivity equal to 0.95, are shown in Figure 17.

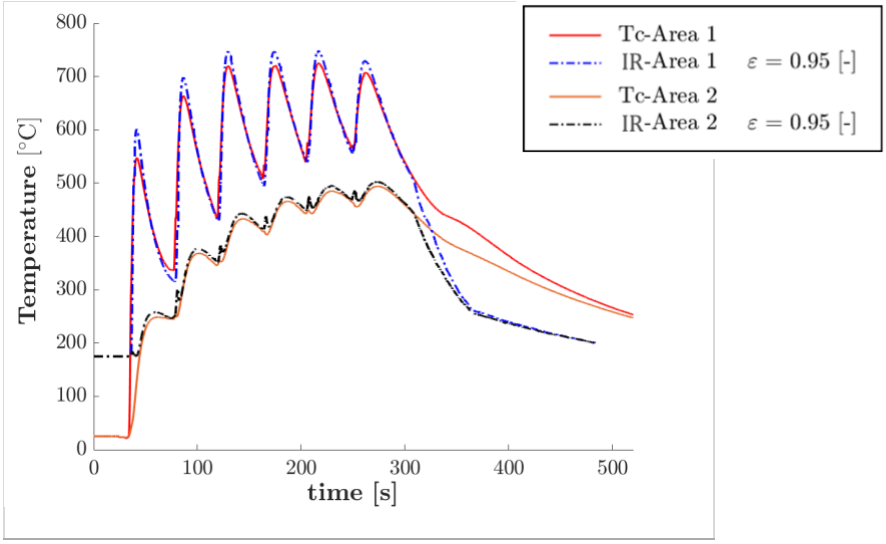

Figure 17: Temperature values recorded by the physically attached K-type thermocouples and the IR camera at the outside surface areas of the component indicated Area 1 and Area 2, considering an emissivity equal to 0.95.

As shown in Figure 17, the temperature values that are recorded by the physically attached K-type thermocouples are in good agreement with the corresponding temperature values that are recorded by the IR camera considering an emissivity equal to 0.95. Indicating that the K-type thermocouple have a high accuracy and stability over a wide temperature range. The deficiency between the temperature values that are recorded by the physically attached K-type thermocouples and the IR camera considering an emissivity of 0.95 is within the +/- 2.5 % error range. While, the deficiency of the thermal cycle peak temperatures and the thermal cycle through temperatures is within the +/- 5.0 % error range.

Further, the physically attached K-type thermocouples demonstrate no loss of consistency. In contrast to the IR camera, for which the consistency of the measurement values is lost during the final cooling stage due to the dramatically deteriorated surface of the weld deposit. Indicating that in the case of temperature measurement by IR imaging, the deteriorated surface conditions should be compensated by a reduced emissivity [27]. According to Figure 17, the temperature values that are recorded by the physically attached thermocouples at $t = 480$ s at the outside surface areas Area 1 and Area 2 are equal to 279.9 °C and 269.1 °C respectively, on average 274.5 °C. The corresponding temperature value that is recorded by the IR camera considering an emissivity of 0.95 is equal to 201.5 °C. While, by considering an emissivity of 0.5, the corresponding temperature value that is recorded by the IR camera is equal to 275 °C, matching the temperature values that are recorded by the physically attached K-type thermocouples.

2.2.3 Data acquisition

The experimental measurement values of both the voltage and current, and the temperature are acquired by the digital scope, as shown in Figure 18.

The digital scope is used to acquire the instantaneous measurement values. The current and voltage measurement values are acquired with a sampling rate of 20 kHz during a sampling time of 50 ms, corresponding to $1{,}000$ measurement values. With regard to the temperature measurement values, the output voltage of the physically attached K-type thermocouples is converted by a preselected program, providing the temperature measurement values. The temperature measurement values are acquired with a sampling rate of 5 Hz during a sampling time of $2{,}000$ s, corresponding to $10{,}000$ measurement values.

Figure 18: The experimental measurement values are acquired by a digital scope; Yokogawa DL716 [28].

2.3 GMAW process

In this research, the gas metal arc welding (GMAW) process is used as the heat source in the wire and arc additive manufacturing process. The GMAW process is operated in the pulsed transfer mode to reduce the heat input of the welding process and control the process stability in terms of both the weld fusion and the weld bead shape during the deposition process.

In the GMAW process, the welding arc is used as a heat source to deposit a consumable electrode into the weld pool. Correspondingly, the component is produced by the subsequent addition of single-pass weld layers of material under the influence of a moving welding heat source. The schematical representation of the GMAW process is shown in Figure 19.

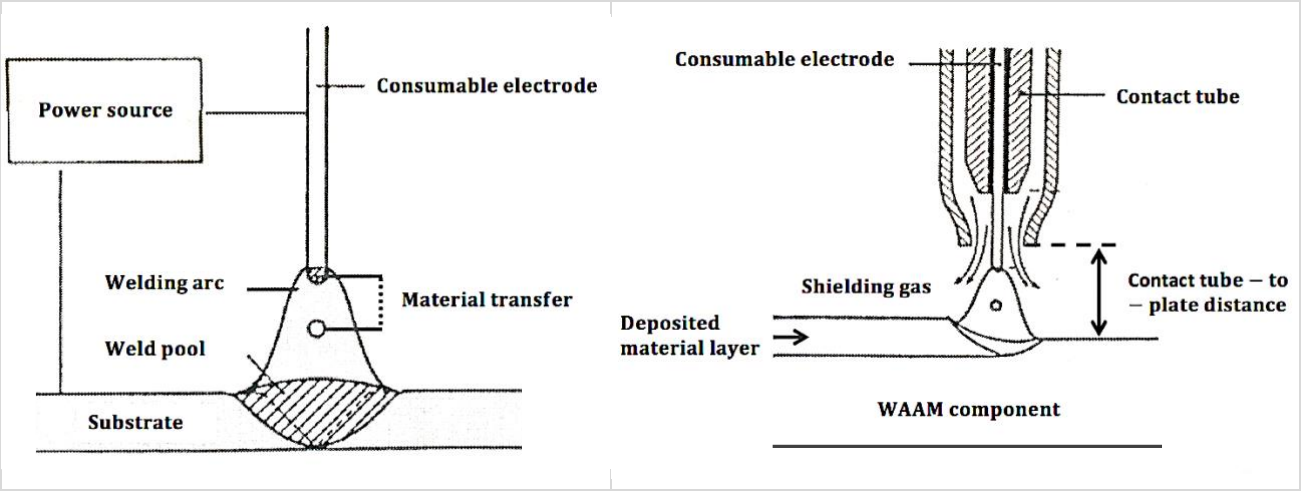

Figure 19: Schematical representation of the GMAW process. [a] Metal transfer process; [b] Material deposition [29].

The GMAW process is an arc welding process, whereby a welding arc is formed between the consumable electrode and the base material by imposing an electrical current. In this research, the GMAW process is operated in the pulsed transfer mode by setting the wire feed speed. In this regard, both the material deposition and the heat input that is transferred to the component are controlled by the wire feed speed and the welding speed [30], [21]. A shielding gas is used to protect both the welding arc and the weld pool from the environmental contamination. The shielding gas affects the mode of metal transfer and the weld bead appearance depending on the welding material [29]. For welding of non-ferrous metals an inert shielding gas is used, while for the welding of steel small amounts of oxygen or CO_2 are added to stabilize the welding arc, ensuring enough weld penetration and improving the fluidity of the weld pool [31].

The process parameters including the heat input, the process stability, the deposition rate and the weld quality are controlled by the current waveform characteristics of the GMAW process. The heat input that is transferred to the component is defined by the arc power that is delivered by the welding heat source, based on the product of the arc voltage and the welding current.

An important aspect of the wire and arc additive manufacturing process is the material addition during the deposition process. The material deposition in the GMAW process results from different metal transfer modes depending on the welding current, the shielding gas, the electrode polarity and the welding material. Further, the heat input that is transferred to the component is defined by the arc power that is delivered by the welding heat source, based on the product of the arc voltage and the welding current. In this regard, the metal transfer is an important aspect of the wire and arc additive manufacturing process.

2.3.1 Metal transfer modes

The metal transfer process includes the droplet formation at the electrode tip, the droplet detachment and the metal transport to the weld pool [29]. When operating the GMAW process with a positive electrode and an argon-rich shielding gas, the material transport is defined for different current levels by the following metal transfer modes:

i. Short-circuiting transfer
ii. Globular transfer
iii. Spray transfer

At low current levels, the material transport is facilitated by the short-circuiting transfer mode. Whereby, the material transport occurs during the short-circuiting period when the electrode is in physical contact with the weld pool. At increased voltage levels, the material transport takes place by the globular transfer mode. As a result of the increased voltage levels, the welding arc is sustained, and the material transfer occurs by the droplet formation and the material transport across the welding arc to the weld pool. In the globular transfer mode, the gravitational force is the driving force for the droplet detachment [20]. The metal transfer in the globular transfer mode is characterized by the irregular detachment of irregular shaped molten droplets, producing a poor weld bead quality and causing significant spatter losses. The molten droplets that are transferred to the weld pool are about two to four times the diameter of the electrode wire. Both the globular and short-circuiting metal transfer modes typically produce poor weld quality cause significant spatter losses [20].

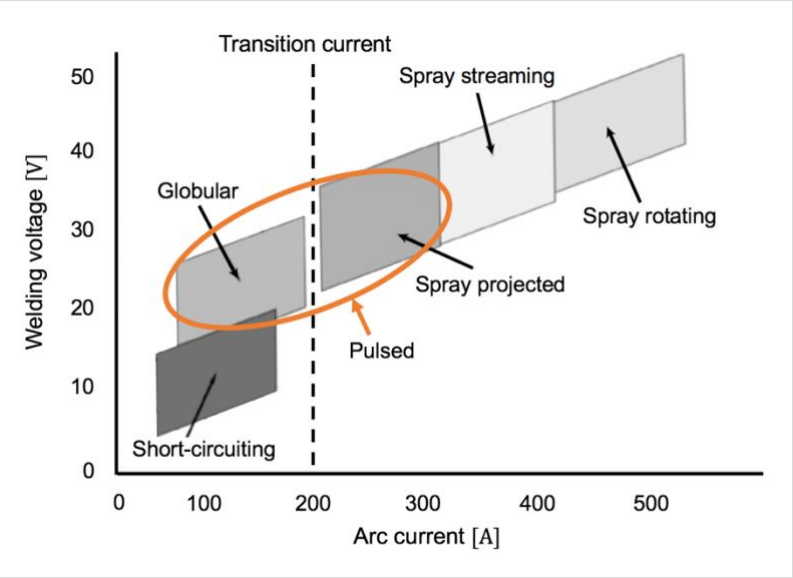

Figure 20: The metal transfer modes of the GMAW process operated with a positive electrode and an argon-rich shielding gas [32].

Concerning the GMAW process operating with a positive electrode and an argon-rich shielding gas, a distinct transition exists between the operating ranges of the globular transfer mode and the spray transfer mode, defined by the transition current. The transition current depends on the electrode diameter, the electrode material and the electrode extension [20]. According to literature, for the electrode material X90 with a diameter of $1.2\ \mathrm{mm}$ and an electrode extension of $20\ \mathrm{mm}$, the transition current is about $200\ \mathrm{A}$ [33], [34]. At current levels exceeding the transition current, the material transport takes place by the spray transfer mode. The metal transfer in the spray transfer mode is characterized by a regular droplet detachment with uniform droplet size, directional droplet transfer to the weld pool and low spatter losses [20].

2.3.1.1 Pulsed GMAW process

The pulsed transfer mode is a controlled method of the spray transfer mode, in which the welding current periodically alternates between a pulse current exceeding the transition current, and a low background current.

The pulsed transfer mode is characterized by the following features:

I. Low heat input
   - Reduced heat input compared to the spray transfer mode

II. Process stability
   - Projected spray transfer during the pulse current time
   - Controllable droplet size
   - Low spatter losses

III. Weld quality
   - Weld fusion similar to the spray metal transfer mode
   - Controllable weld bead shape

The heat input of the pulsed GMAW process is reduced compared to the spray transfer mode, because of the alternating current and voltage waveform characteristics. According to Equation 7, the effective heat input is defined by the product of the arc voltage, the welding current and the arc efficiency. As a result of the low background current, the average current of the pulsed transfer mode is reduced compared to the spray transfer mode. Generally, the average current is in the range of the globular transfer mode [21]. With regard to the process stability, the metal transfer in the pulsed GMAW process takes place by the projected transfer of metal droplets with a controllable size, depending on the current waveform characteristics [21].

2.3.1.1.1 Current waveform characteristics

In the pulsed GMAW process, the heat input, process stability and weld quality are controlled by the current waveform characteristics [33]. The current waveform characteristics and the metal transfer process for a single pulse period are shown in Figure 21. The current waveform of the pulsed GMAW process is defined by the following waveform characteristics [21], [35]:

- Pulse current I_p
- Pulse current time t_p
- Droplet detachment current I_d
- Droplet detachment time t_d
- Background current I_b
- Background current time t_b
- Pulse frequency f

The current waveform characteristics of the pulsed GMAW process are shown in Figure 21. The pulse current is applied at a value exceeding the transition current in order to initiate the detachment of a single droplet per pulse period [33]. The detachment current is applied to add energy to the metal droplet, without effecting the droplet size [19]. The added energy improves the fluidity of the weld pool and stabilizes the welding arc [19]. The background current is required to maintain the welding arc. The value of the background current is minimized to reduce the heat input and prevent the globular metal transfer during the background current time [23]. The pulse frequency is defined by the number of pulse periods per second. As shown in Figure 21, a single pulse period is the sum of the pulse current time and the background current time.

Besides the low heat input and the process stability, the weld quality is controlled by the waveform characteristics of the pulsed GMAW process. Since the wire metal is transferred by the spray transfer mode, the metallurgy bonding is ensured. Further, the weld bead shape is controlled as the time between the pulse periods allows the weld pool to cool and slightly solidify.

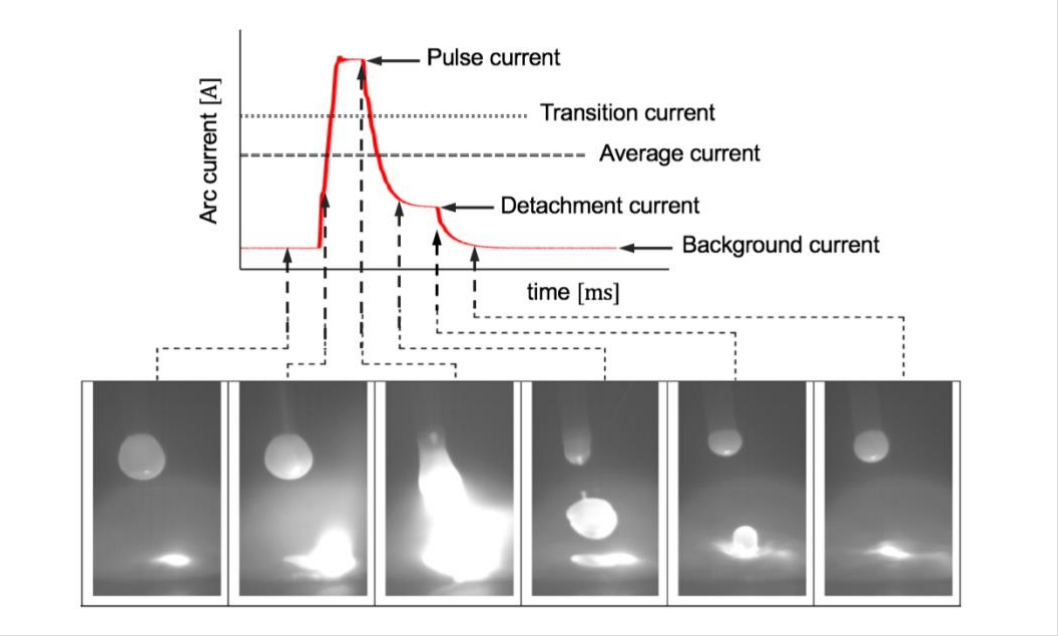

Figure 21: Current waveform characteristics and metal transfer process in the pulsed GMAW process [36].

2.4 Microstructure

The resulting microstructure of the deposited material is evaluated considering the locally attained chemical composition and the temperature field that is experienced by the material constituting the multilayer weld deposit.

2.4.1 Microstructural characteristics

The effect of the temperature field on the microstructure of the deposited material is described in terms of the microstructural characteristics considering the the locally attained chemical composition and the temperature field that is experienced by the material constituting the multilayer weld deposit. The locally attained chemical composition is described in terms of the distribution of alloying elements throughout the deposited material, determined by the chemical composition of the electrode material and the shielding gas that is used to protect both the welding arc and the weld pool from environmental contamination. In addition, the locally attained chemical composition is influenced by the temperature field that is experienced by the experimental fifteen-layer weld deposit. The electrode material X90 is a high-strength low-alloy steel with excellent strength and toughness properties [37]. The excellent material properties are attributed to the alloying elements which provide the strengthening mechanisms including grain refinement, solid solution strengthening, precipitation strengthening and dislocation strengthening [38]. In addition, the low alloy content provides good weldability [39]. The chemical composition of the electrode material X90 and the structural steel S355 are shown in Table 7.

Table 7: Chemical composition of the electrode material X90 and the structural steel S355 [wt.%] [40], [41].

	C	Si	Mn	Cr	Mo	Ni	P	S	Cu
X90	0.1	0.8	1.8	0.35	0.6	2.3	–	–	–
S355	0.24	0.55	1.6	–	–	–	0.035	0.035	0.55

The microalloying elements Mo and Cr are strong carbide forming elements and segregate into the cementite. While, Mn and Ni are moderately strong carbide forming elements which tend to segregate into ferrite when subjected to a subsequent thermal treatment. Both the moderately strong carbide forming elements and the strong carbide forming elements restrict the grain growth. During austenization, these microalloying elements segregate to the prior austenite grain boundaries, thereby slowing the grain growth by a process referred to as solute drag [38]. Further, the microalloying elements Mn and Si are added to neutralize the detrimental effect of the oxidation of alloying elements [39].

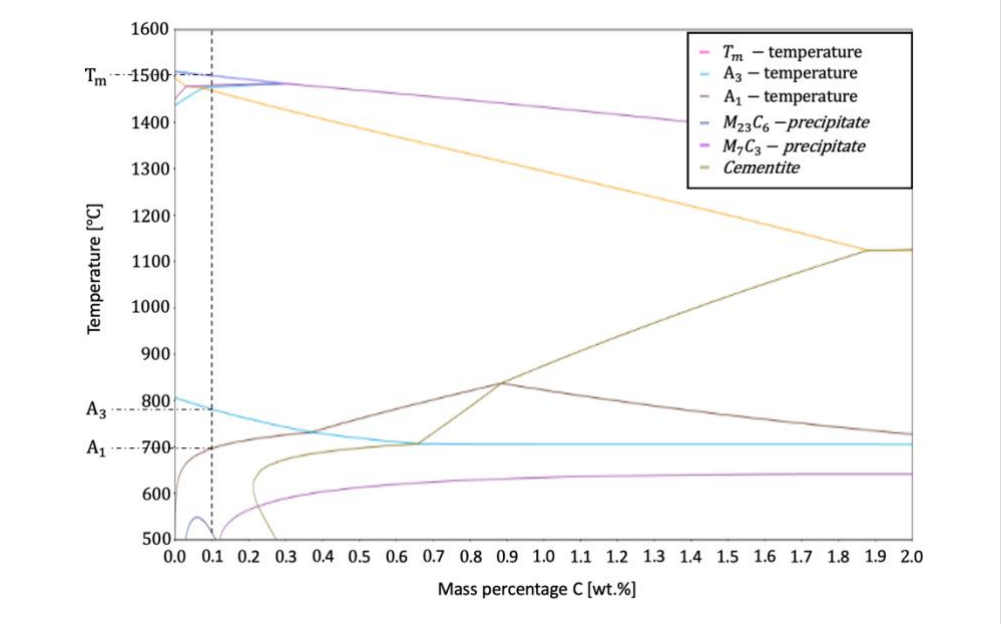

Figure 22: Phase diagram of the electrode material X90, based on dilatometric measurement.

2.4.1.1 Microstructural constituents

The formation of the microstructural constituents is determined by the locally attained chemical composition and the temperature field that is experienced by the experimental fifteen-layer weld deposit. The most common characteristics of the microstructural constituents corresponding to the electrode material X90 are described.

2.4.1.1.1 Pro-eutectoid ferrite

Pro-eutectoid ferrite is formed at temperatures below the A_3-temperature until the A_1-temperature is reached. The pro-eutectoid ferrite microstructure nucleates at the prior austenite grain boundaries in the form of allotriomorphic ferrite or in the microstructural matrix as either polygonal ferrite or Widmanstätten ferrite. At small undercooling below the A_3-temperature, the ferrite nucleates at the prior austenite grain boundaries and grain boundary ferrite also referred to as allotriomorphic ferrite is formed. While, polygonal ferrite is formed as coarse isolated ferrite islands in the microstructural matrix.

At larger undercoolings below the A_3-temperature, side-plate ferrite also referred to as Widmanstätten ferrite is formed [38]. The Widmanstätten ferrite microstructure is characterized by a coarse morphology of elongated Widmanstätten ferrite plates. Widmanstätten ferrite is formed at higher cooling rates than polygonal ferrite, in the temperature range below at which equiaxed ferrite is formed [38]. The Widmanstätten ferrite plates grow into the untransformed austenite along their length by the ledge growth mechanism. The ledge growth mechanism of Widmanstätten ferrite is characterized by the migration of ledges along the axes of the Widmanstätten ferrite plates, causing the thickening of the Widmanstätten ferrite plates normal to the direction of the ledge migration [38]. The growth rate of the Widmanstätten ferrite is controlled by the diffusion of carbon into the untransformed austenite [42].

2.4.1.1.2 Pearlite

The pearlite microstructure is composed of alternating layers of ferrite and cementite. At temperatures below the A_1 -temperature, the pearlite microstructure is formed at sufficiently low cooling rates by the eutectoid transformation whereby austenite is decomposed into the ferrite and cementite phases. The pearlite microstructure is nucleated at the prior austenite grain boundaries. The alternating layers of ferrite and cementite are extended into the untransformed austenite by the concurrent growth of the ferrite and cementite phases [39].

2.4.1.1.3 Bainite

The bainite microstructure consists of bainitic ferrite plates that are separated by thin films of untransformed austenite [42]. Depending on the cooling rate, the untransformed austenite is decomposed into ferrite and cementite or retained austenite and martensite. The bainite microstructure grows by the repeated nucleation of bainitic ferrite subunits. The bainitic ferrite subunits are formed by heterogenous nucleation on the prior austenite grain boundaries. The repeated nucleation of the bainitic ferrite subunits is an autocatalytic process, based on the carbon mobility that becomes sufficient after the bainite reaches a certain size [38]. The size of the bainitic ferrite subunits is restricted by the large amount of dislocations that are introduced by the displacive transformation.

The fraction of bainite constituents depends on the cooling rate. At high cooling rates, the formation of a fine-grained microstructure is promoted, and the microstructure is mainly composed of lath bainite. While at lower cooling rates, the formation of a coarse-grained microstructure is promoted, and the fraction of granular bainite is increased. Lath bainite consists of fine bainitic ferrite laths and strip-like cementite particles that are distributed along the bainitic ferrite lath boundaries. Granular bainite is characterized by the fact that the carbon is partitioned from the bainitic ferrite, stabilizing the residual austenite. The resulting microstructure contains both retained austenite and martensite.

2.4.1.1.4 Acicular ferrite

Acicular ferrite is formed by the heterogeneous nucleation on non-metallic inclusions, primarily oxide inclusions in the case arc welding [43]. As indicated, the oxide inclusions are formed by the reaction of the deoxidizing elements with the dissolved oxygen atoms in the liquid weld metal. Considering the electrode material X90, the microalloying element Ni is added to promote the formation of the acicular ferrite microstructure [37].

The acicular ferrite plates grow by the repeated nucleation of ferrite subunits by the displacive transformation with no partitioning of carbon. The carbon diffusion to the untransformed austenite occurs through a post-transformation event [44]. The acicular ferrite microstructure is characterized by a basket-wave morphology of lenticular ferrite plates. The chaotic arrangement of the ferrite plates provides superior mechanical properties, in particular toughness [37].

2.4.1.1.5 Martensite

The martensite transformation is a diffusionless transformation that results in the formation of a supersaturated solid solution of carbon in the ferrite matrix. The martensite microstructure is dependent on the formation temperature. Lath martensite is formed at the highest temperatures, while thin plate martensite is formed at low temperatures [38]. The microstructure of lath martensite consists predominantly of high densities of dislocations, accommodating the a-thermal transformation from austenite. In the case of lath martensite, the prior austenite grain is divided into large regions of lath groups with the same parallel relationship, referred to as packets. Whereby each packet is subdivided into parallel blocks consisting of lath groups with the same orientation. These lath groups with the same orientation form at the prior austenite grain boundary and are visible in optical microscopy as macroscopic blocks. Both the strength and the toughness are strongly related to the packet size and block size. Both the packet size and block thickness decrease as the austenite grain size is refined [38].

2.4.1.2 Microstructural transformation

The formation of microstructural constituents is related to the locally attained temperature values. For temperature values exceeding the A_3-temperature but below the melting temperature, the material is completely transformed into the austenite phase in accordance with the phase diagram of the electrode material X90. Depending on the cooling rate, the austenite phase is decomposed into the microstructural constituents as shown in Figure 23.

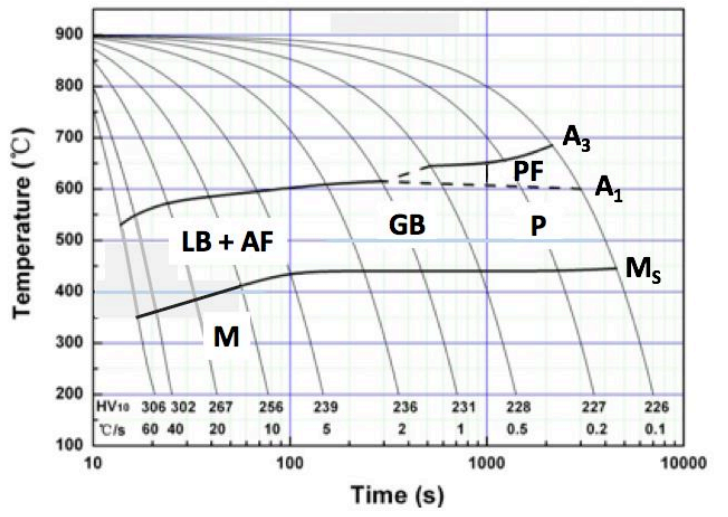

PF	Pro-eutectoid ferrite
P	Pearlite
GB	Granular bainite
LB	Lath bainite
AF	Acicular ferrite
M	Martensite

Figure 23: CCT diagram of the electrode material X90 [45].

According to Figure 23, for low cooling rates the resulting microstructure of the deposited material is mainly composed of pro-eutectoid ferrite and pearlite constituents and a reduced amount of granular bainite. While, for cooling rates in the range of $0.6\ °C/s$ to $15\ °C/s$, the resulting microstructure mainly consists of bainite microstructural constituents. A predominantly martensitic microstructure is formed for cooling rates exceeding $15\ °C/s$. The transformation temperature between the ferrite-austenite field and the ferrite-cementite field is indicated by the A_1-temperature. While, the transformation temperature between the austenite field and the ferrite-austenite field is indicated by the A_3-temperature.

The empirical formulas for the transformation temperatures of the X90 electrode material are provided in Equation 8 and Equation 9, [38].

$$A_1 = 723 - 10.7Mn - 16.9Ni + 29.1Si + 16.9Cr + 290As + 6.38W = 694\ °C \quad [8]$$

$$A_3 = 910 - 203\sqrt{C} - 15.2Ni + 44.7Si + 104V + 31.5Mo + 13.1W = 865\ °C \quad [9]$$

In Equation 7 and Equation 8, the temperature values indicate the transformation temperatures for the arrest on heating, provided that the heating rate is higher than the cooling rate [38]. Further, the effect of the chemical composition on the transformation temperatures is indicated. The empirical formula for the martensitic start temperature is provided In Equation 10, [46].

$$M_s = 539 - 432C - 30.4Mn - 17.7Ni - 12.1Cr - 7.5Mo = 391\ °C \quad [10]$$

The transformation mechanism of pro-eutectoid ferrite and pearlite is diffusion controlled. While, the transformation mechanism of bainite and acicular ferrite is displacive. Both bainite and acicular ferrite are formed when the material is cooled from the austenite phase with complete supersaturation of carbon. During the displacive transformation, there is no long-range partitioning of both substitutional and interstitial elements between the ferrite and the untransformed austenite.

The martensite transformation is induced when the material is rapidly cooled from temperatures exceeding the A_1-temperature and takes place at temperatures below the martensitic start temperature. At temperatures below the martensitic start temperature, both the diffusion of the solute atoms and the alloying elements are suppressed. In this regard, the martensite transformation is independent of the thermal activation, and proceeds if further undercooling is available [38].

3 F.E. model

3.1 Governing equations

The F.E. model is based on the governing equations. The formulation of the moving welding heat source in the F.E. model is based on the Goldak double-ellipsoid heat source model [47], [48]. The convective and radiative heat fluxes are prescribed as thermal boundary conditions at the outside surface areas of the component. The temperature distribution throughout the component is described by the three-dimensional heat conduction equation [49], as defined in Equation 11.

$$Q_v(x,y,z,t) - \rho(T)C_p(T)\frac{\partial T}{\partial t} + \nabla[k(T)\nabla T] = 0 \quad [11]$$

Q_v Volumetric heat source rate $\left[\frac{W}{m^3}\right]$

ρ(T) Density $\left[\frac{kg}{m^3}\right]$

C_p(T) Specific heat $\left[\frac{W}{kgK}\right]$

In Equation 11, Q_v is the heat generated per unit volume within the component. The local temperature field in the component changes according to the volume-specific heat capacity ρC_p, depending on the local heating or cooling rate. The conductive heat flux throughout the component is described by Fourier's law of heat conduction [50], as defined in Equation 12.

$$q_{cond} = -k(T)\nabla T \quad [12]$$

q_{conv} Conductive heat flux $\left[\frac{W}{m^2}\right]$

k(T) Coefficient of thermal conductivity $\left[\frac{W}{mK}\right]$

∇T Temperature gradient $\left[\frac{K}{m}\right]$

According to Equation 12, the conductive heat flux is proportional to the negative temperature gradient within the component. The heat dissipation from the component to the environment is accommodated by both convection and radiation from the outside surface areas of the component. The convective and radiative heat fluxes per unit surface area are defined in Equation 13 and Equation 14 respectively.

$$q_{conv} = -k\frac{\partial T}{\partial n} = h(T - T_{amb}) \quad [13]$$

$$q_{rad} = -k\frac{\partial T}{\partial n} = \varepsilon\sigma(T^4 - T_{amb}^4) \quad [14]$$

q_{conv} Convective heat flux $\left[\frac{W}{m^2}\right]$

q_{rad} Radiative heat flux $\left[\frac{W}{m^2}\right]$

h(T) Convective heat transfer coefficient $\left[\frac{W}{m^2K}\right]$

ε(T) Emissivity $[-]$

σ Stefan-Boltzmann constant $5.67 \cdot 10^{-8}\left[\frac{W}{m^2K^4}\right]$

T Local surface temperature $[K]$

T_{amb} Ambient temperature $[K]$

In Equation 13 and Equation 14, T is the local surface temperature of the component and T_{amb} is the ambient temperature. The convection and radiation heat fluxes at the surface areas of the component are prescribed as boundary conditions to Equation 11. The initial condition of the component domains is defined in Equation 15.

$$T(x, y, z, 0) = T_0(x, y, z) \quad [15]$$

T_0 Initial temperature of the component $[K]$

3.1.1 Goldak heat source model

The heat flux that is transferred from the welding heat source to the weld pool is described by the Goldak double-ellipsoid heat source model [47]. A schematic representation of the Goldak double-ellipsoidal heat source model, is shown in Figure 24.

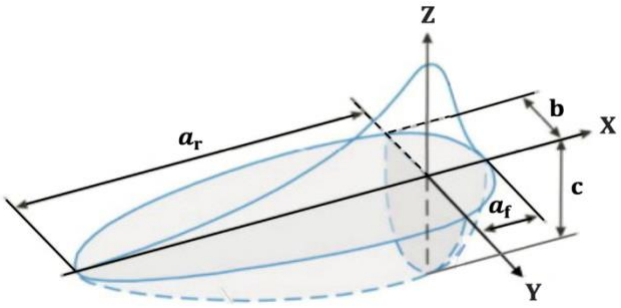

Figure 24: Schematic representation of the Goldak double-ellipsoidal heat source model [6].

According to the Goldak heat source model, a Gaussian distributed heat generation is prescribed throughout the heat source volume [47]. As shown in Figure 24, the Goldak heat source model is defined by a double-ellipsoidal heat source volume representing the size and shape of the weld pool [51]. To account for the asymmetric heat distribution in the weld pool, two distinct power density distributions are defined for the semi-ellipsoids positioned in front and behind the welding arc. The power density distributions inside the semi-ellipsoids positioned in front and behind of the welding arc are defined in Equation 16.a. and Equation 16.b. respectively, [48].

$$q_f(x, y, z) = \frac{6\sqrt{3}\, f_f Q}{\pi\sqrt{\pi}\; a_f bc} exp\left[-3\left(\frac{x^2}{a_f^2} + \frac{y^2}{b^2} + \frac{z^2}{c^2}\right)\right] \quad \text{, for } x \geq 0 \quad [16.a]$$

$$q_r(x, y, z) = \frac{6\sqrt{3}\, f_r Q}{\pi\sqrt{\pi}\; a_r bc} exp\left[-3\left(\frac{x^2}{a_r^2} + \frac{y^2}{b^2} + \frac{z^2}{c^2}\right)\right] \quad \text{, for } x < 0 \quad [16.b]$$

q_f Power density distribution inside the front semi-ellipsoid $\left[\frac{W}{m^3}\right]$

q_f Power density distribution inside the front semi-ellipsoid $\left[\frac{W}{m^3}\right]$

Q Effective heat input $[W]$

a_f, a_r Length of the front, and rear semi-ellipsoid $[mm]$

b Half width of the ellipsoidal heat source volume $[mm]$

c Depth of the ellipsoidal heat source volume $[mm]$

f_f, f_r Power distribution factors of the front semi-ellipsoid $[-]$

According to Equation 16, the volume of the double-ellipsoidal heat source is defined by the heat source parameters a_f, a_r, b and c. The heat source parameters are determined based on the actual weld pool to match the dimensions of the experimental weld pool geometry [51]. The power distribution factors f_f and f_r define the fractions of the arc power that are distributed over the front and rear semi-ellipsoids respectively [47].

The effective heat input Q is the actual arc power that is transferred by the welding heat source to the component [49], as defined in Equation 17.

$$Q = \eta\, UI \qquad [17]$$

Q Effective heat input $[W]$

η Arc efficiency $[-]$

U Arc voltage $[V]$

I Welding current $[A]$

In Equation 17, the total arc power delivered by the welding heat source is defined by the product of the of the arc voltage U and the welding current I [31]. The heat dissipation due to radiation and convection heat losses at the welding arc is accounted for by the arc efficiency η [49].

3.2 F.E. heat source model

The F.E. formulation of the moving welding heat source is based on the Goldak double-ellipsoid heat source model, as defined in Equation 16. In the F.E. model, the position of the welding heat source is described by a moving reference frame with reference to the coordinate system [52]. The interlayer waiting time as defined for the five test cases, is defined in the F.E. heat source model. The F.E. formulation of the moving welding heat source model is defined in Equation 18, [48].

$$q_f(x',y',z',t) = \frac{6\sqrt{3}\, f_f Q}{\pi\sqrt{\pi}\; a_f bc} exp\left[-3\left(\frac{x'^2}{a_f^2}+\frac{y'^2}{b^2}+\frac{z'^2}{c^2}\right)\right] \quad \text{, for } x' \geq 0 \qquad [18.a]$$

$$q_r(x',y',z',t) = \frac{6\sqrt{3}\, f_r Q}{\pi\sqrt{\pi}\; a_r bc} exp\left[-3\left(\frac{x'^2}{a_r^2}+\frac{y'^2}{b^2}+\frac{z'^2}{c^2}\right)\right] \quad \text{, for } x' < 0 \qquad [18.b]$$

$$x' = x_0 + v \cdot t$$

$$y' = y_0$$

$$z' = z_0 + 0.0015 \cdot step(t)$$

$$step(t) = abs\left\{round\left[\frac{t}{t_{layer}} - 0.5\right]\right\}$$

t = time $[s]$

v = welding speed $[m/s]$

t_{layer} = welding time of a single layer $[s]$ + interpass waiting time $[s]$

According to Equation 18, the origin of the moving reference frame coincides with the centre point of the moving double-ellipsoid heat source model, defined by the time dependent coordinates x', y' and z'. The initial position of the welding heat source at the start of the deposition process is defined by the initial coordinates x_0, y_0, and z_0. According to the coordinate system the x-direction is defined as the welding direction, the y-direction is the through-thickness direction and the z-direction is the building direction. The F.E. model representation of the Goldak double-ellipsoidal heat source model, is shown in Figure 25.

As defined in Equation 18, the position of the moving welding heat source along the welding direction is described by the welding speed of the moving welding heat source v and the time t, defined by the time dependent coordinate x'. The position of the welding heat source with respect to the through-thickness direction is constant, expressed by the coordinate y'. The movement of the welding heat source in the building direction is governed by the step-function, expressed by the time dependent coordinate z' of the moving reference frame [53].

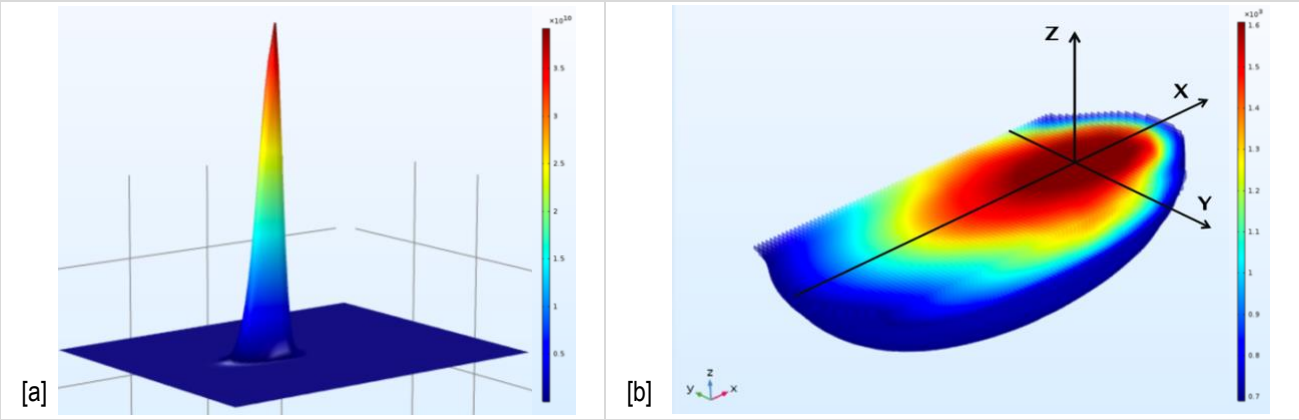

Figure 25: F.E. Goldak double-ellipsoidal heat source model. [a] Heat flux at the surface of the weld pool; [b] Heat generation throughout the volume of the weld pool.

3.3 F.E. material model

An important aspect of the wire and arc additive manufacturing process is the modelling of the material addition during the deposition process [54]. In the F.E. model, the quiet element method is used to model the material deposition in the wire and arc additive manufacturing process. As defined in Equation 11, the temperature distribution throughout the component is described by the three-dimensional heat conduction equation. The three-dimensional heat conduction equation includes the temperature dependent material properties density, specific heat and coefficient of thermal conductivity designated $\rho(T)$, $C_p(T)$ and $k(T)$ respectively.

3.3.1 Material deposition

According to literature, generally two methods can be used to model the material deposition in the wire and arc additive manufacturing process, being the quiet element method and the inactive element method [55]. In this research, the quiet element method is used to model the material deposition in the wire and arc additive manufacturing process.

The main advantage of the quiet element method is that non-convergence issues are avoided during the F.E. calculation, as the number of equations is constant throughout the F.E. analysis [54]. According to the quiet element method, the material elements representing the individual weld layers are defined at the start of the F.E. analysis. The material elements that are not under the influence of the welding heat source are defined quiet. The material addition during the deposition process is modelled by the sequential activation of the quiet elements. The activation of the quiet elements can be triggered based on the temperature, or the position of the welding heat source [54], [48].

In the F.E. model, both the activation of the successive material elements representing the deposition of the individual weld layers, and the activation of the element domains within the material elements are activated based on the position of the welding heat source. The deposition of the successive weld layers is modeled by the sequential activation of the successive material elements. The individual weld layers of the simulated ten-layer weld deposit are modelled by rectangular material elements.

The F.E. formulation of the quiet element method for modelling the material deposition is defined in Equation 19, [54].

$$\begin{aligned} if\ z \le z'(t), \quad & k = k(T) \\ else, \quad & k_{quiet} = s_k \cdot k(T) \end{aligned} \qquad [19]$$

According to Equation 19, the sequential activation of the successive material elements is governed by the step-function, as defined in Equation 18. With regard to the material domains that are under the influence of the welding heat source, the coefficient of thermal conductivity is defined by the material property. While for the quiet elements that are not under the influence of the welding heat source, the coefficient of thermal conductivity is reduced by using a scaling factor.

The material deposition during each individual weld layer is modeled by the progressive activation of element domains within the material elements that are under the influence of the moving welding heat source [48], as defined in Equation 20.

$$\begin{aligned} R(x',y',z',t) = & \sqrt{x'^2 + y'^2 + z'^2} \\ if\ R(x',y',z',t) \le a_f, \quad & q = q_f(x',y',z',t) + q_r(x',y',z',t) \\ else, \quad & q = 0 \end{aligned} \qquad [20]$$

In Equation 20, the centre point of the moving double-ellipsoid heat source model is defined by the term $R(x',y',z',t)$. According to Equation 20, the Gaussian distributed power density is prescribed throughout the heat source volume of the element domains that are under the influence of the welding heat source, as defined by the moving reference frame. Further, the activation of the element domains within the material elements is defined by the heat source parameters, as defined in Equation 16. The F.E. model representation of the material addition and the temperature field that is experienced by the component during the disposition of the of the simulated ten-layer weld deposit by using the quiet element method, is illustrated in Figure 26.

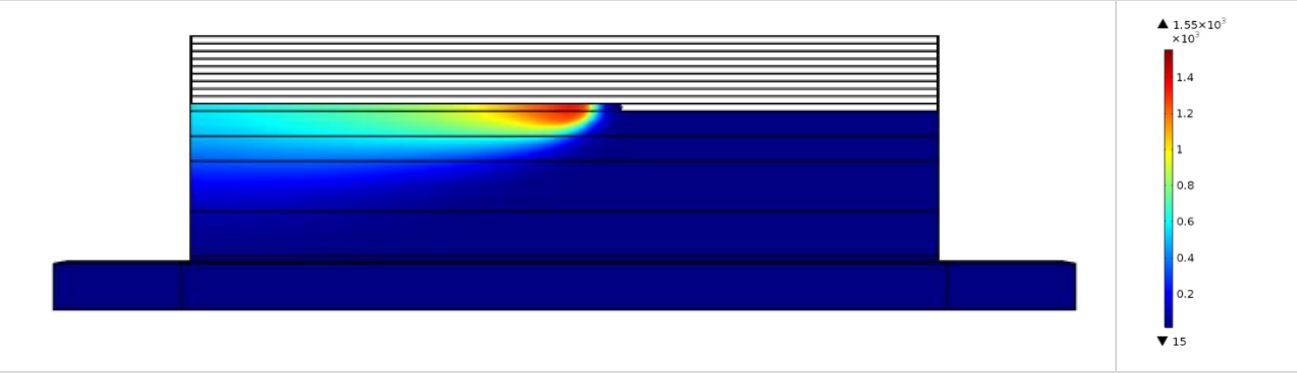

Figure 26: F.E. model representation of the material addition using the quiet element method and the temperature field that is experienced by the component during the disposition of the of the simulated ten-layer weld deposit.

3.3.2 Material properties

As defined in Equation 11, the temperature distribution within the component is described by the three-dimensional heat conduction equation. The three-dimensional heat conduction equation includes the temperature dependent material properties density, specific heat and coefficient of thermal conductivity designated $\rho(T)$, $C_p(T)$ and $k(T)$ respectively.

The temperature dependent material properties of both the structural steel S355 and the electrode material X90 are shown in Figure 27.

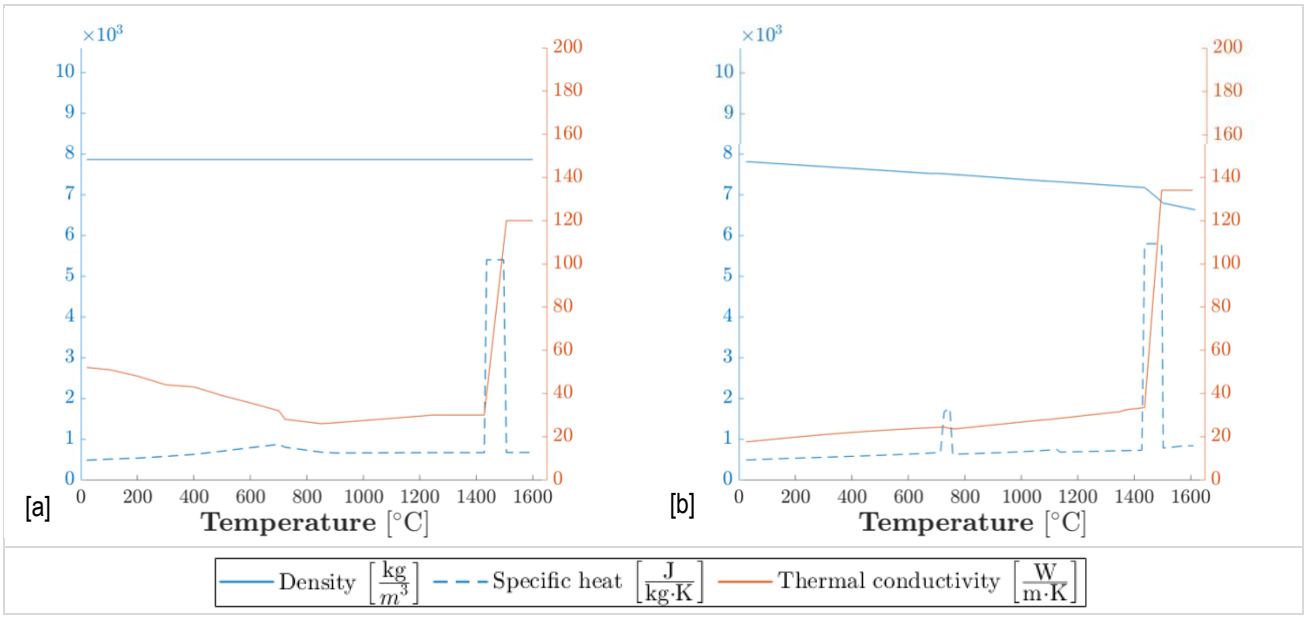

Figure 27: Temperature dependent material properties. [a] Structural steel S355; [b] Electrode material X90.

The temperature dependent material properties $\rho(T)$, $C_p(T)$ and $k(T)$ are assumed isotropic and homogeneous throughout the material domain in the F.E. model [55].

In the F.E. model, the latent heat effects of the ferrite-austenite phase transformation and the solid-liquid phase transformation are not considered. Correspondingly, for both the structural steel S355 and the electrode material X90, the specific heat is assumed constant over the whole temperature range.

The density corresponding to the structural steel S355 is assumed constant over the whole temperature range, having a value of 7860 $\left[\frac{kg}{m^3}\right]$. While, for the electrode material X90 the density is assumed to decrease for increasing temperatures, having a value equal to 7804 $\left[\frac{kg}{m^3}\right]$ at room temperature and 6708 $\left[\frac{kg}{m^3}\right]$ at the liquidus temperature.

The coefficient of thermal conductivity corresponding to both the structural steel S355 and the electrode material X90 are increased by a factor 4 with respect to the value at T_s for temperatures exceeding the melting temperature, to account for the increased convective heat transfer by stirring effects in the weld pool [51].

3.4 Thermal boundary conditions

The heat dissipation from the component to the environment is accommodated by both convection and radiation from the outside surface areas of the component to the environment, as defined in Equation 13 and Equation 14. In the F.E. model, the convective and radiative heat fluxes are prescribed as thermal boundary conditions at the outside surface areas of the component. The application of the cooling method as defined for the test cases 1 to 5 is defined by the appropriate thermal boundary conditions. With regard to the symmetry plane, a symmetry boundary condition is applied [56].

Table 8: Thermal boundary conditions defined in the F.E. model for the test cases 1 to 5.

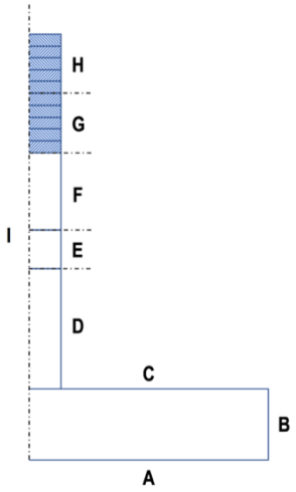

	Test case 1 and 2 Natural cooling			**Test case 3 and 4** Active Substrate cooling			**Test case 5** Active Component cooling		
	h	ε		h	ε		h	ε	
A	2	-		400	-		400	-	
B	4	-		400	-		400	-	
C	2	-		400	-		400	-	
D	4	-		800	-		400	-	
E	4	-		4	-		400	-	
F	4	-		4	-		800	-	
		BC I	**BC II**		**BC I**	**BC II**		**BC I**	**BC II**
G	-	0.95	0.5	-	0.95	0.5	-	0.95	0.5
H	-	0.95	0.95	-	0.95	0.95	-	0.95	0.95
I	Thermal symmetry boundary condition: heat rate $q_0 = 0 \left[\frac{\mathrm{W}}{\mathrm{m}^2}\right]$								

With regard to the substrate and the component base wall, the heat dissipation from the component to the environment is accommodated by convection. As shown in Table 8, the convective heat fluxes are prescribed at the outside surface areas, indicated by A to F.

Concerning the heat dissipation by natural cooling to free air, the convective heat transfer coefficient is defined separately for the vertical and horizontal surface areas [50], [27]. For the vertical outside surface areas of both the substrate and the component base wall, the natural cooling to free air is defined by a convective heat transfer coefficient equal to $4 \left[\frac{W}{m^2 K}\right]$. While, for the horizontal surface areas, the convective heat transfer coefficient for natural cooling to free air is equal to $2 \left[\frac{W}{m^2 K}\right]$.

With regard to the heat dissipation that is accommodated by the cooling medium, a distinction is made between the cooling medium in the liquid phase and the vapor phase [57]. The conductive heat dissipation that is accommodated by the cooling medium in the liquid phase, is defined by an equivalent convective heat transfer coefficient equal to $400 \left[\frac{W}{m^2 K}\right]$. The conductive heat dissipation that is accommodated by the cooling medium in the vapor phase, is accounted for by an equivalent convective heat transfer coefficient equal to $800 \left[\frac{W}{m^2 K}\right]$.

The heat dissipation from the multilayer weld deposit to the environment is accommodated by radiation. The radiative heat fluxes are prescribed at the outside surface areas of the deposited layers of the simulated multilayer weld deposit, indicated by G to H. As shown in Table 8, two sets of radiative boundary conditions are defined, indicated by the radiative boundary condition BC I and the radiative boundary condition BC II.

3.5 Temperature measurement points

The locations of the temperature measurement points in the F.E. model, are shown in Table 9. The temperature measurement points are positioned at the mid-length position of the deposited layers to exclude the start and end-effects [58].

With regard to the substrate and the component base wall. The temperature measurement points indicated by Tc-A and Tc-B are assigned to both the physically attached thermocouples in the experiments and the temperature measurement points in the F.E. model. The temperature measurement points that are positioned at the outside surface areas of the substrate and the component base are wall are indicated by Tc-A and Tc-B respectively.

The temperature measurement points Tc-C and Tc-D refer to the temperature measurement points that are uniquely defined in the F.E. model. As shown in Table 9, the temperature measurement points Tc-C1, Tc-C5 and Tc-C10 are positioned at the centre points of the first, fifth and tenth layer of the simulated ten-layer weld deposit respectively. The temperature measurement points Tc-D1, Tc-D5 and Tc-D10 are positioned at the outside surfaces of the first, fifth and tenth layer of the simulated ten-layer weld deposit respectively.

Table 9: Coordinates of the temperature measurement points at the mid-length position $x = 75\ mm$.

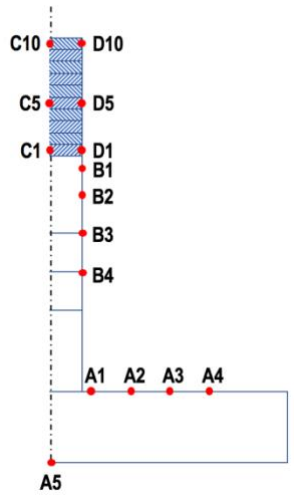

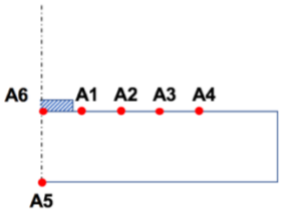

Temperature measurement points		
	y [mm]	z [mm]
Tc-A 1	5	0
Tc-A 2	10	0
Tc-A 3	15	0
Tc-A 4	20	0
Tc-A 5	0	-9
Tc-A 6	0	0
Tc-B 1	4	29
Tc-B 2	4	25
Tc-B 3	4	20
Tc-B 4	4	15
Tc-C 1	0	30.75
Tc-C 5	0	36.75
Tc-C 10	0	44.25
Tc-D 1	4	30.75
Tc-D 5	4	36.75
Tc-D 10	4	44.25

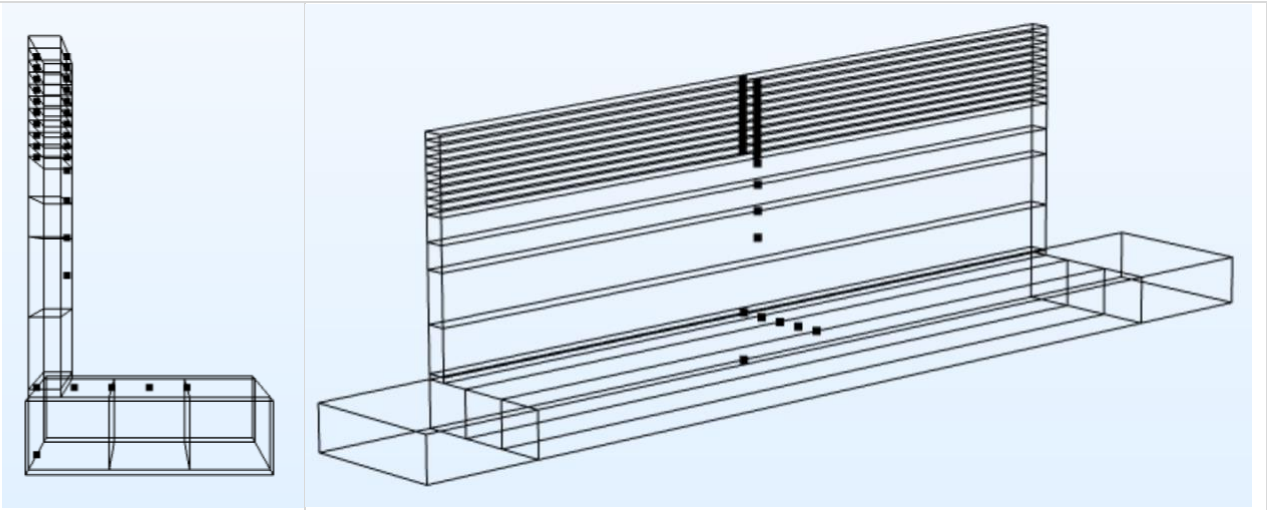

Figure 28: Locations of the temperature measurement points in the F.E. model at the mid-length position $x = 75\ mm$.

3.6 F.E. model calibration

The F.E. model is calibrated by fitting the temperature values that are calculated at the temperature measurement points the F.E. model and the corresponding temperature values that are recorded by the physically attached thermocouples in the experiments, indicated by the temperature measurement points Tc-B1 to Tc-B4. A detailed validation of the F.E. model is provided in Section 5.1.

According to literature, the arc efficiency is calibrated based on the thermal cycle peak temperatures [51]. While, the applied thermal boundary conditions are calibrated based on the thermal cycle through temperatures [51], [48]. In this regard, the arc efficiency is calibrated based on the thermal cycle peak temperatures associated with the deposition of a single weld-pass layer. While the appropriate thermal boundary conditions are calibrated based on the thermal cycle through temperatures associated with the deposition of the multilayer weld deposit.

The discrepancy between the temperature values that are calculated at temperature measurement points in the F.E. model and the corresponding temperature values that are recorded by the physically attached thermocouples in the experiments, is indicated by the calibration error. An overestimation of the experimental temperature values by the F.E. model temperature values is indicated by a positive calibration error, while an underestimation is indicated by a negative calibration error. Both the calibration of the thermal cycle peak temperatures and the thermal cycle through temperatures is based on the smallest calibration error.

3.6.1 Arc efficiency

The arc efficiency is calibrated by fitting the thermal cycle peak temperatures that are calculated at the temperature measurement points the F.E. model and the corresponding temperature values that are recorded by the physically attached thermocouples in the experiments during the deposition of a single weld-pass layer on the component base wall.

The temperature measurement values that are obtained during the deposition of a single weld-pass layer by both the temperature measurement points in the F.E. model and the physically attached thermocouples in the experiments are shown in Figure 29. The values of the thermal cycle peak temperatures that are obtained by both the temperature measurement points in the F.E. model and the physically attached thermocouples in the experiments, indicated by the temperature measurement points Tc-B1 to Tc-B4, are shown in Table 10.

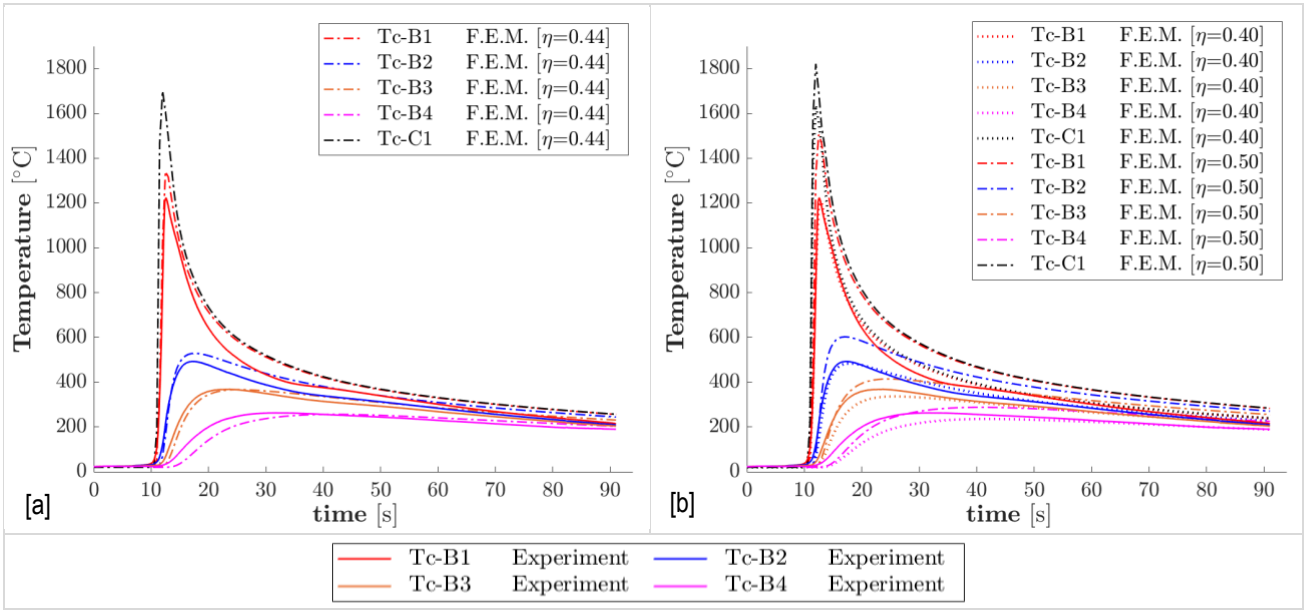

Figure 29: Temperature measurement values of a single-pass layer on the component base wall. [a] Arc efficiency $\eta = 0.44$; [b] Arc efficiencies $\eta = 0.40$ and $\eta = 0.50$.

Table 10: Thermal cycle peak temperatures of a single-pass weld layer on the component base wall; recorded experimental temperature values and calculated F.E. model temperature values for the arc efficiencies: $\eta = 0.40$, $\eta = 0.44$ and $\eta = 0.50$.

	Tc-B 4	Tc-B 3	Tc-B 2	Tc-B 1	Tc-C 1
Experiment	263.0	368.2	492.8	1224	-
F.E.M. $\eta = 0.40$	236.0	336.6	483.8	1204	1634
F.E.M. $\eta = 0.44$	256.5	367.0	529.0	1340	1700
F.E.M. $\eta = 0.50$	288.2	414.5	602.5	1505	1821

The effect of the arc efficiency on the thermal cycle peak temperatures that are calculated by the F.E. model, is shown Figure 29.b. It is found that for an arc efficiency $\eta = 0.40$, the experimental thermal cycle peak temperatures that are recorded by the temperature measurement points Tc-B1 to Tc-B4 are underestimated by the F.E. model. While for an arc efficiency $\eta = 0.50$, the experimental thermal cycle peak temperatures are overestimated by the temperature values that are calculated in the F.E. model with regard to the temperature measurement points Tc-B1 to Tc-B4.

When assuming an arc efficiency $\eta = 0.44$ [(1)], it is found that the thermal cycle peak temperatures that are calculated in the F.E. model are in good agreement with the experimental results, as shown in Figure 29.a. It is observed that for the temperature measurement points Tc-B1 and Tc-B2, the thermal cycle peak temperatures that are calculated in the F.E. model exceed the experimental temperature values, indicated by a calibration error of + 9.5 % and + 7.4 % respectively. While, for the temperature measurement points Tc-B3 and Tc-B4 the experimental thermal cycle peak temperatures are slightly underestimated by the F.E. calculation, indicated by a calibration error of - 0.3 % and - 2.5 % respectively.

3.6.2 Thermal boundary conditions

The appropriate thermal boundary conditions are calibrated by fitting the thermal cycle through temperatures that are calculated at the temperature measurement points in the F.E. model and the corresponding temperature values that are recorded by the physically attached thermocouples in the experiments. Since each thermal cycle through temperature is defined as the minimum temperature value at the end of each cooling stage, the thermal cycle through temperatures are strongly dependent on the applied boundary conditions, as defined in Table 9.

The thermal cycle through temperatures that are obtained by both the temperature measurement points in the F.E. model and the physically attached thermocouples in the experiments indicated by Tc-B1 to Tc-B4, are shown in Table 11. The thermal cycle through temperatures correspond to the temperature measurement values at 60 s after the passage of the welding heat source.

Table 11: Thermal cycle through temperatures of a single-pass weld layer on the component base wall; recorded experimental temperature values and calculated F.E. model temperature values for the arc efficiencies: $\eta = 0.40$, $\eta = 0.44$ and $\eta = 0.50$.

	Tc-B 4	Tc-B 3	Tc-B 2	Tc-B 1	Tc-C 1
Experiment	220.7	241.3	250.7	282.8	-
F.E.M. $\eta = 0.40$	209.4	243.2	260.3	274.5	275.8
F.E.M. $\eta = 0.44$	225.9	262.4	280.8	296.1	297.4
F.E.M. $\eta = 0.50$	251.0	291.0	311.0	327.4	328.8

Similar to the observations regarding the thermal cycle peak temperatures, it is found that the thermal cycle through temperatures that are calculated in the F.E. model are in good agreement with the experimental values when assuming an arc efficiency $\eta = 0.44$. The discrepancy between the thermal cycle through temperatures that are calculated in the F.E. model and the corresponding experimental temperature values is indicated by a calibration error of + 4.7 % and + 2.4 % for the temperature measurement points Tc-B1 and Tc-B4 respectively.

(1) A detailed validation of the arc efficiency is provided in Section 5.1.2

With regard to the multilayer weld deposit, two sets of radiative boundary conditions are defined for the radiative heat transfer at the outside surface areas of the simulated ten-layer weld deposit in the F.E. model, indicated by the radiative boundary condition BC I and the radiative boundary condition BC II, as shown in Table 8. The appropriate radiative boundary conditions for the test cases 1 to 5, are calibrated by fitting the thermal cycle through temperatures that are calculated in the F.E. model and the corresponding temperature values that are recorded in the experiments by the temperature measurement point Tc-B1 during the deposition process of the simulated ten-layer weld deposit. The appropriate radiative boundary conditions for the test cases 1 to 5, are shown in Table 12.

Table 12: The radiative boundary conditions in the F.E. model; defined for the test cases 1 to 5.

	BC I	Average BC I, BC II	BC II
Test case 1	1 to 3	4 to 5	6 to 10
Test case 2	1 to 3	4 to 10	-
Test case 3	1 to 6	7, 8	9, 10
Test case 4	1 to 6	7, 8	9, 10
Test case 5	1 to 10	-	-

In the F.E. model, the radiative boundary conditions are adjusted during the deposition of the simulated ten-layer weld deposit to guarantee the accurate heat dissipation from the deposited material layers to the environment. By the application of the appropriate thermal boundary conditions as defined for the test cases 1 to 5, it is found that for all test cases the calibration error of the thermal cycle through temperatures corresponding to the temperature measurement point Tc-B1 are within the +/- 5.0 % error range, excluding the start and end-effects.

3.6.3 Heat source parameters

The the appropriate heat source parameters of the Goldak heat source model are calibrated by the experimental weld pool dimensions, as shown in Figure 30. The heat source parameters a_f and a_r are estimated from the weld pool surface ripple markings. While, the heat source parameters b and c are estimated from the cross-sectional metallographic profile, whereby the heat source parameter b is equal to the half width of the deposited layer. The parameter c is defined as the average layer height plus the weld penetration [56]. The heat source parameters matching the cross-sectional metallographic profiles of the test cases 1 to 5, are provided in Table 13.

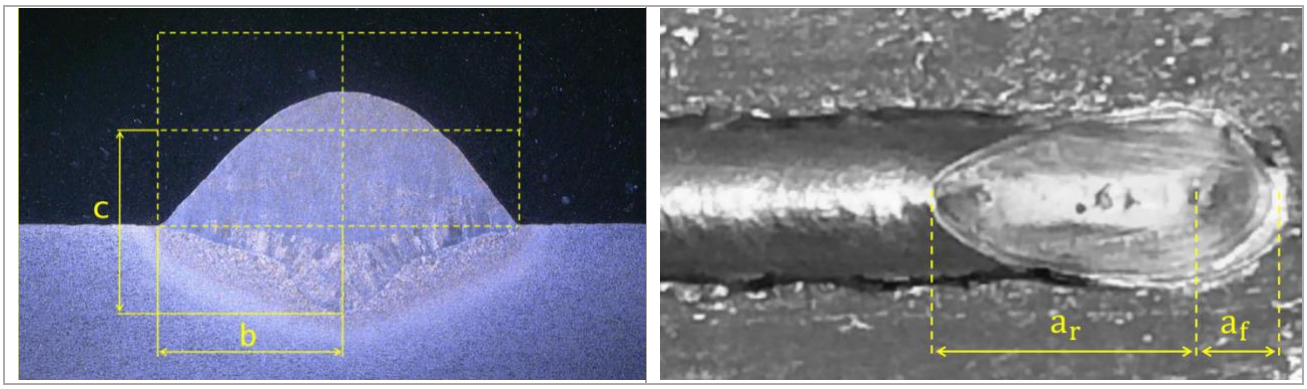

Figure 30: Heat source parameters of the Goldak heat source model. [a] Heat source parameters b and c, cross-sectional metallographic profile; [b] Heat source parameters a_f and a_r, weld pool surface markings.

Table 13: Heat source parameters a_f, a_r, b and c, and the power distribution factors f_f and f_r; defined for the test cases 1 to 5.

	a_f [mm]	a_r [mm]	b [mm]	c [mm]	f_f [-]	f_r [-]
Bead-on-plate	3.85	9.4	3.35	4	0.6	1.4
Test case 1, 2	3.85	9.4	3.5	3	0.6	1.4
Test case 3 to 5	3.85	9.4	3.3	3	0.6	1.4

4 Results and analysis

4.1 Temperature values

The temperature field that is experienced by the component during the wire and arc additive manufacturing process is characterized by the periodic thermal cycling of the temperature values related to the deposition process.

The temperature values are recorded by the physically attached thermocouples in the experiments and calculated at the temperature measurement points in the F.E. model, are shown in Figure 31. With regard to the substrate and the component base wall, the temperature field is described by both the temperature values that are recorded by the physically attached thermocouples in the experiments and calculated at the temperature measurement points in the F.E. model. While the temperature field that is experienced by the simulated multilayer weld deposit is described by the temperature values that are calculated at the temperature measurement points that are uniquely defined in the F.E. model.

4.1.1 Experimental temperature values

The experimental temperature values refer to the temperature values that are recorded by the physically attached thermocouples in the experiments. The experimental temperature values corresponding to the test cases 1 to 5 are provided in Appendix B.1.

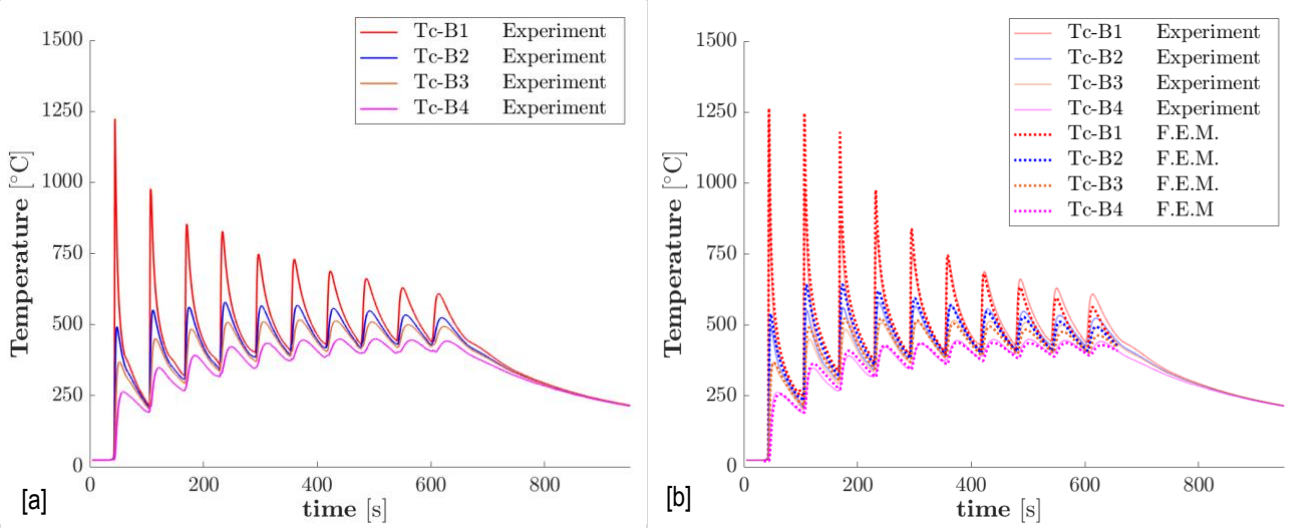

Figure 31: Temperature values corresponding to the temperature measurement points Tc-B1 to Tc-B4. [a] Recorded experimental temperature values; [b] Calculated F.E. model temperature values.

The temperature values that are recorded by the physically attached thermocouples indicated by Tc-B1 to Tc-B4, are illustrated in Figure 31.a. The highest temperature values are recorded by the temperature measurement point Tc-B1 followed by Tc-B2, Tc-B3 and Tc-B4 respectively, corresponding to the relative position of the temperature measurement points with respect to the moving welding heat source during the deposition process of the multilayer weld deposit.

The thermal cycle measurement values that are obtained by both the physically attached thermocouples and the temperature measurement points in the F.E. model indicated by Tc-B1 to Tc-B4, are illustrated in Figure 31.b. The temperature values that are calculated at the temperature measurement points in the F.E. model and the temperature values that are recorded by the physically attached thermocouples in the experiments corresponding to the test cases 1 to 5 are provided in Appendix B.2. As shown, the temperature values that are calculated at the temperature measurement points in the F.E. model are in good agreement with the corresponding temperature values that are recorded by the physically attached thermocouples in the experiments.

4.1.2 F.E. model temperature values

The F.E. model temperature values refer to the temperature values that are calculated at the temperature measurement points in the F.E. model. The temperature measurement points that are located at the outside surface areas of the component base wall are indicated by Tc-B. While, the temperature measurement points indicated by Tc-C and Tc-D refer to the temperature measurement points that are uniquely defined in the F.E. model regarding the simulated multilayer weld deposit, as indicated in Table 9.

The temperature field that is experienced by the middle points of the deposited layers of the multilayer weld deposit is represented by the temperature values that are calculated at the temperature measurement points indicated by Tc-C. The temperature values that are calculated the temperature measurement points Tc-C1, Tc-C5 and Tc-C10 in the F.E. model for test case 1, is shown in Figure 32. As indicated, the temperature values that are calculated in the F.E. model can be related to the microstructural transformation temperatures to define the resulting microstructure of the deposited material in the wire and arc additive manufacturing process considering a simulated multilayer weld deposit, as described in literature for laser-deposited multilayer builds [59], [60].

The temperature values that are calculated the temperature measurement points Tc-C1, Tc-C5 and Tc-C10 in the F.E. model corresponding to the test cases 1 to 5 are provided in Appendix B.3, Appendix B.4 and Appendix B.5 respectively.

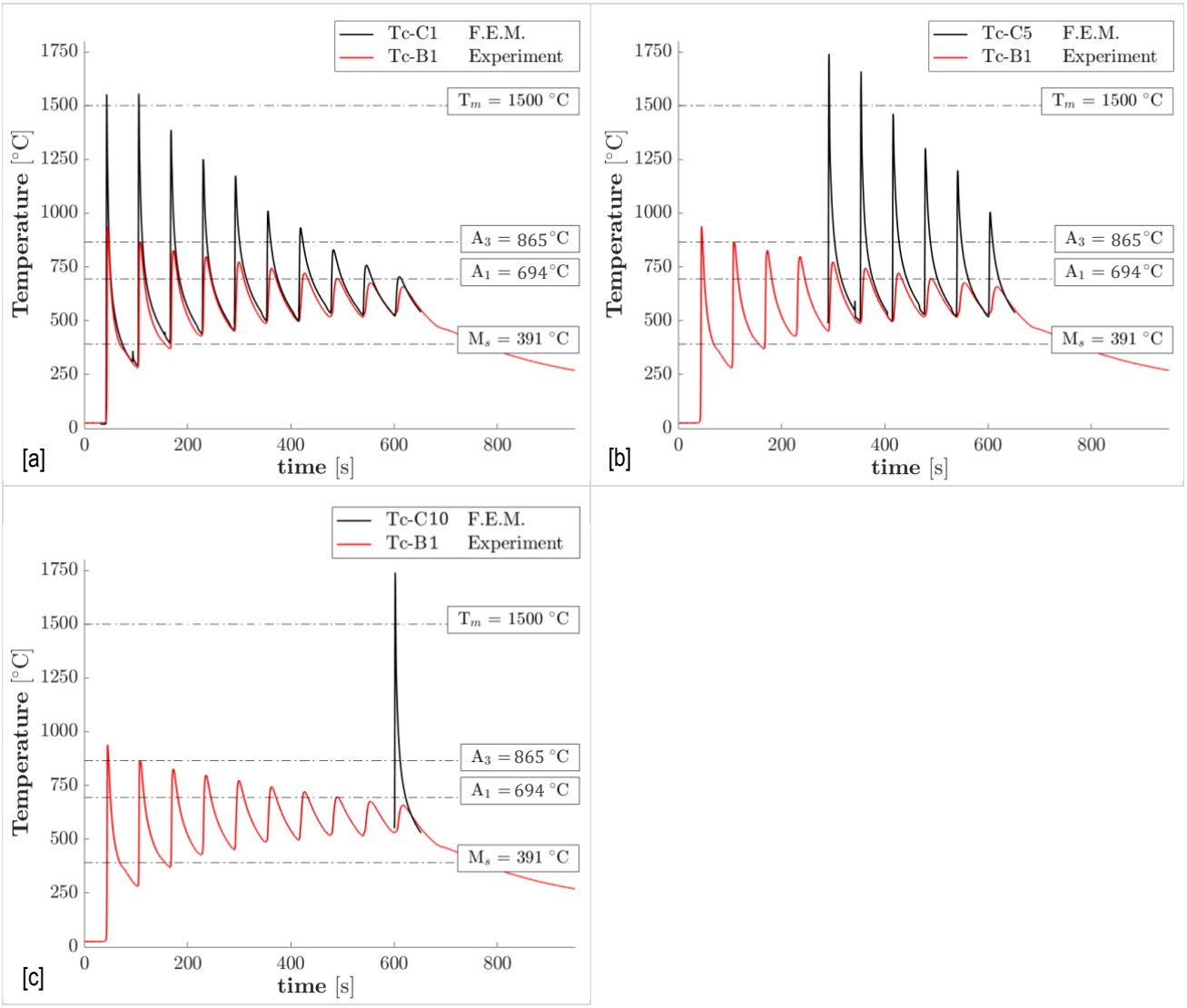

Figure 32: F.E. model temperatures of the simulated ten-layer weld deposit. [a] Calculated at temperature measurement point Tc-C1: middle point layer 1; [b] Calculated at temperature measurement point Tc-C5: middle point layer 5; [c] Calculated at temperature measurement point Tc-C10: middle point layer 10.

4.1.2.1 Multilayer weld deposit

The experimental fifteen-layer weld deposit is simulated in the F.E. model by a simulated ten-layer weld deposit. As shown in Figure 33, the temperature measurement points Tc-C1, Tc-C5 and Tc-C10 correspond to the middle points of the sixth, tenth and fifteenth layer of the experimental fifteen-layer weld deposit respectively.

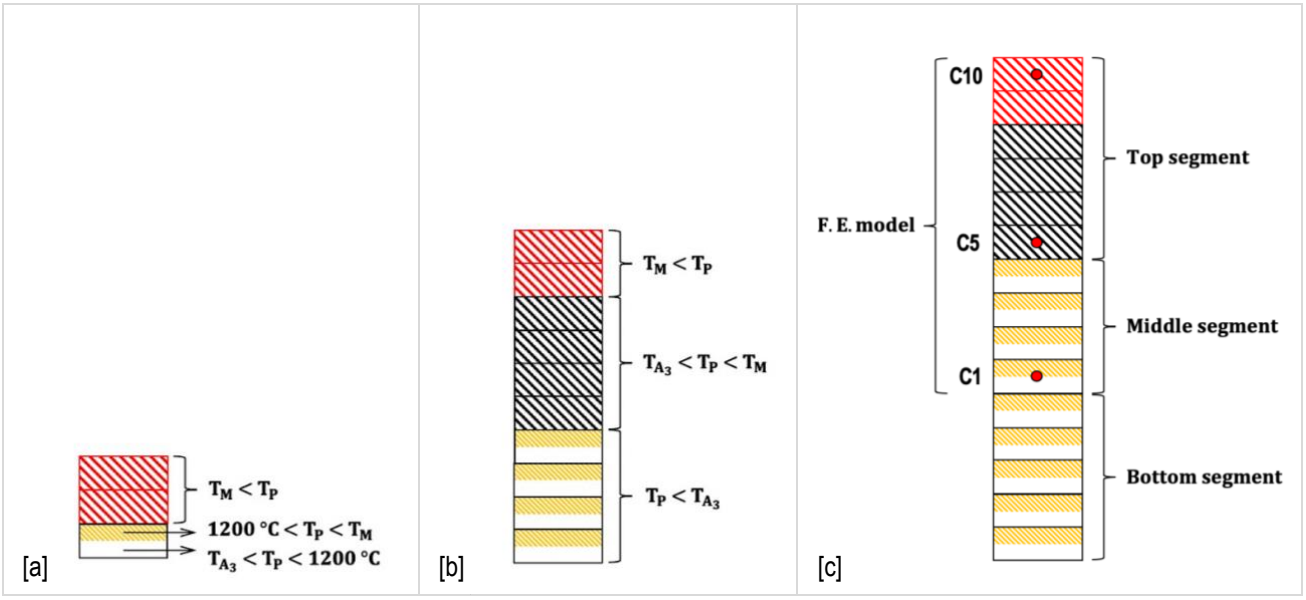

Figure 33: Thermal analysis of the experimental fifteen-layer weld deposit. [a,b] Thermal cycle peak temperatures in relation to the microstructural transformation temperatures; [c] F.E. model approximation of the experimental fifteen-layer weld deposit.

With regard to the temperature field that is experienced by the experimental fifteen-layer weld deposit, three distinct regions are defined: the top segment, the middle segment and the bottom segment.

4.1.2.1.1 Top segment

The top segment of the experimental fifteen-layer weld deposit is defined by the region that experiences no subcritical heat treatment. In this regard, the top segment is defined by the region that is bounded by the bottom layer for which the last thermal cycle peak temperature exceeds the A_3-temperature. While, the upper layer of the top segment is indicated by the measurement point Tc-C10 in the F.E. model.

According to Figure 33, the temperature field that is experienced by the upper layer of the top segment is characterized by one thermal cycle peak temperature according to the temperature values that are calculated at the measurement point Tc-C10. While regarding the bottom layer of the top segment, the temperature field is characterized by six thermal cycle peak temperatures and five thermal cycle through temperatures according to the temperature measurement values that are calculated at the measurement point Tc-C5.

4.1.2.1.2 Middle segment

The middle segment of the experimental fifteen-layer weld deposit is bounded by the region wherein the bottom and upper layer are indicated by the measurement points Tc-C1 and Tc-C5 in the F.E. model respectively. The temperature values that are calculated at the measurement point Tc-C1 correspond to the temperature field that is experienced by both the bottom layer of the middle segment and the upper layer of the bottom segment.

According to Figure 33, the temperature field that is experienced by the upper layer of the middle segment is characterized by six thermal cycle peak temperatures and five thermal cycle through temperatures according to the temperature values that are calculated at the measurement point Tc-C5. The temperature field that is experienced by both the bottom layer of the middle segment and the upper layer of the bottom segment of the experimental fifteen-layer weld deposit is characterized by ten thermal cycle peak temperatures and nine thermal cycle through temperatures according to the temperature values that are calculated at the measurement point Tc-C1.

4.1.2.1.3 Bottom segment

The bottom segment of the experimental fifteen-layer weld deposit is bounded by the region wherein the upper layer is indicated by the measurement point $\mathrm{Tc\text{-}C1}$ in the F.E. model.

The temperature field that is experienced by the layers constituting the bottom segment of the experimental fifteen-layer weld deposit is represented by the successive temperature values succeeding the values that are calculated at the measurement point $\mathrm{Tc\text{-}C1}$. Accordingly, the temperature field that is experienced by the bottom layer of the bottom segment of the experimental fifteen-layer weld deposit is characterized by fifteen thermal cycle peak temperatures and fourteen thermal cycle through temperatures.

4.2 Thermal characteristics

The effect of the temperature values on the microstructure of the material constituting the experimental fifteen-layer weld deposit is described in terms of the thermal characteristics including the temperature distribution, the locally attained temperature values, the cooling rates and the temperature gradients throughout the component.

The periodic thermal cycling of the temperature values is characterized by the thermal cycle peak temperatures, the thermal cycle through temperatures and the cooling rates. For each thermal cycle, the thermal cycle peak temperature is defined as the maximum temperature value that is observed after the passage of the welding heat source. While, the thermal cycle through temperature is defined as the minimum temperature value that is reached at the end of each cooling stage. The cooling rates are determined based on the thermal cycle measurement values that are calculated at the temperature measurement points in the F.E. model.

The temperature distribution throughout the component is represented by the temperature field based on the local outside surface temperatures of the component. In this regard, the temperature field representing the temperature distribution throughout the component is associated with the heat dissipation from the component to the environment by both convection and radiation from the outside surface areas of the component. The cooling rate and the temperature gradient are associated with the temperature distribution throughout the component.

The heat dissipation throughout the component is accommodated by conduction. The conductive heat flux throughout the component is described by Fourier's law of heat conduction. In this regard, the temperature gradients in the x- and z-direction are associated with the heat dissipation throughout the component, accommodated by conduction. While, the temperature gradient in the y-direction is associated with the heat dissipation from the component to the environment, accommodated by both convection and radiation from the outside surface areas of the component.

4.2.1 Overview

Depending on the locally reached temperature values, different microstructural transformations are induced:

i. Grain growth
ii. Grain refinement
iii. Partial transformation
iv. Martensitic transformation
v. Tempering and ageing

The thermal cycle peak temperatures are associated with the amount of grain growth, grain refinement and the formation of partial transformation products. While the thermal cycle through temperatures are related to the martensitic transformation. The component mean temperature affects the substitutional diffusion of alloying elements, recrystallization, grain growth and the amount of grain refinement. Both the microstructural morphology and the formation of microstructural constituents are affected by the cooling rate. Further, the distribution of alloying elements throughout the material is influenced by the locally attained temperature gradient.

4.2.1.1 Thermal cycle peak temperatures

For thermal cycle peak temperatures attaining values in the temperature range between 1200 °C and the melting temperature, grain growth is facilitated. While for thermal cycle peak temperatures reaching temperature values in the temperature range between the A_3-temperature and 1200 °C, limited grain growth and grain refinement is facilitated. Further, the formation of partial transformation products is induced for temperature values reaching the inter-critical temperature range.

4.2.1.1.1 Grain growth

With regard to thermal cycle peak temperatures attaining values in the temperature range between 1200 ℃ and the melting temperature, the material is completely transformed into the austenite phase and the temperature is sufficiently high for grain growth to take place. Further, the austenite grain growth is promoted as a result of the dissolution of precipitates. In addition, at these temperatures the homogenization of the alloying element throughout the microstructure is promoted.

4.2.1.1.2 Grain refinement

With regard to thermal cycle peak temperatures attaining values in the temperature range between the A_3-temperature and 1200 ℃, the material is completely transformed into the austenite phase, but the temperature is not high enough for grain growth to take place.

4.2.1.1.3 Partial transformation

For thermal cycle peak temperatures attaining values in the inter-critical temperature range, the formation of partial transformation products is induced. At temperature values below the A_3-temperature pro-eutectoid ferrite is formed until the A_1-temperature is reached. At small undercooling below the A_3-temperature, the ferrite nucleates at the prior austenite grain boundaries and grain boundary ferrite is formed. While, at larger undercoolings below the A_3-temperature, Widmanstätten ferrite is formed [38].

4.2.1.2 Thermal cycle through temperatures

The thermal cycle through temperatures are related to the amount of martensitic transformation that is induced at temperatures below the martensitic start temperature.

4.2.1.2.1 Martensitic transformation

With regard to thermal cycle through temperatures attaining values below the martensitic start temperature, the martensite transformation is induced when the material is rapidly cooled from temperatures exceeding the A_1-temperature. The martensite transformation is a diffusionless transformation that results in the formation of a supersaturated solid solution of carbon in the ferrite matrix. At temperatures below the martensitic start temperature, both the diffusion of the solute atoms and the alloying elements are suppressed. In this regard, the martensite transformation is independent of the thermal activation, and proceeds if further undercooling is available [39].

4.2.1.3 Component mean temperature

The component mean temperature affects by means of tempering and ageing phenomena the extent in which the substitutional diffusion of alloying elements, recrystallization, grain growth and the amount of grain refinement is facilitated.

4.2.1.3.1 Tempering and ageing

The tempering heat treatment depends on the attained temperature and the tempering time [38]. For temperatures in the range between 250 ℃ and the A_1-temperature, iron carbides precipitate in the form of lath-like cementite within the martensite. While, for temperatures exceeding 500 ℃, the temperature is sufficiently high for the substitutional diffusion of alloying elements to occur and the formation of alloy carbides and the dissolution of cementite is induced. Further, recrystallization and grain growth is facilitated at these temperatures. During recrystallization, grain growth takes place by the growth of newly formed grains by the annihilation of dislocations.

4.2.1.4 Cooling rate

The values of the cooling rate affect both the microstructural morphology and the microstructural constituents of the resulting microstructure. At high cooling rates the formation of a fine-grained microstructural morphology is promoted by the nucleation of new grains at the prior austenite grain boundaries. While at lower cooling rates, grain growth is sustained by diffusion [39].

For temperature values exceeding the A_3-temperature but below the melting temperature, the material is completely transformed into the austenite phase in accordance with the phase diagram of the electrode material X90. Depending on the cooling rate, the austenite phase is decomposed into microstructural constituents as shown in Figure 23. For low cooling rates the resulting microstructure is mainly composed of ferrite and pearlite constituents and a reduced amount of granular bainite. While, for cooling rates in the range of $0.6\ °C/s$ to $15\ °C/s$, the resulting microstructure mainly consists of bainite microstructural constituents. A predominantly martensitic microstructure is formed for cooling rates exceeding $15\ °C/s$.

4.2.1.5 Temperature gradient

In addition to the tempering and ageing phenomena, the distribution of alloying elements throughout the material is influenced by the locally attained temperature field [39]. During the solidification process, the concentration of alloying elements in front of the solidification interface is increased by the local temperature gradient resulting from constitutional supercooling during the solidification process. Further, the redistribution of alloying elements is promoted as a result of the deposition process under the influence of the maximum temperature gradient [38].

4.2.2 Temperature distribution

The temperature distribution throughout the component is evaluated during the deposition of the simulated ten-layer weld deposit in the F.E. model.

The temperature values that are calculated for the test cases 1 to 5 during the deposition of the tenth layer of the simulated ten-layer weld deposit is provided in Appendix C.1 and Appendix C.2. Additionally, the temperature distribution that is observed for the test cases 1 to 5 during the deposition of the tenth layer of the simulated weld deposit in the F.E. model is provided in Appendix C.3 and Appendix C.4 respectively.

4.2.2.1 Substrate

With regard to the temperature field that is experienced by the substrate. It is observed that for all test cases, the temperature values that are calculated at the temperature measurement point Tc-A3 increase as the deposition process of the multilayer weld deposit proceeds.

When comparing the temperature values that are calculated for the test cases 1 to 5 during the deposition of the tenth layer of the simulated ten-layer weld deposit. It is observed that with regard to the temperature values that are calculated at the temperature measurement point Tc-A3, the temperature values that are found for the test cases 1 and 2 are of the same order. While, the temperature values that are found for the test cases 3, 4 and 5 are lower compared to the values that are found for the test cases 1 and 2. According to Appendix C.2, the average temperature value that is calculated at the temperature measurement point Tc-A3 during the deposition of the final layer of the simulated ten-layer weld deposit for the test cases 1 and 2 is equal to 364.0 °C. While for the test cases 3, 4 and 5, the corresponding temperature values are on average equal to 35.0 °C. Indicating that during the deposition of the final layer of the simulated ten-layer weld deposit, the temperature values corresponding to the test cases 3, 4 and 5 are 90.4 % lower compared to the values that are found for the test cases 1 and 2.

4.2.2.2 Component base wall

The component mean temperature is defined as the average value of the thermal cycle through temperatures calculated at the temperature measurement points Tc-B1, Tc-B2, Tc-B3 and Tc-B4. The component mean temperatures that result from the application of the cooling methods as defined for the test cases 1 to 5, is shown in Figure 34.

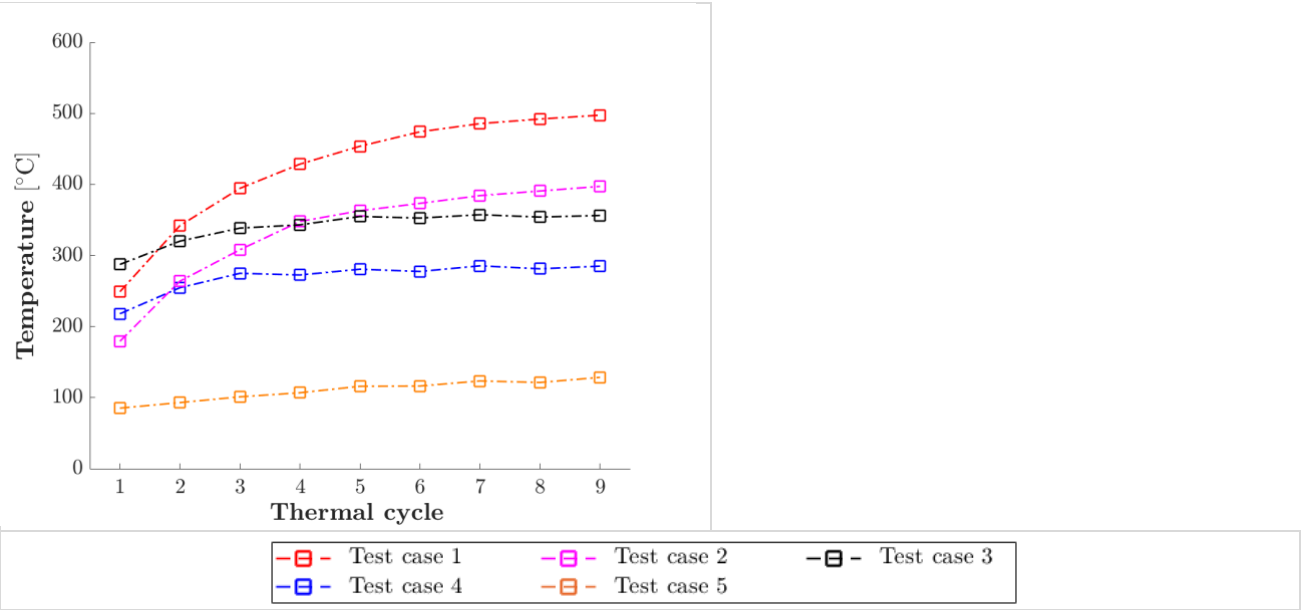

Figure 34: Component mean temperatures of the test cases 1 to 5; defined as the average value of the thermal cycle through temperatures calculated at the temperature measurement points Tc-B1, Tc-B2, Tc-B3 and Tc-B4.

It is observed that for all test cases, the component mean temperature increases as the deposition of the multilayer weld deposit proceeds. The highest values of the component mean temperature are observed for test case 1, followed by the values corresponding to the test cases 2, 3, 4 and 5 respectively. For both the test cases 1 and 2, the values of the component mean temperature continuously increase during the deposition of the simulated ten-layer weld deposit. While for the test cases 3 and 4, the values of the component mean temperature assume constant values from the fifth thermal cycle onward. Indicating that for both the test cases 3 and 4, an equilibrium component mean temperature is reached from the fifth thermal cycle onward. For test case 5, the component mean temperature is found to increase constantly during the deposition process of the simulated ten-layer weld deposit. However, the component mean temperature that is found for test case 5 is relatively low compared to the increase that is found for the test cases 1 to 4.

When comparing the values of the component mean temperature that are found for the test cases 1 to 5. The same evolution is observed for the test cases 1 and 2, and the test cases 3 and 4 respectively. According to Figure 34, the values of the component mean temperature corresponding to test case 2 are consistently $21.6\ \%$ lower compared to the values that are found for test case 1. While, the values of the component mean temperature that are observed for test case 4 are consistently $23.6\ \%$ lower compared to the values that are found for test case 3. Further, it is observed that the component mean temperatures that are found for the test cases 1 to 5 converge toward equilibrium values during the deposition process. According to Figure 34, the equilibrium component mean temperatures of the component base wall that are found for the test cases 1 to 5 are equal to $487.2\ °C$, $386.4\ °C$, $355.0\ °C$, $282.3\ °C$, $122.4\ °C$ respectively. Further, it is observed that the equilibrium component mean temperatures that are found for both the test cases 2 and 3 are of the same order. According to Figure 34, the component mean temperatures corresponding to the test cases 2 and 3 are reduced by $21.6\ \%$ and $23.6\ \%$ respectively, compared to the value that is found for test case 1. While, the component mean temperature that is observed for test case 4 is $41.2\ \%$ lower compared to the value that is found for test case 1. The most significant reduction of the component mean temperature is observed for test case 5. According to Figure 34, the component mean temperature that is found for test case 5 is $74.9\ \%$ lower compared to the temperature value that is found for test case 1.

4.2.2.3 Multilayer weld deposit

With regard to the temperature field that is experienced by the simulated ten-layer weld deposit. It is observed that for the test cases 1 to 5, the temperature values that are calculated at the temperature measurement points of the corresponding layers continuously decrease for longer times after the passage of the welding heat source. While, with regard to the temperature values that are calculated at the temperature measurement points of the underlying layers initially an increase in temperature values is observed. Further, it is found that the maximum temperature values shift toward later times after the passage of the welding heat source.

When comparing the temperature values that are found for the test cases 1 to 5 during the deposition of the tenth layer of the simulated ten-layer weld deposit. It is observed that with regard to the temperature values that are calculated at the temperature measurement point $\mathrm{Tc\text{-}D10}$, the temperature values corresponding to the test cases 1 to 3 are of the same order. While, the temperature values corresponding to the test cases 4 and 5 are lower compared to the values that are found for the test cases 1 and 3. According to Appendix C.2, the temperature values that are calculated for the test cases 1 to 3 during the deposition of the final layer of the simulated ten-layer weld deposit by the temperature measurement point $\mathrm{Tc\text{-}D10}$ at $40\ s$ after the passage of the welding heat source are on average equal to $575.0\ °C$. While, the corresponding temperature values that are found for the test cases 4 and 5 are equal to $469{,}6\ °C$ and $348{,}6\ °C$ respectively. Indicating that during the deposition of the final layer of the simulated ten-layer weld deposit, the temperature values that are calculated at the temperature measurement point $\mathrm{Tc\text{-}D10}$ corresponding to the test cases 4 and 5 are reduced by $17.2\ \%$ and $38.5\ \%$ respectively, compared to the values that are found for the test cases 1 to 3.

With regard to the temperature values that are calculated at the temperature measurement point Tc-D5. It is observed that the temperature values corresponding to the test cases 1 and 3 are of the same order. While, the temperature values that are found for the test cases 2, 4 and 5 are lower compared to the values that are found for both the test cases 1 and 3. According to Appendix C.2, the temperature values that are calculated for the test cases 1 and 3 during the deposition of the final layer of the simulated ten-layer weld deposit by the temperature measurement point Tc-D5 at 2 s after the passage of the welding heat source are equal to 998.7 °C and 973.9 °C respectively. While, the corresponding temperature values that are found for the test cases 2, 4 and 5 are equal to 890.1 °C, 836.8 °C and 678.0 °C respectively. Indicating that during the deposition of the final layer of the simulated ten-layer weld deposit, the temperature values that are calculated at the temperature measurement point Tc-D5 corresponding to the test cases 2, 4 and 5 are reduced by 10.9 %, 16.2 % and 32.1 % respectively, compared to the values that are found for the test cases 1 and 3. Regarding the temperature values that are calculated at the temperature measurement point Tc-D1. The highest temperature values are observed for test case 1, followed by the values corresponding to the test cases 2, 3, 4 and 5 respectively. According to Appendix C.2, the temperature values that are calculated for the test cases 1 to 5 during the deposition of the final layer of the simulated ten-layer weld deposit by the temperature measurement point Tc-D1 at 8 s after the passage of the welding heat source are equal to 703.7 °C, 628.5 °C, 633.7 °C, 538.5 °C and 363.2 °C respectively. Indicating that during the deposition of the final layer of the simulated ten-layer weld deposit, the temperature values that are calculated at the temperature measurement point Tc-D1 corresponding to the test cases 2, 3, 4 and 5 are reduced by 10.7 %, 10.0 %, 23.8 % and 48.4 % respectively, compared to the values that are found for test case 1.

Concerning the equilibrium mean temperatures that are calculated for the five test cases during the deposition of the tenth layer of the simulated ten-layer weld deposit. It is found that the equilibrium mean temperatures associated with the middle segment and the top segment of the experimental fifteen-layer weld deposit of the test cases 1 to 5 are equal to 570.6 °C, 575.4 °C, 547.8 °C, 446.8 °C and 304.4 °C respectively. While, the equilibrium mean temperatures associated with the bottom segment of the experimental fifteen-layer weld deposit corresponding to the test cases 1 to 5 are equal to 539.4 °C, 493.9 °C, 386.2 °C, 313.2 °C and 168.8 °C respectively. Indicating that the equilibrium mean temperatures of the bottom segment corresponding to the test cases 1 to 5 are reduced by 5.5 %, 14.2 %, 29.5 %, 29.9 % and 44.5 % respectively, compared to the values that are observed for the middle segment and the top segment of the experimental fifteen-layer weld deposit.

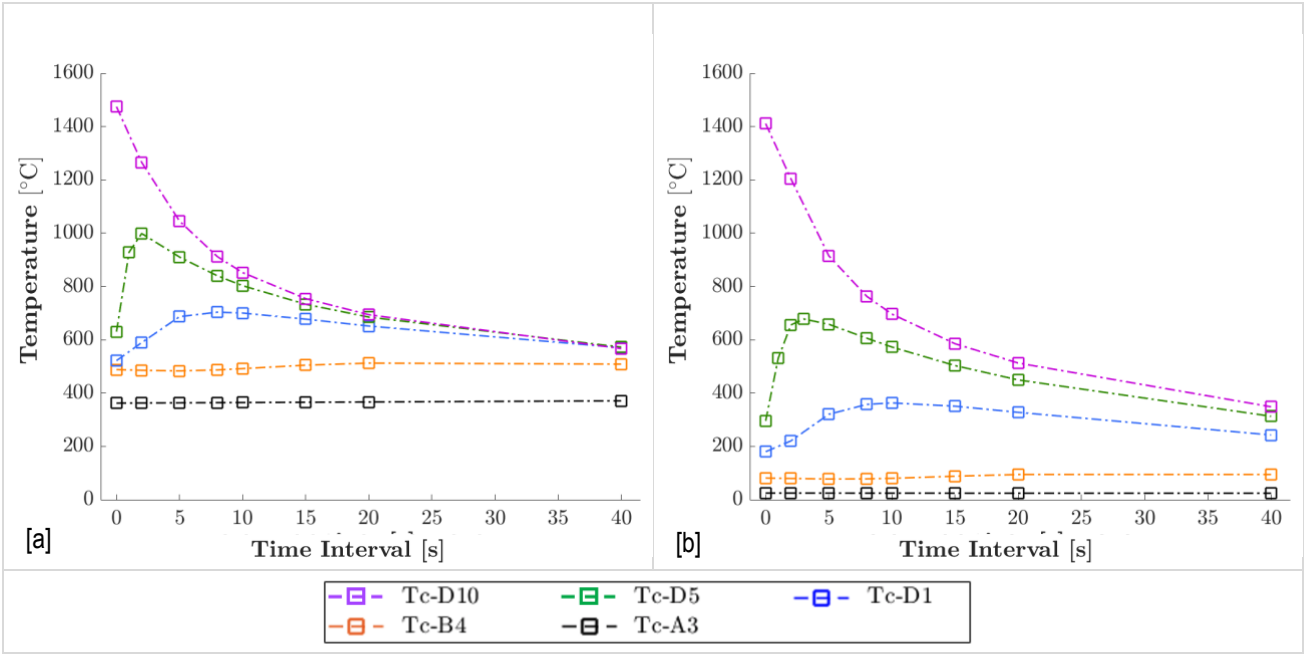

Figure 35: Temperature distribution component, calculated during the deposition of the tenth layer of the simulated ten-layer weld deposit. [a] Test case 1: Natural cooling, interlayer waiting time 40s; [b] Active component cooling, interlayer waiting time 40s.

4.2.3 Thermal cycle peak temperatures

The thermal cycle peak temperatures that are calculated at the measurement points Tc-C1 and Tc-C5 in the F.E. model during the deposition process of the simulated ten-layer weld deposit, are shown in Figure 36.a. and Figure 36.b. respectively.

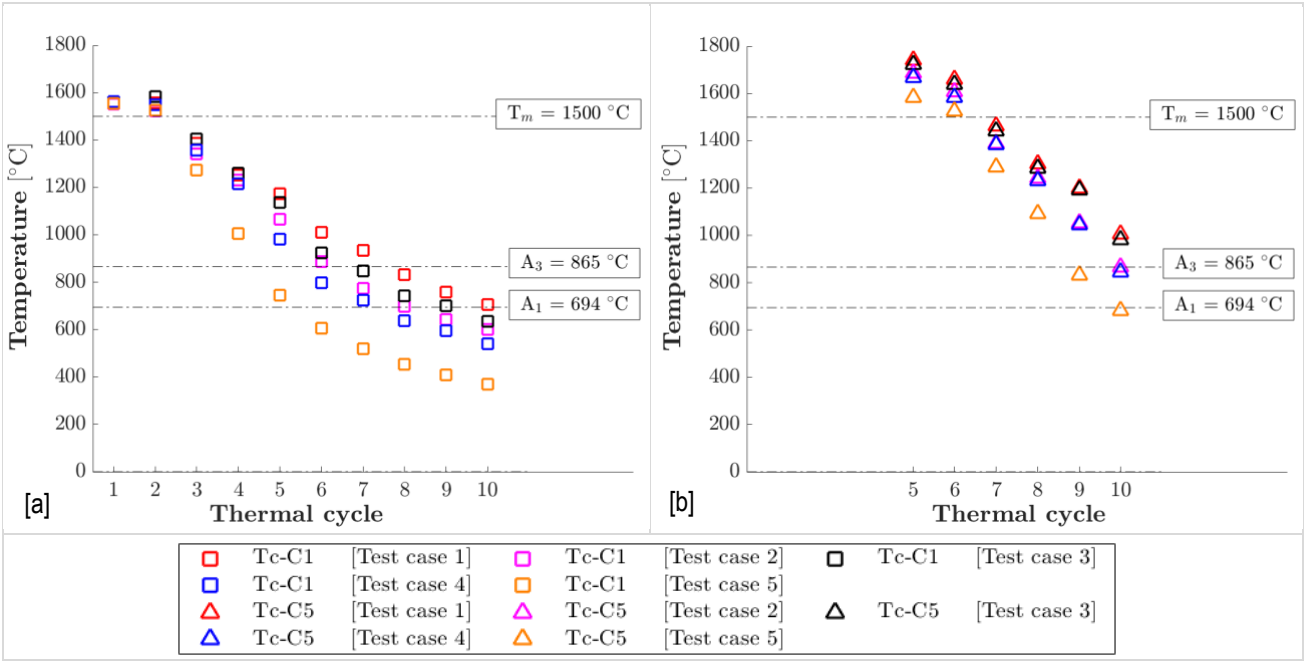

Figure 36: Thermal cycle peak temperatures. [a] Calculated at temperature measurement point Tc-C1: middle point layer 1; [b] Calculated at temperature measurement point Tc-C5: middle point layer 5.

It is observed that for the test cases 1 to 5, the thermal cycle peak temperatures of the first two thermal cycles exceed the melting point. As shown in Figure 36, this applies to both the thermal cycle peak temperatures that are calculated at the temperature measurement points Tc-C1 and Tc-C5 in the F.E. model. The first thermal cycle peak temperature exceeding the melting temperature corresponds to the formation of the weld pool. While, the second thermal cycle peak temperature that exceeds the melting temperature indicates the remelting of previous the layer due to the deposition of the succeeding layer, ensuring the metallurgy bonding of the deposited material [61].

As shown in Figure 36, it is observed that for all test cases the thermal cycle peak temperatures that are calculated at the temperature measurement points Tc-C1 and Tc-C5 decrease as the deposition process proceeds due to the increased distance between the welding heat source and the temperature measurement points. The extent to which the peak temperatures are reduced is directly related to the applied cooling method, as defined for the test cases 1 to 5. Accordingly, the highest thermal cycle peak temperatures are observed for test case 1 followed by the test cases 3, 2, 4 and 5 respectively. This order is consistent for all successive thermal cycles and applies to both the thermal cycle peak temperatures that are calculated at the temperature measurement points Tc-C1 and Tc-C5 in the F.E. model.

When comparing the thermal cycle peak temperatures that are calculated at temperature measurement points Tc-C1 and Tc-C5, as shown in Figure 36.a. and Figure 36.b. respectively. It is observed that the thermal cycle peak temperatures that are calculated at the temperature measurement point Tc-C5 match the corresponding peak temperature values that are calculated at the temperature measurement point Tc-C1. For the test cases 1, 3 and 4, the thermal cycle peak temperatures that are calculated at the temperature measurement point Tc-C5 are increased by 3% compared to the corresponding peak temperature values that are calculated at the temperature measurement point Tc-C1. While, for test case 2 the difference between the thermal cycle peak temperatures that are calculated at the temperature measurement points Tc-C1 and Tc-C5 is found to be less then 1 %. The largest increase is observed for the test case 5, for which the thermal cycle peak temperatures that are calculated at the

temperature measurement point Tc-C5 are increased by 6 % compared to the corresponding temperature values that are calculated at the temperature measurement point Tc-C1. Further, with regard to the temperature values that are calculated at the temperature measurement point Tc-C5, it is found that the thermal cycle peak temperatures that are observed for both the test case 1 and 3, and the test cases 2 and 4 are of the same order.

4.2.4 Thermal cycle through temperatures

The thermal cycle through temperatures that are calculated at the measurement points Tc-C1 and Tc-C5 in the F.E. model during the deposition process of the simulated ten-layer weld deposit, are shown in Figure 37.a and Figure 37.b respectively.

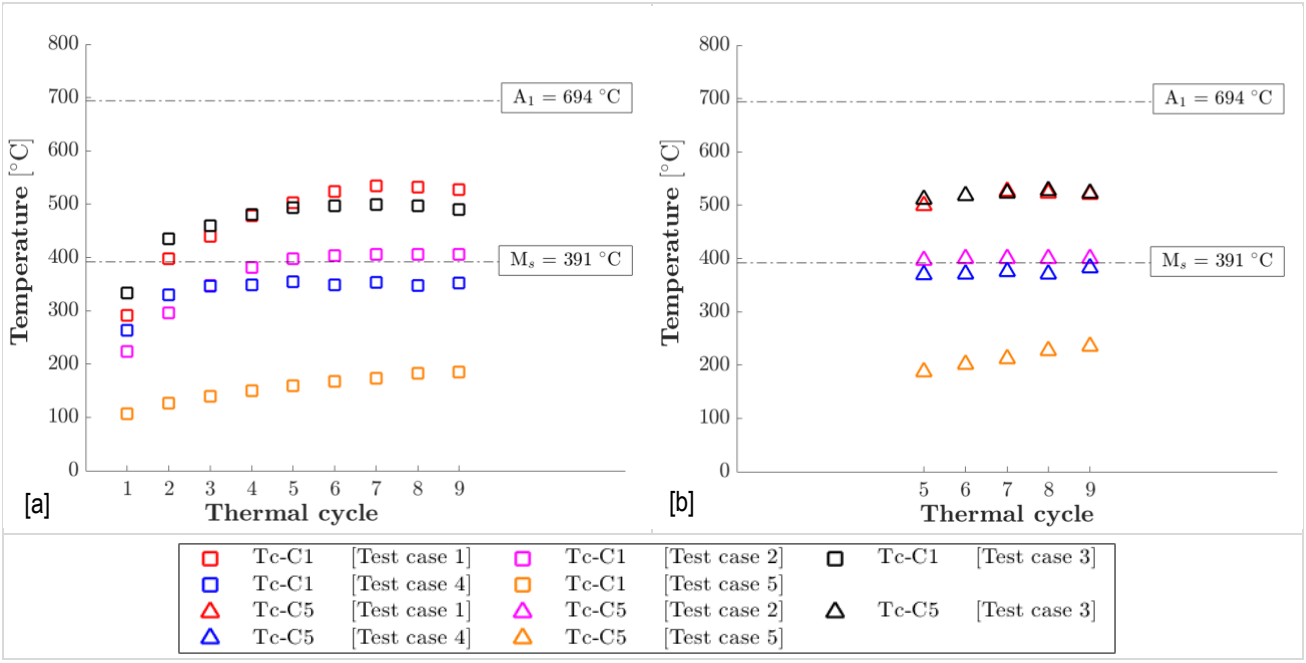

Figure 37: Thermal cycle through temperatures. [a] Calculated at temperature measurement point Tc-C1: middle point layer 1; [b] Calculated at temperature measurement point Tc-C5: middle point layer 5.

It is observed that from the sixth thermal cycle onward, the thermal cycle through temperatures that are calculated for the test cases 1 to 5 at the temperature measurement point Tc-C1 in the F.E. model reach equilibrium temperature values, equal to 529.3 °C, 404.9 °C, 495.7 °C, 350.3 °C and 177.3 °C respectively.

With regard to the thermal cycle through temperatures that are calculated at the measurement point Tc-C5 in the F.E. model. It is observed that for the test cases 1 to 4 equilibrium temperature values are found for the successive thermal cycles, being equal to 521.9 °C, 399.8 °C, 522.5 °C and 375.0 °C respectively. For test case 5, the thermal cycle through temperatures that are calculated at the measurement point Tc-C5 are found to continuously increase for the successive thermal cycles, equal to 186.9 °C and 234.8 °C at the end of the cooling stages of the fifth and ninth thermal cycle respectively.

When comparing the thermal cycle through temperatures that are calculated at temperature measurement points Tc-C1 and Tc-C5. It is observed that the thermal cycle through temperatures that are calculated at the temperature measurement point Tc-C5 match the corresponding peak temperature values that are calculated at the temperature measurement points Tc-C1. For both the test cases 1 and 2, the difference with regard to the thermal cycle though temperatures that are calculated at the temperature measurement points Tc-C1 and Tc-C5 is found to be less then 1 %. While for the test cases 3 and 4, the thermal cycle through temperatures that are calculated at the temperature measurement point Tc-C5 are increased by 5 % compared to the corresponding through temperature values calculated at the temperature measurement point Tc-C1. The largest increase is observed for

test case 5, for which the thermal cycle though temperatures that are calculated at the temperature measurement point Tc-C5 are increased by 22.1% compared to the corresponding temperature values that are calculated at the temperature measurement point Tc-C1.

Further, with regard to the temperature values that are calculated at the temperature measurement point Tc-C5. It is observed that the thermal cycle through temperatures that are found for the test cases 1 and 3 are equivalent. Similarly, the thermal cycle through temperatures that are observed for the test cases 2 and 4 are of the same order with regard to the through temperature values that are calculated at the temperature measurement points Tc-C1. Hereby, the thermal cycle through temperatures that are observed for test case 2 exceed the martensitic transformation temperature. While, the thermal cycle through temperatures that are observed for the test cases 4 and 5 attain values below the martensitic transformation temperature.

4.2.5 Cooling rate

With regard to the cooling rates that are calculated at the temperature measurement point Tc-C1 in the F.E.-model. The first and fifth thermal cycle correspond to the deposition of the first and fifth layer of the simulated ten-layer weld deposit respectively. While the first and fifth thermal cycle that are calculated at the temperature measurement point Tc-C5 are associated with the deposition of the fifth and ninth layer of the simulated ten-layer weld deposit respectively. According to Equation 8, the duration of the cooling stage is defined by the summation of the deposition time of a single layer and the interlayer waiting time. For the test cases 1, 4 and 5, the duration of the cooling stage is equal to 60 s. While for the test cases 2 and 3, the duration of the cooling stage is equal to 100 s and 40 s respectively.

For the test cases 1 to 5, the cooling rates are evaluated for the time interval covering 0-40 s of the corresponding cooling stages that are calculated at the temperature measurement points Tc-C1 and Tc-C5. The cooling rates that are recorded during the cooling stages of the first and fifth thermal cycle by the temperature measurement points Tc-C1 and Tc-C1 are shown in Figure 38 and Figure 39 respectively.

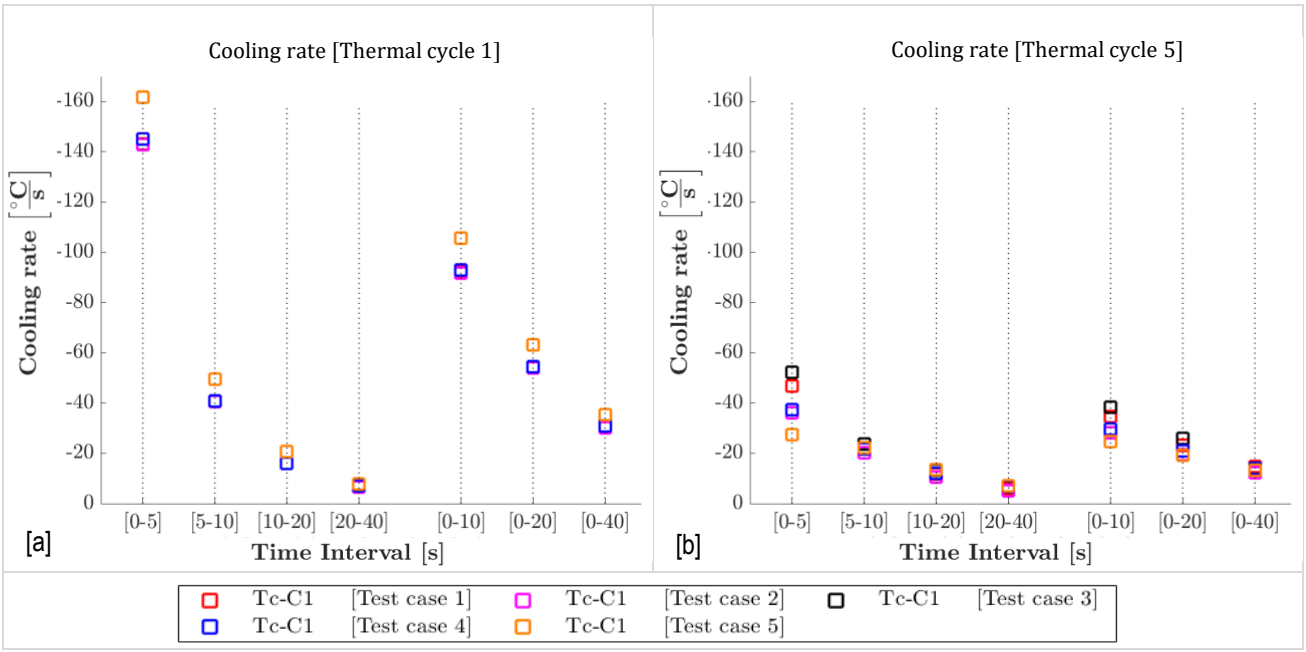

Figure 38: Cooling rates calculated at the temperature measurement point Tc-C1. [a] Thermal cycle 1; [b] Thermal cycle 5.

With regard to the cooling rates that are calculated at the temperature measurement point Tc-C1 during the cooling stage of the first thermal cycle. It is observed that for all considered time intervals the cooling rates associated with test case 5 are significantly higher compared to the cooling rates that are found for the test cases 1 to 4.

The highest cooling rates are observed during the initial time interval of the cooling stages and decrease for later time intervals of the corresponding cooling stages. According to Figure 38, it is observed that during the time interval covering 0-5 s of the cooling stage of the first thermal cycle that is calculated at the temperature measurement point Tc-C1, the average cooling rates are equal to -161.7 $^{\circ C}/_{s}$ for test case 5 and -144.0 $^{\circ C}/_{s}$ for the test cases 1 to 4 respectively. Indicating that during the initial time interval of the cooling stage of the first thermal cycle that is calculated at the temperature measurement point Tc-C1, the average cooling rate that is calculated for test case 5 is 12.3 % higher compared to the cooling rates that are found for the test cases 1 to 4. For the later time intervals, the deficiency between the cooling rates that are found for test case 5 and the test cases 1 to 4 is reduced. For the time interval covering 20-40 s of the cooling stage, the cooling rates corresponding to the test cases 1 to 5 are of the same order, within a margin of 1 %.

With regard to the cooling rates that are calculated at the temperature measurement point Tc-C1 during the cooling stage of the fifth thermal cycle. It is observed that during the initial time interval of the cooling stage, the highest cooling rates are observed for the test cases 1 and 3. While the lowest cooling rate is found for test case 5, in contrast to the cooling rates that are found for the first thermal cycle that is calculated at the temperature measurement point Tc-C1. As shown in Figure 39.b, the cooling rates that are found during the time interval covering 0-5 s of the cooling stage of the fifth thermal cycle that is calculated at the temperature measurement point Tc-C1, are equal to -46.8 $^{\circ C}/_{s}$ and -27.4 $^{\circ C}/_{s}$ for the test cases 1 and 5 respectively. Indicating that during the corresponding time interval, the cooling rate corresponding to test case 5 is 41.4 % lower compared to the cooling rate that is found for test case 1. Further, the cooling rates that are calculated during the initial time interval of the cooling stage of the fifth thermal cycle are reduced by a factor 3 compared to the values associated with the first thermal cycle. As shown in Figure 39, this observation also applies to the cooling rates that are calculated at the temperature measurement point Tc-C5.

With regard to the values of the average cooling rates that are calculated for the test cases 1 to 5. It is observed that for the temperature measurement point Tc-C1, the average cooling rate during the cooling stage of the first thermal cycle is equal to -30.5 $^{\circ C}/_{s}$ for the test cases 1 to 4, and -35.5 $^{\circ C}/_{s}$ for test case 5 respectively. While during the cooling stage of the fifth thermal cycle, the average cooling rate that is observed for the test cases 1 to 5 is of the same order, equal to -14.5 $^{\circ C}/_{s}$. Similarly, with regard to the temperature measurement point Tc-C5, the average cooling rate during the cooling stage of the fifth thermal cycle is equal to -29.9 $^{\circ C}/_{s}$ for the test cases 1 to 5. While during the cooling stage of the ninth thermal cycle, the corresponding value of the average cooling rate that is observed for the test cases 1 to 5 is equal to -14.8 $^{\circ C}/_{s}$. Indicating that for the test cases 1 to 5, the average cooling rates corresponding to the cooling stage of the fifth thermal cycle are reduced by a factor 2 compared to the values that are calculated during the cooling stage of the first thermal cycle. According to Figure 38 and Figure 39, this applies to both the cooling rates that are calculated at the temperature measurement point Tc-C1 and Tc-C5.

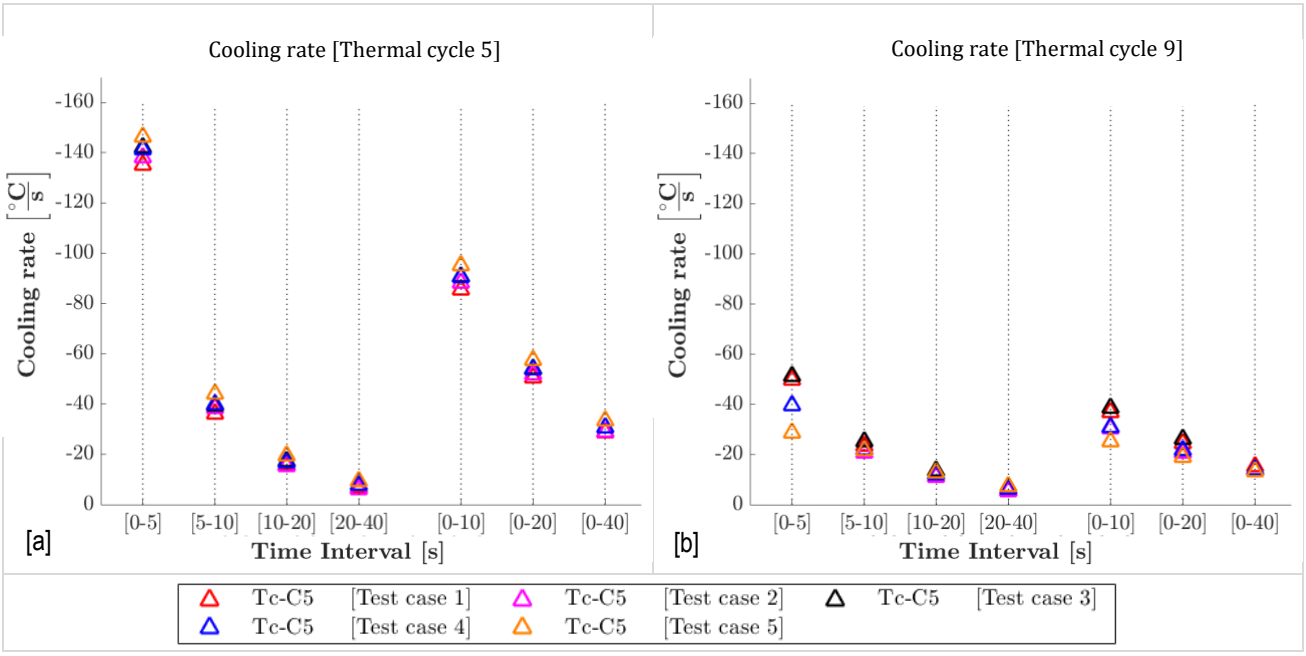

Figure 39: Cooling rates calculated at the temperature measurement point Tc-C5. [a] Thermal cycle 5; [b] Thermal cycle 9.

4.2.6 Temperature gradient

The temperature gradients in the x-, y- and z-direction are evaluated after the passage of the welding heat source during the deposition of the first and tenth layer of the simulated ten-layer weld deposit in the F.E. model, corresponding to the sixth and final layer of the experimental fifteen-layer weld deposit respectively. The values of the temperature gradients in the x-, y- and z-direction that are calculated for the test cases 1 and 5 during the deposition of the first and tenth layer of the simulated ten-layer weld deposit in the F.E. model, are provided in Appendix D.1 to Appendix D.4.

According to Figure 40, it is observed that during the deposition of the first layer of the simulated multilayer weld deposit, the temperature gradient in the z-direction is reduced by the application of active component cooling compared to the application of natural component cooling. While, the temperature gradient in the y-direction that is observed during the deposition of the first layer is increased by the application of active component cooling compared to the application of natural component cooling. According to Figure 40, the values of the maximum temperature gradient in the z-direction corresponding to test case 5 during the deposition of the first layer are on average 5.8 % lower, compared to the values that are found for test case 1. While, the corresponding values of the maximum temperature gradient in the y-direction that are found for test case 5 during the deposition of the first layer are increased by a factor 3, compared to the values corresponding to test case 1.

With regard to the maximum temperature gradients in the x-, y- and z-direction that are observed during the deposition of the tenth layer of the simulated multilayer weld deposit. It is observed that for the test cases 2 to 5, the values of the maximum temperature gradient in the z-direction are increased compared to the values that are found for test case 1. According to Table 14, the values of the maximum temperature gradient in the z-direction corresponding to test case 2 are increased compared to the values that are found for test case 1, ranging from 14.2 % to 17.4 % at 3s and 10s after the passage of the welding heat source respectively. While, the corresponding values that are found for test case 3 are increased by 8.1 % and 42.9 % respectively. For test case 4, the corresponding values are increased by 18.5 % and 50.5 % respectively. For test case 5, the values of the maximum temperature gradient in the z-direction are increased ranging from 34.2 % and 120.9 % at 3s and 10s after the passage of the welding heat source respectively, compared to the values that are found for test case 1.

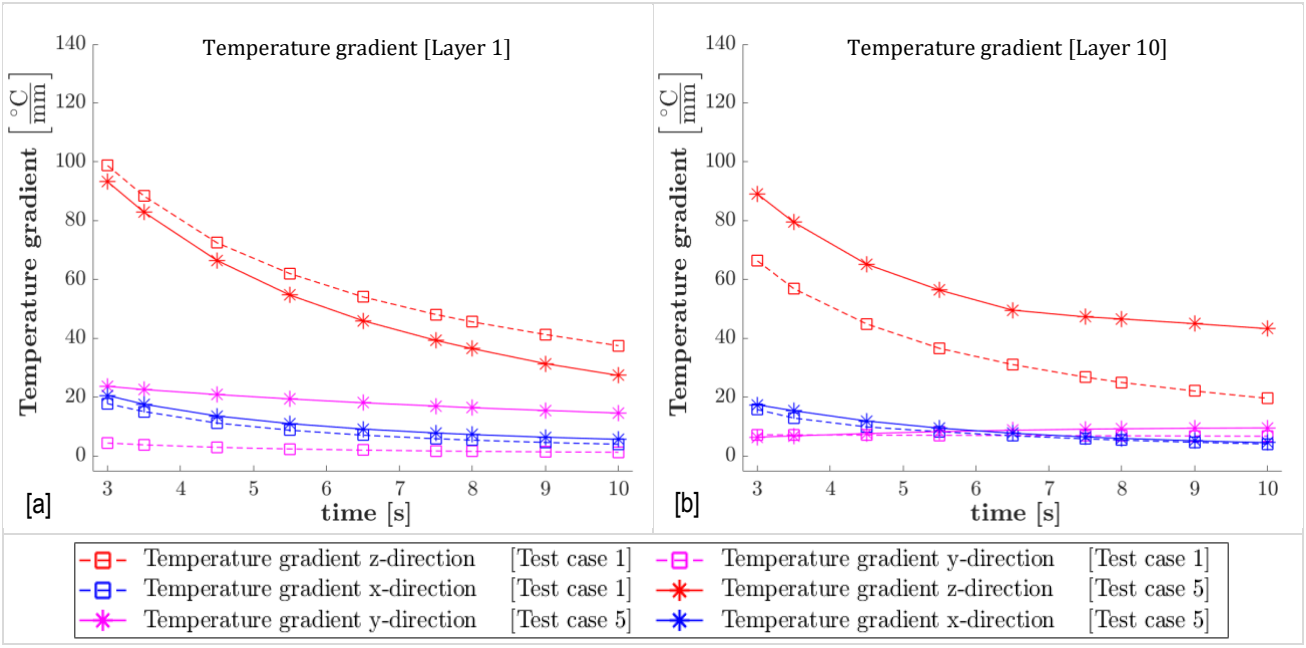

Figure 40: The maximum temperature gradients in the x-, y-, and z-direction calculated for the test cases 1 and 5. [a] During the deposition of the first layer; [b] During the deposition of the tenth layer.

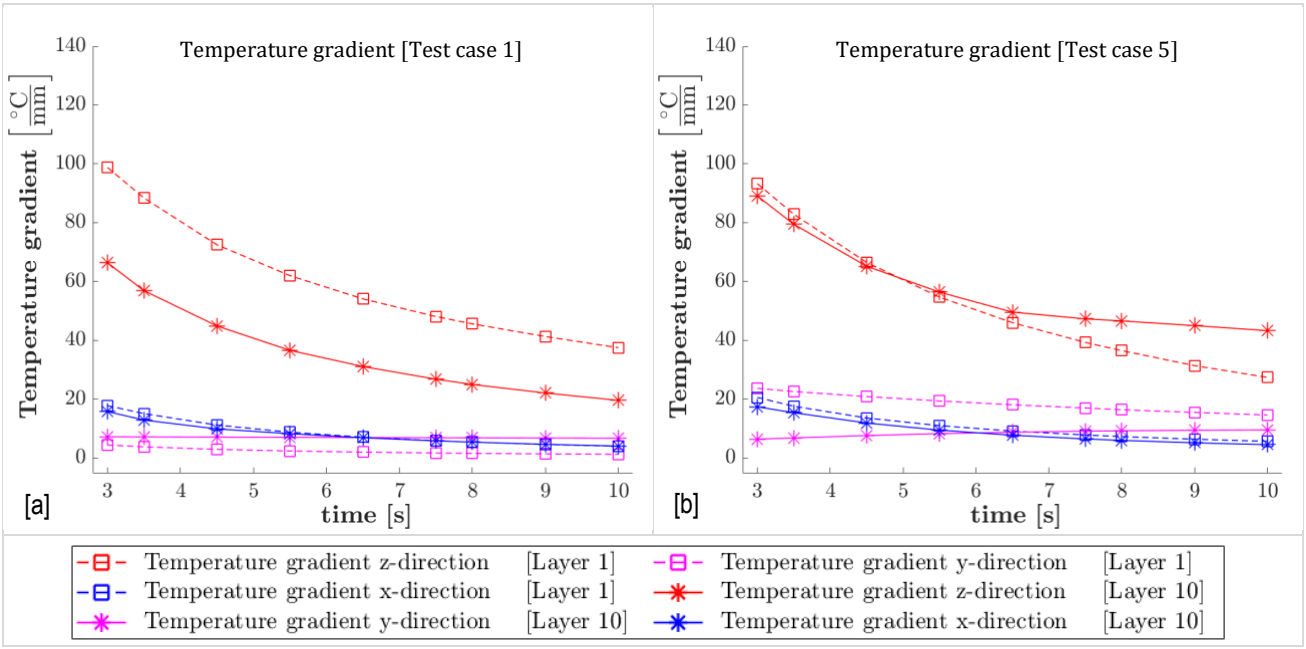

Figure 41: The maximum temperature gradients in the x-, y-, and z-direction calculated during the deposition of the first and tenth layer. [a] Test case 1; [b] Test case 5.

Table 14: The maximum temperature gradients in the x-, y-, and z-direction calculated during the deposition of the tenth layer for test cases 1 to 5.

	z-direction		y-direction		x-direction	
	3 s	**10 s**	**3 s**	**10 s**	**3 s**	**10 s**
Test case 1	66.40	19.60	7.23	6.73	15.80	4.07
Test case 2	75.80	23.00	6.40	2.34	16.20	4.20
Test case 3	71.80	28.00	7.05	6.97	16.40	4.33
Test case 4	78.70	29.50	6.43	5.34	16.60	4.29
Test case 5	89.10	43.30	6.41	9.56	17.40	4.53

Concerning the values of the maximum temperature gradient in the y-direction during the deposition of the tenth layer of the simulated multilayer weld deposit. It is observed that the values corresponding to the test cases 1 and 3 are of the same order. While for the test cases 2 and 4, the values of the maximum temperature gradient in the y-direction are lower compared to the values that are found for test case 1. For test case 5, it is observed that during the initial time interval of the cooling stage, the maximum temperature gradient in the y-direction is decreased. While for later time intervals of the cooling stage, the maximum temperature gradient in the y-direction is increased compared to the values that are found for the reference test case 1. According to Table 14, the values of the maximum temperature gradient in the y-direction corresponding to test case 2 are lower compared to the values that are found for test case 1, ranging from 11.5 % and 65.2 % at 3s and 10s after the passage of the welding heat source respectively. For test case 3, the maximum temperature gradient in the y-direction is decreased by 2.5 % at 3s after the passage of the welding heat source. While at 10s after the passage of the welding heat source, the maximum temperature gradient in the y-direction is increased by 3.6 %, compared to the values that are found for test case 1. The corresponding values that are found for test case 4 are reduced by 11.0 % and 20.7 % respectively. Accordingly for test case 5, the maximum temperature gradient in the y-direction is decreased by 11.3 % at 3s after the passage of the welding heat source. While at 10s after the passage of the welding heat source, the maximum temperature gradient in the y-direction is increased by 42.1 % compared to the values that are found for test case 1.

With regard to the values of the maximum temperature gradient in the x-direction during the deposition of the tenth layer of the simulated ten-layer weld deposit. It is observed the values that are found for the test cases 1 to 4 are of the same order. While, the values of the maximum temperature gradient in the x-direction that are found for test case 5 are increased compared to the values that are found for test case 1. According to Table 14, the values of the maximum temperature gradient in the z-direction corresponding to test cases 1 to 4 are increased on average by $5.0\ \%$, compared to the values that are found for test case 1. For test case 5, the values of the maximum temperature gradient in the x-direction are increased compared to the values that are found for test case 1, ranging from $10.1\ \%$ to $11.3\ \%$ at 3s and 10s after the passage of the welding heat source respectively.

As a general trend it is observed that for all test cases, the values of the temperature gradient in the z-direction are significant higher compared to the corresponding values in the y- and z-direction during the deposition of the multilayer weld deposit. Indicating that the dominant mode of heat dissipation is accommodated by conduction throughout the component in the building direction. The highest values of the temperature gradient in the z-direction are observed during the initial time interval of the cooling stages and attain lower values during later time intervals of the corresponding cooling stages. Further, it is found that during the initial time interval of the cooling stages the highest values of the temperature gradient in the z-direction are observed in the material domain closest to the welding heat source. While, during later time intervals of the corresponding cooling stages the highest values of the temperature gradient in the z-direction are observed in the material domains that are further removed from the welding heat source.

In the case of natural component cooling, the maximum temperature gradient in the z-direction is reduced during the deposition of the multilayer weld deposit. While, the maximum temperature gradient in the y-direction is increased as the deposition process proceeds. Indicating that in the case of natural component cooling, the heat dissipation accommodated by conduction throughout the component in the building direction is deteriorated during the deposition process of the multilayer weld deposit resulting from the heat accumulation that is observed in the case of natural component cooling. According to Figure 41.a, the values of the maximum temperature gradient in the z-direction corresponding to test case 1 during the deposition of the tenth layer are reduced by $45{,}9\ \%$ compared to the values that are observed during the deposition of the first layer of the simulated ten-layer weld deposit. While, the values of the maximum temperature gradient in the y-direction during the deposition of the tenth layer are increased by a factor 4 compared to the values that are found during the deposition of the first layer of the simulated ten-layer weld deposit. In the case of active component cooling, the maximum temperature gradient in the z-direction is maintained during the deposition process of the multilayer weld deposit. As shown in Figure 41.b, the values of the maximum temperature gradient in the z-direction corresponding to test case 5 during the deposition of the tenth layer exceed the values that are observed during the deposition of the first layer, from 4.5 s after the passage of the welding heat source. Indicating that in the case of active component cooling, the heat dissipation accommodated by conduction throughout the component in the building direction remains effective during the deposition process of the multilayer weld deposit.

4.2.7 Conclusions

The F.E. model that is presented in this research allows to describe the temperature field that is experienced by the deposited material in the wire and arc additive manufacturing process. In contrast to the traditional method of monitoring the substrate temperature, the F.E. model allows to describe the temperature field that is experienced by the deposited material constituting both the multilayer weld deposit and the component in terms of the thermal characteristics including the temperature distribution, the locally attained temperature values, the cooling rates, and the temperature gradients throughout the component.

4.2.7.1 Thermal characteristics

The F.E. method allows to describe the temperature field in terms of the thermal characteristics that are calculated for the test cases 1 to 5.

4.2.7.2 Temperature distribution

- The component mean temperatures corresponding to the test cases 1 to 5 increase during the deposition process of the multilayer weld deposit due to the heat accumulation in the component. Further, the same evolution of the component mean temperatures is observed for the test cases 1 and 2, and the test cases 3 and 4 respectively related to the cooling methods that are defined for the corresponding test cases.
- The component mean temperatures are reduced by the application of the different cooling methods, as defined for the test cases 1 to 5. According to the F.E. temperature values, the component mean temperatures corresponding to the test cases 2 to 5 are reduced by $21.6\ \%$, $23.6\ \%$, $41.2\ \%$ and $74.9\ \%$ respectively, compared to the value that is found for test case 1. Indicating that the highest component mean temperatures are observed for test case 1, followed by the values corresponding to the test cases 2, 3, 4 and 5 respectively.

4.2.7.3 Thermal cycle peak temperatures

- The thermal cycle peak temperatures of the subsequent thermal cycles corresponding to the test cases 1 to 5 decrease, as the distance between the welding heat source and the temperature measurement point increases during the deposition process proceeds.
- The reduction of the thermal cycle peak temperatures is directly related to the applied cooling method, as defined for the test cases 1 to 5. The highest thermal cycle peak temperatures are observed for test case 1 followed by the test cases 3, 2, 4 and 5 respectively. This order is consistent for the successive thermal cycles and applies to both the thermal cycle peak temperatures that are calculated at the temperature measurement points $\mathrm{Tc\text{-}C1}$ and $\mathrm{Tc\text{-}C5}$ in the F.E. model.

4.2.7.4 Thermal cycle through temperatures

- The thermal cycle through temperatures of the subsequent thermal cycles corresponding to the test cases 1 to 5 increase, due to the increased heat accumulation in the component during the deposition process of the multilayer weld deposit.
  - For both the test cases 1 and 3, the thermal cycle through temperatures that are calculated at the temperature measurement points $\mathrm{Tc\text{-}C1}$ and $\mathrm{Tc\text{-}C5}$ attain values exceeding the martensitic transformation temperature.
  - For test case 2, the thermal cycle through temperatures that are calculated at the temperature measurement points $\mathrm{Tc\text{-}C1}$ attain both values below the martensitic transformation temperature and values exceeding the martensitic transformation temperature. While, the thermal cycle through temperatures that are calculated at the temperature measurement points $\mathrm{Tc\text{-}C5}$ attain values exceeding the martensitic transformation temperature.

- For both the test cases 4 and 5, that are calculated at the temperature measurement points Tc-C1 and Tc-C5 attain values below the martensitic transformation temperature.

4.2.7.5 Cooling rate

- The highest cooling rates are observed during the initial time interval of the cooling stages and decrease for later time intervals of the corresponding cooling stages.
- The values of the cooling rate of the subsequent thermal cycles decrease during the deposition process of the multilayer weld deposit. The average cooling rates that are calculated at the temperature measurement point Tc-C1 during the cooling stage of the first thermal cycle are equal to -30.5 $^{\circ C}/_{s}$ for the test cases 1 to 4, and -35.5 $^{\circ C}/_{s}$ for test case 5 respectively. While during the cooling stage of the fifth thermal cycle, the average cooling rate is equal to -14.5 $^{\circ C}/_{s}$ for the test cases 1 to 5. Similarly, with regard to the average cooling rates that are calculated at the temperature measurement point Tc-C5.

4.2.7.6 Temperature gradient

- For all test cases, the values of the temperature gradient in the z-direction are significant higher compared to the corresponding values in the y- and z-direction. Indicating that the dominant mode of heat dissipation is accommodated by conduction throughout the component in the building direction.
  - The highest values of the temperature gradient in the z-direction are observed during the initial time interval of the cooling stages and attain lower values during later time intervals of the corresponding cooling stages.
  - The highest values of the temperature gradient in the z-direction are observed in the material domain closest to the welding heat source during the initial time interval of the cooling stages. While during later time intervals of the corresponding cooling stages the highest values of the temperature gradient in the z-direction are observed in the material domains that are further removed from the welding heat source.
- For test case 1, the temperature gradient in the z-direction is reduced during the deposition of the multilayer weld deposit. While, the temperature gradient in the y-direction is increased as the deposition process proceeds. Indicating that in the case of natural component cooling, the heat dissipation that is accommodated by conduction throughout the component in the building direction is deteriorated during the deposition process of the multilayer weld deposit due to the increased heat accumulation.
- For test case 5, the temperature gradient in the z-direction is maintained during the deposition process of the multilayer weld deposit. Indicating that in the case of active component cooling, the heat dissipation that is accommodated by conduction throughout the component in the building direction remains effective during the deposition process of the multilayer weld deposit.

4.3 Microstructure

The F.E. method that is presented in this research allows to describe the effect of the temperature field on the microstructure of the deposited material in the wire and arc additive manufacturing process. Accordingly, the F.E. model is used to describe the effect of the cooling methods on the microstructure of the deposited material considering the locally attained chemical composition in terms of the thermal characteristics including the temperature distribution, the locally attained temperature values, the cooling rates and the temperature gradients throughout the component. The effect of the temperature field on the resulting microstructural is evaluated in terms of the thermal characteristics that are calculated for the test cases 1 to 5.

The resulting microstructure of the deposited material is evaluated considering the locally attained chemical composition and the temperature field that is experienced by the material constituting the experimental fifteen-layer weld deposit. The microstructure that results from the application of the cooling methods is described in terms of the microstructural constituents and the microstructural morphology regarding the material constituting the experimental fifteen-layer weld deposit. The microstructural constituents and the microstructural morphology are identified using optical microscopy based on the average grain size and the distribution of alloying elements throughout the material. In addition, the average grain size and the distribution of the alloying elements throughout the material are evaluated in terms of the hardness values.

4.3.1 Microstructural constituents

The microstructural constituents are identified using optical microscopy, based on the average grain size and the distribution of alloying elements throughout the material. Concerning the pro-eutectoid ferrite microstructure, the carbon rich phases are located along the prior austenite grain boundaries. While in the case of lath bainite and acicular ferrite, the carbon is distributed throughout the ferrite matrix in the form of strip-like cementite particles along the bainitic ferrite lath boundaries or the lenticular ferrite plates in the case of acicular ferrite. Accordingly, the carbon depleted regions are distinguished as white and the carbon rich phases reveal as dark after etching.

With regard to the martensite microstructural constituents, the diffusionless martensite transformation is associated with a supersaturated solid solution of carbon in the ferrite matrix. Accordingly, the martensite microstructural constituents are revealed as dark etching elements that are distributed throughout the ferrite matrix. The tempering heat treatment of the lath bainite and martensite microstructural constituents results in the redistribution of microstructural constituents and the coarsening of the microstructure. As a result, the microstructure of both tempered lath bainite and tempered martensite consists of uniformly dispersed cementite particles embedded within a ferrite matrix. Both the tempered lath bainite and martensite microstructural constituents are revealed faded after etching due to the dispersed cementite particles.

With regard to the granular bainite constituents, individual phases of retained austenite and martensite are distinguished, referred to as M-A constituents. According to literature, the formation of M-A constituents result from the instantaneous cooling of the material in the austenite phase [39]. As described, during the granular bainite formation the residual austenite is stabilized by the carbon partitioning from the bainitic ferrite. Since the continuous cooling prohibits the diffusion-controlled transformation of the residual austenite into ferrite and cementite, the untransformed austenite is decomposed into M-A constituents containing both lath martensite and retained austenite [38].

4.3.1.1 Optical microscopy

The microstructure that results from the application of the cooling methods is described for the test cases 1 to 5 regarding the material constituting the experimental fifteen-layer weld deposit. The microstructural constituents that are observed for the test cases 1 to 5 are shown in Figure 42 to Figure 46.

4.3.1.1.1 Test case 1

A predominantly coarse-grained ferritic microstructure is observed regarding the material constituting the experimental fifteen-layer weld deposit corresponding to test case 1, as shown in Figure 42. With regard to the top segment, colonies of granular bainite are distinguished throughout the ferritic matrix revealing both allotriomorphic and polygonal ferrite constituents. While regarding the material constituting both the middle segment and the bottom segment, colonies of tempered lath bainite are observed along the prior austenite grain boundaries. Further, a reduced amount of pro-eutectoid ferrite and granular bainite is observed compared to the materiel constituting the top segment of the experimental fifteen-layer weld deposit.

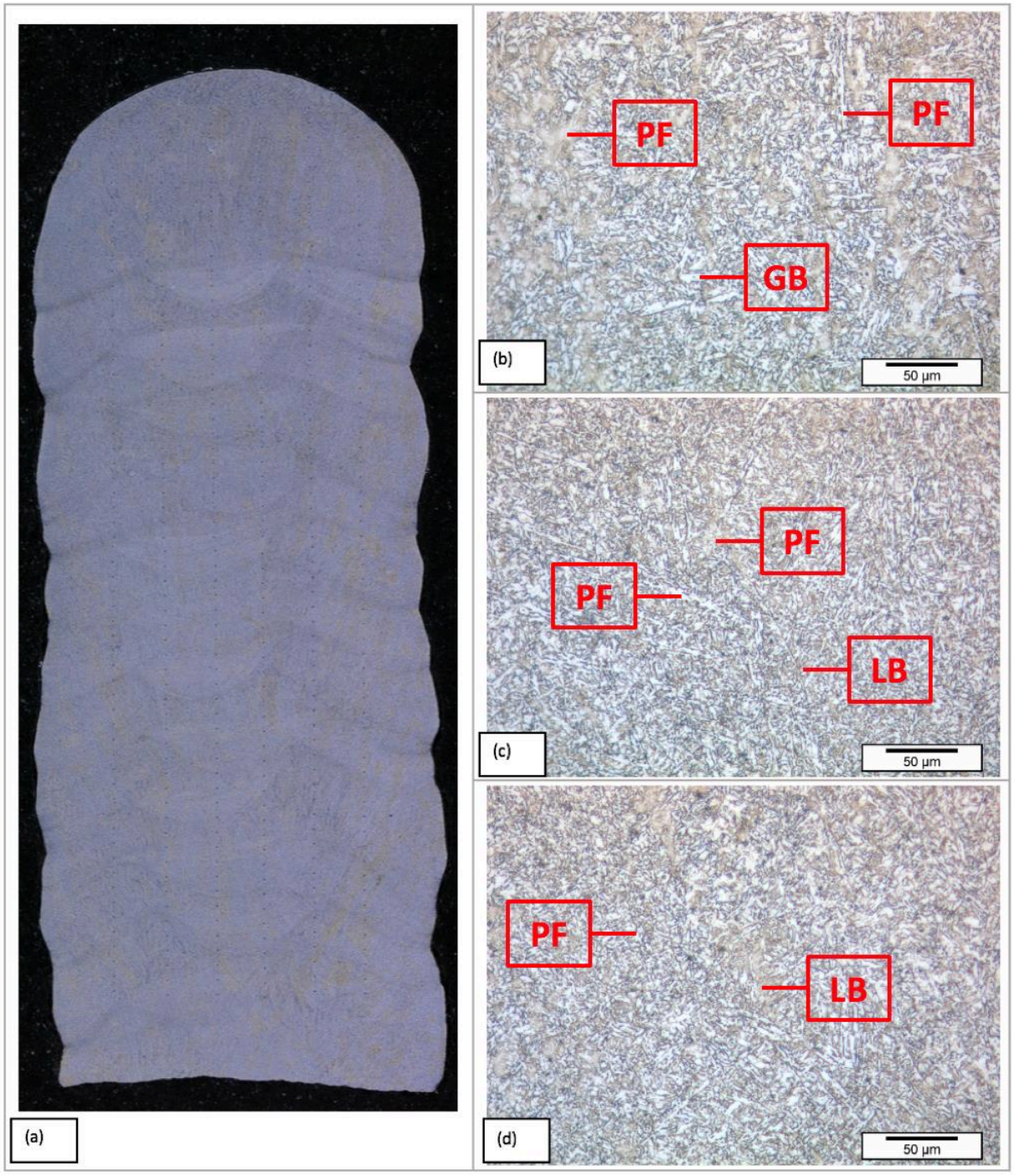

Figure 42: Microstructural morphology of the material constituting the multilayer weld deposit corresponding to test case 1. Indicating the microstructural constituents. [a] Multilayer weld deposit. [b] Top segment of the multilayer weld deposit. [c] Middle segment of the multilayer weld deposit. [d] Bottom segment of the multilayer weld deposit.

4.3.1.1.2 Test case 2

Two distinct microstructural morphologies are observed for test case 2, regarding the materiel constituting both the top segment the middle segment and the material constituting the bottom segment of the experimental fifteen-layer weld deposit. Regarding the top segment, a fine-grained ferritic microstructure interspersed with small colonies of granular bainite is observed, as shown in Figure 43.a. While regarding the material constituting the middle segment, a coarse-grained microstructure of granular bainite and martensite constituents is found, as shown in Figure 43.c. Concerning the materiel constituting the bottom segment shows large fractions of tempered martensite revealing iron carbides precipitated in the form of lath-like cementite particles embedded within the ferrite matrix, as shown in Figure 43.d.

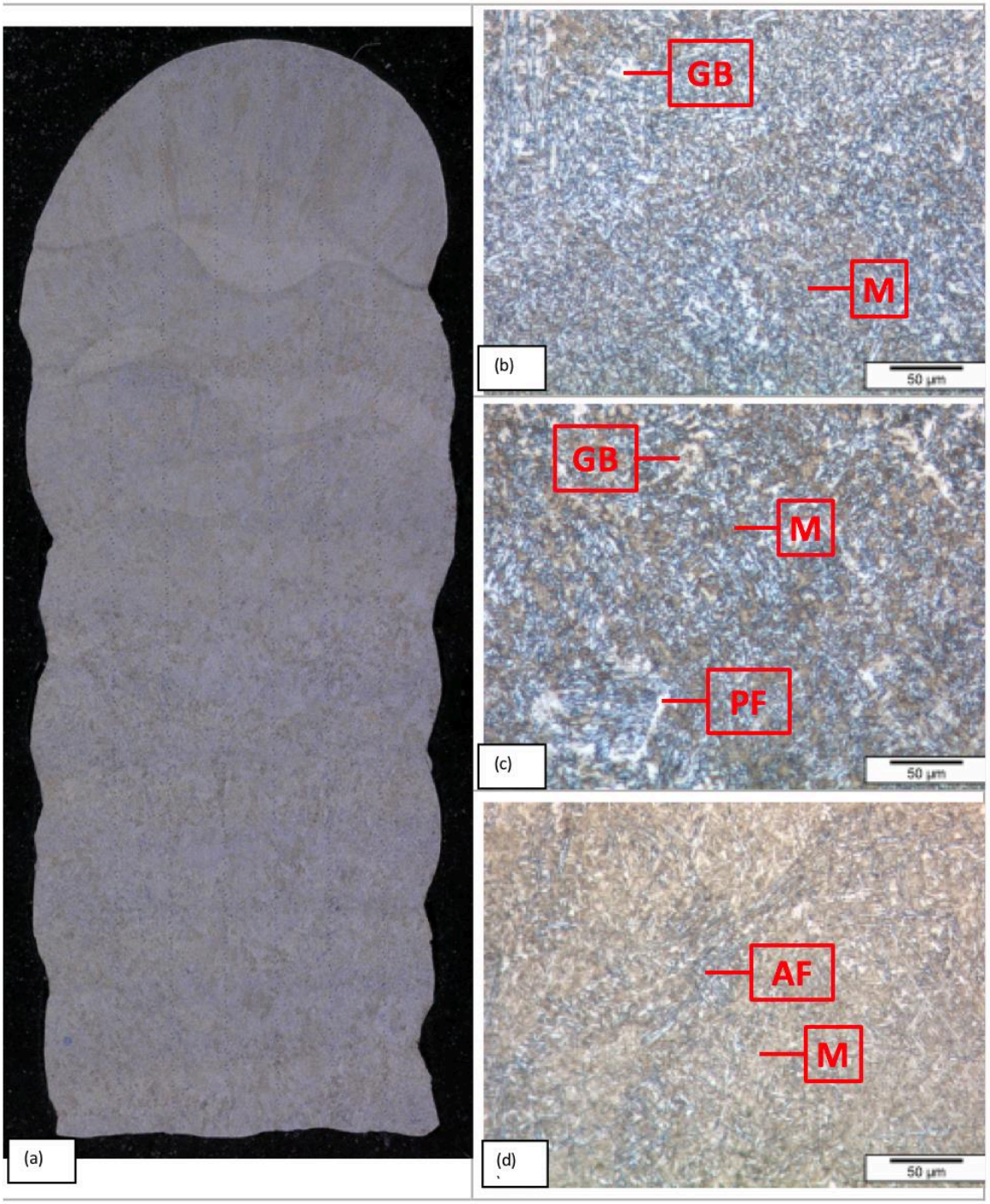

Figure 43: Microstructural morphology of the material constituting the multilayer weld deposit corresponding to test case 2. Indicating the microstructural constituents. [a] Multilayer weld deposit. [b] Top segment of the multilayer weld deposit. [c] Middle segment of the multilayer weld deposit. [d] Bottom segment of the multilayer weld deposit.

4.3.1.1.3 Test case 3

The microstructure of the material constituting the experimental fifteen-layer weld deposit corresponding to test case 3 is composed of bainite and acicular ferrite microstructural constituents. With regard to the top segment, the microstructure is mainly composed of lath bainite and acicular ferrite microstructural constituents and small colonies of granular bainite. As indicated in Figure 44, the lath bainite constituents are observed along the prior austenite grain boundaries. While the acicular ferrite constituents are distinguished throughout the prior austenite grain interiors. The microstructure of the material constituting the middle segment and bottom segment show an increased fraction of acicular ferrite constituents. Further, large colonies of granular bainite are distinguished regarding the material constituting the bottom segment of the experimental fifteen-layer weld deposit.

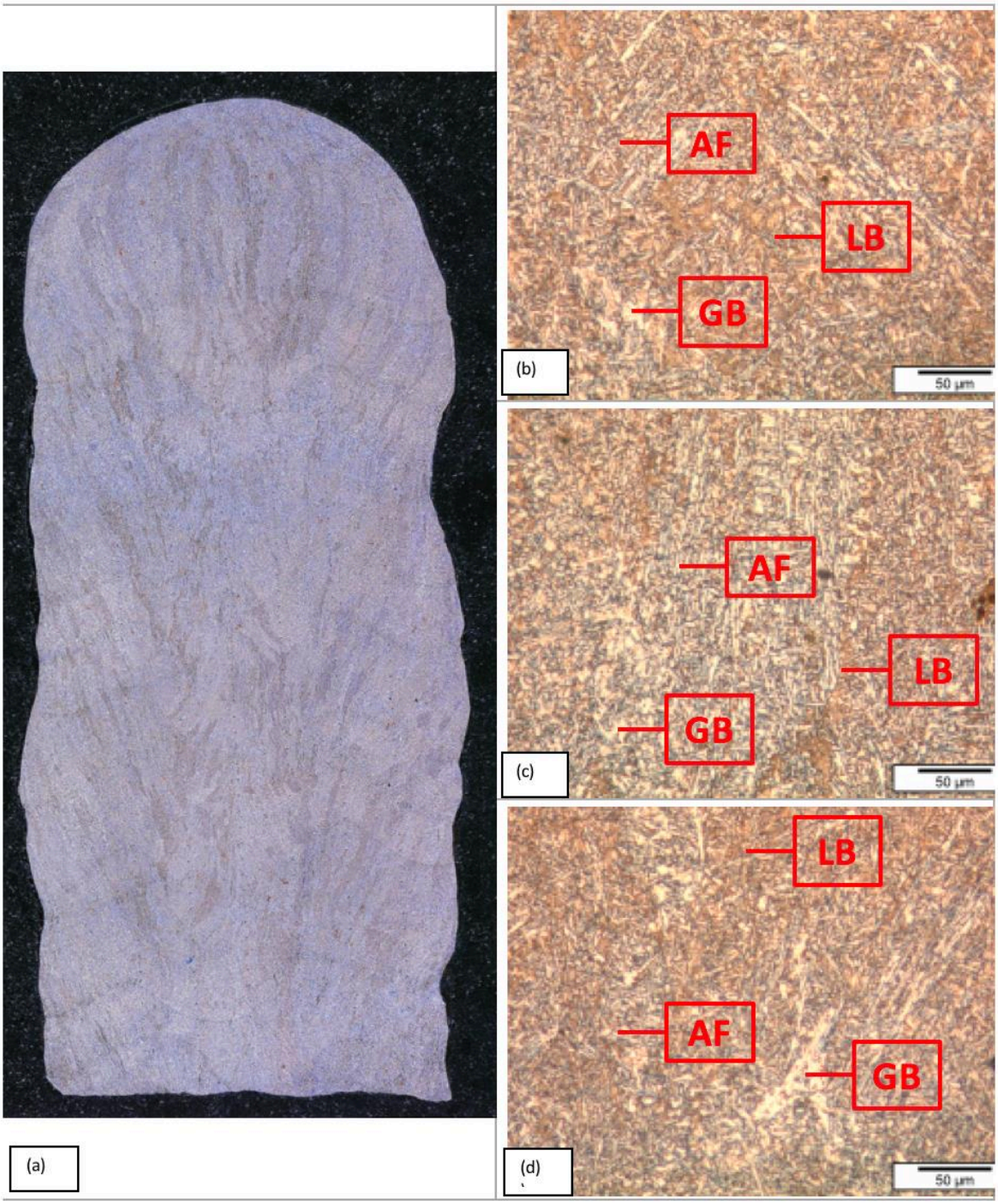

Figure 44: Microstructural morphology of the material constituting the multilayer weld deposit corresponding to test case 3. Indicating the microstructural constituents. [a] Multilayer weld deposit. [b] Top segment of the multilayer weld deposit. [c] Middle segment of the multilayer weld deposit. [d] Bottom segment of the multilayer weld deposit.

4.3.1.1.4 Test case 4

The microstructure of the material constituting the experimental fifteen-layer weld deposit corresponding to test case 4 consists of fine-grained acicular ferrite interspersed with both fine-grained martensite and granular bainite constituents. Regarding the material constituting both the top segment and the middle segment. It is observed that the fine grained granular bainite constituents are formed along specific orientations, in the direction of the maximum temperature gradient, as shown in Figure 45.b and Figure 45.c. The microstructure of the materiel constituting the bottom segment reveals an increased amount of tempered martensite compared to the materiel forming both the top segment and the middle segment of the experimental fifteen-layer weld deposit.

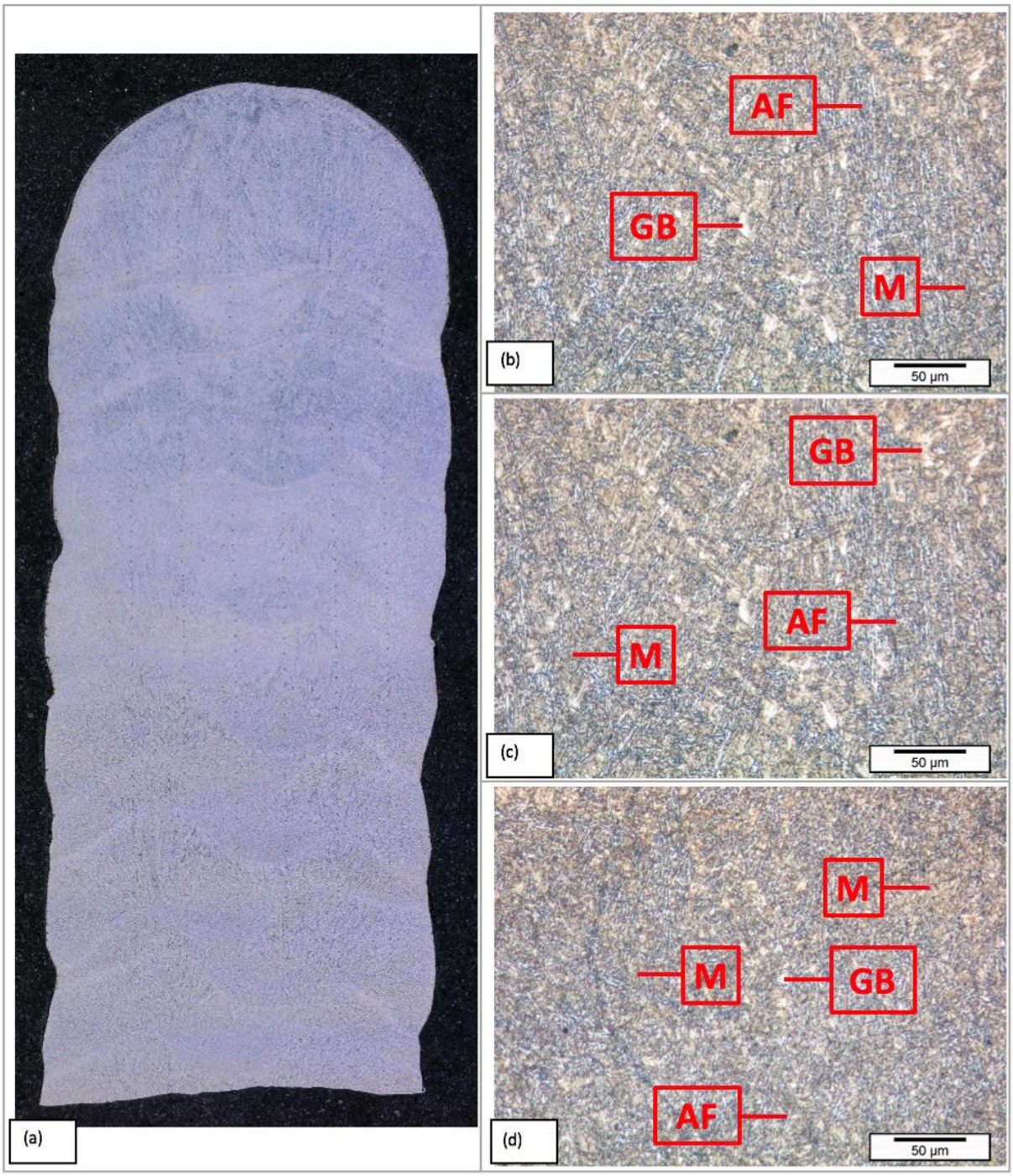

Figure 45: Microstructural morphology of the material constituting the multilayer weld deposit corresponding to test case 4. Indicating the microstructural constituents. [a] Multilayer weld deposit. [b] Top segment of the multilayer weld deposit. [c] Middle segment of the multilayer weld deposit. [d] Bottom segment of the multilayer weld deposit.

4.3.1.1.5 Test case 5

A predominantly martensitic microstructure is observed for test case 5, regarding the material constituting the experimental fifteen-layer weld deposit. Regarding the top segment, a predominantly fine-grained ferritic microstructure revealing martensite microstructural constituents is observed. While with regard to both the middle segment and the bottom segment, a layer band morphology is observed of alternating regions revealing a fine-grained microstructure and regions showing a coarse-grained microstructure, as shown in Figure 46. With regard to the fine-grained layer band regions, the microstructure consists of fine-grained tempered martensite embedded in a ferrite matrix, as shown in Figure 46.c. While in the coarse-grained layer band regions, the iron carbides are precipitated in the form of lath-like cementite particles embedded within a ferrite matrix, as shown in Figure 46.d. Further, the presence of granular bainite constituents is observed in the coarse-grained layer band regions.

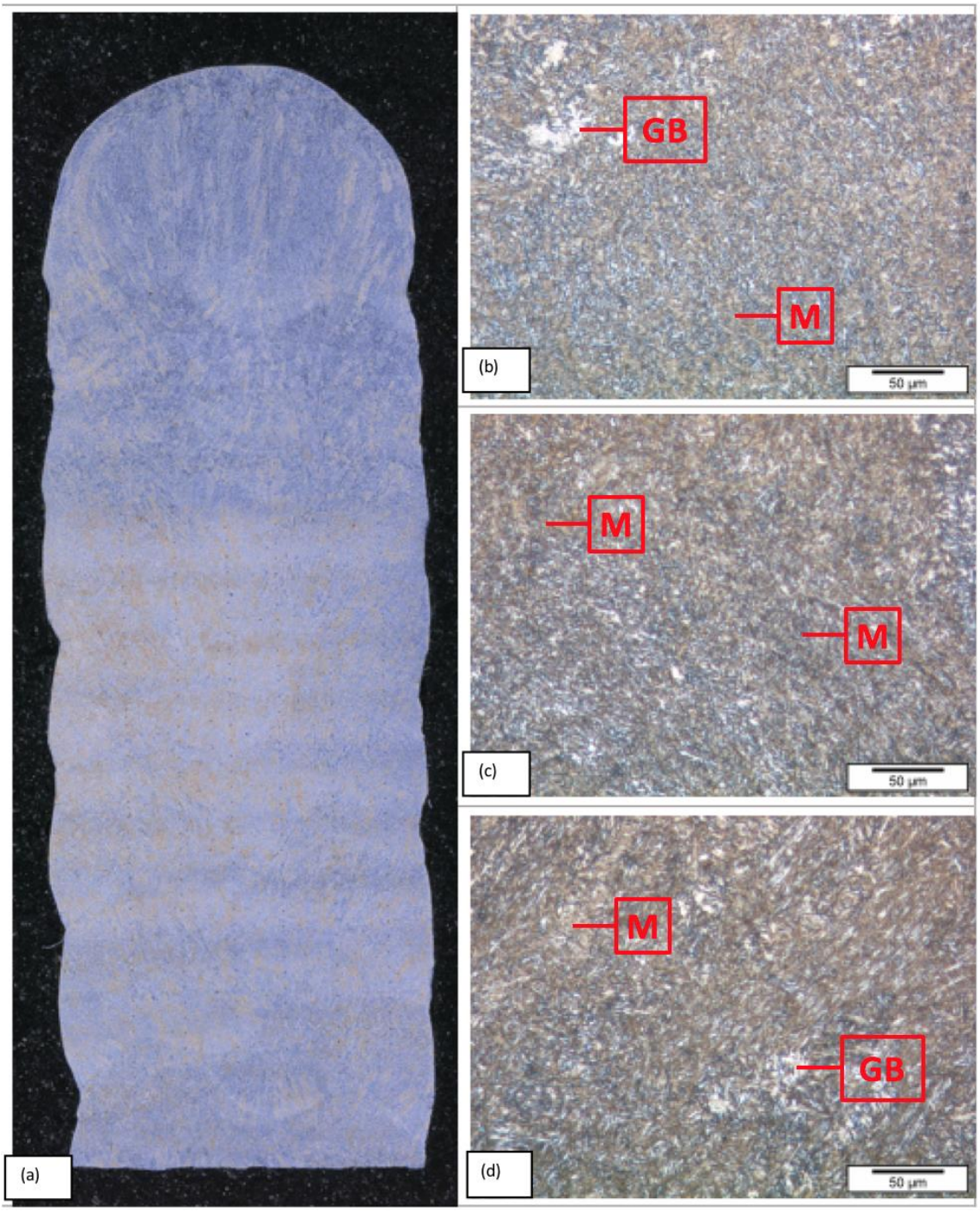

Figure 46: Microstructural morphology of the material constituting the multilayer weld deposit corresponding to test case 5. Indicating the microstructural constituents. [a] Multilayer weld deposit. [b] Top segment of the multilayer weld deposit. [c] Middle segment of the multilayer weld deposit. [d] Bottom segment of the multilayer weld deposit.

4.3.2 Microstructural morphology

The microstructure that results from the application of the cooling methods is described in terms of the microstructural morphology considering the average grain size and the distribution of alloying elements throughout the material constituting the experimental fifteen-layer weld deposit.

Both the average grain size and the distribution of alloying elements are influenced by locally attained chemical composition and temperature field that is experienced by the material constituting the experimental fifteen-layer weld deposit, associated with the formation of three distinct microstructural regions. With regard to the top segment both the average grain size and the distribution of alloying elements are primarily influenced by the solidification process [62], [63]. While regarding the middle segment and the bottom segment, both the average grain size and the distribution of alloying elements are influenced by the periodic thermal cycling of the temperature values related to the deposition process [60]. Further, a layer band morphology of alternating regions of fine-grained and coarse-grained microstructure is formed due to the movement of the welding heat source in the building direction [59].

In addition to the locally attained temperature field, the microstructural morphology affects the formation of the microstructural constituents. A small average grain size results in a refined microstructure as well as the formation of bainite constituents due to the large grain boundary area. While, the formation of acicular ferrite constituents is promoted by an increased average grain size and the homogeneous distribution of alloying elements throughout the material.

4.3.2.1 Average grain size

The average grain size affects both the microstructural morphology and the different microstructural constituents that are formed during the austenite decomposition [64]. A reduced prior austenite grain size promotes a refined microstructure as well as the formation of bainite constituents due to the increased prior austenite grain boundary area. While, the formation of acicular ferrite constituents is promoted by an increased prior austenite grain size and the homogeneous distribution of non-metallic inclusions throughout the prior austenite matrix [44]. Further, the prior austenite grain size affects the transformation temperatures. A reduction of the prior austenite grain size is associated with reduced transformation temperatures [38]. While an increased prior austenite grain size promotes the auto-tempering of both the bainite and martensite constituents, resulting in the formation of more prominent carbide precipitates.

As a general trend, it is observed that the average grain size is reduced as a result of the periodic thermal cycling of the temperature values. Expressed by a reduced average grain size of the microstructure regarding the material constituting the middle segment and bottom segment of the experimental fifteen-layer weld deposit. The most pronounced reduction of the average grain size resulting from the periodic thermal cycling is observed for the test cases 2 and 4 regarding the material constituting the middle segment and bottom segment of the experimental fifteen-layer weld deposit. While for both the test cases 1 and 3, the effect is less evident, and an almost uniform grain size is observed regarding the microstructure of the material constituting the experimental fifteen-layer weld deposit. A clear exception to the general trend is observed for test case 5, for which the smallest average grain size is observed regarding the material constituting the top segment of the experimental fifteen-layer weld deposit. Also, with regard to test case 2, the microstructure of the material constituting the middle segment reveals a larger average grain size compared to the material constituting both the top segment and the bottom segment of the experimental fifteen-layer weld deposit.

A uniform coarse-grained microstructural morphology is observed for the test cases 1 and 3 regarding the material constituting the experimental fifteen-layer weld deposit. While for the test cases 2 and 5, two distinct microstructural morphologies are observed regarding the top segment and the bottom segment. For test case 4 a minimal difference is observed concerning the microstructural morphology of the material constituting the bottom

segment and the top segment of the experimental fifteen-layer weld deposit. The largest average grain sizes are observed for test cases 1 and 3 regarding the material constituting the experimental fifteen-layer weld deposit. While the smallest average grain sizes are observed are observed for the test cases 2, 4 and 5, regarding the bottom segment and the experimental fifteen-layer weld deposit corresponding to the test cases 2 and 4, and both the top segment and the fine-grained layer band regions corresponding to test case 5 respectively. As an approximation, the dimensions of the coarse-grained microstructural morphologies that are observed the test cases 1 and 3 are in the order of 20 μm and 5 μm respectively. While the dimensions of the fine-grained microstructural morphologies that are found for the test cases 2, 4 and 5 are in the order of 5 μm and 1 μm respectively.

4.3.2.1.1 Primary structure

The primary microstructure is formed as a result of the solidification process regarding the material that experiences no subcritical heat treatment. In this regard, the solidification conditions of the primary microstructure are directly related to the weld pool characteristics [39].

The primary microstructure is characterized by the epitaxial growth of columnar grains that are nucleated at the fusion boundary. The columnar grains result from the preferred crystallographic growth directions that develop under the influence of the maximum temperature gradient, related to the weld pool characteristics [39]. The primary microstructure is observed for the test cases 1 to 5, regarding the material constituting the two upper layers of the experimental fifteen-layer weld deposit. This observation is in accordance with the thermal cycle peak temperatures. According to Figure 33, the two upper layers of the multilayer weld deposit are subjected to temperature values exceeding the melting temperature. Also, the columnar grains are aligned in the building direction of the maximum temperature gradient.

In addition, the top segment of the multilayer weld deposit is defined by the region that is bounded by the bottom layer for which the last thermal cycle peak temperature exceeds the A_3-temperature, as indicated in Figure 33. With regard to the test cases 2 and 5, the material constituting the top segment is bounded by eight and six layers respectively. This observation is in agreement with the thermal cycle peak temperatures. According to Figure 33, it is observed that for the test cases 2 and 5 the thermal cycle peak temperatures exceeding the A_3-temperature correspond to the first eight and six thermal cycles respectively.

4.3.2.1.2 Layer band morphology

With regard to both the middle segment and the bottom segment of the experimental fifteen-layer weld deposit. A layer band morphology of alternating regions of fine-grained and coarse-grained microstructures is formed due to the movement of the welding heat source in the building direction.

The layer band morphology results from the locally attained temperature field. Since both the amount of grain growth and grain refinement are related to the thermal cycle peak temperatures. According to Figure 33, the two upper layers of the weld deposit are subjected to temperature values exceeding the melting temperature. While with regard to the underlying layer, the region closest to the welding heat source is subjected to temperature values in the temperature range between 1200 °C and the melting temperature, indicating that grain growth is facilitated. The region further removed from the welding heat source is subjected to temperature values in the temperature range between the A_3-temperature and 1200 °C, indicating that limited grain growth and grain refinement is facilitated.

The most pronounced layer band morphology is observed for test case 5. Whereby, the mutual distance between the layer band regions of the respective layers corresponds to a single layer thickness. This observation is in agreement with the thermal cycle peak temperatures that are observed for test case 5. According to Figure 33, the thermal cycle peak temperatures of the first two thermal cycles exceed the melting temperature. While the thermal cycle peak temperatures corresponding to the third and fourth thermal cycle attain values in the temperature range

between 1200 °C and the melting temperature and the A_3-temperature and 1200 °C respectively. Indicating that with regard to the third layer, the thermal cycle peak temperatures are sufficiently high to facilitate grain growth in the region closest to the welding heat source. While in the region further removed from the welding heat source grain refinement is induced. As a result, layer band morphology of alternating regions of fine-grained and coarse-grained microstructures is formed due to the movement of the welding heat source in the building direction.

4.3.2.2 Distribution of alloying elements

The distribution of alloying elements throughout the material is influenced by the locally attained temperature field. During the solidification process, the concentration of alloying elements is increased in front of the solidification interface due to the local temperature gradient that results from the constitutional supercooling during the solidification process [38]. Further, the distribution of alloying elements is affected by the locally attained temperature gradient that is associated with the deposition process [39]. Meanwhile, the homogeneous distribution of alloying elements throughout the material is promoted by a sufficiently high component mean temperature.

An increased concentration of alloying elements is observed at the fusion boundaries of the individual weld layers constituting the experimental fifteen-layer weld deposit corresponding to the test cases 1 to 5, resulting from the constitutional supercooling during the solidification process. Further, the segregation of alloying elements is observed in the building direction along the direction of the maximum temperature gradient. The most pronounced effect of the local redistribution of alloying elements is observed regarding the coarse-grained microstructure regions, corresponding to the middle segment and the coarse-grained layer band regions of the test cases 2 and 5 respectively. The redistribution of alloying elements results in the formation of carbon rich and carbon depleted regions. According to Figure 43 and Figure 46, the granular bainite constituents are located in the carbon depleted regions. While both the martensite and acicular ferrite constituents are observed in the carbon rich regions.

An important strengthening mechanism of the electrode material X90 is precipitation strengthening whereby the alloying elements form fine carbide and carbonitride precipitates [37]. Therefore, the distribution of the alloying elements affect the resulting microstructure of the material constituting the experimental fifteen-layer weld deposit. Further, the distribution of carbide precipitates throughout the material is influenced by the transformation mechanism. According to Figure 45, the diffusion-controlled transformation results in the localized presence of carbon along the prior austenite grain boundaries. While concerning the displacive transformation, there is no long-range partitioning of both substitutional and interstitial elements between the ferrite and the untransformed austenite. Consequently, the low solubility of carbon in ferrite promotes the diffusion of carbon toward the prior austenite grain boundaries. As observed for the pro-eutectoid ferrite microstructure. While in the case of lath bainite and acicular ferrite, the carbon precipitates are distributed throughout the ferrite matrix in the form of strip-like cementite particles along the bainitic ferrite lath boundaries or the lenticular ferrite plates in the case of acicular ferrite. The diffusionless martensite transformation results in the formation of a supersaturated solid solution of carbon in the ferrite matrix. Further, the microstructure of lath martensite consists predominantly of high densities of dislocations resulting from the diffusionless transformation from austenite. With regard to granular bainite, the carbon is partitioned from the bainitic ferrite to the residual austenite resulting in a microstructure containing both retained austenite and martensite.

4.3.3 Hardness values

The hardness values are related to the average grain size and the distribution of the alloying elements throughout the material. A coarse-grained microstructure and the localized presence of carbide precipitates is associated with low hardness values. While higher hardness values indicate a fine-grained microstructure and the presence of carbon precipitates throughout the ferrite matrix.

The hardness values are correlated to the strengthening mechanisms of the electrode material X90 including grain refinement, solid solution strengthening, precipitation strengthening and dislocation strengthening [37], . Since the formation of the microstructural constituents is influenced by the transformation mechanism, the distribution of the carbide precipitates is correlated to the microstructural constituents throughout the material. As described in Section 2.4.1, the hardness values are correlated to the various microstructural constituents as shown in Figure 23. Regarding the pro-eutectoid ferrite microstructure, the low solubility of carbon in ferrite in combination with the localized presence of carbon precipitates at the prior austenite grain boundaries corresponds to hardness values in the range between 300 HV0.5 and 340 HV0.5. While regarding both lath bainite and acicular ferrite microstructure, the presence of carbon precipitates throughout the ferrite matrix in the form of either cementite or retained austenite and martensite is indicated with hardness values in the range between 340 HV0.5 and 400 HV0.5. The granular bainite microstructure is associated with intermediate hardness values compared to pro-eutectoid ferrite and both lath bainite and acicular ferrite. The highest hardness values corresponding to the martensitic microstructure are in the order of 400 HV0.5.

4.3.3.1 Hardness measurement values

The hardness profile is characterized by the average hardness value and the standard deviation of the hardness values, as expressed in Equation 22.

$$\sigma = \sqrt{\frac{1}{N}\sum_{i=1}^{N}(x_i - \mu)^2} \quad \text{HV0.5} \qquad [22]$$

σ The standard deviation of the hardness values [HV0.5]

μ Average hardness value [HV0.5]

N Number of hardness measurement values

x_i Hardness measurement value [HV0.5]

The distribution of microstructural constituents throughout the material is correlated to the standard deviation of the hardness values [38], [39]. The values of the average hardness and the standard deviation of the hardness values corresponding to the test cases 1 to 5, are shown in Table 15. The values of the hardness measurement values and the standard deviation of the hardness values corresponding to the test cases 1 to 5, are provided in Appendix E.1.

Table 15: The average hardness values and the standard deviation of the hardness values corresponding to the test cases 1 to 5.

	Bottom/Middle segment		**Top segment**	
	μ [HV0.5]	σ [HV0.5]	μ [HV0.5]	σ [HV0.5]
Test case 1	297.2	7.4	Idem	
Test case 2	346.7	7.8	317.6	8.2
Test case 3	309.5	10.3	323.8	13.4
Test case 4	346.5	10.0	Idem	13.2
Test case 5	326.7	14.4	387.6	16.3

The hardness values are measured at the measurement points on the cross-sectional area of the experimental fifteen-layer weld deposit, positioned in six rows with a mutual distance of $1\ \mathrm{mm}$ in the y-direction and a mutual distance of $0.3\ \mathrm{mm}$ in the z-direction. A schematic representation of the hardness values that are measured for the test cases 1 to 5, is shown in Figure 47.

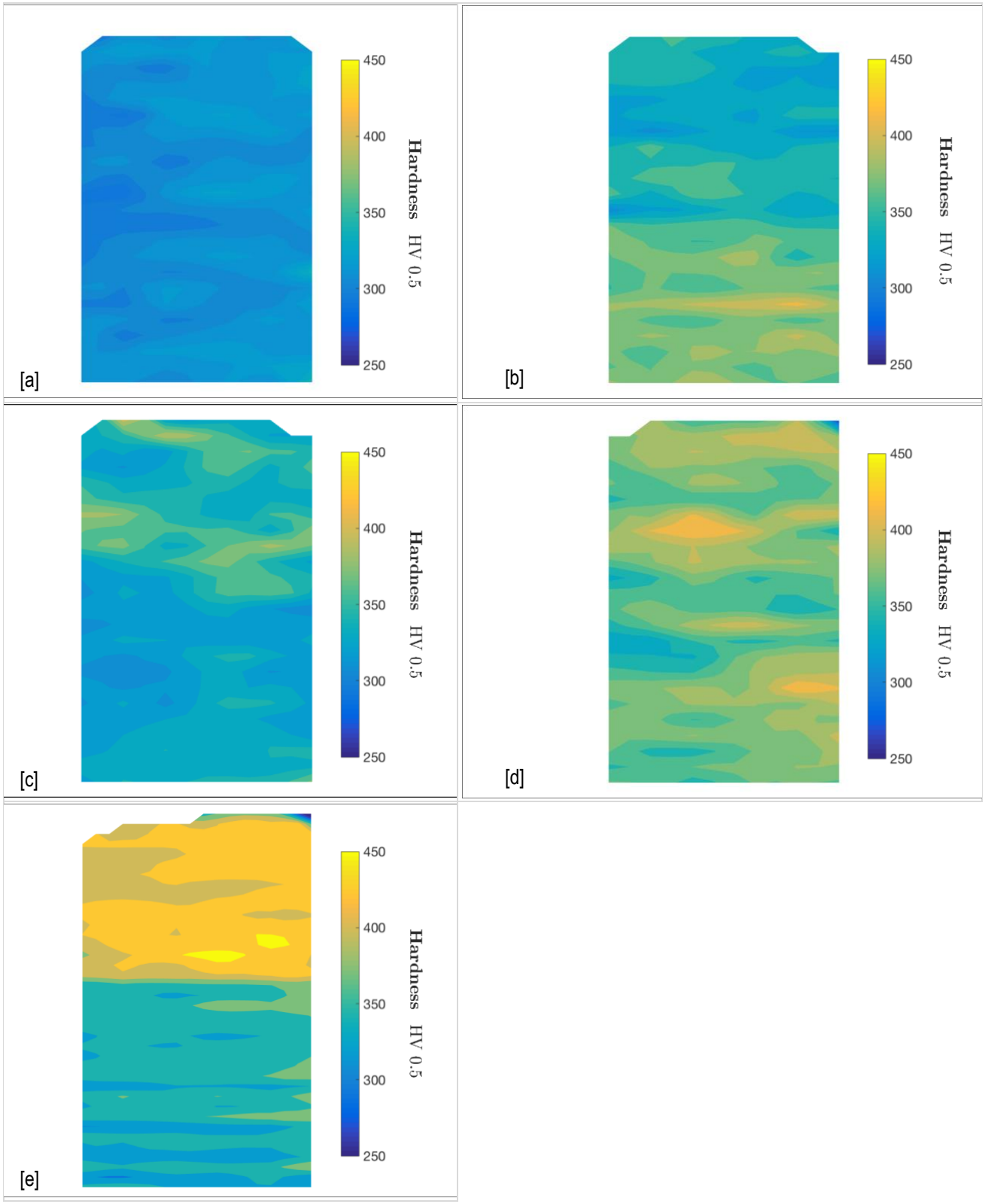

Figure 47: Schematic representation of the hardness measurement values. [a] Test case 1: Natural cooling, interlayer waiting time 40s; [b] Test case 2: Natural cooling, interlayer waiting time 80s; [c] Test case 3: Active substrate cooling, interlayer waiting time 20s; [d] Test case 4: Active substrate cooling, interlayer waiting time 40s; [e] Test case 5: Active component cooling, interlayer waiting time 40s.

The lowest hardness values are observed for the test cases 1 and 3 regarding the material constituting the experimental fifteen-layer weld deposit. While the highest hardness values are found for the material constituting the bottom segment of the experimental fifteen-layer weld deposit corresponding to test case 2, and the material constituting the experimental fifteen-layer weld deposit corresponding to the test cases 4 and 5 respectively. A uniform hardness profile is observed for the test cases 1 and 3 regarding the material constituting the experimental fifteen-layer weld deposit. While for the test cases 2 and 5, two distinct hardness profiles are observed regarding the material constituting the top segment and the bottom segment. For test case 4 a small difference is observed regarding the hardness profiles of the material constituting the bottom segment and the top segment of the experimental fifteen-layer weld deposit.

According to Table 15, the average hardness values that are observed for the test cases 1 and 3 regarding the material constituting the bottom segment are equal to $297.2\ \mathrm{HV0.5}$ and $309.5\ \mathrm{HV0.5}$ respectively. While, the standard deviation of the hardness values of the material constituting the bottom segment are equal to $7.4\ \mathrm{HV0.5}$ and $10.3\ \mathrm{HV0.5}$ for the test cases 1 and 3 respectively. Further, the hardness profile corresponding to test case 3 regarding the top segment is characterized by an average hardness value of $323.8\ \mathrm{HV0.5}$ and a standard deviation of $13.4\ \mathrm{HV0.5}$. Similarly, regarding the test cases 2 and 4, it is observed that the average hardness values regarding the material constituting the bottom segment are of the same order, equal to $346.7\ \mathrm{HV0.5}$ and $346.5\ \mathrm{HV0.5}$ for the test cases 2 and 4 respectively. While, the standard deviation of the hardness values that is found for the test case 4 is a factor two higher compared to the value that is observed for test case 2, equal to $7.8\ \mathrm{HV0.5}$ and $14.3\ \mathrm{HV0.5}$ for the test cases 2 and 4 respectively. Further, it is observed that for test case 2 the hardness profile of the top segment is characterized by an average hardness of $317.6\ \mathrm{HV0.5}$ and a standard deviation of $8.2\ \mathrm{HV0.5}$.

The highest average hardness value is observed for test case 5 regarding the material constituting the top segment of the experimental fifteen-layer weld deposit. According to Table 15, the hardness profile of the material constituting the bottom segment is characterized by an average hardness of $326.7\ \mathrm{HV0.5}$ and a standard deviation of $14.4\ \mathrm{HV0.5}$. While, the hardness profile of the material constituting the top segment is characterized by an average hardness of $387.6\ \mathrm{HV0.5}$ and a standard deviation of $16.3\ \mathrm{HV0.5}$. Concerning the layer band morphology that is observed for the material constituting both the middle segment and the bottom segment of the experimental fifteen-layer weld deposit. The average hardness values corresponding to the fine-grained and coarse-grained layer band regions are equal to $387.6\ \mathrm{HV0.5}$ and $387.6\ \mathrm{HV0.5}$ respectively.

4.3.4 Thermal characteristics

An important aspect of the F.E. model is to describe the temperature field that is experienced by the material constituting the experimental fifteen-layer weld deposit. Accordingly, the F.E. model allows to describe the effect of the cooling methods on the microstructure of the deposited material in terms of the thermal characteristics including the temperature distribution, the locally attained temperature values, the cooling rates and the temperature gradients throughout the component.

In this section, the effect of the thermal characteristics that are calculated in the F.E. model on the resulting microstructure of the material constituting the experimental fifteen-layer weld deposit is evaluated for the test cases 1 to 5. Further, the effect of the thermal characteristics that are calculated in the F.E. model on the formation of the microstructural constituents and the hardness values are evaluated in relation to the microstructural morphology of the material constituting the experimental fifteen-layer weld deposit.

As described in Section 4.2.1, the microstructural transformations are related to the thermal characteristics that are calculated in the F.E. model. The thermal cycle peak temperatures are associated with the amount of grain growth, grain refinement and the formation of partial transformation products. While the thermal cycle through temperatures are related to the martensitic transformation. The component mean temperature affects the substitutional diffusion of alloying elements, recrystallization, grain growth and the amount of grain refinement. Both the microstructural morphology and the formation of microstructural constituents are affected by the cooling rate. Further, the distribution of alloying elements throughout the material is influenced by the locally attained temperature gradient. A schematic overview of the locally attained temperature values that are calculated in the F.E. model in relation to the microstructural transformations corresponding to the test cases 1 to 5, is shown in Table 16 to Table 18.

Table 16: The locally attained temperature values in relation to the microstructural transformations for the test cases 1 to 5, calculated at the temperature measurement point Tc-C1.

	Test case 1	Test case 2	Test case 3	Test case 4	Test case 5
$1200\ °C < T_P < T_M$	■	■	■	■	■
$T_{A3} < T_P < 1200\ °C$	■■■■	■■■	■■■	■■	■
$T_{A1} < T_P < T_{A3}$	■■■	■■	■■■	■■	■
$T_P < T_{A1}$	–	■■	■	■■■	■■■■■
$T_m < T_{Ms}$	–	■	–	■	■

Table 17: The locally attained temperature values in relation to the microstructural transformations for the test cases 1 to 5, calculated at the temperature measurement point Tc-C5.

	Test case 1	Test case 2	Test case 3	Test case 4	Test case 5
$1200\ °C < T_P < T_M$	■	■	■	■	■
$T_{A3} < T_P < 1200\ °C$	■■■	■■	■■■	■■	■
$T_{A1} < T_P < T_{A3}$	–	■	–	■	■
$T_P < T_{A1}$	–	–	–	–	■
$T_m < T_{Ms}$	–	–	–	■	■

Table 18: The component mean temperature in relation to the microstructural transformations for the test cases 1 to 5, calculated as the average value at the temperature measurement points Tc-B2, Tc-D1, Tc-D5 and Tc-D10.

	Test case 1	Test case 2	Test case 3	Test case 4	Test case 5
$T_{Mean} > 500\ °C$	■	■	■	–	–

4.3.4.1 Microstructural morphology

In the experimental results, the microstructural morphology is described in terms of the average grain size and the distribution of alloying elements throughout the material. Both the average grain size and the distribution of alloying elements throughout the material affect the formation of the microstructural constituents. The microstructural transformations that occur during the deposition process of the material constituting the experimental fifteen-layer weld deposit are discussed based on the thermal characteristics corresponding to the test cases 1 to 5.

4.3.4.1.1 Thermal cycle peak temperatures

For temperature values in the temperature range between 1200 ℃ and the melting temperature, grain growth is facilitated. While, for temperature values in the temperature range between the A_3-temperature and 1200 ℃, limited grain growth and grain refinement is induced. Further, the formation of partial transformation products is induced for temperature values reaching the inter-critical temperature range. While for temperature values below the A_1-temperature, tempering and ageing phenomena are induced.

4.3.4.1.1.1 Grain growth

The amount of grain growth that is expected based on the attained thermal cycle peak temperatures is of the same order for the test cases 1 to 5 regarding the material constituting the experimental fifteen-layer weld deposit. According to the thermal cycle peak temperatures that are calculated at the temperature measurement points Tc-C1 and Tc-C5, as shown in Figure 36.a and Figure 36.b respectively. It is observed that for the test cases 1 to 5 grain growth is facilitated during a single thermal cycle regarding the top segment, the middle segment and the bottom segment of the experimental fifteen-layer weld deposit.

4.3.4.1.1.2 Grain refinement

The amount of limited grain growth and grain refinement that is expected considering the attained thermal cycle peak temperatures is in accordance with the order in which the highest thermal cycle peak temperatures are observed for the test cases 1 to 5 regarding the material constituting the bottom segment of the experimental fifteen-layer weld deposit. According to the thermal cycle peak temperatures that are calculated at the temperature measurement point Tc-C1, as shown in Figure 36.a. It is observed that for test case 1, limited grain growth and grain refinement is induced during four successive thermal cycles. While for the test cases 2 and 3, limited grain growth and grain refinement is induced during three successive thermal cycles. For the test cases 4 and 5, limited grain growth and grain refinement is induced during two successive thermal cycles and a single thermal cycle respectively.

With regard to the material constituting middle segment and the bottom segment of the experimental fifteen-layer weld deposit. The amount of limited grain growth and grain refinement that is expected considering the attained thermal cycle peak temperatures is of the same order for both the test cases 1 and 3, and the test cases 2 and 4 respectively. According to the thermal cycle peak temperatures that are calculated at the temperature measurement point Tc-C5, as shown in Figure 36.b. It is observed that for both the test cases 1 and 3, limited grain growth and grain refinement is induced during three successive thermal cycles. While for the test cases 2 and 4, limited grain growth and grain refinement is induced during two successive thermal cycles. For test case 5, limited grain growth and grain refinement is induced during a single thermal cycle.

4.3.4.1.1.3 Partial transformation

The extent to which the formation of partial transformation products is induced considering the attained thermal cycle peak temperatures is expected to be of the same order for both the test cases 1 and 3, and the test cases 2 and 4 respectively regarding the material constituting the experimental fifteen-layer weld deposit. According to the

thermal cycle peak temperatures that are calculated at the temperature measurement points $\mathrm{Tc\text{-}C1}$ and $\mathrm{Tc\text{-}C5}$, as shown in Figure 36.a and Figure 36.b respectively. It is observed that for both the test cases 1 and 3, the formation of partial transformation products is induced during three successive thermal cycles. While for both the test cases 2 and 4, the formation of partial transformation products is induced during two successive thermal cycles. For test case 5, the formation of partial transformation products is induced during a single thermal cycle.

4.3.4.1.2 Thermal cycle through temperatures

With regard to thermal cycle through temperatures attaining values below the martensitic start temperature. The martensite transformation is induced when the material is rapidly cooled from temperatures exceeding the $\mathrm{A_1}$-temperature. Since the thermal cycle peak temperatures of the first two thermal cycles exceed the melting point, the effect of the thermal cycle through temperatures are considered from the second thermal cycle onward.

4.3.4.1.2.1 Martensitic transformation

With regard to both the test cases 1 and 3. It is observed that the thermal cycle through temperatures of the successive thermal cycles attain values exceeding the martensitic transformation temperature. Indicating that for both the test cases 1 and 3, no martensitic transformation is induced with regard to the material constituting the bottom segment, the middle segment and the top segment of the experimental fifteen-layer weld deposit.

For test case 2, a clear distinction is observed with regard to the martensitic transformation regarding the material constituting the bottom segment, the top segment and middle segment of the experimental fifteen-layer weld deposit. With regard to the bottom segment, the thermal cycle through temperatures of the thermal cycles 2 to 4 drop below the martensitic transformation temperature. While from the fifth thermal cycle onward, the thermal cycle through temperatures attain values exceeding the martensitic transformation temperature. Regarding the middle segment, the thermal cycle through temperatures attain values exceeding the martensitic transformation temperature. Indicating that for test case 2, the martensitic transformation is induced during successive thermal cycles regarding the material constituting the bottom segment. While, no martensitic transformation is induced regarding the material constituting both the top segment and the middle segment of the experimental fifteen-layer weld deposit.

For both the test cases 4 and 5, all thermal cycle through temperatures attain values below the martensitic transformation temperature. Indicating that for both the test cases 4 and 5, the martensitic transformation is induced during successive thermal cycles regarding the material constituting the fifteen-layer weld deposit. In addition, the thermal cycle through temperatures corresponding to test case 5 attain lower values below the martensitic transformation temperature compared to the thermal cycle through temperatures that are found for test case 4. According to Figure 37, the thermal cycle through temperatures corresponding to test case 5 are about $49.4\ \%$ lower compared to the thermal cycle through temperatures that are found for test case 4. Indicating that for test case 5, the martensitic transformation is further proceeded during the successive thermal cycles.

4.3.4.1.3 Component mean temperature

The component mean temperature affects by means of tempering and ageing phenomena the extent in which the substitutional diffusion of alloying elements, recrystallization, grain growth and the amount of grain refinement is facilitated. The effect of the tempering heat treatment is described based on the equilibrium mean temperatures of the experimental fifteen-layer weld deposit that are recorded during the deposition process of the experimental fifteen-layer weld deposit.

4.3.4.1.3.1 Tempering and ageing

Based on the component mean temperatures. It is observed that for test cases 1 to 3, the equilibrium mean temperatures regarding the material constituting the experimental fifteen-layer weld deposit attain values in the

range between 500 °C and the A_1-temperature during the deposition process. Indicating that the attained equilibrium mean temperatures are sufficiently high to facilitate the substitutional diffusion of alloying elements, recrystallization and grain growth. Indicating that for test cases 1 to 3, the amount of grain refinement that is expected based on the thermal cycle peak temperatures is reduced by considering the effect of the equilibrium mean temperature values regarding the material constituting the experimental fifteen-layer weld deposit.

In addition, with regard to the test cases 2 and 3, a distinction is observed regarding the tempering heat treatment of the material constituting the bottom segment of the experimental fifteen-layer weld deposit. During the deposition of the bottom segment, the equilibrium mean temperature values regarding the bottom segment corresponding to the test cases 2 and 3 attain values in the range between 500 °C and the A_1-temperature. While during the deposition of the middle segment and the top segment, the equilibrium mean temperature values regarding the bottom segment corresponding to the test cases 2 and 3 attain values in the range between 250 °C and 500 °C. Indicating that with regard to the material constituting the bottom segment, the amount of grain refinement that is expected based on the thermal cycle peak temperatures is reduced by considering the effect of the equilibrium mean temperature values during the deposition of the bottom segment. While during the deposition of the middle segment and the top segment, the precipitation of iron carbides is induced.

For the test cases 4 and 5, the equilibrium mean temperature values regarding the material constituting the experimental fifteen-layer weld deposit attain values in the range between 250 °C and 500 °C during the deposition process. Indicating that the attained equilibrium mean temperature values regarding the experimental fifteen-layer weld deposit prohibit the substitutional diffusion of alloying elements, recrystallization and grain growth. Instead, the precipitation of iron carbides is induced regarding the material constituting the experimental fifteen-layer weld deposit. Hence, for the test cases 4 and 5, the attained equilibrium mean temperature values have no effect on the amount of limited grain growth and grain refinement that is expected based on the thermal cycle peak temperatures.

4.3.4.1.4 Cooling rate

In addition to the locally attained temperature values, the formation of the microstructural constituents is related to the cooling rate. Depending on the cooling rate, the austenite phase is decomposed into the microstructural constituents, as shown in Figure 23.

Considering the values of the average cooling rates, the resulting microstructure of the material constituting the experimental fifteen-layer weld deposit corresponding to the test cases 1 to 5 is expected to consist of mainly bainite and acicular ferrite microstructural constituents. According to the cooling rates that are calculated at the temperature measurement points $Tc\text{-}C1$ and $Tc\text{-}C5$, as shown in Figure 38 and Figure 39 respectively. It is observed that the average values of the cooling rate during the cooling stage of the first thermal cycle corresponding to the test cases 1 to 5 are equal to -30.5 $^{°C}/_{s}$. While concerning the cooling stage of the fifth thermal cycle, the average values of the cooling rate are equal to -14.5 $^{°C}/_{s}$ for the test cases 1 to 5. Indicating that the formation of lath bainite and acicular ferrite is expected to occur during the cooling stages of the first thermal cycle. While an increased amount of granular bainite is expected to be formed during the cooling stages of the subsequent thermal cycles. With regard to the martensite transformation. The average cooling rates corresponding to the test cases 1 to 5 allow for the martensite formation to occur when that the thermal cycle through temperatures attain values below the martensitic start temperature.

4.3.4.1.5 Temperature gradient

With regard to the local temperature gradient that is experienced by the material constituting the experimental fifteen-layer weld deposit. A distinction is made between the local temperature gradient that is directly related to the weld pool characteristics and the deposition process.

Regarding the local temperature gradient that is directly related to the weld pool characteristics. This applies to the primary microstructure that is observed for the test cases 1 to 5 regarding the material constituting the two upper layers of the experimental fifteen-layer weld deposit. As described, the primary microstructure is characterized by the epitaxial growth of columnar grains that result from the preferred crystallographic growth directions that develop under the influence of the maximum temperature gradient, directly related to the weld pool characteristics. In addition, the increased concentration of alloying elements that is observed at the fusion boundaries of the individual weld layers constituting the experimental fifteen-layer weld deposit is related to the local temperature gradient that results from the constitutional supercooling during the solidification process.

The segregation of alloying elements in the building direction is attributed to the maximum temperature gradient related to the deposition process. This observation is in agreement with the values of the maximum temperature gradient that are found for the test cases 1 to 5. According to Figure 40, the values of the temperature gradient in the z-direction are significant higher compared to the corresponding values in the y- and z-direction during the deposition of the multilayer weld deposit. With regard to test case 4, the specific orientation of the fine grained granular bainite constituents that are observed regarding the material constituting both the top segment and the middle segment is attributed to the local value of the maximum temperature gradient.

4.3.4.2 Microstructural constituents

The formation of the microstructural constituents throughout the material constituting the experimental fifteen-layer weld deposit are discussed in relation to the thermal characteristics corresponding to the test cases 1 to 5.

With regard to the granular bainite constituents that are observed for the test cases 1 to 5. It is found that both the amount and size of the granular bainite constituents is increased as a result of the tempering heat treatment regarding the material constituting the middle segment and the bottom segment of the experimental fifteen-layer weld deposit.

In contrast to the general observation, a reduced amount of granular bainite constituents is observed for test case 1 regarding the material constituting both the middle segment and the bottom segment of the experimental fifteen-layer weld deposit. This observation is due to the increased degree of homogenization of the microstructural constituents throughout the material. As indicated, the granular bainite constituents are located in the carbon depleted regions. While both the martensite and acicular ferrite constituents are found in the carbon rich regions. In this regard, the presence of granular bainite constituents is correlated to the inhomogeneous distribution of alloying elements throughout the material. According to the F.E. temperature values, the equilibrium mean temperature values corresponding to test case 1 are sufficiently high to facilitate the substitutional diffusion of alloying elements, recrystallization and grain growth. Confirming that based on the F.E. temperature values, a reduced amount of granular bainite constituents is expected for test case 1 regarding the material constituting both the middle segment and the bottom segment of the experimental fifteen-layer weld deposit.

Similarly, the presence of acicular ferrite constituents can be correlated to the F.E. temperature values. Since the acicular ferrite constituents are formed by the heterogeneous nucleation on non-metallic inclusions inside the prior austenite grain interiors. The formation of acicular ferrite constituents is promoted by an increased prior austenite grain size and the homogeneous distribution of non-metallic inclusions throughout the prior austenite grain interiors. According to the F.E. temperature values, the equilibrium mean temperature values corresponding to the test cases 2 to 5 prohibit the substitutional diffusion of alloying elements, recrystallization and grain growth. Indicating that for the test cases 2 to 5, both the carbide precipitates and non-metallic inclusions are retained throughout the prior austenite matrix. Thus, providing nucleation sites for the acicular ferrite constituents.

Indeed, the presence of acicular ferrite constituents is observed for the test cases 2 to 4 regarding the material constituting the experimental fifteen-layer weld deposit. As indicated, the material corresponding to test case 3 is homogeneously composed of both bainite and acicular ferrite constituents. Although, the material constituting the top segment and the bottom segment show an increased fraction of lath bainite and granular bainite constituents respectively. This observation is explained by the competitive formation of lath bainite and acicular ferrite which depends on both the prior austenite grain size and the distribution of microstructural constituents throughout the material [39]. In this regard, the increased fraction of lath bainite that is observed for the material constituting the top segment is due to a lower degree of homogenization. While regarding the bottom segment, the increased fraction of granular bainite is attributed to the tempering heat treatment as earlier discussed.

Also concerning the martensitic microstructure, it is found that the martensite formation is in agreement with the F.E. thermal cycle through temperatures that are observed for the test cases 2, 4 and 5. Indicating that for test case 2, the martensitic transformation is induced during successive thermal cycles regarding the material constituting the bottom segment. While no martensitic transformation is induced regarding the material constituting both the middle segment and the top segment. While for both the test cases 4 and 5, the martensitic transformation is induced during successive thermal cycles regarding the material constituting the experimental fifteen-layer weld deposit. Confirming that based on the F.E. thermal cycle through temperatures, the martensite formation is induced regarding the material constituting the bottom segment corresponding to test case 2, and the material constituting the experimental fifteen-layer weld deposit corresponding to the test cases 4 and 5.

Further, the presence of tempered martensite is in accordance with the F.E. equilibrium mean temperature values that are observed for the test cases 2 and 4 regarding the material constituting the middle segment and the bottom segment, and the coarse-grained layer band regions corresponding to test case 5 respectively. The same applies to the presence of tempered lath bainite that is observed for test case 1 and the granular bainite constituents that are observed for the test cases 2 to 5, regarding the material constituting both the middle segment and the bottom segment of the experimental fifteen-layer weld deposit. Indicating that both the bainite and martensite microstructural constituents are subjected to a tempering heat treatment regarding the material constituting both the middle segment and the bottom segment of the experimental fifteen-layer weld deposit.

4.3.4.3 Hardness values

The hardness values are discussed in relation to the grain size and the size and distribution of the carbide precipitates throughout the material. Low hardness values are associated with a coarse-grained microstructure and the localized presence of carbide precipitates. While higher hardness values indicate a fine-grained microstructure and the presence of carbon precipitates throughout the ferrite matrix in the form of either cementite or retained austenite and martensite.

The lowest hardness values are observed for the test cases 1 and 3 regarding the material constituting the experimental fifteen-layer weld deposit. While, the highest hardness values are found for the test cases 2, 4 and 5 regarding the material constituting the bottom segment of test case 2, and the material constituting the experimental fifteen-layer weld deposit corresponding to the test cases 4 and 5 respectively. A uniform hardness profile is observed for the test cases 1 and 3 regarding the material constituting the experimental fifteen-layer weld deposit. While for the test cases 2 and 5, two distinct hardness profiles are observed regarding the top segment and the bottom segment. For test case 4 a minimal difference is observed concerning the hardness profiles of the material constituting the bottom segment and the top segment of the experimental fifteen-layer weld deposit. This observation is in agreement with the microstructural morphologies that are observed for the test cases 1 to 5. As described, for the test cases 1 and 3 a uniform coarse-grained microstructural morphology is observed regarding the material constituting the experimental fifteen-layer weld deposit. While for the test cases 2 and 5, two distinct microstructural morphologies are observed regarding the top segment and the bottom segment. For test case 4 a minimal difference is observed concerning the microstructural morphology of the material constituting the bottom segment and the top segment of the experimental fifteen-layer weld deposit.

The low average hardness values that are observed for the test cases 1 and 3 correspond to the coarse-grained ferritic microstructure regarding the material constituting the fifteen-layer weld deposit. As indicated, the microstructure of the material corresponding to test case 1 consists of a ferritic matrix containing both allotriomorphic and polygonal ferrite constituents. While, the microstructure of the material corresponding to test case 3 is mainly composed of lath bainite and acicular ferrite microstructural constituents. In the case of the pro-eutectoid ferritic microstructure, the carbon is localized along the prior austenite grain boundaries. While in the case of lath bainite and acicular ferrite, the carbon is distributed throughout the ferrite matrix in the form of strip-like cementite particles along the bainitic ferrite lath boundaries or the lenticular ferrite plates in the case of acicular ferrite respectively. Both the large average grain size and the localized presence of carbon precipitates are in agreement with the low average hardness values that are observed for the test cases 1 and 3.

The high values of the average hardness that are observed for the test cases 2, 4 and 5, are primarily correlated to the presence of martensitic microstructural constituents and the fine-grained microstructures regarding the material constituting the bottom segment and the experimental fifteen-layer weld deposit corresponding to the test cases 2 and 4, and both the top segment and the fine-grained layer band regions corresponding to test case 5 respectively. With regard to the material constituting the middle segment and the bottom segment of the experimental fifteen-layer weld deposit.

The tempering heat treatment of the bainite and martensite microstructural constituents results both in the redistribution of microstructural constituents and the coarsening of the microstructure. The high density of dislocations in both bainite and lath martensite provides sites for carbon segregation, carbide precipitation, and is a driving force for recovery and recrystallization [38]. During the tempering heat treatment, the carbon is removed from the supersaturated solid solution by the precipitation of iron carbides. Further, the redistribution of alloying elements between the ferrite and cementite is induced. As a result, the microstructure of both tempered bainite and tempered lath martensite consists of uniformly dispersed cementite particles embedded within a ferrite matrix. Both the coarsening of the microstructure and the redistribution of microstructural constituents results in the reduction of the hardness value.

This observation is in agreement with the presence of large fractions of tempered martensite regarding the material constituting the bottom segment corresponding to the test cases 2 and 4 and the fine-grained layer band regions corresponding to 5 respectively. The most pronounced reduction of the hardness values due to the tempering heat treatment is observed for test case 5 regarding the material constituting both the middle segment and the bottom segment of the experimental fifteen-layer weld deposit. According to Table 15, the average hardness value of the material constituting both the middle segment and the bottom segment is equal to $326.7\ \mathrm{HV0.5}$. While the corresponding hardness value regarding the material constituting the top segment is equal to $387.6\ \mathrm{HV0.5}$. Indicating the average hardness value corresponding to test case 5 regarding the material constituting both the middle segment and the bottom segment is reduced by $15.7\ \%$ as a result of the tempering heat treatment.

With regard to the test cases 2 and 4, the hardness values of the material constituting the bottom segment are of the same order. While the standard deviation of the hardness values corresponding to test case 4 are higher compared to the values corresponding to test case 2. Indicating that for test case 2, a higher degree of homogenization of the microstructural constituents is reached compared to test case 4 regarding the material constituting the experimental fifteen-layer weld deposit.

Similarly, the lowest values of the standard deviation of the hardness measurement values are observed for test case 1 followed by the values that are found for the test cases 2, 3, 4 and 5 respectively. Indicating that for the test cases 2 to 5 a lower degree of homogenization of the microstructural constituents is reached compared the material constituting the experimental fifteen-layer weld deposit corresponding to test case 1. This observation is in agreement with the order of the component mean temperatures that are observed for the test cases 1 to 5. According to Figure 34, the highest component mean temperatures are observed for test case 1, followed by the values that are found for the test cases 2, 3, 4 and 5 respectively. With regard to test case 1, both the hardness values and the standard deviation of the hardness values assume constant values. This observation is in agreement with the uniform ferritic microstructure that is observed for test case 1 regarding the material constituting the experimental fifteen-layer weld deposit. While for the test cases 2 to 5, the standard deviation of the hardness values regarding the material constituting the bottom segment are reduced due to the tempering heat treatment. Indicating that for test cases 2 to 5 a higher degree of homogenization of the microstructural constituents is reached regarding the material constituting the bottom segment compared to the values corresponding to the top segment of the experimental fifteen-layer weld deposit.

4.3.5 Conclusions

The F.E. method that is presented in this research allows to describe the effect of the cooling methods on the microstructure of the deposited material considering the locally attained chemical composition in terms of the thermal characteristics including the temperature distribution, the locally attained temperature values, the cooling rates, and the temperature gradients throughout the component.

The microstructure that results from the application of the cooling methods is described in terms of the microstructural constituents and the microstructural morphology regarding the material constituting the experimental fifteen-layer weld deposit. The microstructural constituents and the microstructural morphology are identified using optical microscopy based on the average grain size and the distribution of alloying elements throughout the material and evaluated in terms of the hardness values.

4.3.5.1 Thermal characteristics

The F.E. method allows to describe the effect of the temperature field on the resulting microstructural in terms of the thermal characteristics that are calculated for the test cases 1 to 5.

4.3.5.1.1 Temperature distribution

The component mean temperatures affects by means of tempering and ageing phenomena the extent in which the substitutional diffusion of alloying elements, recrystallization, grain growth and the amount of grain refinement is facilitated:

- For test case 1, the component mean temperature is sufficiently high to facilitate the substitutional diffusion of alloying elements, recrystallization and grain growth regarding the material constituting the experimental fifteen-layer weld deposit.

For the test cases 2 to 5, the component mean temperatures prohibit the substitutional diffusion of alloying elements, recrystallization and grain growth. Instead, the precipitation of iron carbides is induced regarding the material constituting the fifteen-layer weld deposit. Indicating that for the test cases 2 to 5, both the carbide precipitates and non-metallic inclusions are retained throughout the prior austenite matrix. Thus, providing nucleation sites for the acicular ferrite constituents. Further, the tempering heat treatment of the bainite and martensite microstructural constituents result both in the redistribution of microstructural constituents and the coarsening of the microstructure regarding the material constituting both the middle segment and the bottom segment of the experimental fifteen-layer weld deposit.

4.3.5.1.2 Thermal cycle peak temperatures

The thermal cycle peak temperatures affect the amount of grain growth, grain refinement and the formation of partial transformation products:

- For the test cases 1 to 5, the amount of grain growth that is induced based on the thermal cycle peak temperatures is of the same order regarding the material constituting the experimental fifteen-layer weld deposit.
- The amount of grain refinement that is facilitated regarding the material constituting the top segment is consistent with the order in which the thermal cycle peak temperatures are observed for the test cases 1 to 5. While regarding the material constituting both the middle segment and the bottom segment, the amount of grain refinement that is induced based on the thermal cycle peak temperatures is of the same order for both the test cases 1 and 3, and the test cases 2 and 4 respectively.

The extent in which the formation of partial transformation products are formed considering the thermal cycle peak temperatures is of the same order for both the test cases 1 and 3, and both the test cases 2 and 4 respectively regarding the material constituting the experimental fifteen-layer weld deposit.

4.3.5.1.3 Thermal cycle through temperatures

The thermal cycle through temperatures affect the amount of martensite transformation that is induced regarding the thermal cycle through temperatures attaining values below the martensitic start temperature:

- For both the test cases 1 and 3, no martensitic transformation is induced with regard to the material constituting the experimental fifteen-layer weld deposit.
- For test case 2, the martensitic transformation is induced during successive thermal cycles regarding the material constituting the bottom segment. While, no martensitic transformation is induced regarding the material constituting the middle segment, and the top segment of the experimental fifteen-layer weld deposit.
- For both the test cases 4 and 5, the martensitic transformation is induced during successive thermal cycles regarding the material constituting the experimental fifteen-layer weld deposit. In addition, the thermal cycle through temperatures corresponding to test case 5 attain lower values below the martensitic transformation temperature compared to the thermal cycle through temperatures that are found for test case 4. Indicating that for test case 5, the martensitic transformation is further proceeded during the successive thermal cycles.

4.3.5.1.4 Cooling rate

The effect of the cooling rates on the resulting microstructure is determined considering the average values of the cooling rates of the corresponding cooling stages. Indicating that the formation of lath bainite and acicular ferrite is expected to occur during the cooling stages of the first thermal cycle. While an increased amount of granular bainite is expected to be formed during the cooling stages of the subsequent thermal cycles. With regard to the martensite transformation. The average cooling rates corresponding to the test cases 1 to 5 allow for the martensite formation to occur when that the thermal cycle through temperatures attain values below the martensitic start temperature.

4.3.5.2 Microstructural morphology

The microstructure of the deposited material is described in terms of the microstructural morphology and the microstructural constituents that result from the application of the cooling methods as defined in the test cases 1 to 5.

4.3.5.2.1 Average grain size

As a general trend, it is observed that the average grain size is reduced as a result of the periodic thermal cycling of the temperature values. Expressed by a reduced average grain size of the microstructure regarding the material constituting the middle segment and bottom segment of the experimental fifteen-layer weld deposit.

- The most pronounced reduction of the average grain size is observed for the test cases 2 and 4 regarding the material constituting the middle segment and bottom segment of the experimental fifteen-layer weld deposit. While for both the test cases 1 and 3, the effect is less evident, and an almost uniform grain size is observed regarding the microstructure of the material constituting the experimental fifteen-layer weld deposit. A clear exception to the general trend is observed for test case 5, for which the smallest average grain size is observed regarding the material constituting the top segment of the experimental fifteen-layer weld deposit.
- A uniform coarse-grained microstructural morphology is observed for the test cases 1 and 3 regarding the material constituting the experimental fifteen-layer weld deposit. While for the test cases 2 and 5, two distinct microstructural morphologies are observed regarding the top segment and the bottom segment. For test case 4 a small difference is observed regarding the microstructural morphology of the material constituting the experimental fifteen-layer weld deposit.

4.3.5.2.2 Layer band morphology

With regard to the material constituting both the middle segment and the bottom segment of the experimental fifteen-layer weld deposit. A layer band morphology of alternating regions of fine-grained and coarse-grained microstructures is formed due to the movement of the welding heat source in the building direction.

- The most pronounced layer band morphology is observed for test case 5. Whereby, the mutual distance between the layer band regions of the respective layers corresponds to a single layer thickness. This observation is in agreement with the thermal cycle peak temperatures that are observed for test case 5.

4.3.5.2.3 Distribution of alloying elements

The distribution of alloying elements throughout the material is influenced by the locally attained temperature gradient that is directly related to the weld pool characteristics or the deposition process. Meanwhile, the homogeneous distribution of alloying elements throughout the material is promoted by a sufficiently high component mean temperature.

- An increased concentration of alloying elements is observed at the fusion boundaries of the individual weld layers constituting the experimental fifteen-layer weld deposit, resulting from the constitutional supercooling during the solidification process. Further, the segregation of alloying elements is observed in the building direction along the direction of the maximum temperature gradient.
- The most pronounced effect of the local redistribution of alloying elements is observed regarding the coarse-grained microstructure regions, corresponding to the middle segment and the coarse-grained layer band regions of the test cases 2 and 5 respectively resulting in the formation of carbon rich and carbon depleted regions.

4.3.5.3 Hardness values

The hardness values are related to the average grain size and the distribution of the alloying elements throughout the material.

- The lowest hardness values are observed for the test cases 1 and 3 regarding the material constituting the experimental fifteen-layer weld deposit. While the highest hardness values are found for the material constituting the bottom segment corresponding to test case 2, and the material constituting the experimental fifteen-layer weld deposit corresponding to the test cases 4 and 5 respectively.
- A uniform hardness profile is observed for the test cases 1 and 3 regarding the material constituting the experimental fifteen-layer weld deposit. While for the test cases 2 and 5, two distinct hardness profiles are observed regarding the top segment and the bottom segment. For test case 4 a small difference is observed concerning the hardness profiles of the material constituting the bottom segment and the top segment of the experimental fifteen-layer weld deposit.

The hardness values are in agreement with the microstructural morphologies that are observed for the test cases 1 to 5:

- The low average hardness values that are observed for the test cases 1 and 3 correspond to the coarse-grained ferritic microstructure regarding the material constituting the experimental fifteen-layer weld deposit. Both the large average grain size and the localized presence of carbon precipitates are in agreement with the low average hardness values that are observed for the test cases 1 and 3.
- The high average hardness are correlated to the presence of martensitic microstructural constituents and the fine-grained microstructures values that are observed for the test cases 2, 4, and 5, regarding the material constituting the bottom segment of the experimental fifteen-layer weld deposit corresponding to test case 2,

the experimental fifteen-layer weld deposit corresponding to 4, and both the top segment and the fine-grained layer band regions corresponding to test case 5.

- The tempering heat treatment of the bainite and martensite microstructural constituents result both in the redistribution of microstructural constituents and the coarsening of the microstructure regarding the material constituting the middle segment and the bottom segment of the experimental fifteen-layer weld deposit. Both the coarsening of the microstructure and the redistribution of microstructural constituents results in the reduction of the hardness value.

5 Validation

5.1 F.E. model validation

In the F.E. model, assumptions have been used to simplify the calculations and to reduce the computation time. With regard to the material modelling, the latent heat effects of the phase transformations are not considered. Concerning the quiet element method that is used to model the material deposition, it is assumed that the coefficient of thermal conductivity is reduced by a scaling factor regarding the quiet elements that are not under the influence of the welding heat source. The effects of the assumptions that are used regarding the latent heat of transformation and the coefficient of thermal conductivity are validated. Further, the volume of the single-pass weld layers in the F.E. model is validated to the actual volume of the electrode material that is deposited in the experiments.

The measurement accuracy of the F.E. model is validated based on the smallest calibration error regarding the temperature values that are calculated at the temperature measurement points in the F.E. model and the corresponding temperature values that are recorded by the physically attached thermocouples in the experiments. With regard to the thermal cycle peak temperatures, the value of the arc efficiency that is used in the F.E. model is validated based on the deposition of a single-pass weld layer. Regarding the thermal cycle through temperatures, the thermal boundary conditions that are defined for the five test cases in the F.E. model are validated based on the deposition of the multilayer weld deposit.

5.1.1 F.E. material model

In the F.E. model, the latent heat effects of the phase transformations are not considered. Regarding the quiet element method that is used to model the material deposition, the coefficient of thermal conductivity is reduced by a scaling factor regarding the quiet elements that are not under the influence of the welding heat source.

The temperature values that result from considering a temperature dependent specific heat and the application of the quiet element method in the F.E. model, are shown in Figure 48.a. and Figure 48.b. respectively.

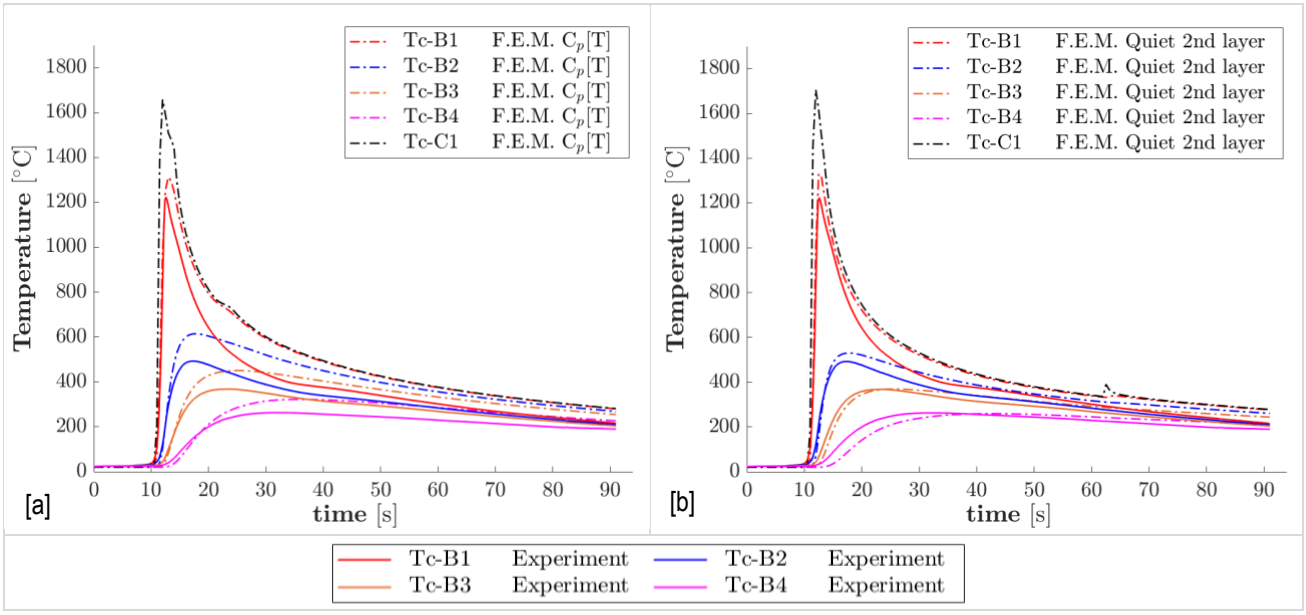

Figure 48: Temperature measurement values of a single-pass layer on the component base wall. Arc efficiency $\eta = 0.44$. [a] Quiet 2nd layer; [b] Temperature dependent heat capacity $C_p[T]$.

The thermal cycle peak temperatures and thermal cycle through temperatures that result from considering a temperature dependent specific heat and the application of the quiet element method in the F.E. model, are shown in Table 19 and Table 20 respectively.

Table 19: Thermal cycle peak temperatures of a single-pass weld layer on the component base wall. Calculated F.E. model temperature values considering a Quiet 2nd layer and a temperature dependent heat capacity $C_p[T]$.

	Tc-B 4	Tc-B 3	Tc-B 2	Tc-B 1	Tc-C 1
Experiment	263.0	368.2	492.8	1224	-
F.E.M. $\eta = 0.44$	256.5	367.0	529.0	1340	1700
F.E.M. $\eta = 0.44$ Quiet 2nd layer	259.6	369.7	530.2	1330	1705
F.E.M. $\eta = 0.44$ $C_P[T]$	322.1	450.4	614.4	1312	1658

Table 20: Thermal cycle through temperatures of a single-pass weld layer on the component base wall. Calculated F.E. model temperature values considering a Quiet 2nd layer and a temperature dependent heat capacity $C_p[T]$.

	Tc-B 4	Tc-B 3	Tc-B 2	Tc-B 1	Tc-C 1
Experiment	220.7	241.3	250.7	282.8	-
F.E.M. $\eta = 0.44$	225.9	262.4	280.8	296.1	297.4
F.E.M. $\eta = 0.44$ Quiet 2nd layer	231.6	272.2	294.7	317.0	320.2
F.E.M. $\eta = 0.44$ $C_P[T]$	260.8	298.3	316.8	331.5	332.8

5.1.1.1 Specific heat

The specific heat is associated with the latent heat of the phase transformations. In the F.E model, the latent heat effects corresponding to the ferrite-austenite phase transformation and the solid-liquid phase transformation are not considered. The effect of not considering the latent heat of the phase transformations in the F.E. model is discussed based on the temperature values that result from using a temperature dependent specific heat.

For the electrode material X90, the latent heat of transformation that is associated with the ferrite-austenite phase transformation between 730 °C and 750 °C, is defined in Equation 23. The latent heat of transformation that is associated with the solid-liquid phase transformation between 1450 °C and 1500 °C, is defined in Equation 24.

$$[\Delta H_{730-750}]_{X90} = \int_{730}^{750} \rho C_p = 258 \cdot 10^3 \quad \frac{kJ}{m^3} \qquad [23]$$

$$[\Delta H_{1450-1500}]_{X90} = \int_{1450}^{1500} \rho C_p = 2.03 \cdot 10^6 \quad \frac{kJ}{m^3} \qquad [24]$$

In Equation 23, the values of the density and the specific heat capacity during the ferrite-austenite phase transformation are equal to $7500\ \left[\frac{kg}{m^3}\right]$ and $1720\ \left[\frac{J}{kg \cdot K}\right]$ respectively. In Equation 24, the density and the specific heat capacity values associated with the solid-liquid phase transformation are equal to $7000\ \left[\frac{kg}{m^3}\right]$ and $5790\ \left[\frac{J}{kg \cdot K}\right]$ respectively.

The heat that is released or absorbed during the corresponding phase transformations is defined by the latent heat of transformation divided by the volume specific heat capacity [51]. The volume specific heat capacity is defined as the average value over the whole temperature range, based on the average values of the density and the specific heat capacity [50]. The volume specific heat capacity of the electrode material X90 is defined in Equation 25.

$$[\rho C_P]_{X90} = 5.15 \cdot 10^3 \quad \frac{kJ}{m^3 \cdot K} \qquad [25]$$

In Equation 25, the average values of the density and the specific heat capacity over the whole temperature range are equal to $7360\ \left[\frac{kg}{m^3}\right]$ and $700\ \left[\frac{J}{kg \cdot K}\right]$ respectively, according to Figure 27.

Accordingly, it is found that for the electrode material X90, the latent heat that is released or absorbed during the ferrite-austenite phase transformation is equal to $50.1\ °C$. While, the latent heat corresponding to the solid-liquid phase transformation is associated with a temperature change of $393.3\ °C$.

With regard to the thermal cycle peak temperatures that are calculated at the temperature measurement points Tc-C1 and Tc-B1 in the F.E. model. It is found that when considering a temperature dependent specific heat, the calculated temperature values are lower compared to the temperature values considering a constant specific heat. While, the temperature values that are calculated at the temperature measurement points Tc-B2, Tc-B3 and Tc-B4 considering a temperature dependent specific heat are higher, compared to the corresponding temperature values assuming a constant specific heat.

The decrease in temperature values that is observed concerning the thermal cycle peak temperatures that are calculated at the temperature measurement points Tc-C1 and Tc-B1 in the F.E. model considering a temperature dependent specific heat is attributed to the fact that during the temperature rise the latent heat is absorbed, causing lower temperature values. According to Table 11, the thermal cycle peak temperatures corresponding to the measurement points Tc-C1 and Tc-B1 considering a temperature dependent specific heat are reduced by $42\ °C$ and $28\ °C$ respectively, compared to the values considering a constant specific heat. Indicating that the decrease of the corresponding temperature values is relatively small compared to the latent heat of the solid-liquid phase transformation. This observation is explained by the fact that only a small material volume is subjected to temperatures exceeding the melting temperature.

With regard to the temperature values that are calculated at the temperature measurement points Tc-B2, Tc-B3 and Tc-B4 in the F.E. model. The increase of the temperature values that result from using a temperature dependent specific heat is attributed to the fact that upon cooing the latent heat is released, resulting in higher temperature values. According to Table 19, the thermal cycle peak temperatures corresponding to the temperature measurement points Tc-B2, Tc-B3 and Tc-B4 in the F.E. model using a temperature dependent specific heat are increased by $65.6\ °C$, $83.4\ °C$ and $85.4\ °C$ respectively, compared to the temperature values considering a constant specific heat. Correspondingly, this also applies to the thermal cycle through temperatures that are calculated at the temperature measurement points Tc-C1 and Tc-B1 in the F.E. model. According to Table 20, the thermal cycle through temperatures that are calculated at the temperature measurement points Tc-C1 and Tc-B1 to Tc-B4 in the F.E. model considering a temperature dependent specific heat are on average increased by $36\ °C$, compared to the temperature values considering a constant specific heat.

5.1.1.2 Coefficient of thermal conductivity

The coefficient of thermal conductivity is associated with the activation method that is used to model the material deposition in the wire and arc additive manufacturing process. In the quiet element method, the deposition of the individual weld layers is modeled by the sequential activation of the successive material elements. According to Equation 19, the coefficient of thermal conductivity is defined by the material property concerning the material elements that are under the influence of the welding heat source. While for the quiet elements that are not under the influence of the welding heat source, the coefficient of thermal conductivity is reduced by using a scaling factor.

5.1.1.2.1 Scaling factor

With regard to the scaling factor that is used in the quiet element method, the following is considered [54]:

- For not small enough scaling factors: the thermal energy is conducted towards the quiet elements, inducing scaling errors;
- For too small scaling factors: non-convergence issues occur during the F.E. simulation, due to ill-conditioned solutions.

The thermal cycle peak temperatures and thermal cycle through temperatures that result from the application of the quiet element method using a scaling factor equal to 0.01 and 0.0001, are shown in Table 21 and Table 22 respectively.

Table 21: Thermal cycle peak temperatures of a single-pass weld layer on the component base wall. Quiet 2nd layer.

	Tc-B 4	Tc-B 3	Tc-B 2	Tc-B 1	Tc-C 1
Experiment	263	368.2	492.8	1224	-
F.E.M. $[\eta = 0.44]$ $s_k = 0.01$	256.5	367.0	529.0	1340	1700
F.E.M. $[\eta = 0.44]$ $s_k = 0.0001$	256.1	366.2	527.7	1360	1594

Table 22: Thermal cycle through temperatures of a single-pass weld layer on the component base wall. Quiet 2nd layer.

	Tc-B 4	Tc-B 3	Tc-B 2	Tc-B 1	Tc-C 1
Experiment	220.7	241.3	250.7	382.8	-
F.E.M. $[\eta = 0.44]$ $s_k = 0.01$	225.9	262.4	280.8	296.1	297.4
F.E.M. $[\eta = 0.44]$ $s_k = 0.0001$	225.6	262.1	280.5	295.7	297.1

According to Figure 48.b, the scaling factor 0.01 leads to reasonable temperature values. While the scaling factor 0.0001 introduces scaling errors in the temperature values close to the weld pool due to the thermal energy that is conducted towards the quiet elements. Accordingly, the scaling factor that is used in the F.E. model is equal to 0.01. This value is in agreement with literature [54].

The most significant effect that is observed as a result of the application of the quiet element method in the F.E. model is a rise in the temperature values that are calculated at the temperature measurement point $\mathrm{Tc\text{-}C1}$ at $62.5\mathrm{s}$ after the passage of the welding heat source, as shown in Figure 48.b. The temperature rise is caused by artificially heating effects, resulting from the addition of the quiet 2nd layer [65], [54]. The application of the quiet element method has a minimal effect on the thermal cycle peak temperatures, compared to the temperature values that are obtained by the F.E. model considering the deposition of a single layer, as shown in Table 21. With regard to the thermal cycle through temperatures, it is found that the thermal cycle through temperatures that result from the application of the quiet element method are slightly higher compared to the values that are obtained by the F.E. model without the application of a quiet 2nd layer. According to Table 22, the thermal cycle through temperatures that are calculated at the temperature measurement points $\mathrm{Tc\text{-}C1}$ and $\mathrm{Tc\text{-}B1}$ in the F.E. model by the application of the quiet element method are increased by $22.8\ °\mathrm{C}$, $20.9\ °\mathrm{C}$ respectively, compared to the values that are obtained by the F.E. model considering the deposition of a single layer.

5.1.1.3 F.E. material elements

The single-pass weld layers of the simulated ten-layer weld deposit are modelled by rectangular material elements in the F.E. model, as defined in Table 3. Hence, the volume of the rectangular material elements in the F.E. model, is defined in Equation 26.

$$V_{Layer,\ F.E.\ model} = L_{Width} \cdot L_{Height} \cdot L_{Length} = 1{,}800\ mm^3 \quad [26]$$

$$V_{Layer,\ Actual} = A_{Electrode} \cdot t_{weld} \cdot WFS_{Electrode} = 1{,}739.96\ mm^3 \quad [27]$$

$A_{Electrode}$ Surface area of the electrode wire $[mm^2]$

t_{weld} Welding time of a single layer $[s]$

$WFS_{Electrode}$ Wire feed speed $[mm/s]$

The actual volume of electrode material that is deposited during a single-pass weld layer in the experiments, is defined in Equation 27. Indicating that the volume of the single-pass weld layers is modelled in the F.E. model by an accuracy of $96.5\ \%$,.

5.1.1.4 Mesh elements

In the F.E. model, tetrahedral mesh elements are used throughout the material domains constituting both the component and the simulated ten-layer weld deposit. A refined mesh size is used for the rectangular material elements representing the single-pass weld layers to account for the calculation of both the material deposition and the welding heat source. Also, in the material domains of the component base wall adjacent to the simulated ten-layer weld deposit and the interface between the component base wall and the substrate a refined mesh size is applied to account for the steep temperature gradients that are expected in these regions. Regarding the other material domains, a coarse mesh size is used for efficiency considerations.

The minimum and maximum element sizes are $2\ \mathrm{mm}$ and $16\ \mathrm{mm}$ respectively. Regarding the refined mesh elements that are used throughout the rectangular material elements consists of two elements in the y-direction while covering the layer height. An illustration of the mesh elements that are used throughout the material domains in the F.E model, is shown in Figure 49.

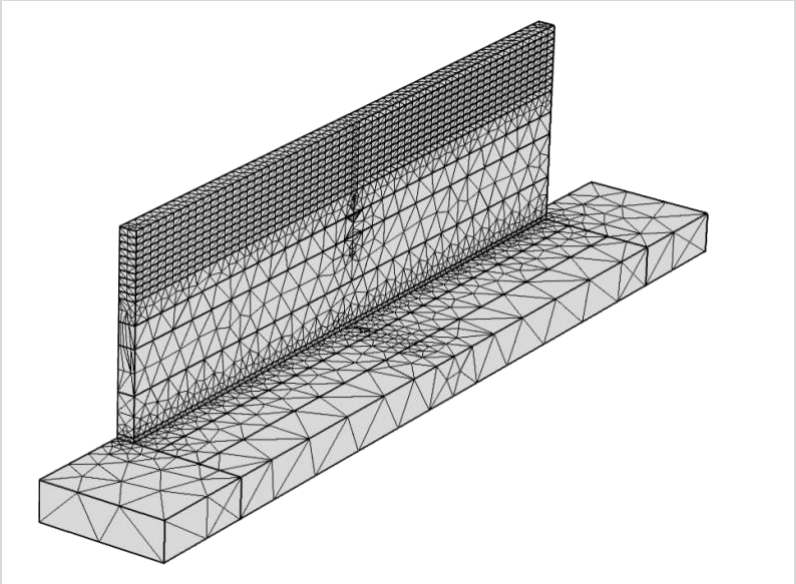

Figure 49: Mesh elements throughout the material domains in the F.E model.

5.1.2 F.E. model measurement accuracy

The measurement accuracy of the F.E. model is validated based on the smallest calibration error regarding the temperature values that are calculated at the temperature measurement points in the F.E. model and the corresponding temperature values that are recorded by the physically attached thermocouples in the experiments.

With regard to the thermal cycle peak temperatures, the value of the arc efficiency that is used in the F.E. model is validated based on the deposition of a single-pass weld layer. Regarding the thermal cycle through temperatures, the values of the calibration error that result from the application of the thermal boundary conditions as defined in the F.E. model is evaluated. Further, the effect of the thermal boundary conditions on the heat dissipation from the component to the environment is evaluated.

5.1.2.1 Thermal cycle peak temperatures

With regard to the thermal cycle peak temperatures that are calculated at the temperature measurement points in the F.E. model and recorded by the physically attached thermocouples in the experiments. It is found that the F.E. model temperature values are consistent for all test cases. While for the experimental temperature values a measurement error is introduced due to the varying position of the physically attached thermocouples in the experiments.

According to Figure B.1, the thermal cycle peak temperatures that are recorded by the physically attached thermocouple Tc-B1 in the experiments during the deposition of the first layer of the experimental fifteen-layer weld deposit, are equal to 1224 °C, 1337 °C, 1294 °C, 1108 °C and 1318 °C for the test cases 1 to 5 respectively. While, the corresponding thermal cycle peak temperatures that are calculated at the temperature measurement point Tc-B1 in the F.E. model during the deposition of the first layer of the simulated ten-layer weld deposit in the F.E. model, are equal to 1263 °C, 1263 °C, 1262 °C, 1260 °C and 1242 °C for the test cases 1 to 5 respectively. The consistency of the thermal cycle peak temperatures that are calculated in the F.E. model is explained by the fact that the positions of the temperature measurement points in the F.E. model are precisely defined and identical for all test cases, as indicated in Figure 28. The discrepancy with regard to the experimental temperature values is due to the varying position of the physically attached thermocouples in the experiments, inherent to the attachment method. As an illustration, the thermal cycle peak temperatures that are calculated during the deposition of the first layer of the simulated ten-layer weld deposit by the temperature measurement points in the F.E. model positioned at 29 mm, 28 mm and 27 mm, are equal to 1263 °C, 1196 °C and 945 °C respectively. Indicating that a deviancy of 1 mm from the position of the temperature measurement point can induce a measurement error up to 241 °C.

5.1.2.1.1 Arc efficiency

The actual arc power that is that is transferred by the welding heat source to both the deposited material and the component is described by the effective heat input, as defined in Equation 17. The heat dissipation due to radiation and convection heat losses at the welding arc is accounted for by the arc efficiency.

As described in Section 3.6.1, the arc efficiency is calibrated by fitting the thermal cycle peak temperatures that are calculated at the temperature measurement points the F.E. model and the corresponding temperature values that are recorded by the physically attached thermocouples in the experiments during the deposition of a single weld-pass layer on the component base wall. Considering the average instantaneous arc power, it is found that the thermal cycle peak temperatures that are calculated in the F.E. model are in good agreement with the experimental results when assuming an arc efficiency $\eta = 0.44$. However, the arc efficiency is equal to $\eta = 0.59$ and $\eta = 0.69$ considering the values of the calculated average arc power and the experimental average arc power respectively.

Regarding the arc efficiency that is calculated in the F.E. model considering the average instantaneous arc power, the thermal cycle peak temperatures match the experimental results when assuming an arc efficiency $\eta = 0.58$. Correspondingly, the values of the arc efficiency are equal to $\eta = 0.91$ and $\eta = 0.78$ considering the values of the calculated average arc power and the experimental average arc power respectively. The temperature values that are obtained during the deposition of a single-pass weld layer on the substrate, are shown in Figure 50.

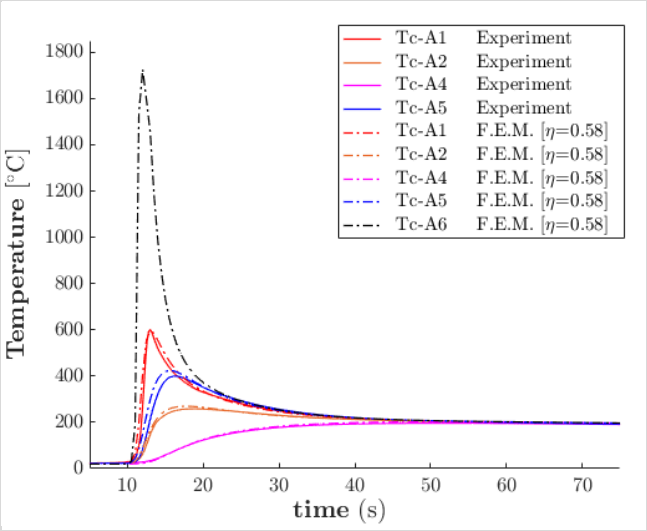

Figure 50: Temperature measurement values of a single-pass layer on the substrate; arc efficiency η=0.58.

According to literature, the arc efficiency that is calculated based on the values of the experimental average arc power during the deposition of a single weld-pass layer on the substrate is equal to $\eta = 0.85$, considering the process parameters that are used in the experiments [66]. Hence, it is found that the values of the arc efficiency that are calculated based on the values of the calculated average arc power and the experimental average arc power are of the same order as the arc efficiency that is reported in literature considering the deposition of a single weld-pass layer on the substrate.

With regard to the reduced values of the arc efficiency that are observed during the deposition of the single-pass weld layers on the component base wall compared to the values regarding the deposition of a single-pass weld layer on the substrate. According to Equation 17, the heat dissipation due to radiation and convection heat losses at the welding arc is accounted for by the arc efficiency. Hence, the reduced heat dissipation at the component base wall is accounted for by a reduced value of the arc efficiency regarding the deposition of a single weld-pass layer on the component base wall compared to the deposition of a single-pass weld layer on the substrate.

Concerning the lower values of the arc efficiency that are observed considering the average instantaneous arc power. The discrepancy between the values of the arc efficiency that are calculated considering the average instantaneous arc power and both the values considering the calculated average arc power and the experimental average arc power respectively is induced by an overestimation of the instantaneous current measurement values, as provided in Appendix A.4. According to Figure 20, the pulse current is expected in the range of $300\ \mathrm{A}$. While, the pulse current that is observed based on the instantaneous current measurement values is in the range of $500\ \mathrm{A}$. This effect is also expressed by the overestimation of the average current values that are calculated based on the instantaneous current measurement values compared to the experimental current values that are recorded by the power supply, as shown in Table 5.

5.1.2.2 Thermal cycle through temperatures

In the F.E. model it is assumed that with regard to the substrate and the component base wall, the heat dissipation from the component to the environment is accommodated by convection. While, the heat dissipation from the simulated ten-layer weld deposit to the environment is accommodated by radiation. The thermal boundary conditions that are defined in the F.E. model for the test cases 1 to 5, are shown Table 8.

The values of the calibration error that result from the application of the thermal boundary conditions as defined in the F.E. model for the five test cases, are shown in Figure 51. In Table 23, the values of the calibration error are provided that result from the application of the thermal boundary conditions as defined in the F.E. model for the test cases 1 to 5.

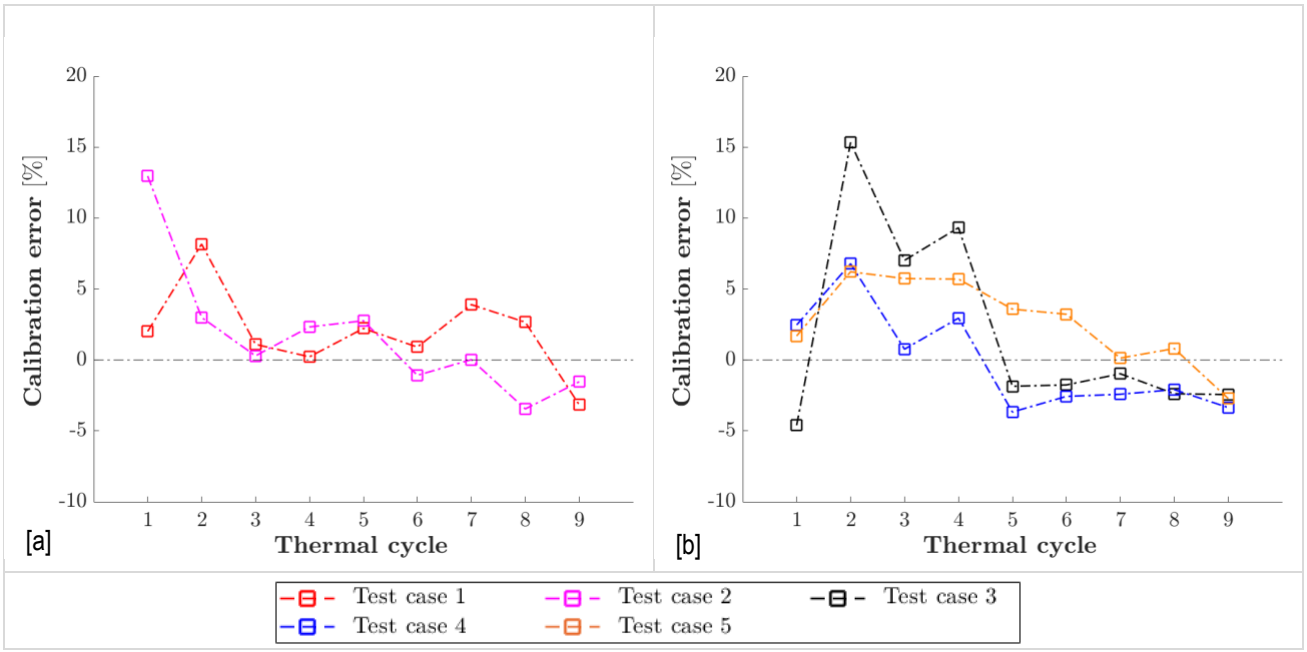

Figure 51: The values of the calibration error regarding the thermal cycle through temperatures that are recorded by the temperature measurement point Tc-B1 during the deposition of the ten-layer weld deposit for the test cases 1 to 5; indicated for the thermal cycles 1 to 9.

Table 23: The values of the calibration error regarding the thermal cycle through temperatures that are recorded by the temperature measurement point Tc-B1 for the test cases 1 to 5.

	Thermal cycle								
	1	**2**	**3**	**4**	**5**	**6**	**7**	**8**	**9**
Test case 1	+ 2.0 %	+ 8.2 %	+ 1.1 %	+ 0.2 %	+ 2.2 %	+ 0.9 %	+ 3.9 %	+ 2.7 %	− 3.2 %
Test case 2	+ 13.0 %	+ 3.0 %	+ 0.3 %	+ 2.3 %	+ 2.8 %	− 1.1 %	0.0 %	− 3.5 %	− 1.5 %
Test case 3	− 4.6 %	+ 15.3 %	+ 7.0 %	+ 9.3 %	− 1.9 %	− 1.8 %	− 1.0 %	− 2.4 %	− 2.4 %
Test case 4	+ 2.5 %	+ 6.8 %	+ 0.8 %	+ 3.0 %	− 3.7 %	− 2.6 %	− 2.4 %	− 2.1 %	− 3.4 %
Test case 5	+ 1.7 %	+ 6.2 %	+ 5.7 %	+ 5.7 %	+ 3.6 %	+ 3.2 %	+ 0.1 %	+ 0.8 %	− 2.7 %

According to Table 23, it is found that by the application of the appropriate thermal boundary conditions as defined in the F.E. model for the test cases 1 to 5, for all test cases the calibration error of the thermal cycle through temperatures corresponding to the temperature measurement point Tc-B1 are within the +/- 5.0 % error range, excluding the start and end-effects.

As shown in Figure 51, during the deposition of the layers 1 to 4, the experimental temperature values are overestimated by the F.E. temperature values, indicated by a positive calibration error. While, during the deposition of the layers 5 to 9, the experimental temperature values are underestimated by the F.E. temperature values, indicated by a negative calibration error. This observation is attributed to the contribution of the heat dissipation by radiative heat transfer at the outside surface areas of the simulated ten-layer weld deposit. During the deposition of the layers 1 to 4, the heat dissipation by radiative heat transfer at the outside surface areas of the deposited layers is underrated by the applied boundary conditions in the F.E. model. While, during the deposition of the layers 6 to 10, the heat dissipation by radiative heat transfer at the outside surface areas of the deposited layers is overrated by the applied boundary conditions in the F.E. model.

In addition to the effect of the heat dissipation that is accommodated by radiative heat transfer at the outside surface areas of the simulated weld deposit. The contribution of the heat dissipation by convective heat transfer at the outside surface areas of the component base wall to the environment is discussed. The values of the calibration error that result from the application of the radiative boundary condition BC I regarding the thermal cycle through temperatures that are recorded by the temperature measurement points Tc-B1 to Tc-B4 for the test cases 1 to 5, are provided in Appendix F.1.

When comparing the values of the calibration error that are found for the test cases 1 to 5. It is observed that for test case 1, the values of the calibration error follow the general trend corresponding to the heat dissipation that is dominated by radiative heat transfer at the outside surface areas of the simulated weld deposit. For test case 2, the values of the calibration error regarding the temperature values that are recorded by the temperature measurement points Tc-B2 to Tc-B4 diverge from the fifth thermal cycle onward. The experimental temperature values that are recorded by the temperature measurement point Tc-B4 are overestimated by the F.E. model temperature values. While, the experimental temperature values that are recorded by the temperature measurement point Tc-B1 are underestimated by the F.E. model temperature values. With regard to the temperature values that are recorded by the temperature measurement points Tc-B2 and Tc-B3, intermediate values of the calibration error are found. The positive calibration error that is observed regarding the temperature values that are recorded by the temperature measurement point Tc-B4 during the thermal cycles 5 to 9, is attributed to the underrated heat dissipation at the outside surface areas of the component base wall. Indicating that from the fifth thermal cycle onward, the heat dissipation by convective heat transfer at the outside surface areas of the component base wall is underrated by the applied boundary conditions.

For the test cases 3 and 4, the largest values of the calibration error regarding the thermal cycle through temperatures that are recorded by the temperature measurement points Tc-B1 are observed regarding the thermal cycles 2 to 4. Further it is observed that the values of the calibration error regarding the thermal cycle through temperatures of the thermal cycles 2 to 4 corresponding to test case 4 are lower compared to the values that are found for test case 3. According to Table 23, for test case 3, the values of the calibration error regarding the thermal cycle through temperatures of the thermal cycles 2, 3 and 4 are equal to +15,3 %, +7,0 %, and +9,3 % respectively. While, the corresponding values of the calibration error for test case 4 are equal to +6,8 %, +0,8 %, and +3,0 % respectively. The discrepancy that is observed for the test cases 3 and 4, with regard to the values of the calibration error regarding the thermal cycle through values of the thermal cycles 2 to 4 is explained by the mode of heat transfer from the component to the environment. For both test cases 3 and 4, the heat dissipation from the component to the environment is dominated by the convective heat transfer at the outside surface area D of the component base wall. As shown in Table 8, the outside surface area D is located at 15 mm from the fifteen-layer weld deposit. To support the convective heat transfer at the outside surface area D, the heat that is introduced by the welding heat source must be dissipated throughout the component by conductive heat transfer. Since the cooing stage of test case 4 is increased by 20 s with respect to test case 3, the heat that is introduced by the welding heat source is dissipated more effectively throughout the component during the cooling stage of test case 4 to

support the convective heat transfer at the outside surface area D. Indicated by the lower values of the calibration error corresponding to test case 4 compared to the values that are found for test case 3, regarding the thermal cycle through temperatures of the thermal cycles 2 to 4. With regard to the thermal cycles 5 to 9, the values of the calibration error corresponding to both test the cases 3 and 4 are of the same order. As shown in Figure 34, for both the test cases 3 and 4, the equilibrium component mean temperature is reached from the fifth thermal cycle onward. Indicating that the heat dissipation by convective heat transfer at the outside surface area D becomes effective when the equilibrium component mean temperature is reached.

With regard to test case 5, it is observed that the application of the radiative boundary condition BC I is sufficient to keep the calibration error within the +/- 5.0 % error range. This is explained by the contribution of the heat dissipation by convective heat transfer at the outside surface area F of the component base wall compared to the radiative heat transfer at the outside surface areas of the weld deposit.

5.1.2.2.1 Thermal boundary conditions

The effect of the thermal boundary conditions on the heat dissipation from the component to the environment is evaluated for the test cases 1 and 5.

According to the Fourier's law of heat conduction, the temperature gradients in the x- and z-direction are associated with the heat dissipation throughout the component accommodated by conduction, as defined in Equation 12. While, the temperature gradient in the y-direction is associated with the heat dissipation from the component to the environment accommodated by both convection and radiation from the outside surface areas of the component, as defined in Equation 13 and Equation 14. The values of the convective and radiative heat fluxes per unit outside surface area as a function of the surface temperature, are shown in Figure 52.

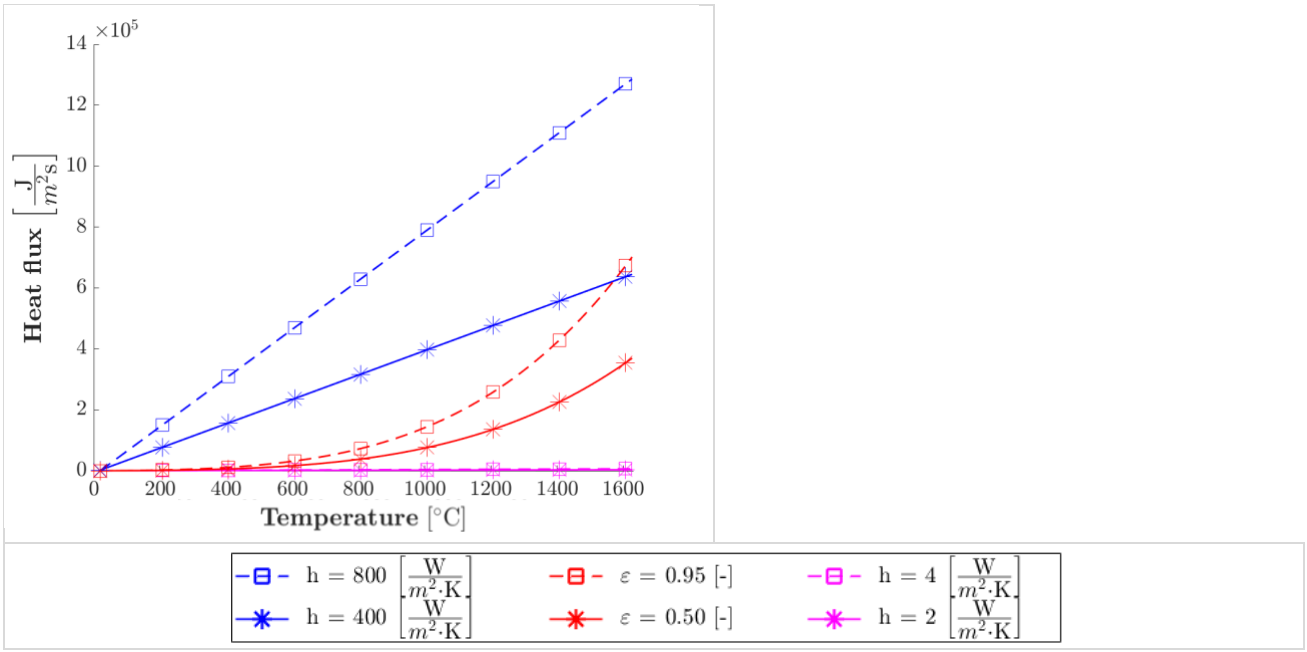

Figure 52: Component mean temperature; based on the thermal cycle through temperatures calculated at the temperature measurement points Tc-B1, Tc-B2, Tc-B3 and Tc-B4 in the F.E. model.

The values of the convective and radiative heat transfer at the outside surface areas of the component, are defined by the product of the corresponding heat flux values and the relevant outside surface areas of the component. The heat dissipation throughout the component is accommodated by conduction, expressed by the conductive heat transfer. The conductive heat transfer is defined by the product of the conductive heat flux value and the relevant cross-sectional area.

The temperature gradients in the y- and z-direction that are observed during the deposition of the first and tenth layer of the simulated weld deposit for the test cases 1 and 5, are provided in Appendix D.

The relevant outside surface areas regarding the component base wall and the layers of the simulated weld deposit are expressed in Equation 28.

$$A_{Layer,\ Outside\ surface} = H_{Layer} \cdot L_{Layer} = 225\ mm^2 \quad [28.a]$$

$$A_{Layer,\ Top\ surface} = W_{Layer} \cdot L_{Layer} = 600\ mm^2 \quad [28.b]$$

$$A_{Domain\ D,\ Outside\ surface} = H_{Domain\ D} \cdot L_{Layer} = 2250\ mm^2 \quad [28.c]$$

$$A_{Domain\ E,\ Outside\ surface} = H_{Domain\ E} \cdot L_{Layer} = 750\ mm^2 \quad [28.d]$$

$$A_{Domain\ F,\ Outside\ surface} = H_{Domain\ F} \cdot L_{Layer} = 1500\ mm^2 \quad [28.e]$$

The dominant modes of heat transfer during the deposition of the first and tenth layer of the simulated ten-layer weld deposit is evaluated for the test cases 1 and 5.

For test case 1, it is observed that during the deposition of both the first and tenth layer of the simulated ten-layer weld deposit, the heat dissipation from the component to the environment is dominated by the radiative heat transfer at the outside surface areas of the simulated weld deposit. During the deposition of the first layer, the maximum temperature gradient in the y-direction is observed at the outside surface area of the first layer of the ten-layer weld deposit. As indicated in Appendix D.1, the temperature of the outside surface area of the first layer is equal to 900 °C at 4s after the passage of the welding heat source during the deposition of the first layer. According to Figure 52, the radiative heat flux is equal to $0.1\ \left[\frac{W}{mm^2}\right]$ for surface temperatures of 900 °C and an emissivity of 0.95. Indicating that for test case 1, the heat dissipation by radiative heat transfer at the outside surface area of the first layer evaluated at 4s after the passage of the welding heat source during the deposition of the first layer is equal to 22.5 W, as expressed in Equation 29.

$$Q_{rad,\ Outside\ surface\ Layer} = q_{rad} \cdot A_{Layer,\ Outside\ surface} = 22.5\ W \quad [29]$$

Similarly, the heat dissipation by radiative heat transfer at the top surface area of the first layer, at 4s after the passage of the welding heat source during the deposition of the first layer, is equal to 61.6 W. Indicating that for test case 1, the total heat dissipation by radiative heat transfer at 4s after the passage of the welding heat source during the deposition of the first layer is equal to 84.1 W.

For test case 5, it is found that during the deposition of the first layer, the heat dissipation from the component to the environment is dominated by the convective heat transfer at the outside surface area F of the component base wall. While during the deposition of the tenth layer of the simulated weld deposit. It is observed that the heat dissipation from the component to the environment is accommodated by both the radiative heat transfer at the outside surface areas of the simulated ten-layer weld deposit and convective heat transfer at the outside surface area F of the component base wall. During the deposition of the first layer, the maximum temperature gradient in the y-direction is observed at the outside surface area F. As indicated in Appendix D.2, at 4s after the passage of the welding heat source during the deposition of the first layer, the temperature of the outside surface of the area F is equal to 650 °C. The convective heat flux is equal to $0.5\ \left[\frac{W}{mm^2}\right]$, considering a surface temperature of 650 °C and a convective heat transfer coefficient of $800\ \left[\frac{W}{m^2K}\right]$, according to Figure 52. Indicating that for test case 5, at 4s after the passage of the welding heat source during the deposition of the first layer, the heat dissipation by convective heat transfer at the outside surface area F is equal to 750 W, as expressed in Equation 30.

$$Q_{conv,\ Domain\ F} = q_{conv} \cdot A_{Domain\ F} = 750\ W \quad [30]$$

Similarly, during the deposition of the tenth layer, the values of the radiative heat transfer at the outside surface areas of the simulated ten-layer weld deposit and the convective heat transfer at the outside surface area F of the component base wall are equal to 170 W and 350 W respectively, at 1 s after the passage of the welding heat source during the deposition of the tenth layer. The corresponding values at 20 s after the passage of the welding heat source during the deposition of the tenth layer, are equal to 30 W and 300 W respectively. Indicating that during the deposition of the tenth layer, the contribution of the heat dissipation accommodated by convective heat transfer at the outside surface area F of the component base wall is increased from a factor 2 to a factor 10 compared to the radiative heat transfer at the outside surface areas of the simulated ten-layer weld deposit.

While for test case 1, the corresponding values of the radiative heat transfer at the outside surface areas of the simulated ten-layer weld deposit and the convective heat transfer at the outside surface area F of the component base wall during the deposition of the tenth layer are equal to 470 W and 3 W respectively, at 1 s after the passage of the welding heat source. The corresponding values at 20 s after the passage of the welding heat source during the deposition of the tenth layer, are equal to 80 W and 3 W respectively.

The temperature gradient in the y-direction, calculated during the deposition of the tenth layer for the test cases 1 and 5, is shown in Figure 53 and Figure 54 respectively.

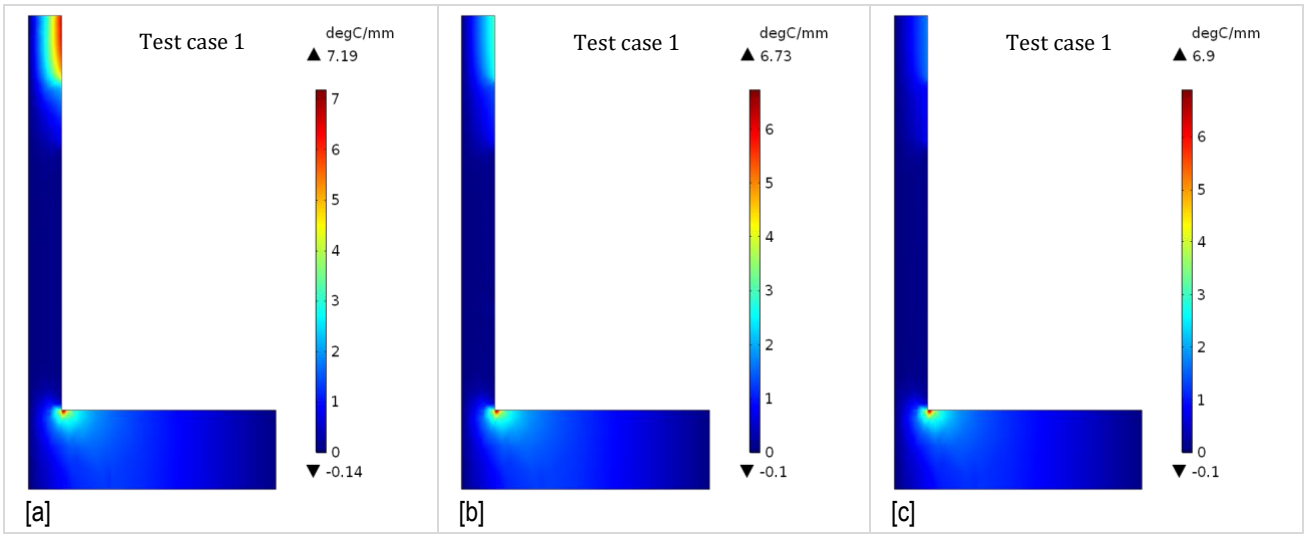

Figure 53: Temperature gradient in the Y-direction calculated at the mid-point cross-section during the deposition of the tenth layer. [a] 4s after the passage of the heat source; [b] 10s after the passage of the heat source; [c] 20s after the passage of the heat source.

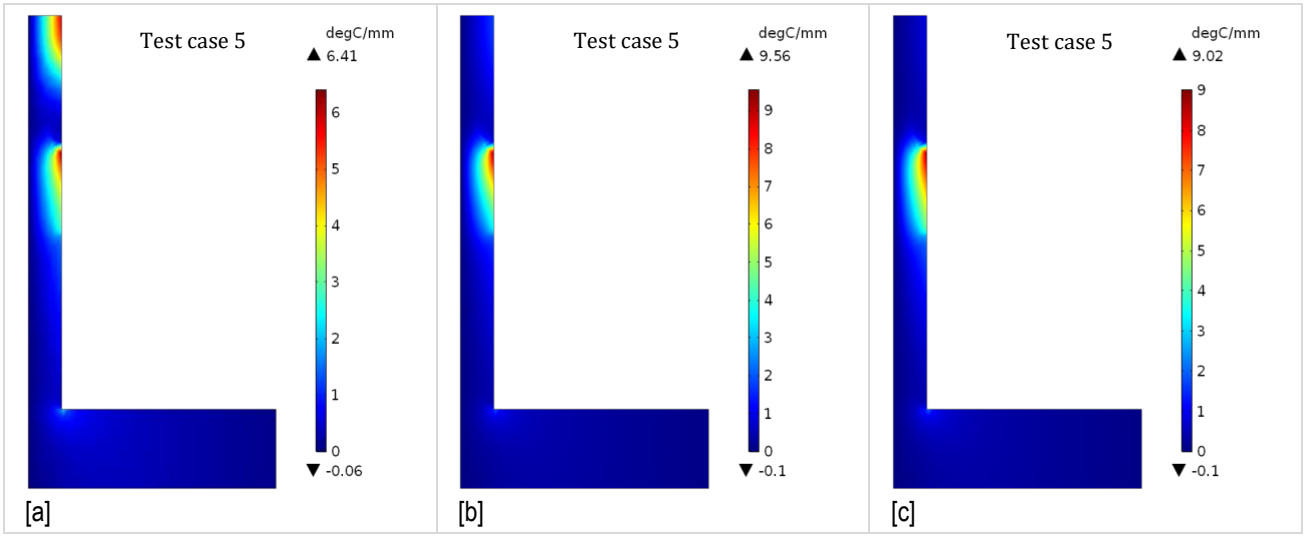

Figure 54: Temperature gradient in the Y-direction calculated at the mid-point cross-section during the deposition of the tenth layer. [a] 4s after the passage of the heat source; [b] 10s after the passage of the heat source; [c] 20s after the passage of the heat source.

6 Conclusions and recommendations

6.1 Conclusions

In this research, a F.E. model is presented to provide a thermal analysis of the wire and arc additive manufacturing process. An important quality of the F.E. model that is presented in this research is to describe the temperature field that is experienced by the deposited material in the wire and arc additive manufacturing process. In contrast to the traditional method of monitoring the substrate temperature, the F.E. model allows to describe the temperature field that is experienced by the deposited material constituting both the multilayer weld deposit and the component.

Two cooling methods are proposed to control the heat dissipation from the component to the environment based on the application of an interlayer waiting time and immersing the component into a cooling medium. The effect of the cooling methods on the temperature field and the resulting microstructure of the deposited material is evaluated by reviewing variations of the cooling methods considering five test cases, whereby a multilayer weld deposit is deposited on top of a component base wall. The test case are defined as: natural cooling; interlayer waiting time of 40s (1), natural cooling; interlayer waiting time of 80s (2), active substrate cooling; interlayer waiting time of 20s (3), active substrate cooling; interlayer waiting time of 40s (4), active component cooling; interlayer waiting time of 40s (5).

The results show a significant effect of the cooling methods on the temperature field that is experienced by the material constituting both the component and the multilayer weld deposit. Indicating that the cooling methods that are proposed in this research are effective to control the temperature field that is experienced by the component during the deposition process of the wire and arc additive manufacturing process.

6.1.1 F.E. model

The F.E. model allows to describe the effect of the cooling methods on the microstructure of the deposited material in terms of the thermal characteristics including the temperature distribution, the locally attained temperature values, the cooling rates, and the temperature gradients throughout the component.

As a general trend, the component mean temperatures corresponding to the five test cases increase during the deposition process of the multilayer weld deposit due to the heat accumulation in the component. Additionally, the thermal cycle peak temperatures of the subsequent thermal cycles decrease, as the distance between the welding heat source and the temperature measurement point increases during the deposition process proceeds.

For a detailed description of the results, reference is made to Section 4.2.7 and Section 4.3.5. The most important conclusions are summarized:

- The equilibrium component mean temperatures that are calculated in the F.E. model for the test cases 1 to 5 are about $487.2\,°C$, $386.4\,°C$, $355.0\,°C$, $282.3\,°C$, $122.4\,°C$ respectively. Indicating that the equilibrium component mean temperatures corresponding to the test cases 2 to 5 are reduced by $21.6\,\%$, $23.6\,\%$, $41.2\,\%$ and $74.9\,\%$ respectively, compared to the reference test case 1.
- The thermal cycle peak temperatures that are calculated in the F.E. model attain the highest values for test case 1 followed by the test cases 3, 2, 4 and 5 respectively.
- The thermal cycle through temperatures that are calculated in the F.E. model for the test cases 1 to 4 attain equilibrium temperature values in the order of $521.9\,°C$, $399.8\,°C$, $522.5\,°C$ and $375.0\,°C$ respectively, the thermal cycle through temperatures corresponding to test case 5 are in the range of $186.9\,°C$ to $234.8\,°C$.
- The average cooling rates that are calculated in the F.E. model during the successive cooling stages attain values in the order of -30.5 $^{°C}/_{S}$ for the test cases 1 to 4, and -35.5 $^{°C}/_{S}$ for test case 5 respectively.

The values of the temperature gradient in the z-direction corresponding to the five test cases are significant higher compared to the corresponding values in the y- and z-direction. Indicating that the dominant mode of heat dissipation is accommodated by conduction throughout the component in the building direction.

- The temperature gradient in the z-direction that is calculated in the F.E. model for test case 1 is reduced during the deposition of the multilayer weld deposit. While, the maximum temperature gradient in the y-direction is increased as the deposition process proceeds.
- The temperature gradient in the z-direction that is calculated in the F.E. model for test case 5 is maintained during the deposition process of the multilayer weld deposit.

Indicating that in the case of natural component cooling, the heat dissipation that is accommodated by conduction throughout the component in the building direction is deteriorated during the deposition process of the multilayer weld deposit due to the increased heat accumulation in the case of natural component cooling. While, in the case of active component cooling, the heat dissipation that is accommodated by conduction throughout the component in the building direction remains effective during the deposition process of the multilayer weld deposit.

6.1.2 Microstructure

The most favourable microstructure is obtained by the application of active substrate cooling in combination with a reduced interlayer waiting time. According to the experimental results, a uniform microstructural morphology composed of bainite and acicular ferrite microstructural constituents is observed. Attributed to the reduced component mean temperature that prohibits the substitutional diffusion of alloying elements, recrystallization, and grain growth. The chaotic arrangement of the ferrite plates provides superior mechanical properties, in particular toughness. Further, productivity of the wire and arc additive manufacturing process is increased due to the reduced interlayer waiting time compared to the reference process.

The natural cooling in combination with the reference interlayer waiting time as defined in test case 1 results in a predominantly ferritic microstructure regarding the material constituting the multilayer weld deposit. Although a uniform microstructural morphology is observed, the formation of a coarse-grained microstructure is considered detrimental for the mechanical properties in terms of a lower strength, and a reduced corrosion resistance at normal operating temperatures.

With regard to the cooling methods as defined in the test cases 2, 4 and 5, considering natural cooling in combination with an increased interlayer waiting time and both active substrate cooling and active component cooling in combination with the reference interlayer waiting time result in the reduction of the temperature values respectively. The reduced thermal cycle through temperatures result in the formation of martensite constituents throughout the material constituting the multilayer weld deposit. The presence of martensite constituents is considered unfavourable, because of the internal stresses that result of the high densities of dislocations accommodating the a-thermal transformation from austenite. The stress induced deformations result in a poor dimensional accuracy, a poor surface finish and the loss of the structural integrity of the component. Further, the cooling methods defined in the test cases 2, 4 and 5 result in the formation of an anisotropic microstructural morphology regarding the material constituting both the middle segment and the bottom segment of the multilayer weld deposit. According to the experimental results, a layer band morphology of alternating regions of fine-grained and coarse-grained microstructures is formed due to the movement of the welding heat source in the building direction. The most pronounced layer band morphology is observed for test case 5 considering active component cooling in combination with the reference interlayer waiting time.

6.2 Recommendations

The recommendations focus on the topics that are investigated in this research. Aside from the many challenges and opportunities that need to be investigated to further improve the wire and arc additive manufacturing process.

6.2.1 F.E. Model

The F.E. model that is presented in this research can be customized to study modifications of the wire and arc additive manufacturing process including deposition patterns, component geometries and cooling strategies. In addition, the thermal analysis of the wire and arc additive manufacturing based on the F.E. method can be extended to describe the effect of the locally attained temperature field on the microstructure development and mechanical properties in a quantitative manner, as proposed in literature [67], [68].

A thermo-mechanical analysis of the wire and arc additive manufacturing process can be incorporated in the F.E. model by considering the mechanical properties of the deposited material [69], [70]. As indicated, the components that are produced by the wire and arc additive manufacturing process are prone to high residual stresses and distortions due to the high heat input and the high deposition rates that are associated with the arc welding heat source. Considering the mechanical properties of the deposited material allows to mitigate the thermal induced residual stresses and distortions that result from the deposition process [71], [72].

6.2.2 Cooling method

In this research, the heat dissipation from the component to the environment is increased by immersing the component into a cooling medium for practical considerations. However, this cooling method is complicated to be applied on existing machine tools [73]. Moreover, the effectiviness of this method decreases during the building process of large components as the distance between the heat source and the cooling medium is increased.

An alternative method to increase the heat dissipation from the component to the environment is the localized cooling of the deposited material through the application of a thermoelectric, or a cooling gas [17] [74] [75] [76]. An important advantage of this cooling strategy is that it allows to continuously control the heat transfer condition close to the weld pool throughout deposition process. Accordingly, the localized cooling methods can be effectively applied to control the weld bead geometry and solidification conditions during the deposition process [77]. Since the weld bead geometry is a critical parameter in the wire and arc additive manufacturing process, the geometric accuracy, the material utilization and the productivity can be significantly improved through the application of a localized cooling strategy [17], [47]. In addition, it has been demonstrated that the localized cooling through the application of a cooling gas can be effectively applied to control the resulting microstructure of the deposited material constituting the component in the wire and arc additive manufacturing process [74], [75].

6.2.3 Microstructure

In this research, the optical microscopy and hardness measurements are used as techniques to describe the microstructure of the deposited material and to evaluate the effectiveness of the F.E. model to describe the effect of the cooling methods on the microstructure of the deposited material in terms of the thermal characteristics. Although the optical microscopy is a practical technique to describe the microstructure of the deposited material in terms of the microstructural morphology and the microstructural constituents. Additional microstructural analysis is required to quantify both the average grain size and the distribution of the microstructural constituents throughout the deposited material [78]. Furthermore, additional microstructural analysis allows to describe the effect of the cooling methods on the mechanical properties of the deposited material that constitutes the component in the wire and arc additive manufacturing [79].

Bibliography

[1] T. Rodrigues, V. Duarte, R. Miranda, T. Santos en J. Oliveira, „Current Status and Perspectives on Wire and Arc Additive Manufacturing (WAAM),” Materials, 12, 1121, MDPI, 2019. [Online]. Available: doi:10.3390/ma12071121.

[2] D. Jafari, T. Vaneker and I. Gibson, “Wire and arc additive manufacturing: Opportunities and challenges to control the quality and accuracy of manufactured parts,” *Materials and Design,* vol. 202, Article 109471, 2021.

[3] J. Liu, Y. Xu, Y. Ge, Z. Hou and S. Chen, “Wire and arc additive manufacturing of metal components: a review of recent research developments,” *The International Journal of Advanced Manufacturing Technology,* vol. 111, pp. 149–198, 2020.

[4] D. Ding, Z. Pan, D. Cuiuri and H. Li, “Wire-feed additive manufacturing of metal components: technologies, developments and future interests,” *The International Journal of Advanced Manufacturing Technology,* vol. 81, pp. 465–481, 2015.

[5] O. Yilmaz and A. Ugla, “Shaped metal deposition technique in additive manufacturing: A review,” *Proceedings of the Institution of Mechanical Engineers, Part B: Journal of Engineering Manufacture,* vol. 230, no. 10, pp. 1781-1798, 2016.

[6] “WAAM for manufacturing,” MX3D - Robotic 3D metal printing, [Online]. Available: https://mx3d.com/industries/manufacturing/.

[7] F. Martina, *Investigation of methods to manipulate geometry, microstructure and mechanical properties in titanium large scale Wire+Arc Additive Manufacturing,* Cranfield University: PhD Thesis , 2014.

[8] A. Garcia-Colomo, D. Wood, F. Martina and S. Williams, „A comparison framework to support the selection of the best additive manufacturing process for specific aerospace applications,” *International Journal of Rapid Manufacturing,* vol. 9, no. Issue 2-3, pp. 194-211, 2020.

[9] H. Zhao, G. Zhang, Z. Yin and L. Wu, “A 3D dynamic analysis of thermal behavior during single-pass multi-layer weld-based rapid prototyping,” *Journal of Materials Processing Technology,* vol. 211, no. 3, pp. 488–495, 2011.

[10] B. Wu, D. Ding, Z. Pan, D. Cuiuri, H. Li, J. Han and Z. Fei, “Effects of heat accumulation on the arc characteristics and metal transfer behavior in Wire Arc Additive Manufacturing of Ti6Al4V,” *Journal of Materials Processing Technology,* vol. 250, pp. 304-312, 2017.

[11] J. Xiong, R. Li, Y. Lei and H. Chen, “Heat propagation of circular thin-walled parts fabricated in additive manufacturing using gas metal arc welding,” *Journal of Materials Processing Technology,* vol. 251, pp. 12-19, 2018.

[12] D. Ding et al., „Wire-feed additive manufacturing of metal components: technologies, developments and future interests,” *Int J Adv Manuf Technol,* vol. 81, pp. 465-481, 2015.

[13] X. Lu, Y. Zhou, X. Xing, L. Shao, Q. Yang en S. Gao, „Open-source wire and arc additive manufacturing system: formability, microstructures, and mechanical properties,” *The International Journal of Advanced Manufacturing Technology,* vol. 93, p. 2145–2154, 2017.

[14] F. Montevecchi, G. Venturini, N. Grossi, A. Scippa and G. Campatelli, “Idle time selection for wire-arc additive manufacturing: A finite element-based technique,” *Additive Manufacturing,* vol. 21, pp. 479–486, 2018.

[15] Y. Lei, J. Xiong and R. Li, “Effect of inter layer idle time on thermal behavior for multi-layer single-pass thin-walled parts in GMAW-based additive manufacturing,” *The International Journal of Advanced Manufacturing Technology,* vol. 96, p. 1355–1365, 2018.

[16] P. Henckell et al., „The Influence of Gas Cooling in Context of Wire Arc Additive Manufacturing - A Novel Strategy of Affecting Grain Structure and Size,” in *TMS 2017 146th Annual Meeting & Exhibition Supplemental Proceedings*, San Diego, 2017.

[17] F. Li, S. Chen, J. Shi, Y. Zhao and H. Tian, “Thermoelectric Cooling-Aided Bead Geometry Regulation in Wire and Arc-Based Additive Manufacturing of Thin-Walled Structures,” *Applied Sciences,* vol. 8(2), 2018.

[18] X. Bai, H. Zhang and G. Wang, „Improving prediction accuracy of thermal analysis for weld-based additive manufacturing by calibrating input parameters using IR imaging,” *The International Journal of Advanced Manufacturing Technology,* vol. 69, no. 5-8, pp. 1087–1095, 2013.

[19] J. Nadzam, Gas Metal Arc Welding Guidelines, Cleveland, Ohio: The Lincoln Electric Company, 2014.

[20] K. Chaudhary, “A Study on Metal Transfer Mechanism in Gas Metal Arc Welding,” *International Journal of Scientific Research in Science, Engineering and Technology,* vol. 3, no. 8, pp. 82-93, 2017.

[21] P. Ghosh, Pulse Current Gas Metal Arc Welding; Characteristics, Control and Applications, Singapore: Springer, 2017.

[22] M. Bosworth, „Effective Heat Input in Pulsed Current Gas Metal Arc Welding with Solid Wire Electrodes,” *Supplement to the Welding Journal, American Welding Society and the Welding Research Council,* pp. 111s-117s, May 1991.

[23] D. Harwig, “Arc behaviour and metal transfer of the VP-GMAW process,” PhD Thesis, Cranfield University, 2003.

[24] J. Verhoeven, „Appendix A: Temperature Measurement,” in *Steel Metallurgy for the Non-Metallurgist*, Ohio, ASM International, 2007, pp. 201-207.

[25] B. Perrin, „The basics of Thermocouples,” Circuit Cellar, December 1999. [Online]. Available: https://zeus.phys.uconn.edu/wiki/images/The_Basics_of_Thermocouples.pdf.

[26] „Basics of non contact temperature measurement,” Micro-Epsilon, [Online]. Available: https://www.micro-epsilon.com/download/products/dat--infrared-basics--en.pdf#zoom=Fit.

[27] A. Mills, Basic Heat and Mass Transfer, Los Angeles: Prentice Hall, Inc., 1999.

[28] „DL716 Digital Scope: User's Manual,” Yokogawa Electric Corporation, January 1999. [Online]. Available: https://xdevs.com/doc/Yokogawa/dl716_234921880-dl716-manual-im701830-01e-011.pdf.

[29] G. den Ouden and M. Hermans, Welding Technology, Delft: VSSD, 2009.

[30] P. Kah, R. Suoranta and J. Martikainen, “Advanced gas metal arc welding processes,” *The International Journal of Advanced Manufacturing Technology,* vol. 67, pp. 655–674, 2013.

[31] P. van Lent, Handboek MIG/MAG-Lassen, Voorschoten: Nederlands Instituut voor Lastechniek, 1992.

[32] D. Iordachescu and L. Quintino, “Steps toward a new classification of metal transfer in gas metal arc welding,” *Journal of Materials Processing Technology,* vol. 202, no. 1-3, pp. 391-397, 2008.

[33] P. Palani and N. Murugan, “Selection of parameters of pulsed current gas metal arc welding,” *Journal of Materials Processing Technology,* vol. 172, no. 1, pp. 1-10, 2006.

[34] C. Wu, D. Zou and J. Gao, “Determining the critical transition current for metal transfer in gas metal arc welding (GMAW),” *Frontiers of Materials Science in China,* vol. 2, no. 4, pp. 397-401, 2008.

[35] C. Wu, M. Chen and Y. Lu, “Effect of current waveforms on metal transfer in pulsed gas metal arc welding,” *Measurement Science and Technology,* vol. 16, pp. 2459-2465, 2005.

[36] A. Joseph, D. Farson, D. Harwig en R. Richardson, „Measurement and calculation of arc power and heat transfer efficiency in pulsed gas metal arc welding,” *Science and Technology of Welding & Joining,* vol. 8, nr. 6, pp. 400-436, 2003.

[37] B. Guo, J. Xu, L. Cui and Q. Wang, “Process, Microstructure and Mechanical Properties of X90 Pipeline Steel,” *Materials Science Forum,* vol. 850, pp. 894-898, 2016.

[38] G. Krauss, Steels: Processing, Structure, and Performance (Second Edition), ASM International, 2015.

[39] K. Easterling, Introduction to the Physical Metallurgy of Welding (Second Edition), Oxford: Butterworth-Heinemann, 1992.

[40] Böhler Welding Product Catalogue, Voestalpine; https://www.voestalpine.com/welding/, 2014.

[41] “S355JR Steel Material Properties & Chemical Composition,” Weltstahl, [Online]. Available: https://www.theworldmaterial.com/s355jr-steel/.

[42] G. Totten [editor], Steel Heat Treatment handbook: Metallurgy and Technologies, Portland, Oregon: Talyor and Francis, 2006.

[43] Y. Shao, C. Liu, Z. Yan, H. Li and Y. Liu, “Formation mechanism and control methods of acicular ferrite in HSLA steels: A review,” *Journal of Materials Science & Technology,* vol. 34, no. 5, pp. 737-744, 2018.

[44] S. Babu, “The mechanism of acicular ferrite in weld deposits,” *Current Opinion in Solid State and Materials Science,* vol. 8, pp. 267–278, 2004.

[45] Y. Liu, A. Ma and B. Feng, “Simulated HAZ Continuous Cooling Transformation of X90 Pipeline Steel,” *Materials Science Forum,* vol. 850, pp. 905-909, 2016.

[46] K. Andrews, “Empirical formulae for the calculation of some transformation temperatures,” *Journal of the Iron and Steel Institute,* vol. 203, pp. 721-727, 1965.

[47] J. Goldak, A. Chakravarti and M. Bibby, “A New Finite Element Model for Welding Heat Sources,” *Metallurgical Transactions B,* vol. 15B, pp. 299-305, 1984.

[48] F. Montevecchi, G. Venturini, A. Scippa and G. Campatelli, “Finite element modelling of Wire-Arc-Additive-Manufacturing process,” in *5th CIRP Global Web Conference Research and Innovation for Future Production*, 2016.

[49] D. Radaj, Heat Effects of Welding: Temperature field, Residual stress, Distortion, Berlin: Springer-Verlag, 1992.

[50] D. Poirier and G. Geiger, Transport Phenomena in Materials Processing, Pennsylvania: The Minerals, Metals and Materials Society, 1994.

[51] J. Goldak, M. Bibby, J. Moore, R. House and B. Patel, “Computer Modeling of Heat Flow in Welds,” *Metallurgical Transactions B,* vol. 17B, pp. 587-600, 1986.

[52] J. Ding, P. Colegrove, J. Mehnen, S. Ganguly, P. Sequeira Almeida, F. Wang en S. Williams, „Thermo-mechanical analysis of Wire and Arc Additive Layer Manufacturing process on large multi-layer parts,” *Computational Materials Science ,* vol. 50, nr. 12, pp. 3315-3322, 2011.

[53] P. Peyre, P. Aubrey, R. Fabbro, R. Neveu en A. Longuet, „Analytical and Numerical Modelling of the direct metal deposition laser process,” *Journal of Physics D: Applied Physics ,* vol. 41, nr. 025403, pp. 10, 2008.

[54] P. Michaleris, “Modeling metal deposition in heat transfer analyses of additive manufacturing processes,” *Finite Elements in Analysis and Design,* vol. 86, pp. 51-60, 2014.

[55] M. Qureshi, “Analysis of Residual Stresses and Distortions in circumferentially welded thin-walled cylinders,” PhD Thesis, National University of Sciences and Technology; Rawalpindi, Pakistan, 2008.

[56] J. Ding, “Thermo-mechanical Analysis of Wire and Arc Additive Manufacturing Process,” PhD Thesis, Cranfield University, 2012.

[57] “Overall Heat Transfer Coefficients for Fluids - Heat Exchanger Surface Combinations,” EngineeringToolbox, [Online]. Available: https://www.engineeringtoolbox.com/overall-heat-transfer-coefficients-d_284.html.

[58] Z. Hu, X. Qin, T. Shao and H. Liu, “Understanding and overcoming of abnormity at start and end of the weld bead in additive manufacturing with GMAW,” *The International Journal of Advanced Manufacturing Technology,* vol. 95, pp. 2357–2368, 2018.

[59] S. Kelly and S. Kampe , “Microstructural Evolution in Laser-Deposited Multilayer Ti-6Al-4V Builds: Part I. Microstructural Characterization,” *Metallurgical and Materials Transactions A,* vol. 35, pp. 1861–1867, 2004.

[60] S. Kelly and S. Kampe, “Microstructural Evolution in Laser-Deposited Multilayer Ti-6Al-4V Builds: Part II. Thermal Modeling,” *Metallurgical and Materials Transactions A,* vol. 35, pp. 1869–1879, 2004.

[61] H. Zhao, G. Zhang, Z. Yin en L. Wu, „A 3D dynamic analysis of thermal behavior during single-pass multi-layer weld-based rapid prototyping,” *Journal of Materials Processing Technology,* vol. 211, pp. 488-495, 2011.

[62] W. Zhao, W. Wang, S. Chen and J. Qu, “Effect of simulated welding thermal cycle on microstructure and mechanical properties of X90 pipeline steel,” *Materials Science and Engineering A,* vol. 528, no. 24, pp. 7417–7422, 2011.

[63] I. Nuruddin, “Effect of welding thermal cycles on the heat affected zone microstructure and toughness of multi-pass welded pipeline steels,” PhD Thesis, Cranfield University, 2012.

[64] J. Hidalgo and M. Santofimia, “Effect of Prior Austenite Grain Size Refinement by Thermal Cycling on the Microstructural Features of As-Quenched Lath Martensite,” *Metallurgical and Materials Transactions A,* vol. 47, pp. 5288–5301, 2016.

[65] J. Da Nóbrega, D. Diniz, A. Silva, T. Maciel, V. De Albuquerque en J. Tavares, „Numerical Evaluation of Temperature Field and Residual Stresses in an API 5L X80 Steel Welded Joint Using the Finite Element Method,” *Metals; Molecular Diversity Preservation International,* vol. 6, pp. 28, 2016.

[66] M. Bosworth, „Effective Heat Input in Pulsed Current Gas Metal Arc Welding with Solid Wire Electrodes,” *Welding Journal, American Welding Society and the Welding Research Council,* pp. Supplement 111-117, May 1991.

[67] X. Yang, R. Barrett, M. Tong, N. Harrison and S. Leen, “Prediction of Microstructure Evolution for Additive Manufacturing of Ti-6Al-4V,” *Procedia Manufacturing,* vol. 47, pp. 1178-1183, 2020.

[68] V. Mishra, A. Babu, R. Schreurs, K. Wu, M. Hermans and C. Ayas, “Microstructure estimation and validation of ER110S-G steel structures produced by wire and arc additive manufacturing,” *Journal of Manufacturing Science and Engineering,* vol. 23, pp. 3579-3601, 2023.

[69] J. Ding, „Thermo-mechanical Analysis of Wire and Arc Additive Manufacturing Process,” PhD Thesis, Cranfield University , 2012.

[70] J. Ding, P. Colegrove, J. Mehnen, S. Ganguly, P. Sequeira Almeida, F. Wang en S. Williams, „Thermo-mechanical analysis of Wire and Arc Additive Layer Manufacturing process on large multi-layer parts,” *Computational Materials Science,* vol. 50, nr. 12, pp. 3315-3322, 2011.

[71] H. Zhao, G. Zhang, Z. Yin and L. Wu, “Three-dimensional finite element analysis of thermal stress in single-pass multi-layer weld-based rapid prototyping,” *Journal of Materials Processing Technology,* vol. 212, no. 1, pp. 276–285, 2012.

[72] M. Liberini, A. Astarita, G. Campatelli, A. Scippa, F. Montevecchi, G. Venturini et al., “Selection of optimal process parameters for wire arc additive manufacturing,” *Procedia CIRP; 10th CIRP Conference on Intelligent Computation in Manufacturing Engineering,* vol. 62, pp. 470-474, 2017.

[73] B. Wu, Z. Pan, D. Ding, D. Cuiuri, H. Li, J. Xu and J. Norrish, “A review of the wire arc additive manufacturing of metals: properties, defects and quality improvement,” *Journal of Manufacturing Processes,* vol. 35, pp. 127–139, 2018.

[74] P. Henckell, K. Günther, Y. Ali, J. Bergmann, J. Scholz and P. Forêt, “The Influence of Gas Cooling in Context of Wire Arc Additive Manufacturing - A Novel Strategy of Affecting Grain Structure and Size,” *TMS 2017 146th Annual Meeting & Exhibition Supplemental Proceedings,* pp. 147-156, 2017.

[75] T. Węgrzyn, J. Piwnik, D. Hadrys and Ł. Wszołek, “Low Alloy Steel Structures After Welding with Micro-Jet Cooling,” *Archives of Metallurgy and Materials,* vol. 62, no. 1, pp. 115-118, 2017.

[76] F. Montevecchi, G. Venturini, N. Grossi, A. Scippa and G. Campatelli, “Heat accumulation prevention in Wire-Arc-Additive-Manufacturing using air jet impingement,” *Manufacturing Letters,* vol. 17, pp. 14-18, 2018.

[77] B. Wu, Z. Pan, D. Ding, D. Cuiuri, H. Li and Z. Fei, “The effects of forced interpass cooling on the material properties of wire arc additively manufactured Ti6Al4V alloy,” *Journal of Materials Processing Technology,* vol. 258, pp. 97-105, 2018.

[78] P. Zhou, B. Wang, L. Wang, Y. Hu and L. Zhou, “Effect of welding heat input on grain boundary evolution and toughness properties in CGHAZ of X90 pipeline steel,” *Materials Science & Engineering A,* vol. 722, pp. 112–121, 2018.

[79] M. Mughal, H. Fawad, R. Mufti and M. Siddique, “Deformation modelling in layered manufacturing of metallic parts using gas metal arc welding: effect of process parameters,” *Modelling and Simulation in Materials Science and Engineering,* vol. 13, no. 7, pp. 1187-1204, 2005.

Appendices

Appendix A.1 Experimental setup: control script CNC machine

```
INPUT
x_cnts = 1600  '[counts/mm]
y_cnts = 8000
z_cnts = 12500
x_v = 6.5  '[mm/s]
y_v = 6.5
z_v = 1
x = 0  '[mm]
y = 0
z = 0
length = 150  '[mm]
height = 1.5   '[mm]
n = 15  '[-]

#RUN
i = 0
t0 = TIME
#LOOP
MG TIME
WT interlayer waiting time as defined in the test cases 1 to 5  '[s]
MC
SB2
SHX
PRX = length*x_cnts
SPX = x_v*x_cnts
BGX
MC
CB2
SHZ
PRZ = - height*z_cnts
SPZ = z_v*z_cnts
BGZ
MG TIME
WT interlayer waiting time as defined in the test cases 1 to 5  '[s]
MC
SB2
SHX
PRX = - length*x_cnts
SPX = x_v*x_cnts
BGX
MC
CB2
SHZ
PRZ = - height*z_cnts
SPZ = z_v*z_cnts
BGZ
i = i + 2
JP #LOOP, i<n
MG "DONE"
END
```

Appendix A.2 Experimental setup: Experiments

Experimental setup: Experiments

[a]

[b]

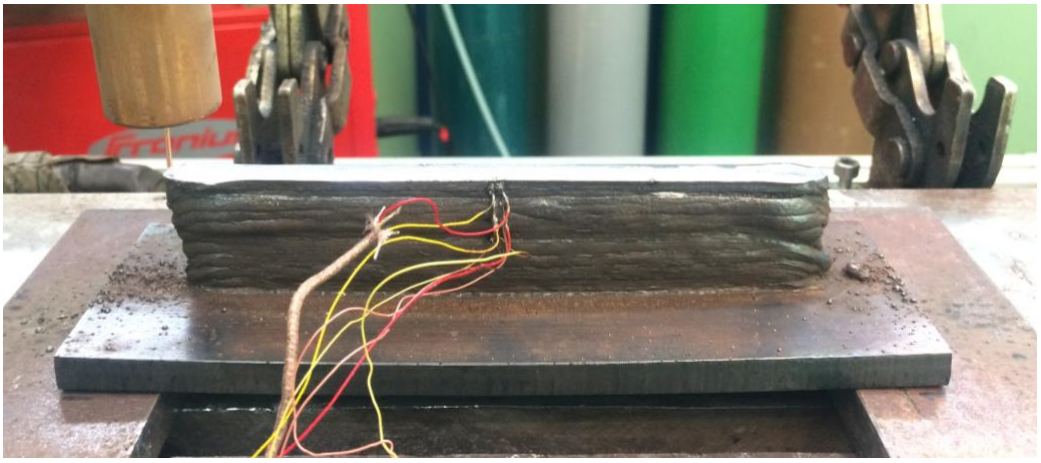

Figure A.2: Experimental setup. [a] Material deposition on top of a component base wall; [b] Temperature measurement by physically attached K-type thermocouples.

Appendix A.3 Experimental setup: F.E. model

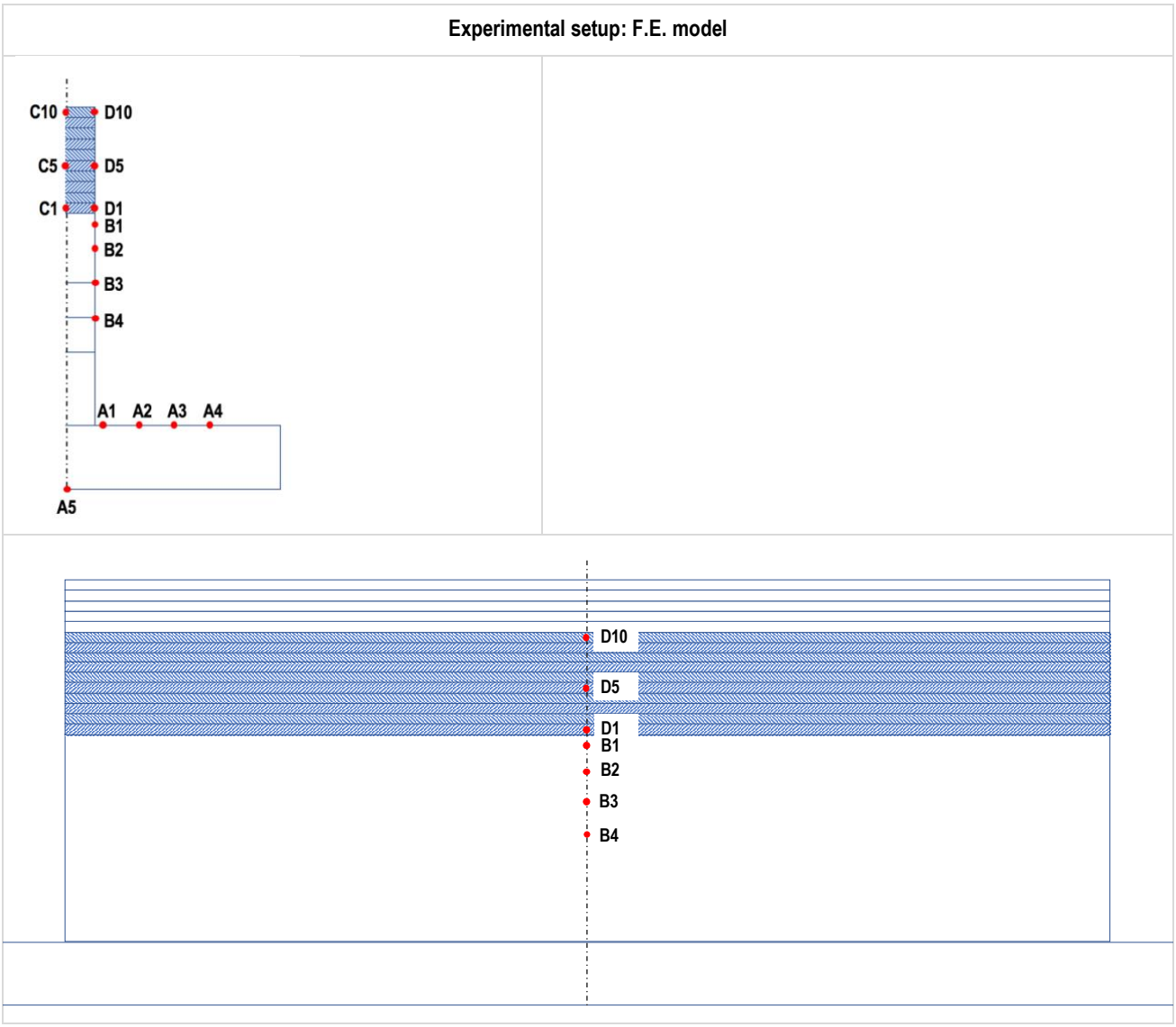

Figure A.3: Locations of the temperature measurement points in the F.E. model at the mid-length position $x = 75\ mm$.

Appendix A.4 Experimental current and voltage values

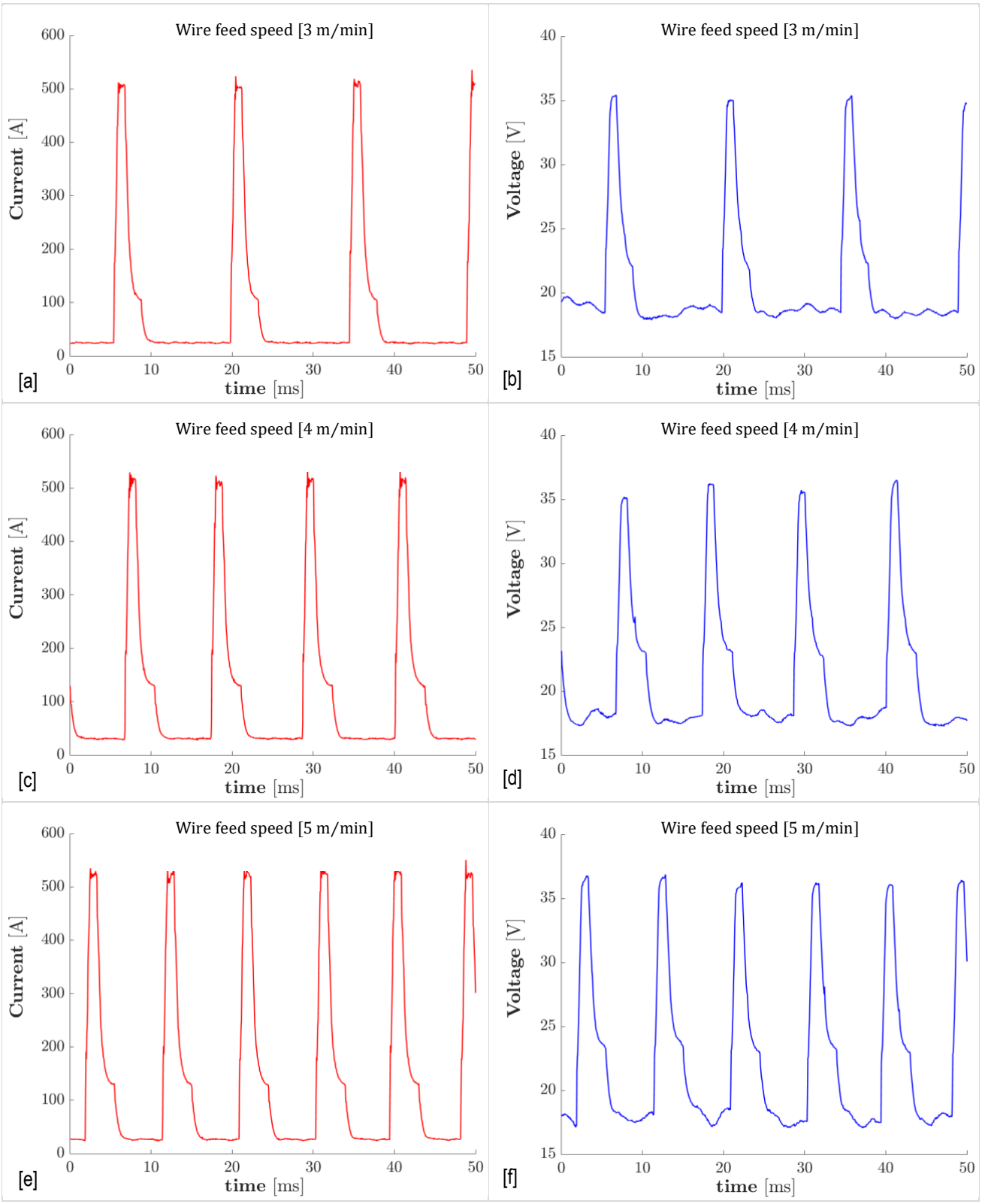

Figure A.4: Experimental current and voltage values, recorded at a sampling rate 20 kHz and bandwidth 50 kHz. [a] Current measurement values 3 m/min; [b] Voltage measurement values 3 m/min; [c] Current measurement values 4 m/min; [d] Voltage measurement values 4 m/min; [e] Current measurement values 5 m/min; [f] Voltage measurement values 5 m/min.

Appendix B.1 Experimental temperature values

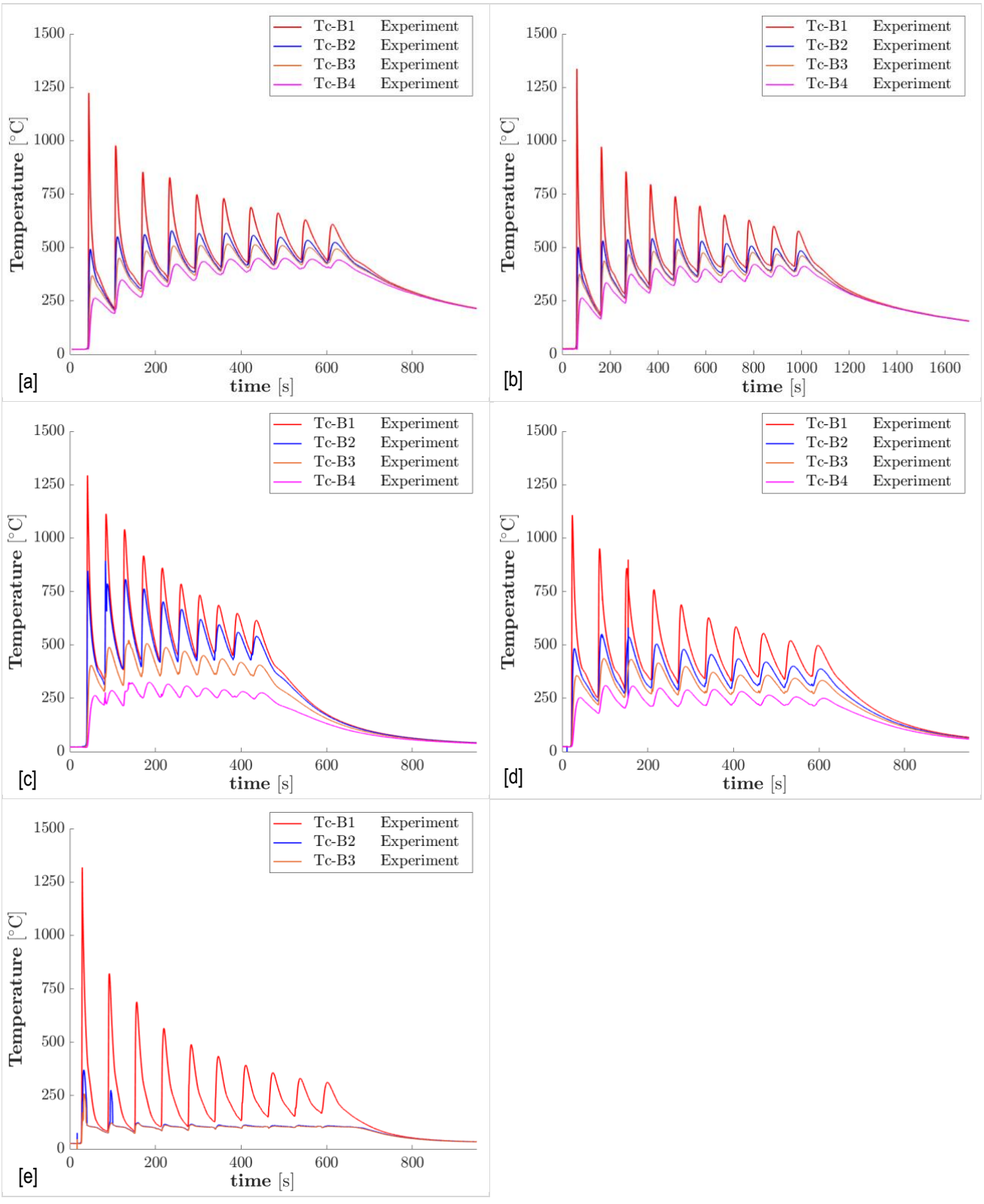

Figure B.1: Experimental temperature values, recorded at the temperature measurement points Tc-B1 to Tc-B4. [a] Test case 1: Natural cooling, interlayer waiting time 40s; [b] Test case 2: Natural cooling, interlayer waiting time 80s; [c] Test case 3: Active substrate cooling, interlayer waiting time 20s; [d] Test case 4: Active substrate cooling, interlayer waiting time 40s; [e] Test case 5: Active component cooling, interlayer waiting time 40s.

Appendix B.2 F.E. model temperature values

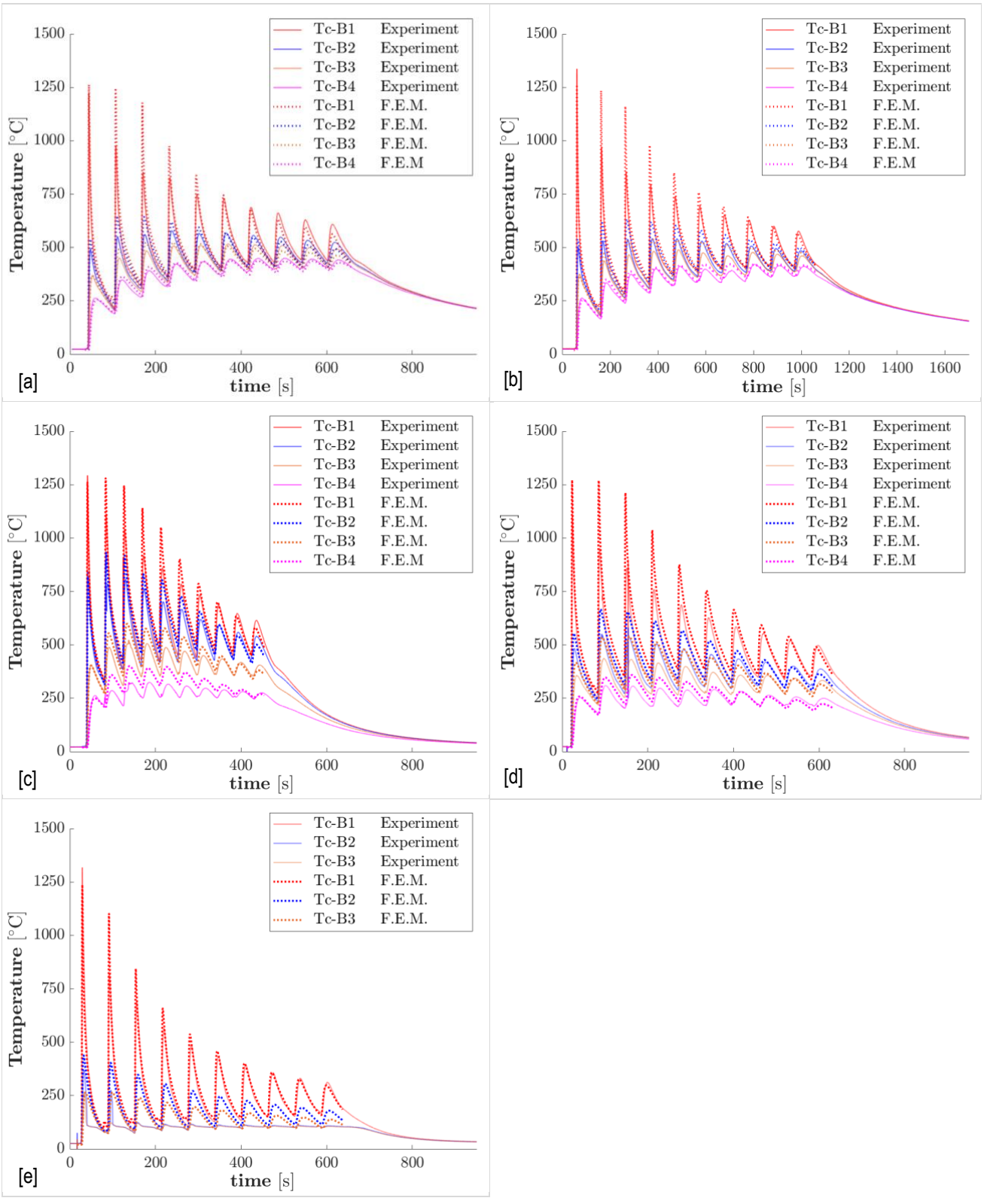

Figure B.2: F.E. model temperature values, calculated at the temperature measurement points Tc-B1 to Tc-B4. [a] Test case 1: Natural cooling, interlayer waiting time 40s; [b] Test case 2: Natural cooling, interlayer waiting time 80s; [c] Test case 3: Active substrate cooling, interlayer waiting time 20s; [d] Test case 4: Active substrate cooling, interlayer waiting time 40s; [e] Test case 5: Active component cooling, interlayer waiting time 40s.

Appendix B.3 F.E. model temperature values: layer 1

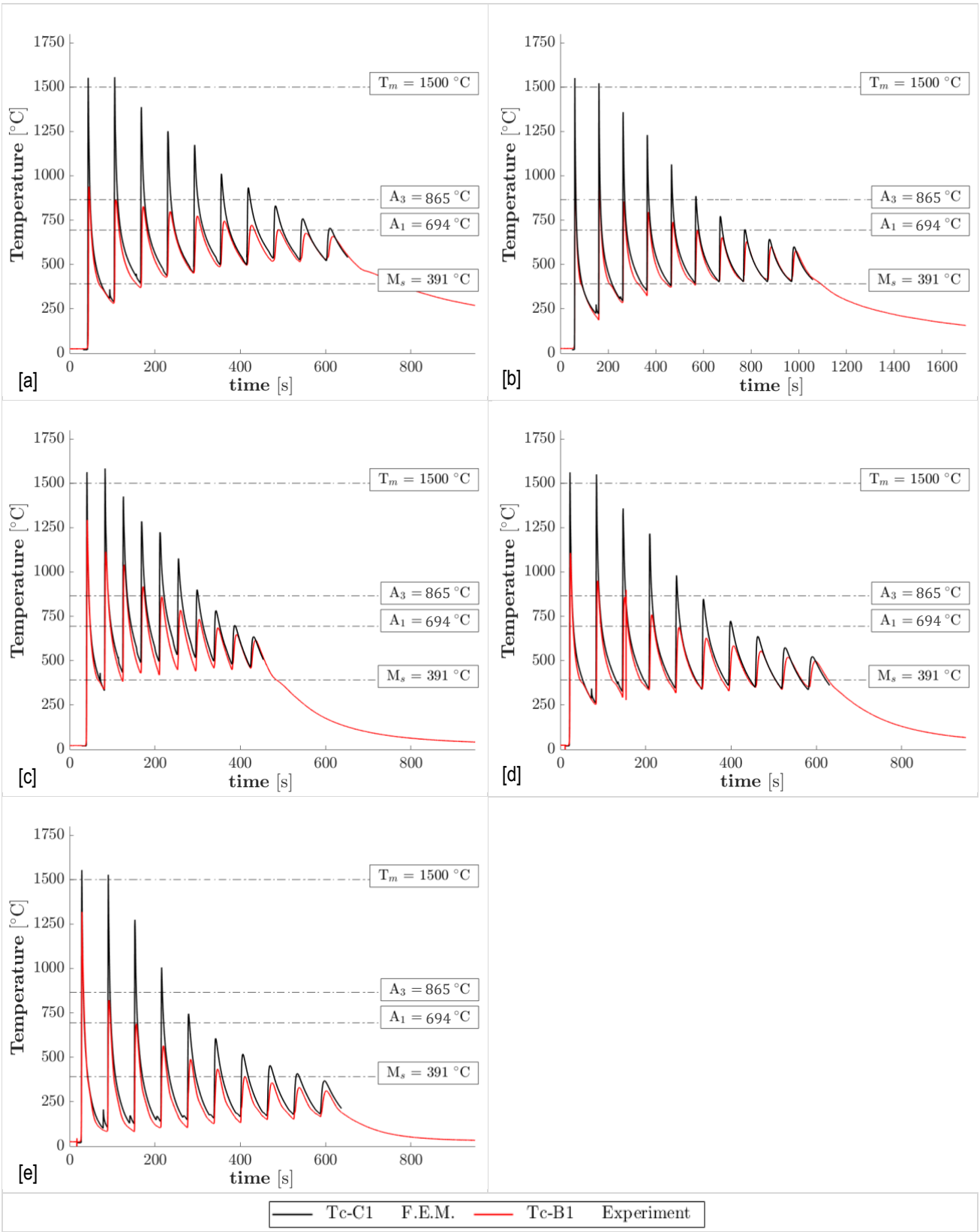

Figure B.3: F.E. model temperature values, calculated at the temperature measurement Tc-C1; middle point layer 1. [a] Test case 1: Natural cooling, interlayer waiting time 40s; [b] Test case 2: Natural cooling, interlayer waiting time 80s; [c] Test case 3: Active substrate cooling, interlayer waiting time 20s; [d] Test case 4: Active substrate cooling, interlayer waiting time 40s; [e] Test case 5: Active component cooling, interlayer waiting time 40s.

Appendix B.4 F.E. model temperature values: layer 5

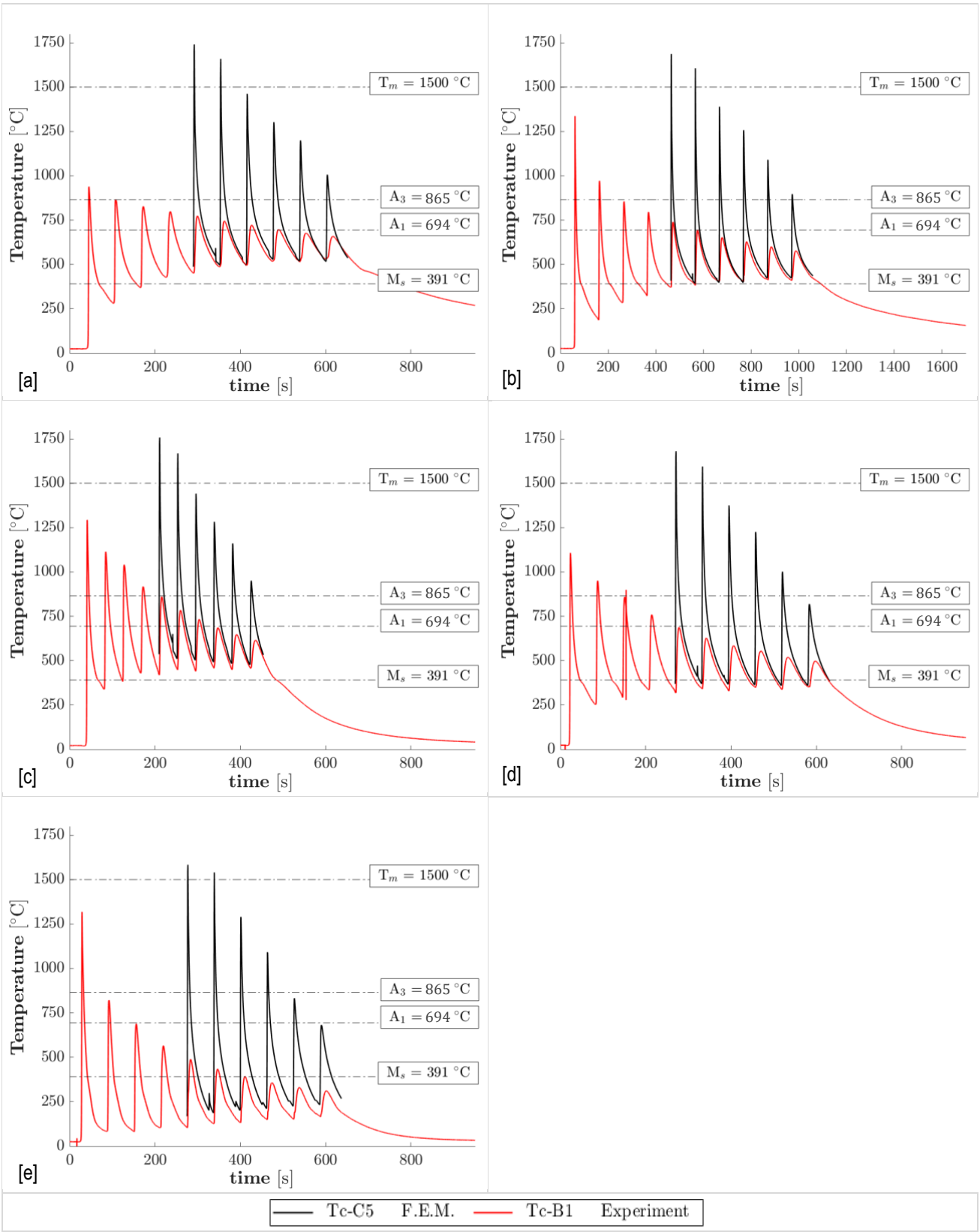

Figure B.4: F.E. model temperature values, calculated at the temperature measurement Tc-C5; middle point layer 5. [a] Test case 1: Natural cooling, interlayer waiting time 40s; [b] Test case 2: Natural cooling, interlayer waiting time 80s; [c] Test case 3: Active substrate cooling, interlayer waiting time 20s; [d] Test case 4: Active substrate cooling, interlayer waiting time 40s; [e] Test case 5: Active component cooling, interlayer waiting time 40s.

Appendix B.5 F.E. model temperature values: layer 10

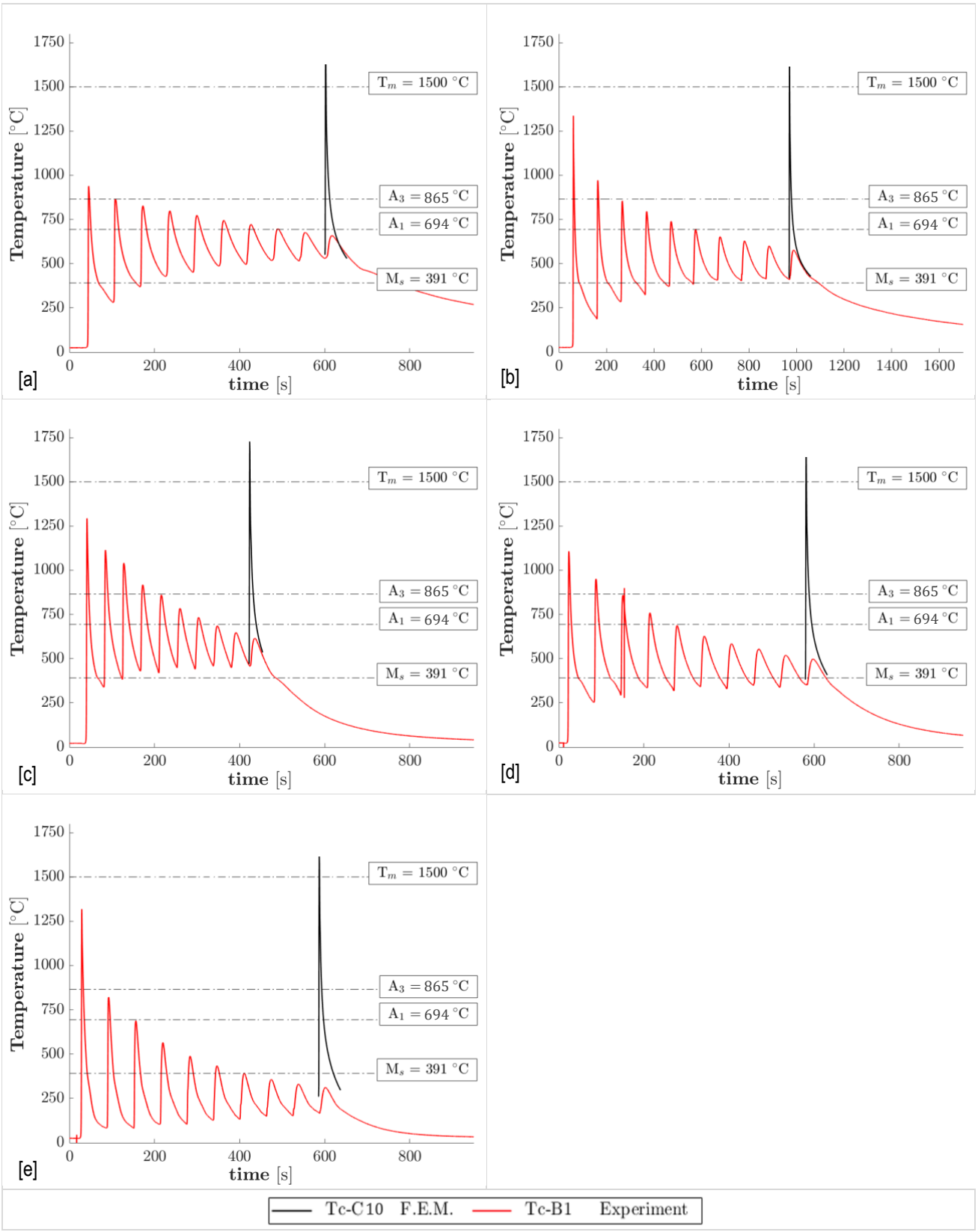

Figure B.5: F.E. model temperature values, calculated at the temperature measurement point Tc-C10; middle point layer 10. [a] Test case 1: Natural cooling, interlayer waiting time 40s; [b] Test case 2: Natural cooling, interlayer waiting time 80s; [c] Test case 3: Active substrate cooling, interlayer waiting time 20s; [d] Test case 4: Active substrate cooling, interlayer waiting time 40s; [e] Test case 5: Active component cooling, interlayer waiting time 40s.

Appendix C.1 Temperature distribution component

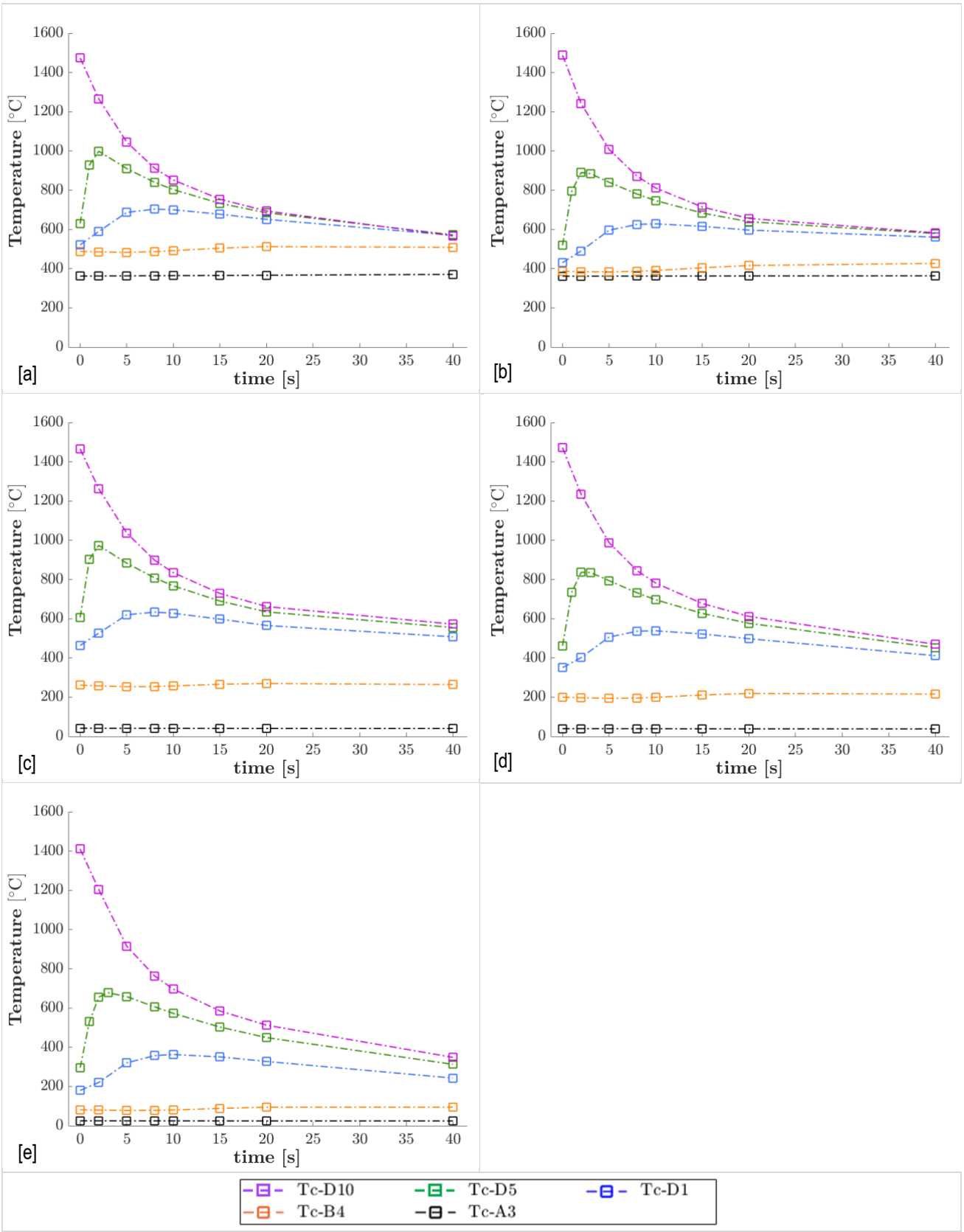

Figure C.1: Temperature distribution component, calculated during the deposition of the tenth layer of the simulated ten-layer weld deposit. [a] Test case 1: Natural cooling, interlayer waiting time 40s; [b] Test case 2: Natural cooling, interlayer waiting time 80s; [c] Test case 3: Active substrate cooling, interlayer waiting time 20s; [d] Test case 4: Active substrate cooling, interlayer waiting time 40s; [e] Test case 5: Active component cooling, interlayer waiting time 40s.

Appendix C.2 Temperature distribution component

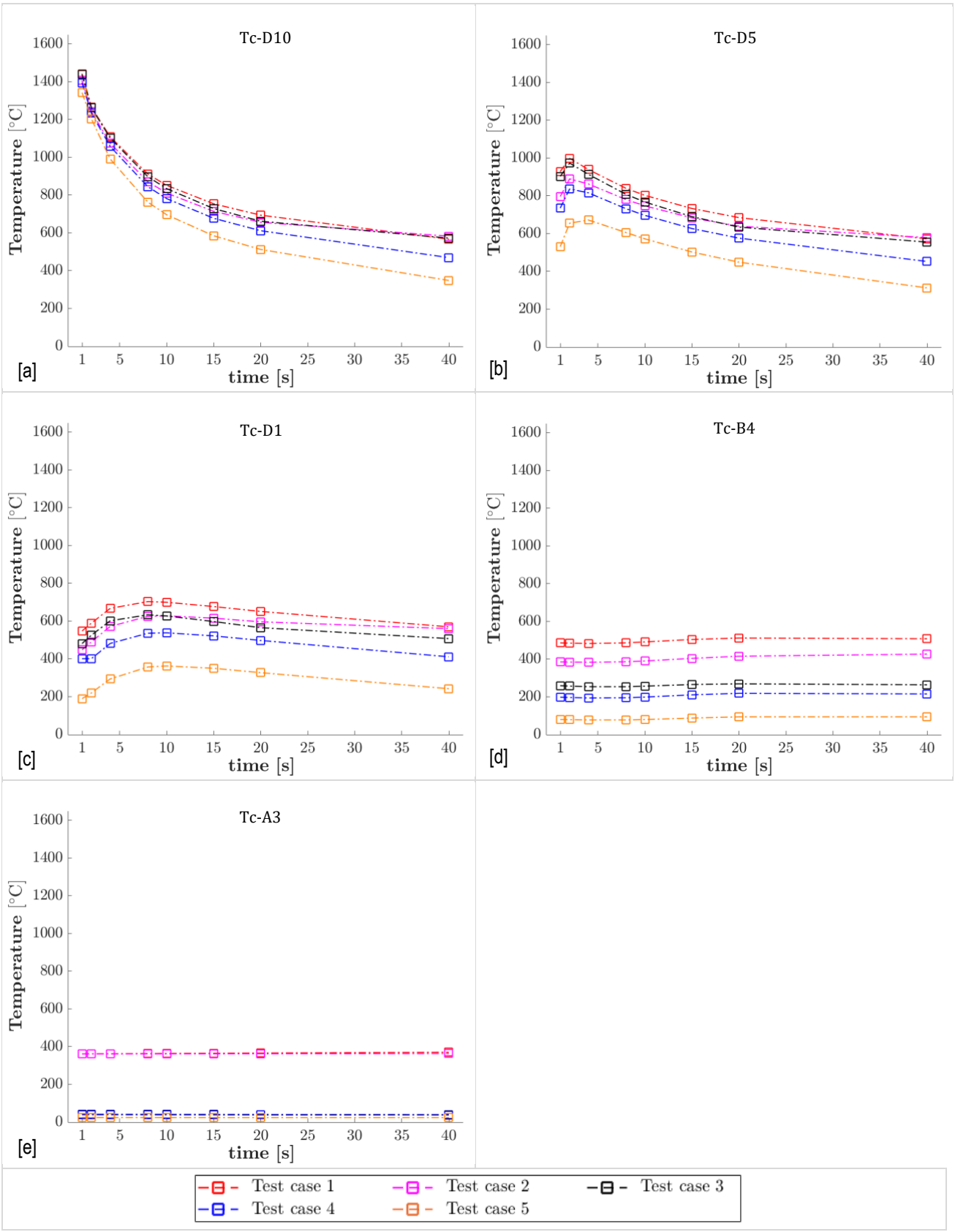

Figure C.2: Temperature distribution component, calculated during the deposition of the tenth layer of the simulated ten-layer weld deposit. *[a] Temperature measurement point Tc-D10; [b] Temperature measurement point Tc-D5; [c] Temperature measurement point Tc-D1; [d] Temperature measurement point Tc-B4; [e] Temperature measurement point Tc-A3.*

Appendix C.3 Temperature distribution component. Test case 1

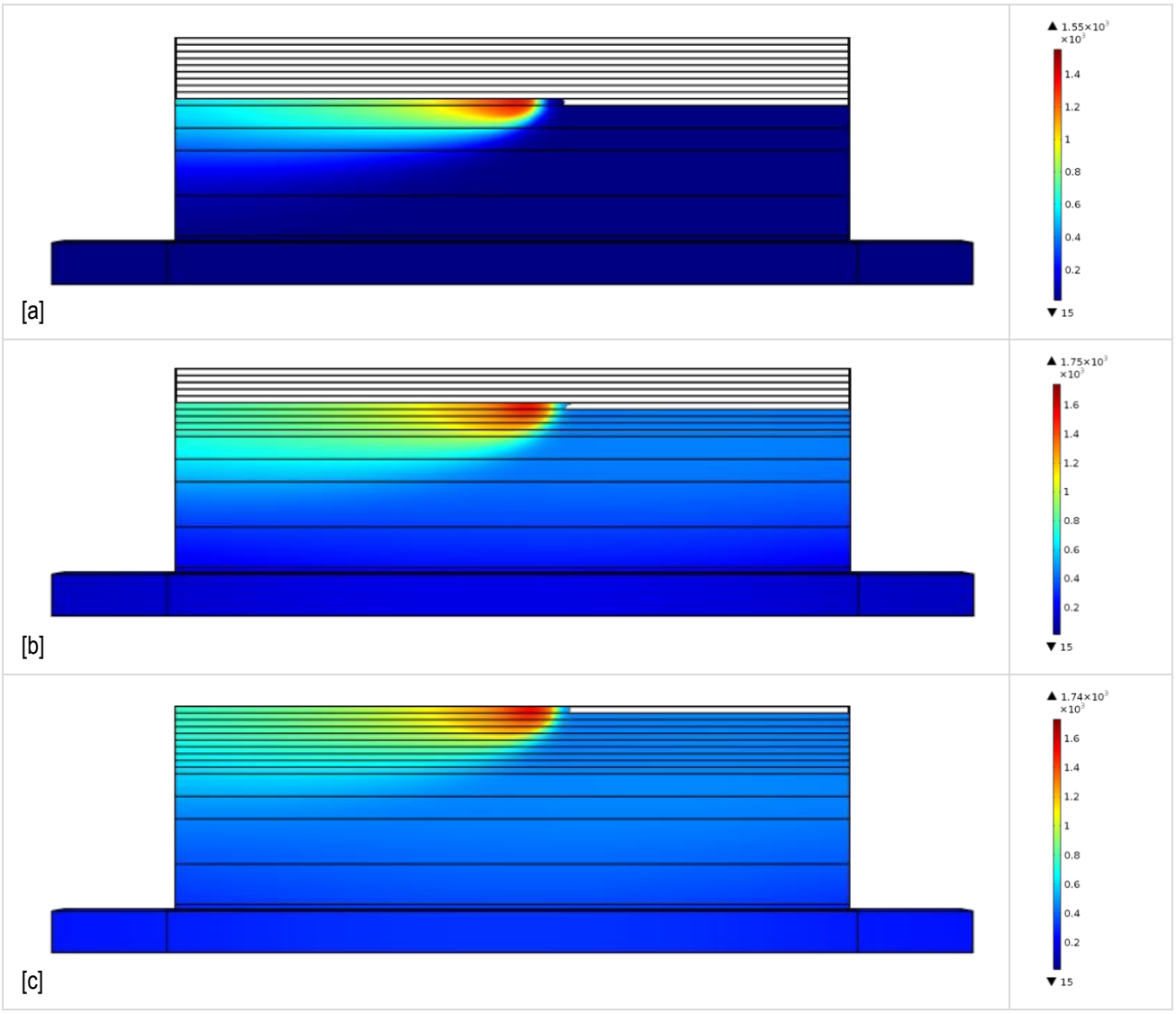

Figure C.3: Temperature distribution of the component, calculated in the F.E. model. [a] During the deposition of the first layer; [b] During the deposition of the fifth layer; [c] During the deposition of the tenth layer.

Table C.3 [a]: F.E. model temperature values, calculated during the deposition of the first layer; test case 1.

	0 s	2 s	4 s	8 s	10 s	20 s	40 s
Tc-C 1	1552,51	1144,51	910,08	694,41	633,34	473,42	342,37
Tc-D 1	1323,70	1131,19	902,84	690,15	629,74	471,25	341,17
Tc-B 4	20,36	32,86	77,72	169,37	198,48	251,43	244,38
Tc-A 3	20,00	20,00	20,00	20,03	20,10	22,71	36,44

Table C.3 [b]: F.E. model temperature values, calculated during the deposition of the fifth layer; test case 1.

	0 s	2 s	4 s	8 s	10 s	20 s	40 s
Tc-C 5	1703,30	1248,65	1065,20	942,23	885,02	727,93	588,99
Tc-D 5	1424,20	1244,61	1055,57	934,94	878,72	723,93	586,54
Tc-C 1	1043,65	1121,36	963,32	879,38	837,88	710,37	583,75
Tc-D 1	992,65	1115,40	958,34	875,57	834,57	708,26	582,47
Tc-B 4	417,76	417,10	438,73	468,55	484,00	509,05	482,83
Tc-A 3	210,40	211,65	213,46	215,19	216,31	222,15	235,50

Appendix C.4 Temperature distribution component. Test case 5

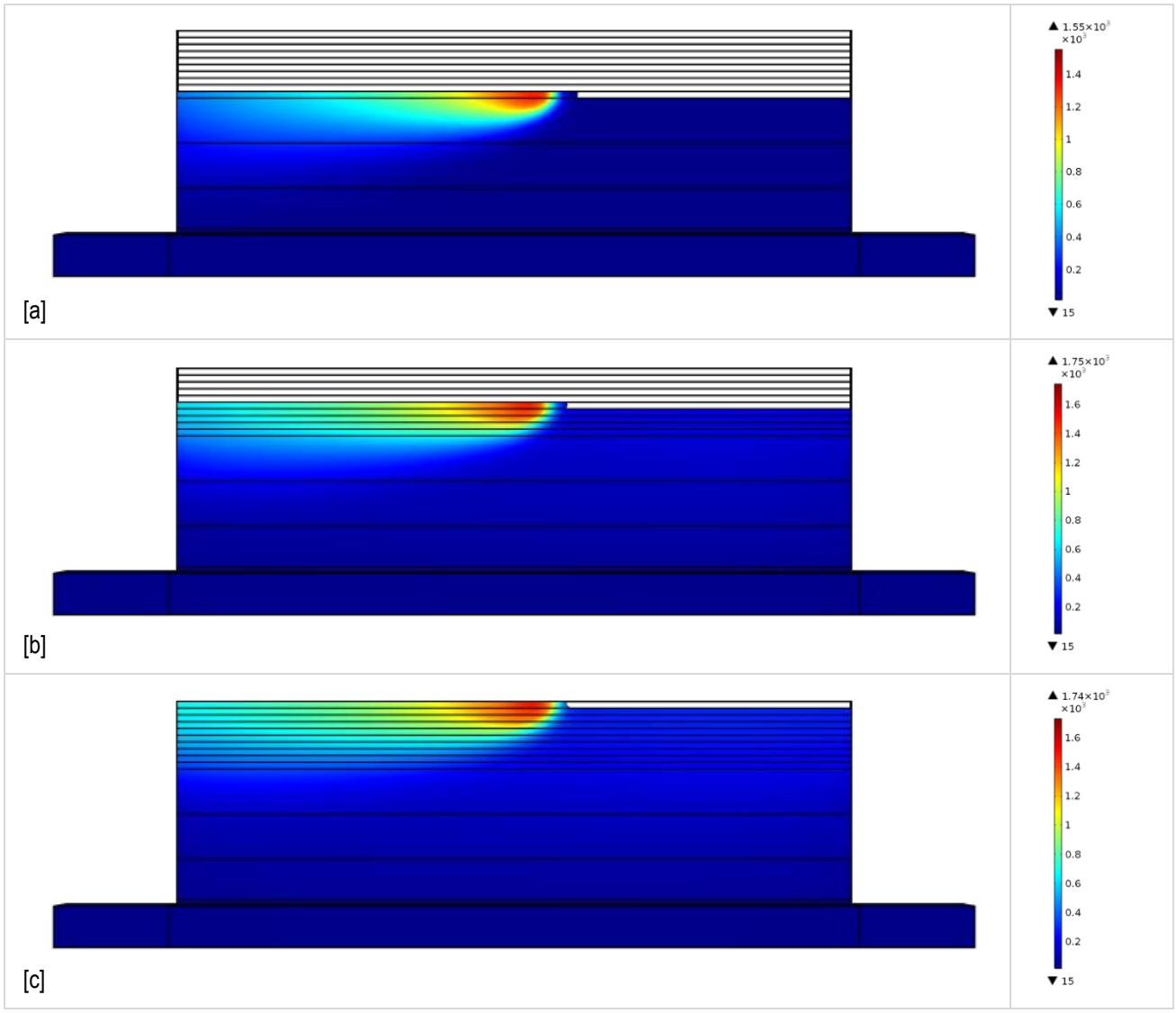

Figure C.4: Temperature distribution of the component, calculated in the F.E. model. [a] During the deposition of the first layer; [b] During the deposition of the fifth layer; [c] During the deposition of the tenth layer.

Table C.4 [a]: F.E. model temperature values, calculated during the deposition of the first layer; test case 5.

	0 s	2 s	4 s	8 s	10 s	20 s	40 s
Tc-C 1	1552,51	1144,51	910,08	694,41	633,34	473,42	342,37
Tc-D 1	1323,70	1131,19	902,84	690,15	629,74	471,25	341,17
Tc-B 4	20,36	32,86	77,72	169,37	198,48	251,43	244,38
Tc-A 3	20,00	20,00	20,00	20,03	20,10	22,71	36,44

Table C.4 [b]: F.E. model temperature values, calculated during the deposition of the fifth layer; test case 5.

	0 s	2 s	4 s	8 s	10 s	20 s	40 s
Tc-C 5	1703,30	1248,65	1065,20	942,23	885,02	727,93	588,99
Tc-D 5	1424,20	1244,61	1055,57	934,94	878,72	723,93	586,54
Tc-C 1	1043,65	1121,36	963,32	879,38	837,88	710,37	583,75
Tc-D 1	992,65	1115,40	958,34	875,57	834,57	708,26	582,47
Tc-B 4	417,76	417,10	438,73	468,55	484,00	509,05	482,83
Tc-A 3	210,40	211,65	213,46	215,19	216,31	222,15	235,50

Appendix D.1 Temperature gradient layer 1. Test case 1

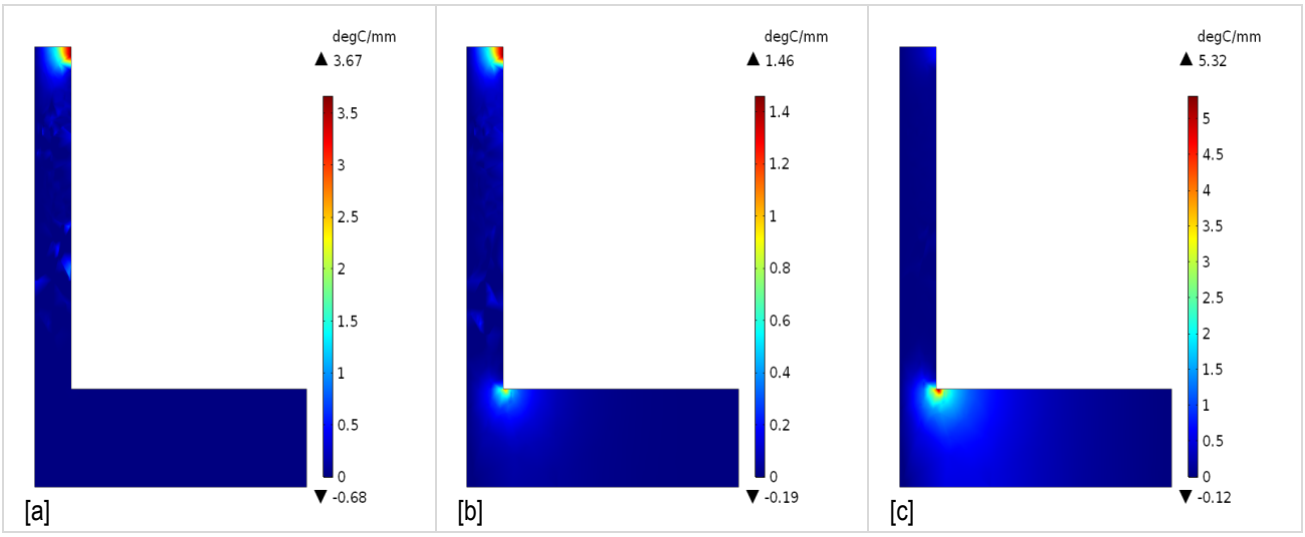

Figure D.1a: Temperature gradient in the Y-direction, calculated at the mid-point cross-section during the deposition of the first layer. [a] 4s after the passage of the heat source; [b] 10s after the passage of the heat source; [c] 20s after the passage of the heat source.

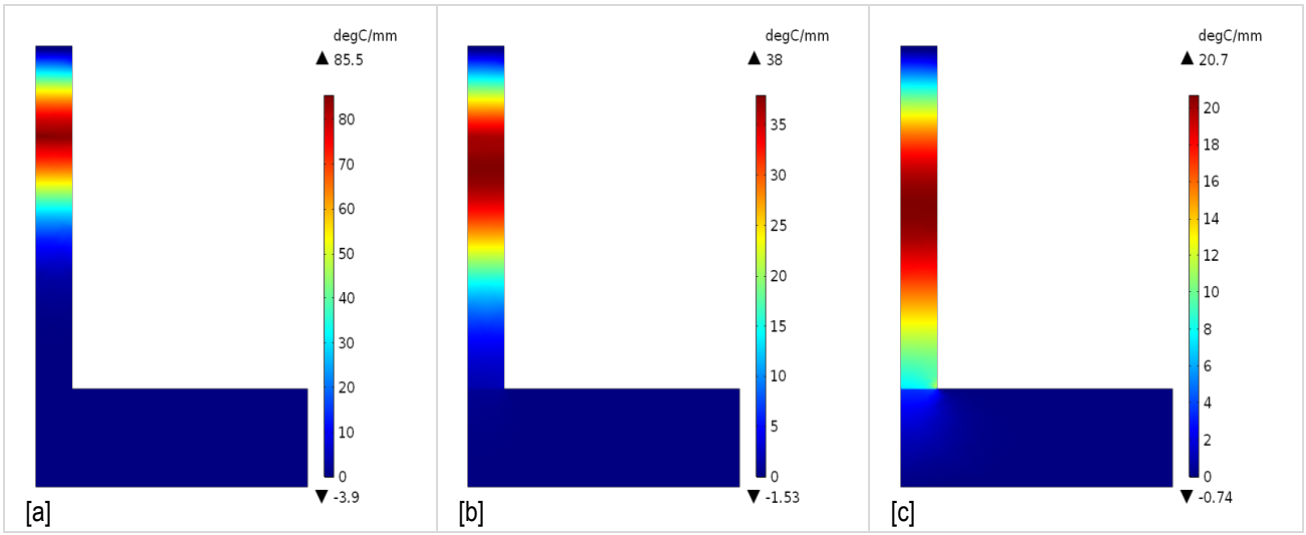

Figure D.1b: Temperature gradient in the Z-direction, calculated at the mid-point cross-section during the deposition of the first layer: [a] 4s after the passage of the heat source; [b] 10s after the passage of the heat source; [c] 20s after the passage of the heat source.

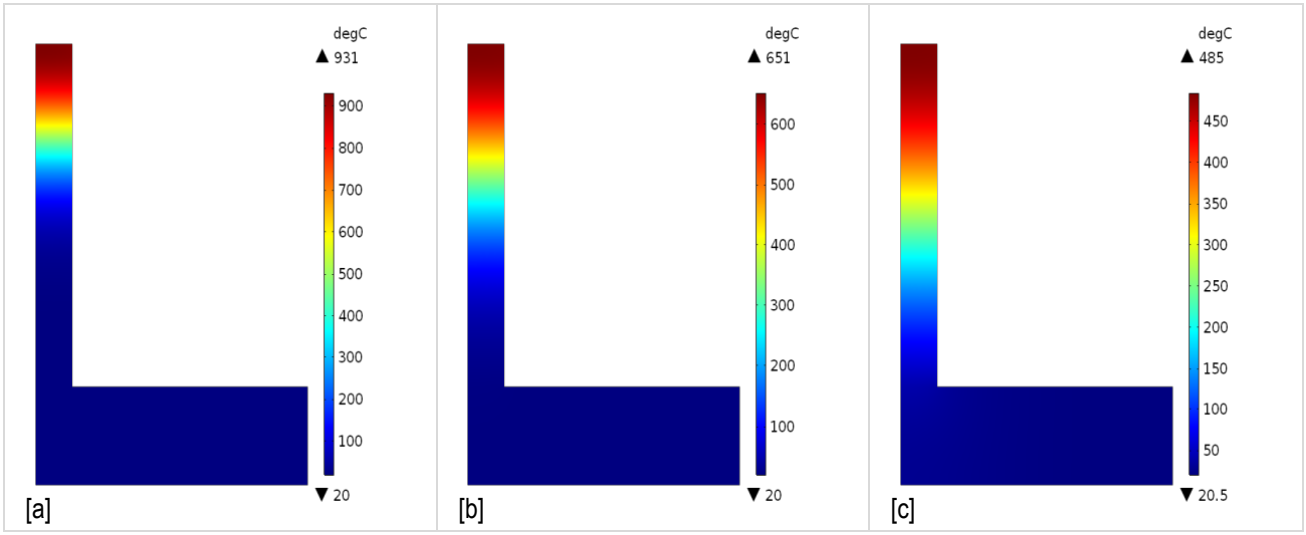

Figure D.1c: Temperature gradient in the X-direction, calculated at the mid-point cross-section during the deposition of the first layer. [a] 4s after the passage of the heat source; [b] 10s after the passage of the heat source; [c] 20s after the passage of the heat source.

Appendix D.2 Temperature gradient layer 1. Test case 5

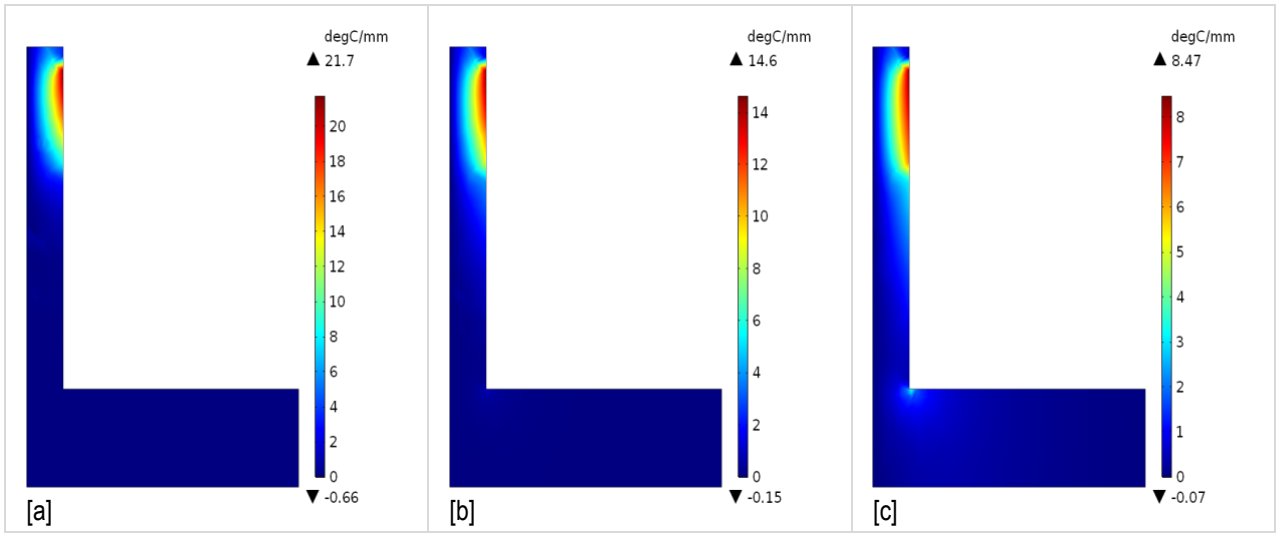

Figure D.2a: Temperature gradient in the Y-direction, calculated at the mid-point cross-section during the deposition of the first layer. [a] 4s after the passage of the heat source; [b] 10s after the passage of the heat source; [c] 20s after the passage of the heat source.

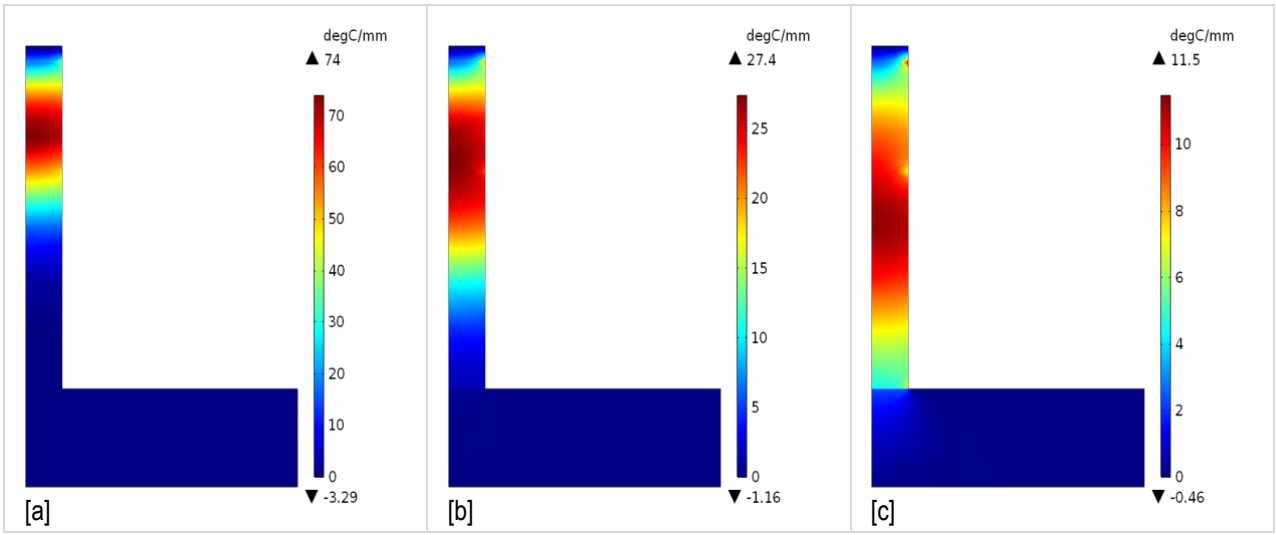

Figure D.2b: Temperature gradient in the Z-direction, calculated at the mid-point cross-section during the deposition of the first layer: [a] 4s after the passage of the heat source; [b] 10s after the passage of the heat source; [c] 20s after the passage of the heat source.

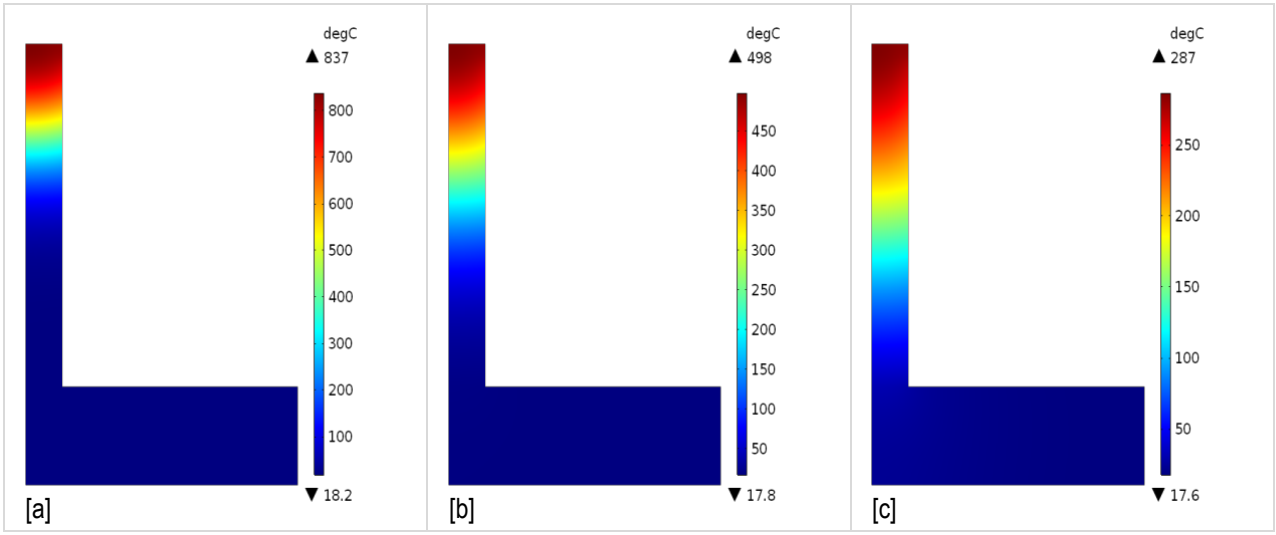

Figure D.2c: Temperature gradient in the X-direction, calculated at the mid-point cross-section during the deposition of the first layer. [a] 4s after the passage of the heat source; [b] 10s after the passage of the heat source; [c] 20s after the passage of the heat source.

Appendix D.3 Temperature gradient layer 10. Test case 1

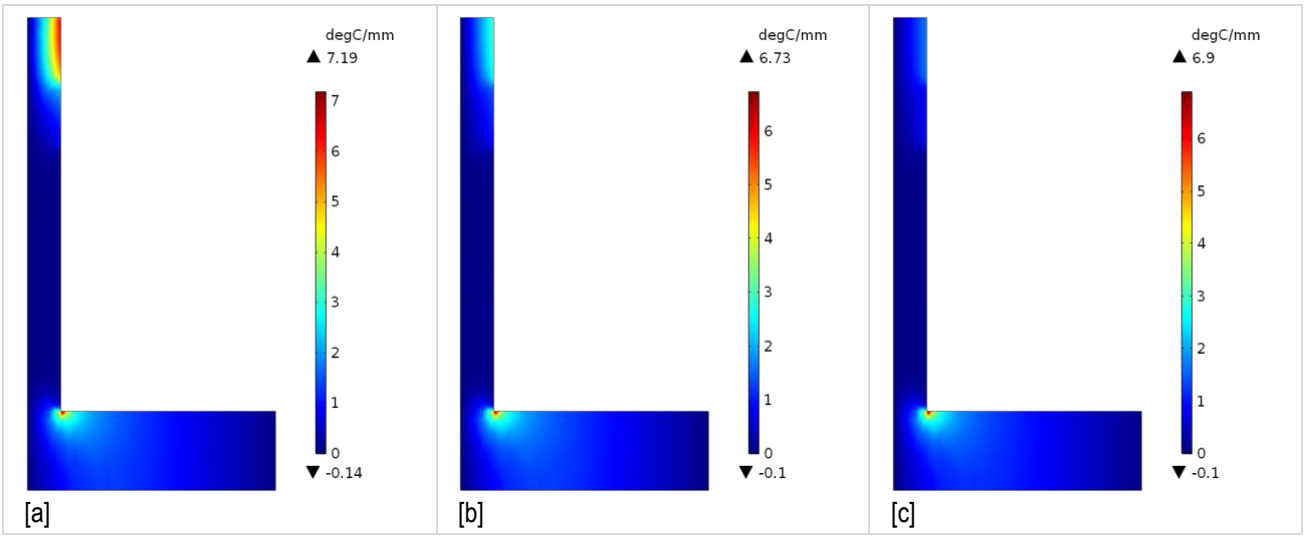

Figure D.3a: Temperature gradient in the Y-direction, calculated at the mid-point cross-section during the deposition of the tenth layer. [a] 4s after the passage of the heat source; [b] 10s after the passage of the heat source; [c] 20s after the passage of the heat source.

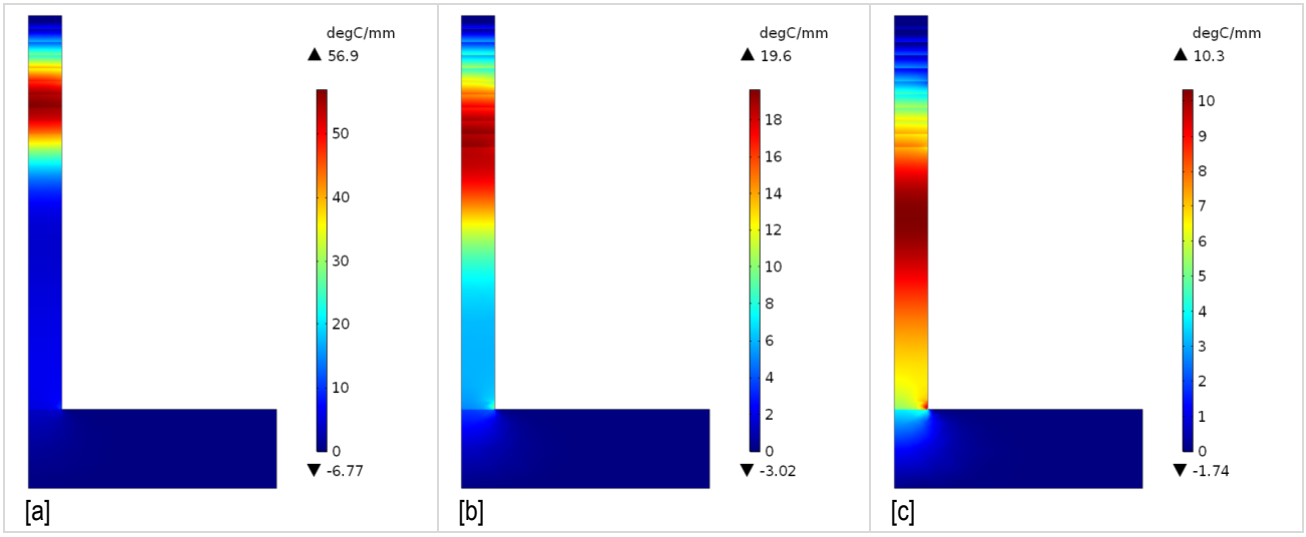

Figure D.3b: Temperature gradient in the Z-direction, calculated at the mid-point cross-section during the deposition of the tenth layer: [a] 4s after the passage of the heat source; [b] 10s after the passage of the heat source; [c] 20s after the passage of the heat source.

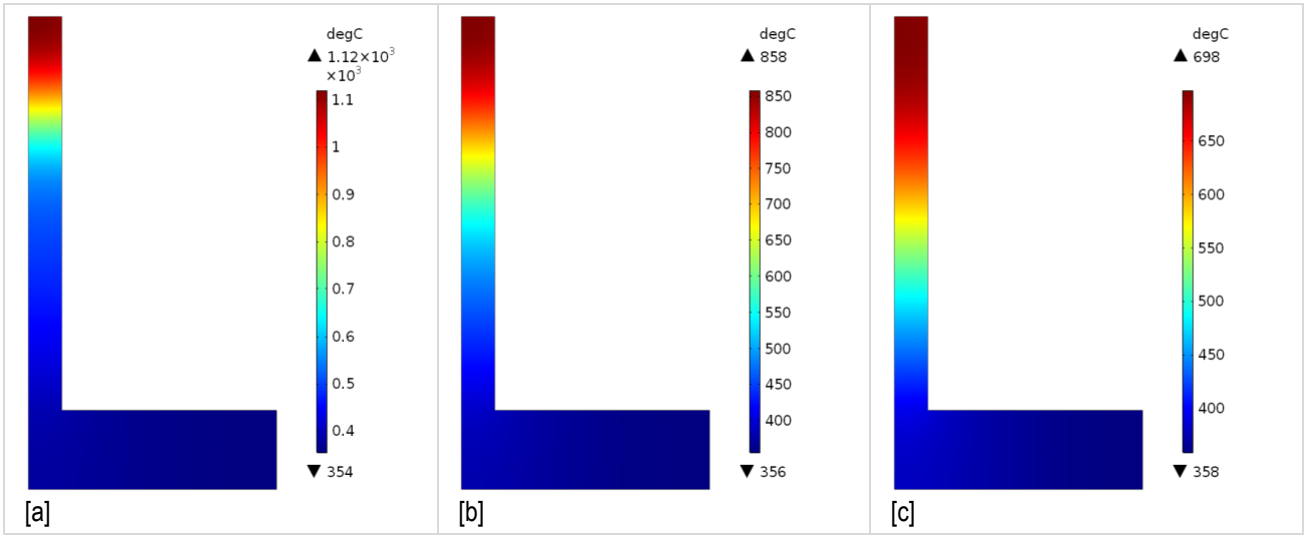

Figure D.3c: Temperature gradient in the X-direction, calculated at the mid-point cross-section during the deposition of the tenth layer. [a] 4s after the passage of the heat source; [b] 10s after the passage of the heat source; [c] 20s after the passage of the heat source.

Appendix D.4 Temperature gradient layer 10. Test case 5

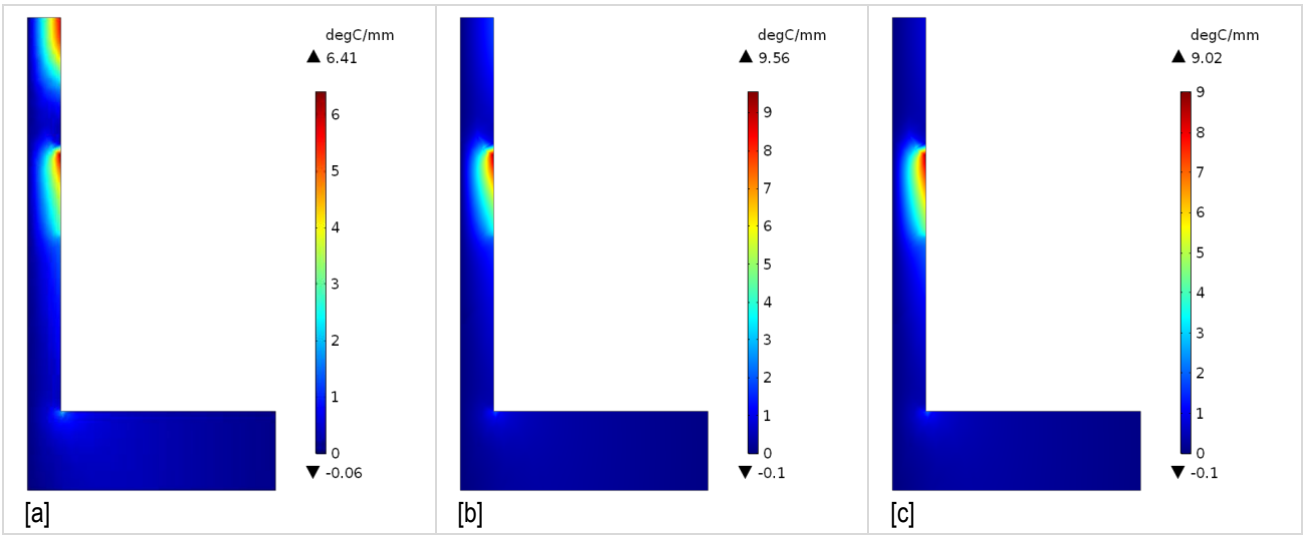

Figure D.4a: Temperature gradient in the Y-direction, calculated at the mid-point cross-section during the deposition of the tenth layer. [a] 4s after the passage of the heat source; [b] 10s after the passage of the heat source; [c] 20s after the passage of the heat source.

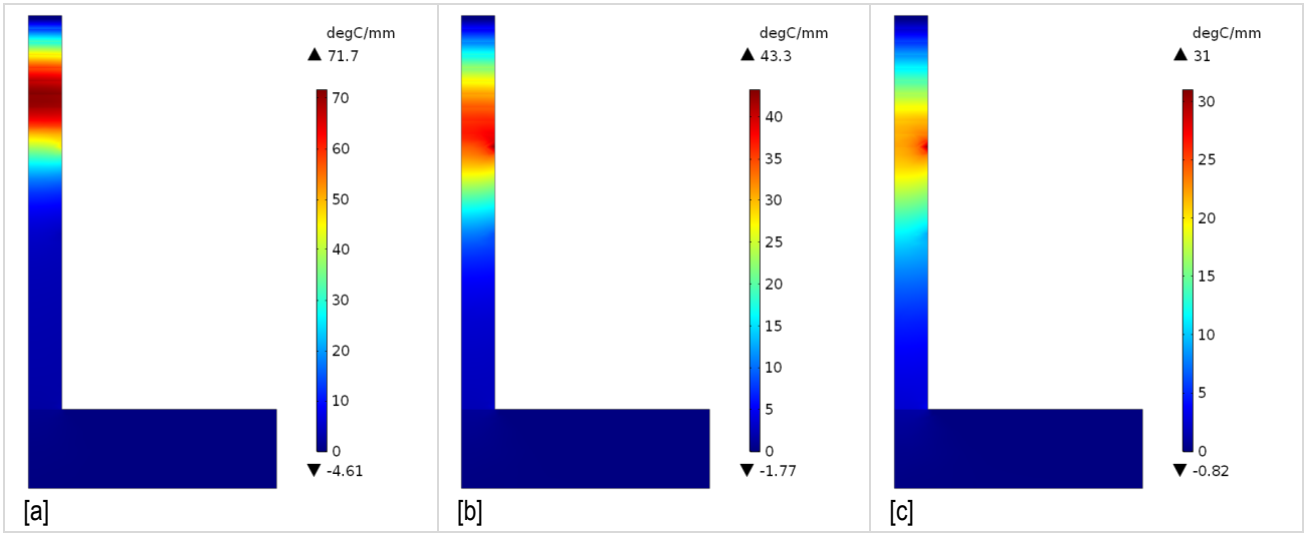

Figure D.4b: Temperature gradient in the Z-direction, calculated at the mid-point cross-section during the deposition of the tenth layer: [a] 4s after the passage of the heat source; [b] 10s after the passage of the heat source; [c] 20s after the passage of the heat source.

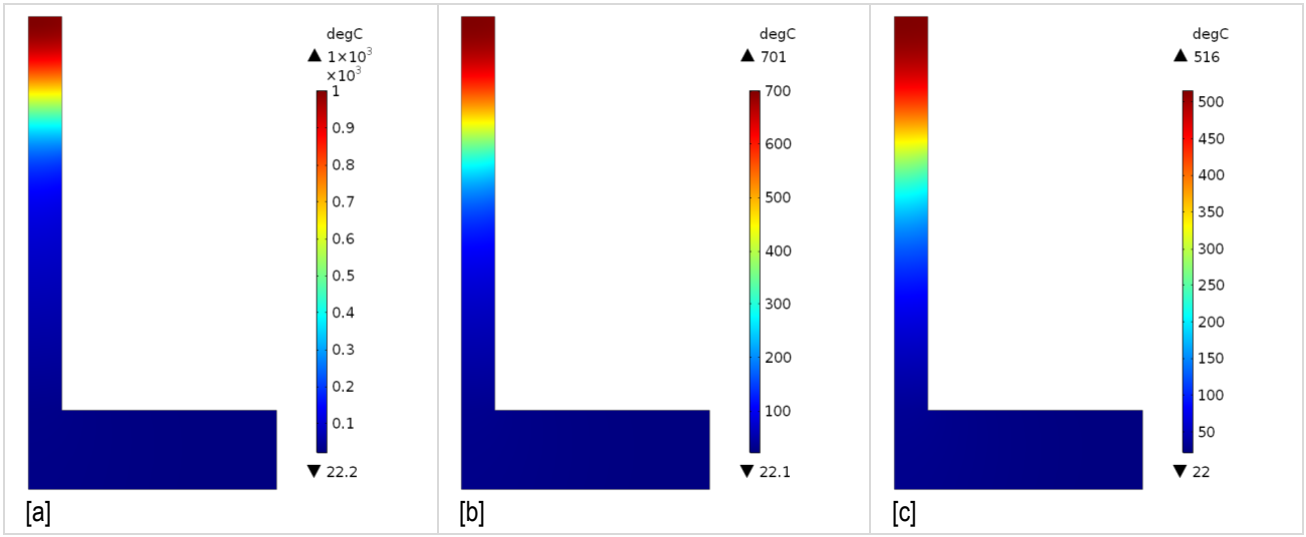

Figure D.4c: Temperature gradient in the X-direction, calculated at the mid-point cross-section during the deposition of the tenth layer. [a] 4s after the passage of the heat source; [b] 10s after the passage of the heat source; [c] 20s after the passage of the heat source.

Appendix E.1 Hardness measurement values

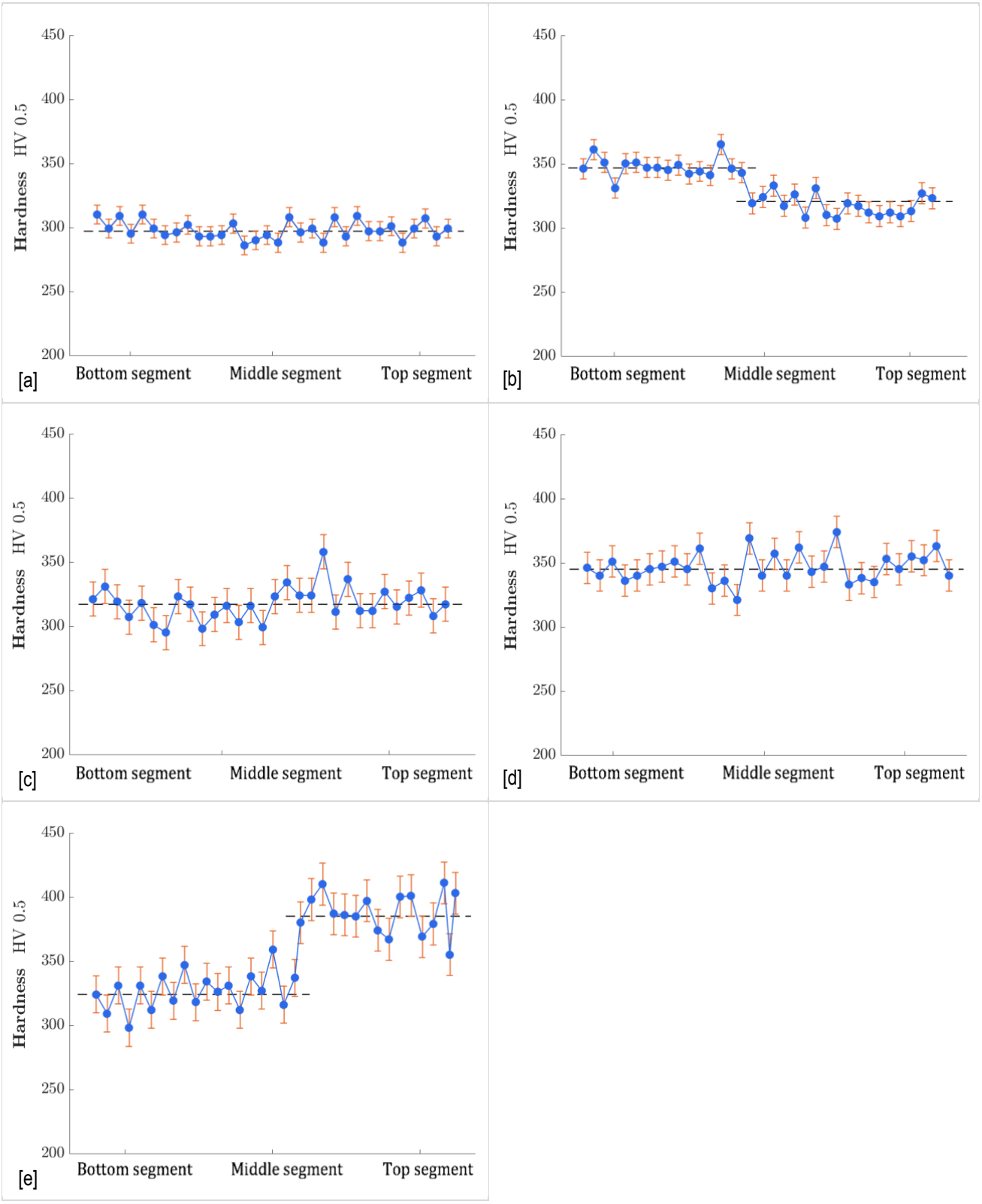

Figure E.1: The hardness measurement values and the standard deviation of the hardness measurement values for the test cases 1 to 5. [a] Test case 1: Natural cooling, interlayer waiting time 40s; [b] Test case 2: Natural cooling, interlayer waiting time 80s; [c] Test case 3: Active substrate cooling, interlayer waiting time 20s; [d] Test case 4: Active substrate cooling, interlayer waiting time 40s; [e] Test case 5: Active component cooling, interlayer waiting time 40s.

Appendix F.1 Calibration error F.E. model

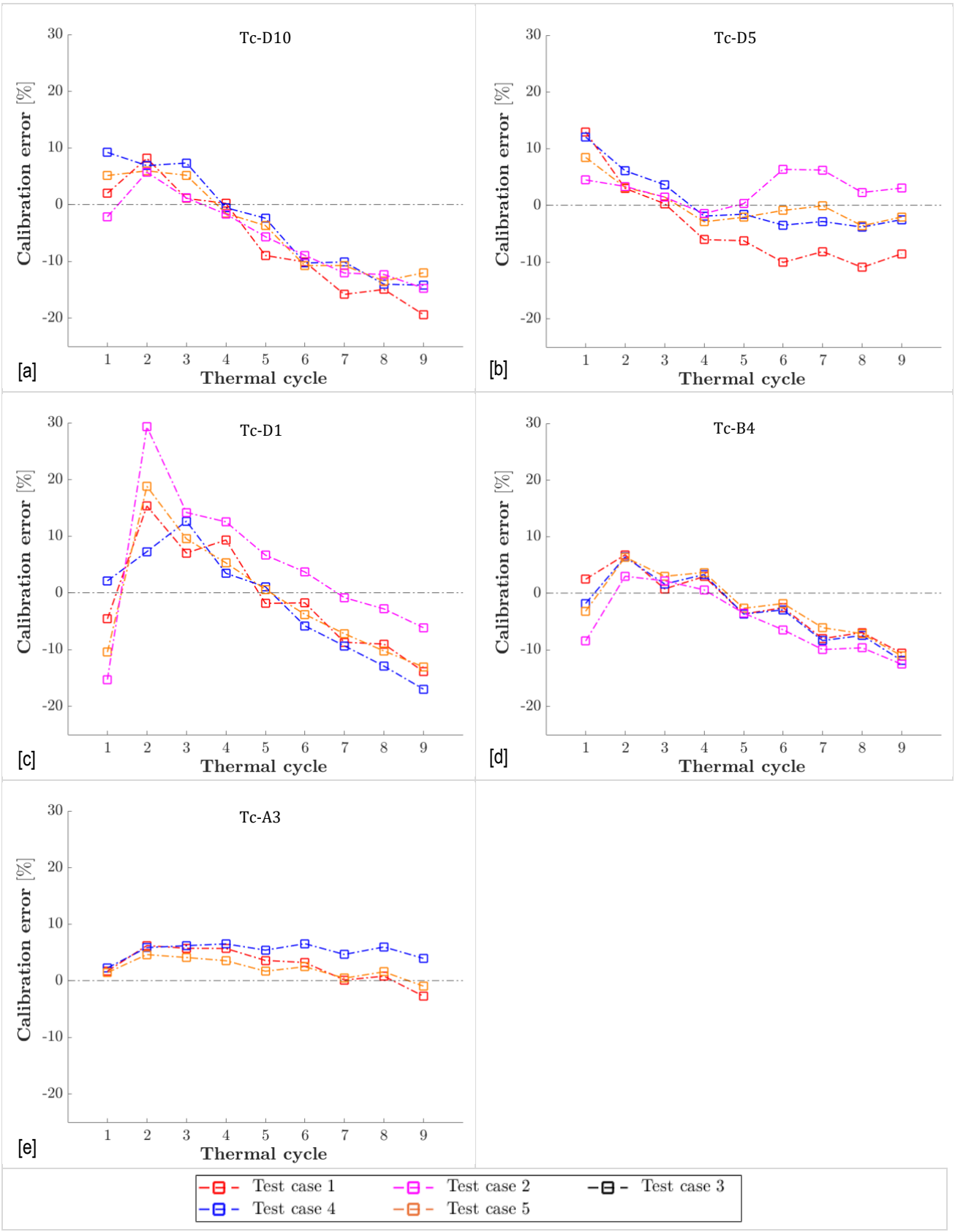

Figure F.1: Calibration error of the F.E. model, calculated during the deposition of the simulated ten-layer weld deposit. [a] Temperature measurement point Tc-D10; [b] Temperature measurement point Tc-D5; [c] Temperature measurement point Tc-D1; [d] Temperature measurement point Tc-B4; [e] Temperature measurement point Tc-A3.